

Electronic Deactivation and Reaction
Dynamics of H-bonded Molecular Systems
Studied by Femtosecond Time-Resolved
Vibrational Absorption Spectroscopy

DISSERTATION

zur Erlangung des Doktorgrades

Dr. rer. nat.

der Mathematisch-Naturwissenschaftlichen Fakultät
der Christian-Albrechts-Universität zu Kiel

vorgelegt von

HENDRIK BÖHNKE

Institut für Physikalische Chemie

Kiel 2019

Erster Gutachter: Prof. Dr. Friedrich Temps
Zweiter Gutachter: Prof. Dr. Bernd Hartke

Tag der mündlichen Prüfung: 09. Juli 2019
Zum Druck genehmigt: 09. Juli 2019

Erklärung

Hiermit erkläre ich, dass die vorliegende Abhandlung – abgesehen von der Beratung durch meinen Betreuer Prof. Dr. Friedrich Temps – nach Inhalt und Form meine eigene Arbeit ist. Diese Arbeit hat weder in Auszügen noch in ganzer Form einer anderen Stelle im Rahmen eines Prüfungsverfahrens vorgelegen. Sie wurde in ihrer Gesamtheit nicht veröffentlicht und auch nicht zur Veröffentlichung eingereicht. Teile dieser Arbeit, im Speziellen die Arbeiten zu 2-Aminopurin (2AP) und dem 2-Aminopurin–Thymin Basenpaar (2AP·T) sowie die Untersuchungen zum H-Transfer-Schalter NPPCA wurden in fachwissenschaftlichen Zeitschriften veröffentlicht.

KAPITEL 3

H. Böhnke, K. Röttger, R. A. Ingle, H. J. B. Marroux, M. Bohnsack, A. J. Orr-Ewing and F. Temps, „Efficient Intersystem Crossing in 2-Aminopurine Riboside Probed by Femtosecond Time-Resolved Transient Vibrational Absorption Spectroscopy“, *Phys. Chem. Chem. Phys.*, 2018, **20**, 20033–20042.

KAPITEL 4

H. Böhnke, K. Röttger, R. A. Ingle, H. J. B. Marroux, M. Bohnsack, N. K. Schwalb, A. J. Orr-Ewing and F. Temps, „Electronic Relaxation Dynamics of UV-Photoexcited 2-Aminopurine–Thymine Base Pairs in Watson–Crick and Hoogsteen Conformations“, *J. Phys. Chem. B*, 2019, **123**, 2904–2914.

KAPITEL 5

H. Böhnke, J. Bahrenburg, X. Ma, K. Röttger, C. Näther, M. F. Rode, A. Sobolewski and F. Temps, „Ultrafast Dynamics of the ESIPT Photoswitch *N*-(3-Pyridinyl)-2-Pyridine-carboxamide“, *Phys. Chem. Chem. Phys.*, 2018, **20**, 2646–2655.

Diese Arbeit ist unter Einhaltung der Regeln guter wissenschaftlicher Praxis der Deutschen Forschungsgemeinschaft entstanden. Ein akademischer Grad wurde mir nicht entzogen.

Kiel, im Mai 2019

HENDRIK BÖHNKE

Danksagung

If I have seen further it is by standing on ye shoulders of Giants

Die vorliegende Arbeit wäre ohne die Unterstützung einer Vielzahl von Personen in dieser Form nicht möglich gewesen. An dieser Stelle möchte ich all denjenigen danken, die zum Gelingen dieser Dissertation auf die eine oder andere Weise beigetragen haben.

An erster Stelle bedanke ich mich ganz herzlich bei meinem Doktorvater Prof. Friedrich Temps für die vielen interessanten Jahre in seinem Arbeitskreis und die Möglichkeit, auf diesem spannenden Forschungsgebiet tätig sein zu dürfen. Die Leuchtkraft Ihrer Begeisterung für die Forschung und Ihre engagierte Unterstützung haben maßgeblich zum Gelingen dieser Arbeit beigetragen.

Dem gesamten Arbeitskreis – Mats, Shuangqing, Uta, Deef, Schatzi, Rebecca, Megow, Jonas, Birthe, Pascal, Simone, Monika, Joachim und Falk – danke ich für die kollegial-freundschaftliche Atmosphäre während der gesamten Zeit.

Inbesondere bedanke ich mich bei meinen wissenschaftlichen Patentanten Mayra, Julia und Käthe, die mich über die Jahre mit viel Geduld in die femto-Thematik eingearbeitet haben. Auch Ole Hüter möchte ich an dieser Stelle dankend erwähnen. Ganz besonders danke ich Käthe für die Erfahrungen über die Grenzen von Kiel hinaus.

Special thanks goes out to Prof. Andrew Orr-Ewing and his co-workers for the opportunity to visit his labs in Bristol twice for very fertile TVAS measurement times. A significant amount of this Thesis was possible thanks to your kind and welcoming nature.

Regarding the establishment of the TVA spectrometer in Kiel, I want to thank Xiaonan and Käthe for laying invaluable solid experimental and LabVIEW-related foundations at the early stages of the project.

Also, I want to thank Prof. Andrej Sobolewski and his co-workers for our collaboration on the ESIPT switch NPPCA.

Ich danke „meinen“ F3-Praktikanten, Bachelor- und Master-Kandidaten/-innen Carsten, Birthe, Markus, Jana, Hendrik und Amke für ihren fleißigen Einsatz. Auch wenn die Untersuchungen zu den Zimtsäure-Derivaten und den schaltbaren mini-Proteinen ihren

Weg nicht in diese Arbeit gefunden haben, haben wir doch einiges zusammen entwickelt und gelernt.

In diesem Zusammenhang bedanke ich mich ebenso bei den Lebensmittel-Technologinnen Julia Keppler und Prof. Karin Schwarz sowie bei Matze Lipfert und Prof. Frank Sönnichsen für stets engagierte und freundliche Zusammenarbeit.

Bei Tanja Stojić und Sonja Ehmke bedanke ich mich für das schnelle und unbürokratische Lösen so machner alltäglicher Angelegenheiten.

Ferner bedanke ich mich bei allen technischen Mitarbeitern aus Werkstatt und Institut. Insbesondere gilt mein Dank Timo für sein Engagement, den TVAS Spülgas-Kasten möglichst praktikabel und gleichsam ästhetisch zu gestalten. Andreas und Frank Laasch danke ich für das kurzfristige Bearbeiten von unzähligen Bitten à la „ähm, ich bräuchte da bitte mal was, das muss Folgendes können und am besten gestern ...“. In eine ähnliche Kategorie fallen auch die Anfragen bei Klaus, Kerstin, Mark und Haxhi, bei denen ich mich ebenfalls für ihre Hilfe bedanken möchte. Für seinen steten Einsatz um das betagte FTIR-Experiment, die Wartung von Spülgas-Generatoren und den kontinuierlichen Nachschub mit deuterierten Lösungsmitteln bedanke ich mich herzlich bei Joachim. Falk danke ich für seine unerschöpfliche Begeisterungsfähigkeit, seine Liebe zum Detail und seine stets herzlichen Zusprüche.

Alexander Thrun danke ich neben der Hilfestellung bei unzähligen LaTeX-Problemen vor allem für Quatsch und Tratsch in Büro 317. Ich werde so manches so schnell nicht vergessen – wie auch? Nein. Immer nie nicht – merken!

Für die Duldung von mongolischem Kehlkopf-Gesang und die musikalische Untermalung der femto-Messungen mit ost-europäischen Männer-Chören bedanke ich mich bei meinem Keller-(Geschwister)Kind Jonas.

Für die Gestaltung von Freizeitaktivitäten danke ich Hendrik, Jonas und Lambert. Vielen Dank für die schönen Momente am NOK, bei WoW & HotS und beim Abhängen im NORDBLOC.

Bei den „Kielern“ Björn, Jan&Yasi, Jones, Jule&Sven, Schulz, Audi&Sandra, Base&Steffi, Dina, Max&Astrid und Mats bedanke ich mich für entspannte sit-ins, (Rollen-)Spieleabende und legendäre Doppelkopf-Duelle. Danke für 25 Jahre Freundschaft.

Großer Dank geht an meine Eltern sowie an Anna, Oma, Barbara, Ernie, Frank, Barbara und Anna für rücksichtsvolles Verständnis, familiären Rückhalt und Hilfe in allen Lebenslagen.

Paula danke ich für ihre unendliche Geduld, bedingungslose Unterstützung, ihre Liebe in guten, wie in schlechten Tagen und so vieles mehr – DANKE.

Abstract

The central goal of this Thesis was the investigation of ultrafast electronic deactivation pathways in both *intra*- and *intermolecularly* H-bonded systems in a time-resolved and structure-sensitive manner by a combination of spectroscopic pump–probe techniques and quantum chemical calculations. Towards these ends, a transient vibrational absorption spectrometer was built, which allows for the investigation of the temporal evolution of characteristic vibrational marker bands in the spectral region from 4000–800 cm^{-1} after UV excitation. Using this setup, 2-aminopurine (2AP), the highly fluorescent structural isomer of adenine (\equiv 6-aminopurine), was investigated in monomeric form and upon H-bonding with thymine (T) in Watson–Crick (WC) and Hoogsteen (HS) conformations as a model system for *intermolecular* H-bonding. An exploratory study on free 2AP revealed the involvement of an intermediate state ($\tau < 100$ ps) of $n\pi^*$ character in the deactivation dynamics towards concurrent efficient ground-state recovery and triplet state formation by $^1\pi\pi^*$ decay within $\tau_{2AP} = 740 \pm 15$ ps. Upon H-bonding of 2AP with T in the WC conformation, internal conversion towards the $n\pi^*$ state is hindered by an increased potential energy barrier. Thus, the excited-state lifetime of the 2AP chromophore in the H-bonded 2AP·T network is increased to $\tau_{2AP\cdot T, WC} = 1.6 \pm 0.4$ ns. In the HS form, however, the 2AP moiety features a distorted excited-state minimum structure. Induced by H-bonds with T, this bent structure of 2AP opens up novel deactivation pathways for efficient ground-state recovery with $\tau_{2AP\cdot T, HS} = 68 \pm 15$ ps. The observed kinetics are discussed in terms of excited-state *interbase* double-proton transfer. Moreover, in another case study, the influence of excited-state *intramolecular* proton transfer (ESIPT) on electronic deactivation and reaction dynamics was investigated for 2-acetylpyrrole (2AcPy), 3-hydroxypicolinic acid (3HPA) and *N*-(3-pyridinyl)-2-pyridinecarboxamide (NPPCA). Although more elaborate quantum chemical calculations are required to ascribe all experimental TVA features to distinct transient species in 2AcPy and 3HPA, unambiguous indications for ESIPT were found in the dynamics of NPPCA. Aided by excited-state computations, electronic deactivation within $\tau_{NPPCA, 1} = 90 \pm 10$ fs and $\tau_{NPPCA, 2} = 610 \pm 10$ fs after UV excitation could be attributed to transient formation of a twisted intermediate species by *intramolecular* H-transfer. Back in the ground state, the dynamics are completed within $\tau_{NPPCA, 3} = 5.10 \pm 0.80$ ps and $\tau_{NPPCA, 4} = 20.0 \pm 1.0$ ps towards incomplete recovery of the initially excited isomer and formation of a novel photochromic proton-transferred product, which survives on the nanosecond scope of the time-resolved experiments.

Zusammenfassung

In der vorliegenden Dissertation wurden die ultraschnellen elektronischen Desaktivierungswege von *intramolekular* sowie *intermolekular* über H-Brücken gebundenen Systemen zeitaufgelöst und struktur-spezifisch durch eine Kombination aus spektroskopischen Anregung–Abfrage Methoden und quantenchemischen Rechnungen untersucht. Zu diesem Zweck wurde ein transientes Schwingungs-Absorptionsspektrometer aufgebaut, welches die Untersuchung der zeitlichen Entwicklung charakteristischer molekularer Schwingungs-Moden im spektralen Bereich von $4000\text{--}800\text{ cm}^{-1}$ nach UV-Anregung ermöglicht. Mithilfe dieses Aufbaus wurde 2-Aminopurin (2AP), das stark fluoreszierende Struktur-Isomer von Adenin (\equiv 6-Aminopurin), sowohl in seiner freien Form als auch nach Paarung mit Thymin (T) in Watson–Crick (WC) und Hoogsteen (HS) Motiven als ein Modellsystem für *intermolekular* H-Brücken gebundene Systeme untersucht. Eine erste Studie zu freiem 2AP zeigte, dass ein transienter $n\pi^*$ Zustand ($\tau < 100\text{ ps}$) die Dynamik zum Wiederauffüllen des Grundzustandes und zur gleichzeitigen Bildung eines Triplet-Zustandes aus dem initial bevölkerten $^1\pi\pi^*$ -Zustand mit $\tau_{2AP} = 740 \pm 15\text{ ps}$ dirigiert. Durch die Ausbildung von H-Brücken mit T in der WC-Form wird die Zugänglichkeit für innere Umwandlung erschwert. Folglich wurde eine verlängerte Lebenszeit des angeregten Zustands von $\tau_{2AP\cdot T, WC} = 1.6 \pm 0.4\text{ ns}$ ermittelt. Im Gegensatz zur WC-Konformation ermöglicht die Ausbildung von H-Brücken in der HS-Form des 2AP·T Basenpaares neue Desaktivierungswege für das Wiederauffüllen des Grundzustandes in $\tau_{2AP\cdot T, HS} = 68 \pm 15\text{ ps}$ aufgrund einer verzerrten Struktur im elektronisch angeregten Zustand. Die deutlich verkürzte Lebenszeit des 2AP·T(HS) Dimers wurde im Hinblick auf einen *intermolekularen* Protonen-Transfer im angeregten Zustand diskutiert. Außerdem wurde der Einfluss von *intramolekularem* Protonen-Transfer innerhalb von elektronisch angeregten Zuständen (excited-state *intramolecular* proton transfer, ESIPT) auf die Desaktivierungs- und Reaktions-Dynamik an den Beispielen von 2-Acetylpyrrol (2AcPy), 3-Hydroxypicolinsäure (3HPA) und *N*-(3-Pyridinyl)-2-Pyridincarboxamid (NPPCA) untersucht. Während weitere quantenchemische Rechnungen benötigt werden, um die experimentell beobachteten Schwingungsbanden von 2AcPy und 3HPA expliziten strukturellen Spezies zuordnen zu können, konnten eindeutige Beweise für ESIPT-Prozesse in der Dynamik von NPPCA gefunden werden. Unterstützt von Rechnungen im elektronisch angeregten Zustand konnte die ultraschnelle Desaktivierung nach UV-Anregung innerhalb von $\tau_{NPPCA, 1} = 90 \pm 10\text{ fs}$ und $\tau_{NPPCA, 2} = 610 \pm 10\text{ fs}$ einer intermediären Zwischenstruktur nach *intramolekularem* H-Transfer zugeordnet werden. Anschließend wird die Dynamik nach Rückkehr in den Grundzustand über das partielle Wiederauffüllen der Ausgangsstruktur sowie die Bildung eines Protonen-Transfer-Produktes, welches auf der Nanosekunden-Skala der zeitaufgelösten Experimente überlebt, innerhalb von $\tau_{NPPCA, 3} = 5.10 \pm 0.80\text{ ps}$ und $\tau_{NPPCA, 4} = 20.0 \pm 1.0\text{ ps}$ abgeschlossen.

Contents

INTRODUCTION AND EXPERIMENTAL SECTION	1
1 Introduction	1
2 Experimental Section	17
2.1 Experimental Setup	18
2.2 Coherent Artifacts and Data Analysis	26
2.3 Assignment of Experimental Vibrational Bands	27
RESULTS AND DISCUSSION	35
3 Efficient Intersystem Crossing in 2-Aminopurine Riboside	35
3.1 Introduction	36
3.2 Methods	37
3.3 Results	39
3.4 Discussion	45
3.5 Conclusions	51
3.6 Supplementary Information	59
4 Electronic Relaxation Dynamics of 2-Aminopurine–Thymine Base Pairs	65
4.1 Introduction	66
4.2 Methods	67
4.3 Results	69
4.4 Discussion	78
4.5 Conclusions	82
4.6 Supplementary Information	89
5 Ultrafast Dynamics of the ESIPT Photoswitch NPPCA	91
5.1 Introduction	92
5.2 Methods	94
5.3 Results	96
5.4 Discussion	105
5.5 Conclusion	108
5.6 Supplementary Information	115
5.7 Additional Information	130

6	Electronic Deactivation Pathways of 2-Acetylpyrrole	133
6.1	Introduction	134
6.2	Methods	135
6.3	Results and Discussion	139
6.4	Conclusion	150
6.5	Supplementary Information	154
7	Deactivation and Reaction Dynamics of 3-Hydroxypicolinic Acid	155
7.1	Introduction	156
7.2	Methods	158
7.3	Results and Discussion	159
7.4	Conclusion	164
	CONCLUDING REMARKS	169
8	Summary	169
	ADDENDUM	175
9	TVAS LabVIEW Program	175
	List of Figures	179
	List of Tables	183

Despite mankind's interest in chemical transformations for millennia,^[1] a deep understanding of the underlying reaction mechanisms remained elusive for a vast amount of time. On a fundamental level, the motion of atoms, *i.e.* the breaking and making of chemical bonds, proceeds on the femtosecond ($1 \text{ fs} = 10^{-15} \text{ s}$) timescale. Thus, elementary reaction processes remained veiled until the advent of ultrafast pulsed laser systems and their application for time-resolved pump-probe experiments. In order to elucidate fundamental reaction pathways on the ultrafast timescale, a variety of pump-probe spectroscopic techniques has been developed ever since their birth in the 1980s.^[2] In short, a pair of coherent laser pulses is used to follow the ensuing molecular reaction and deactivation dynamics upon photo-induced electronic excitation. Towards these ends, the individual pump and probe pulse trains are modulated by means of non-linear optical frequency conversion processes after splitting the laser fundamental into two separate beam paths. In a first step, the photodynamics are initiated by electronic excitation by irradiation of the sample chromophores in the UV/vis spectral region by the prepared pump pulses. The molecular dynamics are then resolved by interaction of the sample ensemble with the probe pulses at discrete points in time after photoexcitation. Finally, by delaying the temporal arrival of the probe pulses with respect to the pump pulses (or *vice versa*), the entire molecular dynamics can be monitored by a series of pump-probe measurements at distinct time steps after photoexcitation (*cf.* Chapter 2). Prominent examples of time-resolved techniques probing electronic transitions in the UV/vis region are transient electronic absorption spectroscopy (TEAS) and time-resolved fluorescence (TRFL) techniques like fluorescence up-conversion and broad-band fluorescence Kerr-gating spectroscopy.

Determined by the respective absorption bands of a given organic sample chromophore, electronic absorption is commonly bound to the UV/vis region. Probing of the molecular dynamics, however, can in principle be achieved by a variety of pump-probe geometries and in different spectral regions. In this Thesis, time-resolved vibrational absorption spectroscopy (TVAS) has been employed to follow the photo-induced molecular reaction and deactivation pathways, as this particular time-resolved pump-probe method is sensitive not only to the character of excited electronic states, but also to the structural identity of the involved molecular species.

Probably the most archetypical chemical reaction constitutes the transfer of an H-atom or a proton.¹ To name but a few examples, H-bonding exerts a major impact on the structural stability of the double-helix DNA and its binding to proteins. Furthermore, in a more dynamic way, H-transfer constitutes a widespread motif for electronic deactivation and reaction pathways upon photo-induced electronic excitation.^[3-5] Although the transfer of a single H atom or proton may arguably be regarded as the simplest chemical reaction

¹For simplicity, H-transfer and proton-transfer processes are referred to as plain H-transfer from here on.

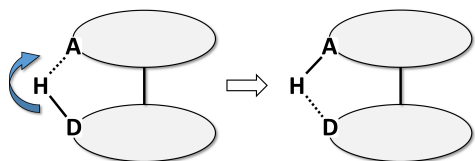
possible, experimental investigation of such processes is a challenging task as it unwinds on the ultrafast timescale. In fact, H-transfer dynamics are amongst the fastest chemical processes known.^[6–15]

Generally, H-bonding and H-transfer processes can occur between two individual molecules (*intermolecular*, cf. Fig. 1.1 (a)) or within two separated moieties of a single molecule (*intramolecular*, cf. Fig. 1.1 (b)).

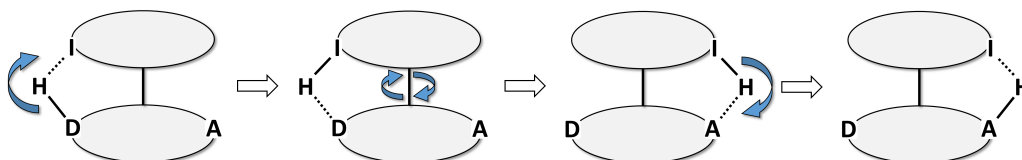
a) *intermolecular* single H-transfer



b) *intramolecular* single H-transfer



c) twist-assisted *intramolecular* H-transfer



d) *intramolecular* double H-transfer

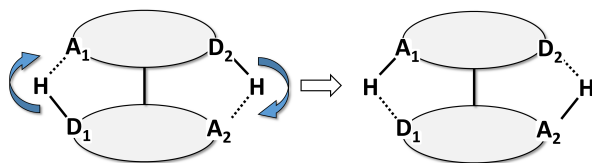


Figure 1.1: Schematic illustration of H-transfer mechanisms from donor sites (**D**) to acceptor sites (**A**) after photoexcitation. (a) *Intermolecular* single H-transfer, (b) *intramolecular* single H-transfer, (c) twist-assisted *intramolecular* H-transfer *via* an intermediate acceptor site (**I**) and (d) *intramolecular* double H-transfer *via* concerted or sequential reaction pathways.

Intermolecular H-transfer

A prominent example for *intermolecular* H-bonding is the double-helical structure of deoxyribonucleic acid (DNA). The entire genetic information of life as we know it is encrypted in the supramolecular framework of the DNA.^[16–18] In a nutshell, duplex DNA consists of two intertwined helices. Each helix is made up of the four canonical nucleobases – adenine (Ade), thymine (Thy), guanine (Gua) and cytosine (Cyt) – linked to

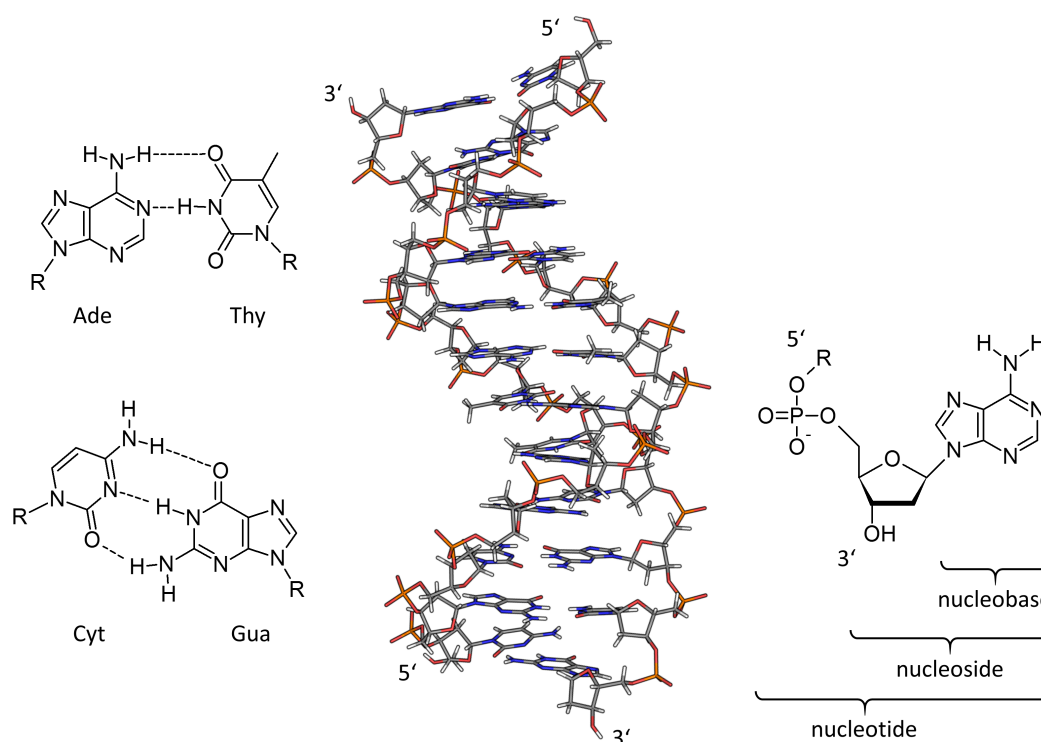


Figure 1.2: Illustration of Watson–Crick H-bonded canonical nucleobases Ade, Thy, Cyt, Gua and a double-stranded dodecamer (5'-CGCGAATTCGCG-3') in B-DNA conformation.

the deoxyribose phospho-diester backbone as pictured in Fig. 1.2. Within a single strand, the helical structure is corroborated by π -stacking of the adjacent nucleobases. In duplex DNA, two individual strands are combined and held together by *interstrand*, *i.e.* *interbase*, H-bonds. As illustrated in Fig. 1.2, Ade pairs with Thy, while Gua complexes with Cyt, in the Watson–Crick conformations in DNA. Thus, the complexity of life is ultimately encoded in the sequence of just the four canonical nucleobases in a single strand and the H-bonding with the corresponding nucleobase partners.^[16–18]

Upon decoding the genetic genome, the question why life evolved around these particular nucleobases has raised substantial interest. Investigation of the free individual bases by transient electronic absorption spectroscopy and time-resolved fluorescence techniques revealed ultrashort excited-state lifetimes in the femtosecond-to-picosecond regime.^[16,17,19–21] In general, ultrafast electronic deactivation dumps the electronic energy introduced by the UV pump pulses into vibrational degrees of freedom, which can efficiently be dissipated to the surrounding solvent as heat back in the electronic ground state. Thus, the short excited-state lifetimes of the free nucleobases render these compounds exceptionally photostable. Principally, intrinsic photostability minimizes the probability of mutagenic photoproduct formation^[22–33] and thus diminishes the need for energy-intensive enzymatic repair mechanisms.^[34–36]

While the ultrashort lifetimes of the nucleobases are considered to be beneficial for the emergence of life, they aggravate elucidation of the underlying photophysical deactivation pathways for spectroscopists. Especially for Ade, which features an ultrashort excited-state

lifetime below 1 ps, investigation of the de-excitation dynamics, both experimentally and by means of quantum chemical calculations, gets complicated by coupled, close-lying electronic states.^[16–20,37]

One approach to circumvent these limitations is to follow the deactivation dynamics of closely related model systems by structural modification of the parent molecule. For instance, 2-aminopurine (2AP, *cf.* Fig. 1.3) has been investigated for a deeper understanding of the relaxation pathways of Ade (\equiv 6-aminopurine).^[38,39] When compared to Ade and all other nucleobases, 2AP features a red-shifted UV/vis absorption band and a prolonged excited-state lifetime.^[40–45] Hence, 2AP has been subject to a number of experimental^[45–54] and theoretical^[38,39,47,55–63] studies. Time-resolved spectroscopic techniques probing the electronic transitions of 2AP in the UV/vis region yielded excited-state lifetimes in the nanosecond regime^[43–45] and emphasized the delicate transient ordering of different excited states during electronic deactivation by solvent effects and H-bonding motifs.^[43–45,64–75] However, a clear identification of the character of the electronic states involved in the de-excitation pathways remained elusive.^[38,39,45,51,61–63,74,76–81] Towards a deeper understanding of the transient pathways of photo-excited 2AP, time-resolved vibrational absorption spectroscopy has been employed in this Thesis due to its capability of resolving vibrational marker bands in a time-resolved and state-specific fashion. The observed bands are characteristic for the involved molecular species in their distinct electronic states (*cf.* Chapter 3).

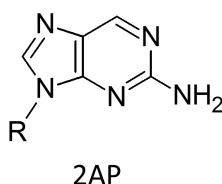


Figure 1.3: Representation of 2-aminopurine (2AP), the structural analogue of adenine (Ade).

Most importantly, due to its structural similarity to Ade, 2AP is not only used as a model system to further understand the dynamics of photo-excited free Ade, but is also employed as an intrinsic fluorescence probe for reporting on the micro-environment of the DNA by excited-state quenching.^[43,44,64–75,77–80,82–97] When incorporated into DNA as a substitute for Ade, 2AP pairs with Thy in the Watson–Crick conformation without substantial perturbation of the helical structure.^[98–103]

Currently, structural information within DNA is inferred from specific lifetimes observed in 2AP's fluorescence as an internal probe. The established picture ascribes excited-state quenching effects solely to dynamic *intrastrand* processes like charge-transfer and exciplex/excimer formation.^[70] In fact, many photo-initiated reaction and deactivation processes in DNA are associated with charge-transfer and exciplex/excimer formation within a single strand.^[70] However, as recently found as a major deactivation pathway for the G-C base pair for example,^[16,17] dynamics induced by H-bonding and H-transfer are widely ignored in the pathways responsible for excited-state quenching in 2AP-labeled

duplex DNA. Also, recent research reported that transient Hoogsteen motifs in duplex DNA enhance the structural complexity beyond the Watson–Crick limitations.^[104,105] In order to contribute to the established picture for excited-state quenching in 2AP-labeled DNA, structure-sensitive transient vibrational absorption spectroscopy has been performed on the dynamics of purely H-bonded 2AP with Thy (2AP·Thy) in the Watson–Crick and Hoogsteen conformations (*cf.* Fig. 1.4 and Chapter 4 of this Thesis).

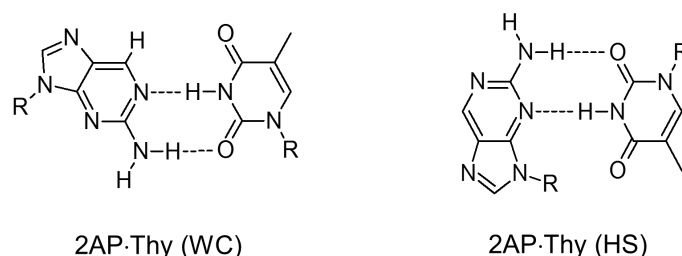


Figure 1.4: Structural motifs of the 2AP·Thy base pair in the Watson–Crick (WC) and Hoogsteen (HS) conformations.

Intramolecular H-transfer

Once the transfer of a proton in the excited-state manifold proceeds from one moiety to the other in a single molecule, the associated process is referred to as excited-state *intramolecular* proton transfer (ESIPT). Although ESIPT belongs to the fastest chemical reactions known, proceeding on timescales down to ~ 10 – 50 fs,^[6–15] it is not necessarily connected to a pathway for electronic deactivation *per se*. Hence, there are ESIPT chromophores with excited-state lifetimes in the nanosecond regime.^[3,4,106] The involvement of ESIPT in the deactivation and reaction pathways of the long-lived 2-acetylpyrrole (2AcPy, Fig. 1.5) was investigated in Chapter 6 of this Thesis.

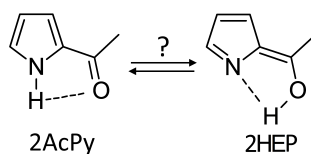


Figure 1.5: Structural representation of 2-acetylpyrrole (2AcPy) and its ESIPT species 2-(1-hydroxyethylidene)-pyrrole (2HEP).

If, however, the ESIPT is associated with electronic deactivation back to the ground state on the ultrafast timescale, conversion of electronic excitation energy to vibrational excess levels and subsequent dissipation to the solvent as heat renders such compounds exceptionally photostable. In fact, such chromophores find frequent use as photo-stabilizers and protective agents in sunscreens and polymers.^[107–113]

Lately, the concept of molecular switches has raised substantial attention for its application potential in molecular machines^[114–119] and data storage^[120–124] down on the nanometer scale. In short, molecular switches can be interconverted between at least two stable conformations by application of an external stimulus. In case of photochromic species, irradiation with light at different wavelengths can trigger the photo-induced formation of the corresponding photoproduct, preferentially featuring altered physical properties like dipole moment, conductivity or color. For structural molecular switches like azobenzene, stilbene and spiropyran as illustrated in Fig. 1.6, altered physical properties are achieved *via* structural transformations in the excited electronic state and the efficient de-excitation towards the ground state at a twisted geometry.^[125–129]

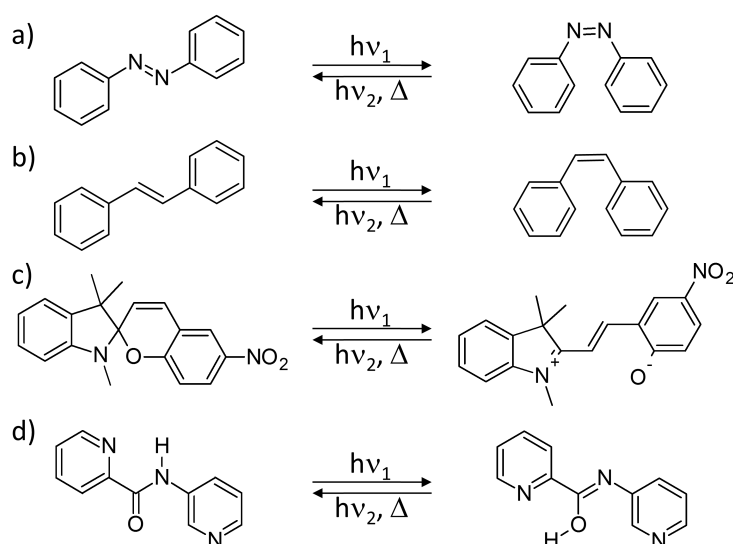


Figure 1.6: Selected bistable photochromic switches and their back-reaction: (a) azobenzene, (b) stilbene, (c) spiropyran and (d) the twist-assisted ESIPT switch NPPCA.

Recently, corroboration of the ultrafast timescale for ESIPT with efficient electronic deactivation *via* a S_1/S_0 conical intersection at a twisted structure towards formation of a thermally stable photoproduct back in the ground state has been proposed for so-called photochromic bistable molecular twist-assisted ESIPT switches (*cf.* Fig. 1.1 (c) and Fig. 1.6 (d)). Following the general concept illustrated in Fig. 1.1 (c), the deactivation and reaction dynamics are initiated by H-transfer upon UV photoexcitation from an initial donor site **D** towards an intermediate acceptor site **I** within the excited state. Subsequently, the excited-state population evolves towards a conical intersection with the electronic ground state at a twisted geometry. Back in the ground state, the cycle is completed by H-transfer towards the final acceptor site **A** to form the photoproduct. Hence, as a net result, the H-atom is transferred from the initial donor site to the final acceptor site *via* a large-scale motion along the molecular scaffold.^[130] Although electronic pump-probe methods like TEAS and TRFL provide the temporal resolution to investigate the ultrafast primary processes, they inherently lack in structural sensitivity to identify the transient species involved in geometric ESIPT switches. Thus, TVAS measurements have been performed in the present Thesis on the proposed ESIPT switch NPPCA (*cf.* Fig. 1.7 and Chapter 5).

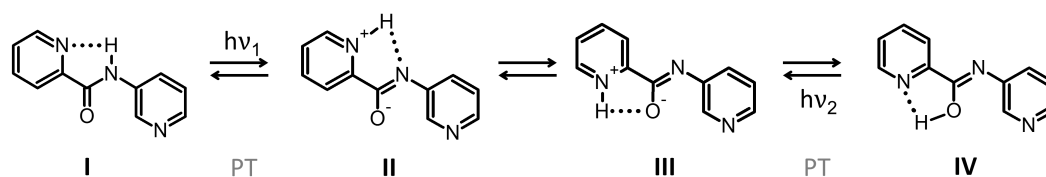


Figure 1.7: Schematic illustration of photo-induced reaction and deactivation pathways of the ESIPT switch NPPCA. Upon excitation of species **I**, the transient excited-state species **II** is formed *via* ESIPT. After de-excitation towards the electronic ground state at a twisted geometry, the transient species **III** undergoes isomerization towards the stable photoproduct **IV** *via* a second proton transfer back in the ground state.

Furthermore, other ESIPT switching pathways like excited-state double proton transfer (ESDPT, *cf.* Fig. 1.1 (d)) have been proposed^[131,132] and were measured by structure sensitive TVAS as well (*cf.* Fig. 1.8 and Chapter 7).

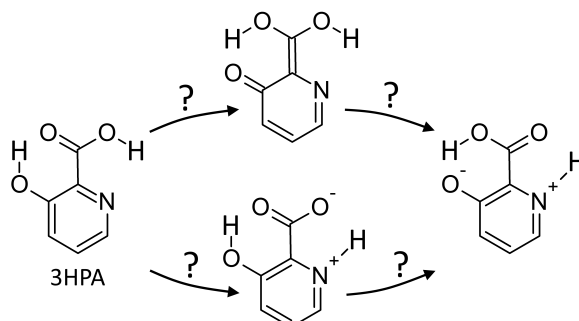


Figure 1.8: Proposed photo-induced reaction and deactivation pathways of the ESDPT switch 3HPA.

References

- [1] A. H. Zewail, *Angew. Chem. Int. Ed.*, 2000, **39**, 2586–2631.
- [2] M. Dantus, M. J. Rosker and A. H. Zewail, *J. Chem. Phys.*, 1987, **87**, 2395–2397.
- [3] L. G. Arnaut and S. J. Formosinho, *J. Photochem. Photobiol. A: Chem.*, 1993, **75**, 1–20.
- [4] S. J. Formosinho and L. G. Arnaut, *J. Photochem. Photobiol. A: Chem.*, 1993, **75**, 21–48.
- [5] J. Wierzchowski, *Nucleosides, Nucleotides and Nucleic Acids*, 2014, **33**, 626–644.
- [6] J. L. Herek, S. Pedersen, L. Bañares and A. H. Zewail, *J. Chem. Phys.*, 1992, **97**, 9046–9061.
- [7] S. Lochbrunner, A. J. Wurzer and E. Riedle, *J. Chem. Phys.*, 2000, **112**, 10699–10702.
- [8] S. Ameer-Beg, S. M. Ormson, R. G. Brown, P. Matousek, M. Towrie, E. T. J. Nibbering, P. Foggi and F. V. R. Neuwahl, *J. Phys. Chem. A*, 2001, **105**, 3709–3718.
- [9] S. Lochbrunner, T. Schultz, M. Schmitt, J. P. Shaffer, M. Z. Zgierski and A. Stolow, *J. Chem. Phys.*, 2001, **114**, 2519–2522.
- [10] K. Stock, T. Bizjak and S. Lochbrunner, *Chem. Phys. Lett.*, 2002, **354**, 409–416.
- [11] S. Lochbrunner, A. J. Wurzer and E. Riedle, *J. Phys. Chem. A*, 2003, **107**, 10580–10590.
- [12] C. Schrieffer, M. Barbatti, K. Stock, A. J. A. Aquino, D. Tunega, S. Lochbrunner, E. Riedle, R. de Vivie-Riedle and H. Lischka, *Chem. Phys.*, 2008, **347**, 446–461.
- [13] C. H. Kim and T. Joo, *Phys. Chem. Chem. Phys.*, 2009, **11**, 10266–10269.
- [14] M. Higashi and S. Saito, *J. Phys. Chem. Lett.*, 2011, **2**, 2366–2371.
- [15] J. Lee, C. H. Kim and T. Joo, *J. Phys. Chem. A*, 2013, **117**, 1400–1405.
- [16] C. T. Middleton, K. de la Harpe, C. Su, Y. K. Law, C. E. Crespo-Hernández and B. Kohler, *Annu. Rev. Phys. Chem.*, 2009, **60**, 217–239.

- [17] C. E. Crespo-Hernández, B. Cohen, P. M. Hare and B. Kohler, *Chem. Rev.*, 2004, **104**, 1977–2019.
- [18] J. D. Watson and F. H. Crick, *Nature*, 1953, **4356**, 737–738.
- [19] K. Kleineremanns, D. Nachtigallová and M. S. de Vries, *Int. Rev. Phys. Chem.*, 2013, **32**, 308–342.
- [20] M. Barbatti, A. J. A. Aquino, J. J. Szymczak, D. Nachtigallová, P. Hobza and H. Lischka, *Proc. Nat. Acad. Sci. U.S.A.*, 2010, **107**, 21453–21458.
- [21] N. K. Schwalb and F. Temps, *Science*, 2008, **322**, 243–245.
- [22] S. Marguet and D. Markovitsi, *J. Am. Chem. Soc.*, 2005, **127**, 5780–5781.
- [23] M. Boggio-Pasqua, G. Groenhof, L. V. Schaefer, H. Grubmueller and M. A. Robb, *J. Am. Chem. Soc.*, 2007, **129**, 10996–10997.
- [24] W. J. Schreier, T. E. Schrader, F. O. Koller, P. Gilch, C. E. Crespo-Hernández, V. N. Swaminathan, T. Carell, W. Zinth and B. Kohler, *Science*, 2007, **315**, 625–629.
- [25] W. J. Schreier, J. Kubon, N. Regner, K. Haiser, T. E. Schrader, W. Zinth, P. Clivio and P. Gilch, *J. Am. Chem. Soc.*, 2009, **131**, 5038–5039.
- [26] T. Climent, I. González-Ramírez, R. González-Luque, M. Merchán and L. Serrano-Andrés, *J. Phys. Chem. Lett.*, 2010, **1**, 2072–2076.
- [27] D. Roca-Sanjuan, G. Olaso-González, I. González-Ramírez, L. Serrano-Andrés and M. Merchán, *J. Am. Chem. Soc.*, 2008, **130**, 10768–10779.
- [28] D. L. Mitchell, *Photochem. Photobiol.*, 1988, **48**, 51–57.
- [29] C. Sheu and C. S. Foote, *J. Am. Chem. Soc.*, 1995, **117**, 6439–6442.
- [30] J. Cadet, T. Douki and J.-L. Ravanat, *Acc. Chem. Res.*, 2008, **41**, 1075–1083.
- [31] L. Sanche, *Nature*, 2009, **461**, 358–359.
- [32] S. Kanvah, J. Joseph, G. B. Schuster, R. N. Barnett, C. L. Cleveland and U. Landman, *Acc. Chem. Res.*, 2010, **43**, 280–287.

- [33] A. Kumar and M. D. Sevilla, *Chem. Rev.*, 2010, **110**, 7002–7023.
- [34] R. S. Lahue, K. G. Au and P. Modrich, *Science*, 1989, **245**, 160–164.
- [35] T. Lindahl, *Proc. Nat. Acad. Sci. U.S.A.*, 1974, **71**, 3649–3653.
- [36] A. Sancar and W. D. Rupp, *Cell*, 1983, **33**, 249–260.
- [37] R. Improta and V. Barone, *Photoinduced Phenomena in Nucleic Acids I. Topics in Current Chemistry* in M. Barbatti, A. Borin and S. Ullrich (eds.), 2014, **355**.
- [38] S. Perun, A. L. Sobolewski and W. Domcke, *Mol. Phys.*, 2006, **104**, 1113–1121.
- [39] L. Serrano-Andrés, M. Merchán and A. C. Borin, *Proc. Natl. Acad. Sci. U. S. A.*, 2006, **103**, 8691–8696.
- [40] D. C. Ward, E. Reich and L. Stryer, *J. Biol. Chem.*, 1969, **244**, 1228–1237.
- [41] J. Smagowicz and K. L. Wierzchowski, *J. Lumin.*, 1974, **8**, 210–232.
- [42] C. Santhosh and P. Mishra, *Spectrochim. Acta, Part A*, 1991, **47**, 1685–1693.
- [43] E. L. Rachofsky, E. Seibert, J. T. Stivers, R. Osman and J. B. A. Ross, *Biochemistry*, 2001, **40**, 957–967.
- [44] R. Neely, S. Megennis, D. Dryden and A. Jones, *J. Phys. Chem. B*, 2004, **108**, 17606–17610.
- [45] S. Lobsiger, S. Blaser, R. K. Sinha, H.-M. Frey and S. Leutwyler, *Nat. Chem.*, 2014, **6**, 989–993.
- [46] E. Nir, K. Kleinermanns, L. Grace and M. de Vries, *J. Phys. Chem. A*, 2001, **105**, 5106–5110.
- [47] K. A. Seefeld, C. Plützer, D. Löwenich, T. Häber, R. Linder, K. Kleinermanns, J. Tatchen and C. M. Marian, *Phys. Chem. Chem. Phys.*, 2005, **7**, 3021–3026.
- [48] K. Feng, G. Seefeld and K. Kleinermanns, *ChemPhysChem*, 2009, **10**, 886–889.
- [49] R. K. Sinha, S. Lobsiger and S. Leutwyler, *J. Phys. Chem. A*, 2011, **116**, 1129–1136.

- [50] R. K. Sinha, S. Lobsiger, M. Trachsel and S. Leutwyler, *J. Phys. Chem. A*, 2011, **115**, 6208–6217.
- [51] S. Lobsiger, R. K. Sinha, M. Trachsel and S. Leutwyler, *J. Chem. Phys.*, 2011, **134**, 114307.
- [52] M. A. Trachsel, S. Lobsiger, T. Schaär and S. Leutwyler, *J. Chem. Phys.*, 2014, **140**, 044331.
- [53] S. Smolarek, A. M. Rijs, W. J. Buma and M. Drabbels, *Phys. Chem. Chem. Phys.*, 2010, **12**, 15600–15606.
- [54] C. Canuel, M. Mons, F. Piuzzi, B. Tardivel, I. Dimicoli and M. Elhanine, *J. Chem. Phys.*, 2005, **122**, 074316.
- [55] R.-X. He, X.-H. Duan and X.-Y. Li, *Phys. Chem. Chem. Phys.*, 2006, **8**, 587–591.
- [56] A. Holmén, B. Nordén and B. Albinsson, *J. Am. Chem. Soc.*, 1997, **119**, 3114–3121.
- [57] A. Broo, *J. Phys. Chem. A*, 1998, **102**, 526–531.
- [58] J. M. Jean and K. B. Hall, *J. Phys. Chem. A*, 2000, **104**, 1930–1937.
- [59] B. Mennucci, A. Toniolo and T. Jacopo, *J. Phys. Chem. A*, 2001, **105**, 4749–4757.
- [60] E. L. Rachofsky, J. B. A. Ross, M. Krauss and R. Osman, *J. Phys. Chem. A*, 2001, **105**, 190–197.
- [61] V. Ludwig, M. S. do Amaral, Z. M. da Costa, A. C. Borin, S. Canuto and L. Serrano-Andrés, *Chem. Phys. Lett.*, 2008, **463**, 201–205.
- [62] J. Liang and S. Matsika, *J. Am. Chem. Soc.*, 2011, **133**, 6799–6808.
- [63] M. Barbatti and H. Lischka, *Phys. Chem. Chem. Phys.*, 2015, **17**, 15452–15459.
- [64] J. M. Jean and K. B. Hall, *Biochemistry*, 2004, **43**, 10277–10284.
- [65] J. M. Jean and B. P. Krueger, *J. Phys. Chem. B*, 2006, **110**, 2899–2909.
- [66] S. K. Pal, J. Peon and A. H. Zewail, *Chem. Phys. Lett.*, 2002, **363**, 57–63.

- [67] S. K. Pal, L. Zhao, T. Xia and A. H. Zewail, *Proc. Natl. Acad. Sci. U. S. A.*, 2003, **100**, 13746–13751.
- [68] O. J. G. Somsen, L. B. Keukens, M. N. de Keijzer, A. van Hoek and H. van Amerongen, *ChemPhysChem*, 2005, **6**, 1622–1627.
- [69] O. J. Somsen, A. van Hoek and H. van Amerongen, *Chem. Phys. Lett.*, 2005, **402**, 61–65.
- [70] A. C. Jones and R. K. Neely, *Q. Rev. Biophys.*, 2015, **48**, 244–279.
- [71] L. Zhao and T. Xia, *J. Am. Chem. Soc.*, 2007, **129**, 4118–4119.
- [72] T. Gelot, P. Tourón-Touceda, O. Creégut, J. Léonard and S. Haacke, *J. Phys. Chem. A*, 2012, **116**, 2819–2825.
- [73] E. Rachofsky, R. Osman and J. Ross, *Biochemistry*, 2001, **40**, 946–956.
- [74] O. F. Larsen, I. H. van Stokkum, M.-L. Groot, J. T. Kennis, R. van Grondelle and H. van Amerongen, *Chem. Phys. Lett.*, 2003, **371**, 157–163.
- [75] O. F. A. Larsen, I. H. M. van Stokkum, F. L. de Weerd, M. Vengris, C. T. Aravindakumar, R. van Grondelle, N. E. Geacintov and H. van Amerongen, *Phys. Chem. Chem. Phys.*, 2004, **6**, 154–160.
- [76] C. Reichardt, C. Wen, R. A. Vogt and C. E. Crespo-Hernández, *Photochem. Photobiol. Sci.*, 2013, **12**, 1341–1350.
- [77] D. A. Smith, L. F. Holroyd, T. van Mourik and A. C. Jones, *Phys. Chem. Chem. Phys.*, 2016, **18**, 14691–14700.
- [78] J. Liang, Q. L. Nguyen and S. Matsika, *Photochem. Photobiol. Sci.*, 2013, **12**, 1387–1400.
- [79] J. M. Remington, A. M. Philip, M. Hariharan and B. Kohler, *J. Chem. Phys.*, 2016, **145**, 155101.
- [80] T. Fiebig, C. Wan and A. H. Zewail, *ChemPhysChem*, 2002, **3**, 781–788.
- [81] R. González-Luque, T. Climent, I. González-Ramírez, M. Merchán and L. Serrano-Andrés, *J. Chem. Theory Comput.*, 2010, **6**, 2103–2114.
- [82] J. M. Jean and K. B. Hall, *Proc. Natl. Acad. Sci. U. S. A.*, 2001, **98**, 37–41.

- [83] S. M. Law, R. Eritja, M. F. Goodman and K. J. Breslauer, *Biochemistry*, 1996, **35**, 12329–12337.
- [84] K. Liebert, A. Hermann, M. Schlickerrieder and A. Jeltsch, *J. Mol. Biol.*, 2004, **341**, 443–454.
- [85] R. K. Neely and A. C. Jones, *J. Am. Chem. Soc.*, 2006, **128**, 15952–15953.
- [86] B. J. Lee, M. Barch, E. W. Castner, J. Völker and K. J. Breslauer, *Biochemistry*, 2007, **46**, 10756–10766.
- [87] N. N. Degtyareva, M. J. Reddish, B. Sengupta and J. T. Petty, *Biochemistry*, 2009, **48**, 2340–2346.
- [88] M. Li, Y. Sato, S. Nishizawa, T. Seino, K. Nakamura and N. Teramae, *J. Am. Chem. Soc.*, 2009, **131**, 2448–2449.
- [89] S. J. O. Hardman and K. C. Thompson, *Biochemistry*, 2006, **45**, 9145–9155.
- [90] E. Y. M. Bonnist and A. C. Jones, *ChemPhysChem*, 2008, **9**, 1121–1129.
- [91] H.-N. Nguyen, L. Zhao, C. W. Gray, D. M. Gray and T. Xia, *Biochemistry*, 2011, **50**, 8989–9001.
- [92] T. van Mourik and S. W. L. Hogan, *Struct. Chem.*, 2016, **27**, 145–158.
- [93] W. Frey, L. Sowers, D. Millar and S. Benkovic, *Biochemistry*, 1995, **34**, 9185–9192.
- [94] C. Hariharan, L. B. Bloom, S. A. Helquist, E. T. Kool and L. J. Reha-Kranz, *Biochemistry*, 2006, **45**, 2836–2844.
- [95] S. Kelley and J. Barton, *Science*, 1999, **283**, 375–380.
- [96] J. Genereux, S. Wuerth and J. Barton, *J. Am. Chem. Soc.*, 2011, **133**, 3863–3868.
- [97] J. Genereux and J. Barton, *Chem. Rev.*, 2010, **10**, 1642–1662.
- [98] L. C. Sowers, G. V. Fazakerley, R. Eritjat, B. E. Kaplant, M. F. Goodman and S. W. Benson, *Proc. Natl. Acad. Sci. U. S. A.*, 1986, **83**, 5434–5438.

- [99] T. M. Nordlund, S. Andersson, L. Nilsson, R. Rigler, A. Gråslund and L. W. Mclaughlin, *Biochemistry*, 1989, **28**, 9095–9103.
- [100] M. Kawai, M. J. Lee, K. O. Evans and T. M. Nordlund, *J. Fluoresc.*, 2001, **11**, 23–32.
- [101] K. Evans, D. Xu, Y. Kim and T. M. Nordlund, *J. Fluoresc.*, 1992, **2**, 209–216.
- [102] N. P. Johnson, W. A. Baase and P. H. von Hippel, *Proc. Natl. Acad. Sci. U. S. A.*, 2004, **101**, 3426–3431.
- [103] A. Dallmann, L. Dehmel, T. Peters, C. Mügge, C. Griesinger, J. Tuma and N. Ernsting, *Angew. Chem., Int. Ed.*, 2010, **49**, 5989–5992.
- [104] E. N. Nikolova, E. Kim, A. A. Wise, P. J. O'Brien, I. Andricioaei, and H. M. Al-Hashimi, *Nature*, 2011, **470**, 498–502.
- [105] D. Chakraborty and D. J. Wales, *J. Phys. Chem. Lett.*, 2018, **9**, 229–241.
- [106] A. Douhal, F. Lahmani and A. H. Zewail, *Chem. Phys.*, 1996, **207**, 477–498.
- [107] L. A. Baker, S. E. Greenough and V. G. Stavros, *J. Phys. Chem. Lett.*, 2016, **7**, 4655–4665.
- [108] J. Pospíšil and S. Nešpurek, *Prog. Polym. Sci.*, 2000, **25**, 1261–1335.
- [109] M. Zayat, P. Garcia-Parejo and D. Levy, *Chem. Soc. Rev.*, 2007, **36**, 1270–1281.
- [110] R. Kumasaka, A. Kikuchi and M. Yagi, *Photochem. Photobiol.*, 2014, **90**, 727–733.
- [111] M. Wiechmann, H. Port, F. Laermer, W. Frey and T. Elsaesser, *Chem. Phys. Lett.*, 1990, **165**, 28–34.
- [112] M. Wiechmann, H. Port, W. Frey, F. Laermer and T. Elsaesser, *J. Phys. Chem.*, 1991, **95**, 1918–1923.
- [113] A. L. Sobolewski, W. Domcke and C. Hättig, *J. Phys. Chem. A*, 2006, **110**, 6301–6306.
- [114] W. R. Browne and B. L. Feringa, *Nat. Nanotechnol.*, 2006, **1**, 25–35.
- [115] T. Muraoka, K. Kinbara and T. Aida, *Nature*, 2006, **440**, 512–515.

- [116] V. Balzani, A. Credi and M. Venturi, *Molecular Devices and Machines: Concepts and Perspectives for the Nanoworld*, Wiley-VCH: Weinheim, 2008.
- [117] V. Balzani, A. Credi and M. Venturi, *Chem. Soc. Rev.*, 2009, **38**, 1542–1550.
- [118] B. L. Feringa and W. R. Browne, eds., *Molecular Switches*, Wiley-VCH: Weinheim, 2011, Vol. 1&2.
- [119] S. Iamsaard, S. J. Aßhoff, B. Matt, T. Kudernac, J. J. Cornelissen, S. P. Fletcher and N. Katsonis *Nature Chemistry*, 2014, **6**, 229-235.
- [120] S. Kawata and Y. Kawata, *Chem. Rev.*, 2000, **100**, 1777–1788.
- [121] D. Gindre, A. Boeglin, A. Fort, L. Mager and K. D. Dorkenoo, *Opt. Express*, 2006, **14**, 9896–9901.
- [122] Y. Chen, J. P. Xiao, B. Yao and M. G. Fan, *Opt. Mater.*, 2006, **28**, 1068–1071.
- [123] A. S. Dvornikov, E. P. Walker and P. M. Rentzepis, *J. Phys. Chem. A*, 2009, **113**, 13633–13644.
- [124] H. Li, Q. Xu, N. Li, R. Sun, J. Ge, J. Lu, H. Gu and F. Yan, *J. Am. Chem. Soc.*, 2010, **132**, 5542–5543.
- [125] J. Bahrenburg, K. Röttger, R. Siewertsen, F. Renth and F. Temps, *Photochem. Photobiol. Sci.*, 2012, **11**, 1210–1219.
- [126] J. Bahrenburg, F. Renth, F. Temps, F. Plamper and W. Richtering, *Phys. Chem. Chem. Phys.*, 2014, **16**, 11549–11554.
- [127] J. Bao and P. M. Weber, *J. Am. Chem. Soc.*, 2011, **133**, 4164–4167.
- [128] J. Buback, M. Kullmann, F. Langhojer, P. Nuernberger, R. Schmidt, F. Würthner and T. Brixner, *J. Am. Chem. Soc.*, 2010, **132**, 16510–16519.
- [129] M. Sanchez-Lozano, C. M. Estévez, J. Hermida-Ramón and L. Serrano-Andres, *J. Phys. Chem. A*, 2011, **115**, 9128–9138.
- [130] L. Lapinski, M. J. Nowak, J. Nowacki, M. F. Rode and A. L. Sobolewski, *ChemPhysChem*, 2009, **10**, 2290–2295.

[131] M. F. Rode and A. L. Sobolewski, *J. Chem. Phys.*, 2014, **140**, 84301.

[132] M. F. Rode and A. L. Sobolewski, *Chem. Phys.*, 2012, **409**, 41–48.

In the following Section, the experimental setup for transient vibrational absorption spectroscopy (TVAS) will be discussed in some detail. In order to investigate photo-initiated molecular electronic deactivation and reaction processes in a time-resolved manner, TVAS follows the general concept of pump–probe spectroscopic techniques. As schematically shown in Fig. 2.1, irradiation of the sample with a UV excitation (pump) pulse results in population of an electronically excited state. The molecular response, which encodes the ensuing deactivation pathways towards recovery of the electronic ground state, or the reaction dynamics towards formation of photoproducts, can be followed in time by application of an appropriate probe pulse. By scanning the molecular response signal in small steps, snapshots of the ensuing processes can be taken at different points in time, thus allowing for the detection of the ensuing kinetic processes in a time-resolved fashion. Probing the molecular response at different times with respect to the initial photo-excitation is realized by spatially delaying the arrival of the probe pulse in the sample cell with respect to the pump pulse. Generally, the nature of the employed probe pulses may vary according to the molecular quantities of interest. For example, UV/vis probe pulses can be exploited to observe electronic transitions to higher-lying electronic states or non-radiative processes towards the electronic ground state (transient electronic absorption spectroscopy, TEAS). In order to utilize the inherent molecular structure sensitivity of infrared spectroscopy for time-resolved investigations, however, mid-IR probe pulses have been applied in a UV pump–mid-IR probe transient vibrational absorption setup in this work. As no stand-alone lasers with tunable and sufficiently short pulses are currently available in the mid-IR region, non-linear optical frequency conversion methods are exploited to obtain the required pulses. The detailed implementation of mid-IR probe pulses into a pump–probe scheme, the origin of coherent artifacts during data acquisition, as well as the methods for data analysis will be given in this Chapter.

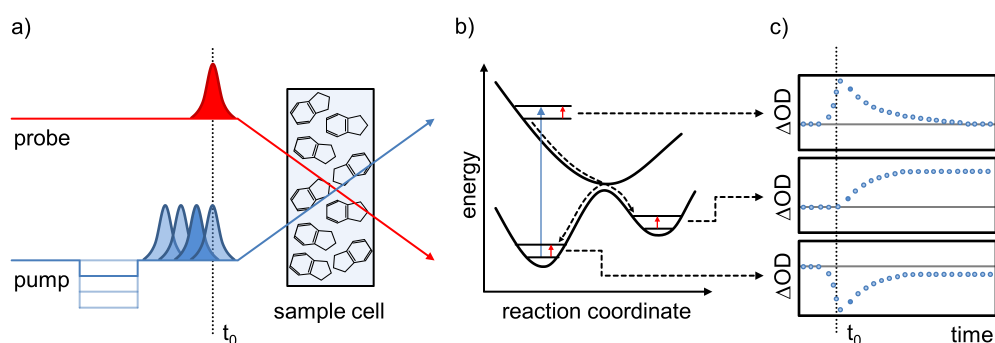


Figure 2.1: Schematic illustration of transient vibrational absorption spectroscopy (TVAS) as an example of time-resolved pump–probe spectroscopic techniques. (a) Pump–probe setup, (b) potential energy surfaces of an excited-state and a ground-state molecule undergoing electronic deactivation and photoisomerization through a conical intersection, (c) observable time traces of the different processes indicated by the transient change in optical density (ΔOD).

2.1 Experimental Setup

The present TVAS experiment employed 0.9 W (0.9 mJ per pulse) from a commercially available Ti:Sa amplifier (Libra HE, 800 nm, 90 fs, 1 kHz, 3.7 mJ per pulse, Coherent). As shown in Fig. 2.2, a fraction of the laser fundamental (0.3 mJ) was used for generation of UV pump pulses by third harmonic generation (THG). In principle, the generation of tunable pump pulses could readily be realized by a non-collinear optical parametric amplifier (NOPA) followed by frequency doubling *via* second harmonic generation (SHG) or three wave mixing *via* sum frequency generation (SFG). The remaining power of 0.6 W was used for the generation of mid-IR probe pulses. For wide tunability of the mid-IR pulses, a type-II BBO crystal was used for signal and idler generation in the near-IR region *via* optical parametric amplification (OPA). Subsequently, the near-IR pulses were mixed in a difference frequency generation (DFG) process in a type-I AgGaS₂ crystal, resulting in mid-IR pulses tunable from 2.6–11 μm (4000–800 cm^{-1}). After passing through the sample, the transient change in absorbance was detected on a mercury-cadmium-telluride (MCT) array detector as function of pump–probe temporal delay. The experimental design is similar to that described in Refs. [1-3].

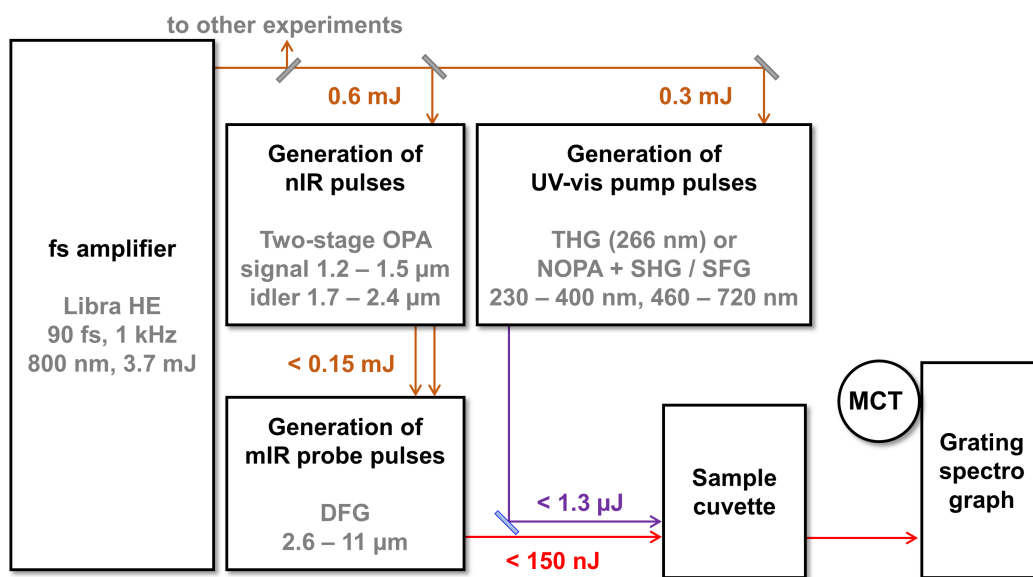


Figure 2.2: Schematic flow chart of the experimental transient vibrational absorption (TVA) setup.

Generation of UV Pump Pulses

Molecular electronic deactivation and reaction dynamics studied by time-resolved pump–probe spectroscopic techniques are typically induced by irradiation of the sample with excitation pulses in the UV/vis region. Generally, non-collinear optical parametric amplifiers can be utilized to obtain tunable UV/vis excitation pulses from 480–660 nm. Employing

further non-linear conversion steps as second harmonic generation or sum frequency generation with the laser fundamental may extend the accessible spectrum even further into the UV down to ~ 230 nm. However, as the molecular systems studied within the framework of the TVAS setup in Kiel demanded an excitation wavelength of ~ 266 nm, excitation pulses were readily provided by third harmonic generation (THG) of the laser's fundamental. For convenience and enhanced long-term stability due to collinear arrangement of the beams, a modified version of a commercially available THG kit (FKE-800-100, Femtokit FK Series, Eksma Optics) was used in this work. In short, 800 nm pulses from the laser fundamental with energies of 0.3 mJ per pulse were steered through a SHG-BBO crystal without focusing to generate 400 nm pulses. After passing through a compensation plate to correct for undesired group velocity delays between the 800 and 400 nm pulses, a half-wave plate was used to rotate the polarization of the 800 nm pulses to parallel with respect to the frequency-doubled pulses. Finally, as shown in Fig. 2.3, 266 nm pulses of energies up to 1.3 μ J per pulse were generated in a type-I THG-BBO crystal. The pulses were temporally delayed *via* a computer-controlled optical translation stage (M-521.DG, Physik Instrumente) equipped with a retroreflector (prot. Al, Edmund Optics) and guided to the sample cell by dielectric mirrors for excitation of the sample.

Generation of mid-IR Probe Pulses

The generation of mid-IR pulses was divided into two consecutive frequency conversion steps. First, near-IR signal (1.2–1.5 μ m) and idler (1.7–2.4 μ m) pulses were obtained in a two-stage optical parametric amplifier (OPA) in a BBO crystal pumped by the 800 nm fundamental. Subsequently, the desired mid-IR pulses were generated by difference frequency generation (DFG) in an AgGaS₂ crystal to yield tunable probe pulses (2.6–11.0 μ m, *cf.* Table 2.1).

As illustrated in Fig. 2.3, the near-IR pulses were generated in a type-II OPA-BBO crystal ($\theta = 27^\circ$, $\phi = 30^\circ$, 6 mm x 6mm x 4 mm, GWU-Lasertechnik). Towards these ends, broadband seed pulses, spectrally spreading into the near-IR region, were provided *via* super continuum generation by focusing a small fraction ($\ll 1\%$) of the 800 nm fundamental into a 2 mm sapphire window. In a first amplification stage, the white-light continuum was focused into the OPA-BBO crystal while overlapping spatially and temporally with 125 mW of the laser fundamental. In order to fulfil type-II phase matching conditions, the polarization of the seed pulses was rotated to perpendicular with respect to the 800 nm pump beam. While the idler pulses were removed by a dichroic mirror, the generated signal pulses were re-collimated and used as seed pulses for a second amplification process. In this second amplification stage, the remaining fraction ($\sim 80\%$) of the 800 nm pump pulses was overlapped with the signal pulses in the OPA-BBO from the rear side to generate intense signal and idler pulses with total energies of ~ 100 –150 μ J per pulse, corresponding

to an overall conversion efficiency of $\sim 25\%$. In order to prevent photo-degradation, both beams propagated unfocused through the crystal. The phase matching of the near-IR signal and idler pulses is shown in Fig. 2.4 (a). By variation of the phase matching angle from $25.4\text{--}27.6^\circ$, the signal and idler pulses were continuously tunable from $1220\text{--}1490\text{ nm}$ and $2310\text{--}1725\text{ nm}$, respectively, corresponding to $2.6\text{--}11.0\text{ }\mu\text{m}$ in the subsequent DFG stage.

Once undesired spectral components in the visible region were blocked by a long-pass filter, the collimated signal and idler pulses were delivered into the DFG stage in order to obtain the desired mid-IR pulses. Before focusing the signal and idler pulses in a collinear fashion into the AgGeS_2 -DFG crystal ($\theta = 39^\circ$, $\phi = 45^\circ$, $5\text{ mm} \times 5\text{ mm} \times 1.5\text{ mm}$, TOPAG Lasertechnik), the two beams were separated and recombined by a pair of dichroic mirrors. While the beam path of the idler pulses was fixed, the relative temporal arrival of the signal pulses into the DFG crystal could be altered by a mechanical translation stage. Spatial and temporal overlap of the signal and idler pulses in the DFG crystal finally resulted in the generation of the mid-IR pulses. As shown in Fig. 2.4 (b), broad mid-IR tunability from $2.6\text{--}11\text{ }\mu\text{m}$ ($4000\text{--}800\text{ cm}^{-1}$) could be achieved by changing the DFG phase matching angle from $45.5\text{--}33.9^\circ$.

In general, the DFG process could be realized in both type-I and type-II phase matching conditions in an AgGaS_2 crystal. In fact, as shown in Fig. 2.4 (c), type-II DFG features higher effective non-linearities compared to type-I phase matching conditions. However, as type-I DFG facilitates broadband tunability over a wide spectral region due to a rather flat phase matching curve (*cf.* Fig. 2.4 (b)), the final frequency conversion in the present setup takes place under type-I phase matching conditions. Consequently, tunable broadband (FWHM $\sim 250\text{ cm}^{-1}$) mid-IR probe pulses could be provided from $4000\text{--}800\text{ cm}^{-1}$. Due to the poor conversion efficiency of the DFG process ($\sim 4\%$), residuals of collinear signal and idler beams had to be removed by a long-pass filter. Thus, after passing through a germanium plate ($d = 2\text{ mm}$), pure mid-IR pulses were provided for the final pump–probe experiment as illustrated in Fig. 2.5. To prevent undesired absorption of mid-IR light by atmospheric CO_2 or water vapor, the entire optical setup was covered by a housing, which was permanently purged with dried air using a purge generator (PG 85 L, cmc-Instruments, $p_{\text{CO}_2} < 1\text{ ppm}$, $p_{\text{H}_2\text{O}} < 1\text{ ppm}$).

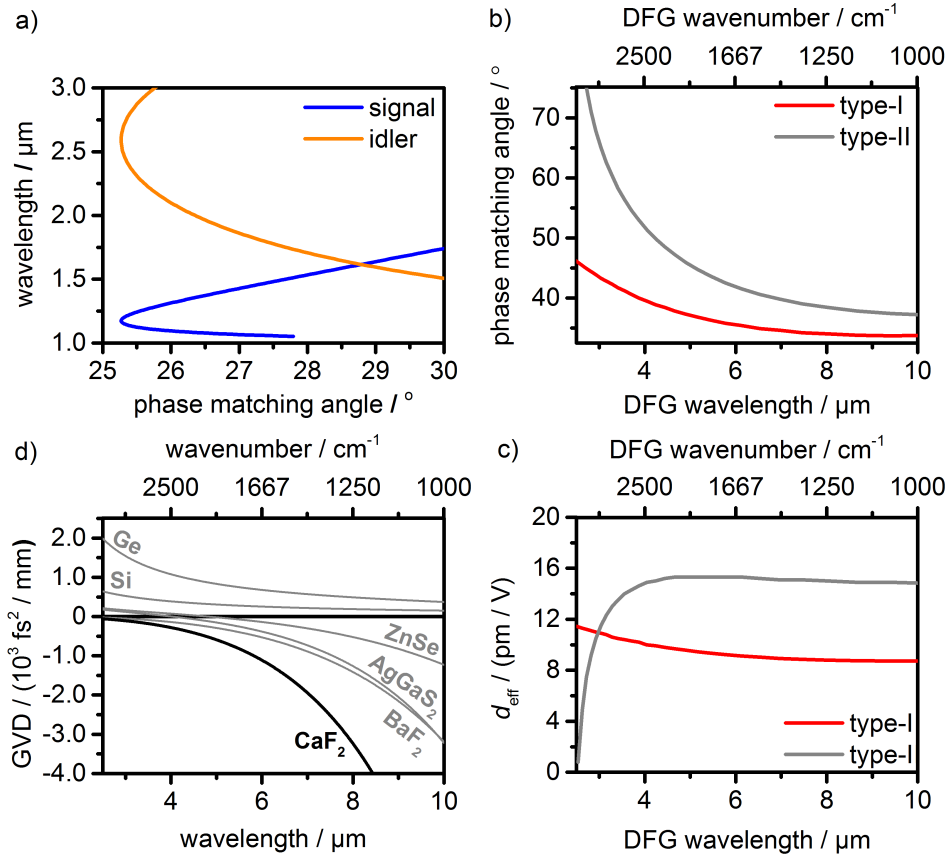


Figure 2.4: (a) Calculated phase matching conditions for signal and idler generation in a type-II optical parametric amplification in a BBO crystal pumped at 800 nm. (b) Comparison of type-I vs. type-II phase matching conditions for difference frequency generation in the AgGeS₂ crystal. (c) Associated effective nonlinearities d_{eff} . (d) Calculated second-order group velocity dispersion (GVD) for common IR materials per millimeter transmission depth, cf. Refs.[4–6].

Pump–Probe Setup

For time-resolved measurements, the UV excitation pulses and mid-IR probe pulses were aligned to obtain optimal spatial and temporal overlap inside the sample cell. As for any other transient absorption spectroscopic technique, the transient change in absorbance may be calculated by

$$\Delta\text{OD}(\lambda, \Delta t) = A^*(\lambda, \Delta t) - A^\circ(\lambda) \quad (2.1)$$

$$= -\log T^*(\lambda, \Delta t) - (-\log T^\circ(\lambda)) \quad (2.2)$$

$$= -\log \frac{I_{\text{pr}}^*(\lambda, \Delta t) \cdot I_{\text{ref}}^\circ(\lambda)}{I_{\text{ref}}^*(\lambda) \cdot I_{\text{pr}}^\circ(\lambda)} \quad (2.3)$$

Here, I_{pr}^* and I_{pr}° denote the intensities of two consecutive mid-IR probe pulses, where I_{pr}^* refers to the intensity after passing through the excited sample and I_{pr}° reflects the intensity probing the unexcited sample. Experimentally, the recording of consecutive intensities after passing through excited/unexcited molecules, was realized by using an

optical chopper (MC2000, Thorlabs) equipped with a 10 shot blade (MC1F10, Thorlabs) in the pathway of the excitation beam before the sample cell, operating at half the repetition rate of the Ti:Sa amplifier. Thus, every second pump pulse is blocked so that alternating sample transmissions can be recorded with and without photoexcitation. A second pair of pump on/off mid-IR pulses denoted as I_{ref}^* and I_{ref}° can be recorded after passing only through non-excited sample volume. As the transmission of the reference pulses will not be affected by the presence or absence of the pump pulses, the simultaneous detection of probe and reference pulses should – in principle – account for pulse-to-pulse fluctuations of the laser, therefore improving the transient data significantly. In the TVAS setup illustrated in Fig. 2.3, a germanium beam splitter (50%) can be inserted after generation of the mid-IR pulses in the DFG process to produce mid-IR probe and reference pulse pairs. UV excitation pulses and mid-IR probe pulses were focused into a home-built sample flow cell inspired by Bredenbeck *et al.*^[7] and equipped with O-rings (Chemraz, Greene, Tweed & Co. GmbH), a PTFE spacer ($d = 0.1\text{--}0.5$ mm) and CaF_2 windows ($d = 2$ mm, 25 mm diameter, Korth Kristalle). A gear pump (Reglo-Z analog, Ismatec) equipped with organic solvent resistant tubes was employed to flow the sample solutions continuously through the cell.

After passing through the sample flow cell, the mid-IR pulses were re-collimated and focused adequately with respect to f -matching onto the entrance slit of the grating spectrometer (iHR320, HORIBA). As illustrated in Fig. 2.6, the collimated mid-IR probe pulses are spectrally dispersed by a grating (75, 150 or 300 grooves/mm, corresponding to a spectral resolution of 26, 13 or 6 nm, respectively) before they were delivered onto a 32 pixel liquid N_2 cooled HgCdTe (MCT) detector array. To prevent undesired absorption of mid-IR

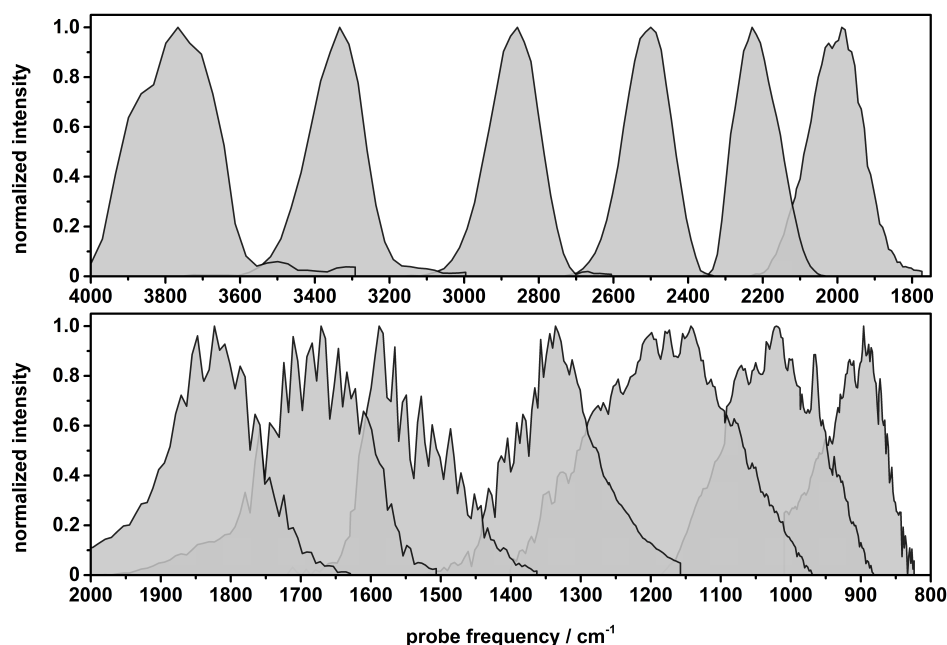


Figure 2.5: Broadband spectral range of mid-IR probe pulses from $4000\text{--}800$ cm^{-1} . Broadband tunability of mid-IR pulses was established and recorded by Dr. Xiaonan Ma. Absorption by atmospheric H_2O and CO_2 in the spectral region below 2000 cm^{-1} reflected by the “noisy” spectra was later eliminated by purging the entire experiment with dry air.

intensity by atmospheric CO₂ or water vapor, the entire spectrograph was permanently purged with dried air. For data acquisition, the spectrally dispersed and thus spatially separated infrared light hitting the MCT detector array, which acts as a photoresistor, changes the bias current in each of the 32 elements individually. The transient change in current is then integrated by a boxcar-type integrator (FPAS-6416, integration time 54–5154 ns, integration delay 50–1325 ns) synchronized with the Q-switch of the Ti:Sa amplifier. Finally, the integrator output is fed into a fast AD-converter for multi-channel single-shot data acquisition.

As the detector consists of two individual 32 pixel MCT arrays, probe and reference spectra can in principle be recorded simultaneously. However, the statistical thermal noise between the two individual MCT arrays outbalances the comparably little bias induced by pulse-to-pulse fluctuations of the Ti:Sa amplifier. As a consequence, the data quality suffers from utilizing reference pulses according to Equation 2.3. Thus, using the current detector, the data quality was drastically improved by simplifying the calculation of the transient change in optical density according to

$$\Delta OD(\lambda, \Delta t) = -\log \frac{I_{pr}^*(\lambda, \Delta t)}{I_{pr}^o(\lambda)} \quad (2.4)$$

in a probe-only configuration. From this, two-dimensional spectro-temporal transient absorption maps can be obtained by recording the spectrally resolved difference spectra at various time delays after photoexcitation. The implementation of the measurement routine in LabVIEW has been established by Dr. Katharina Röttger.

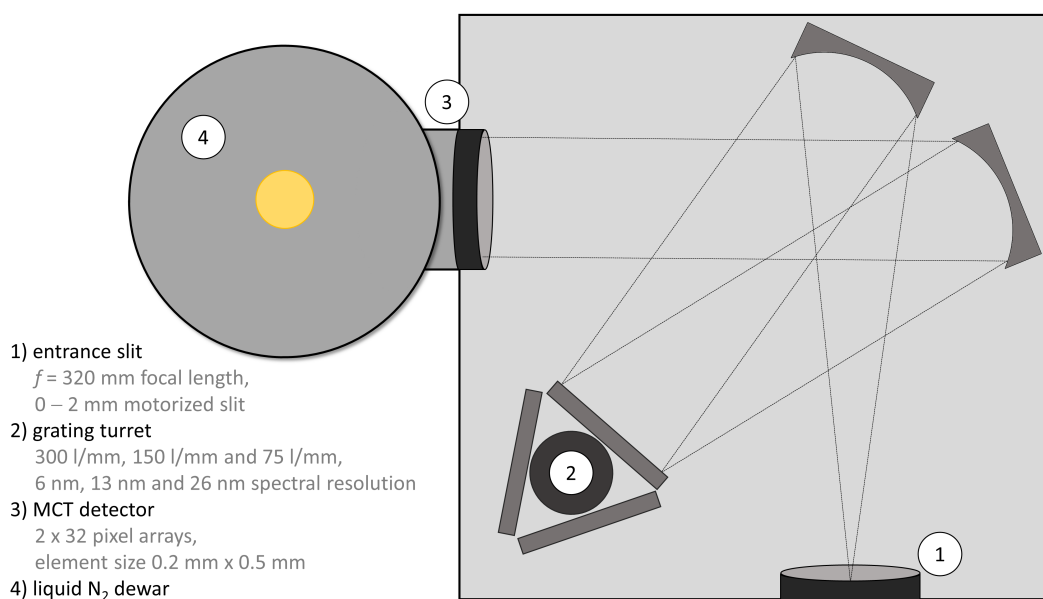


Figure 2.6: Illustration of the mid-IR beampath within the grating spectrograph.

Illustrating rather simple transient responses, Fig. 2.7 maps the spectro-temporal behavior of the solid semiconductor ZnSe upon excitation with 266 nm pump pulses. As can be seen from the two-dimensional representation of the transient data, the mid-IR probe pulses are not subject to significant group velocity dispersions. In fact, in the mid-IR region, chirped pulses can readily be corrected by insertion of commonly used materials in the beam path (*cf.* Fig. 2.4 (d)). Featuring virtually unchirped probe pulses, the temporal resolution of the transient absorption data is principally limited solely by the temporal width of the UV excitation pulses. Congruently, the instrument response function (IRF), displayed as a finite temporal rise in the transient data in Fig. 2.7, features a width of ≤ 150 fs.

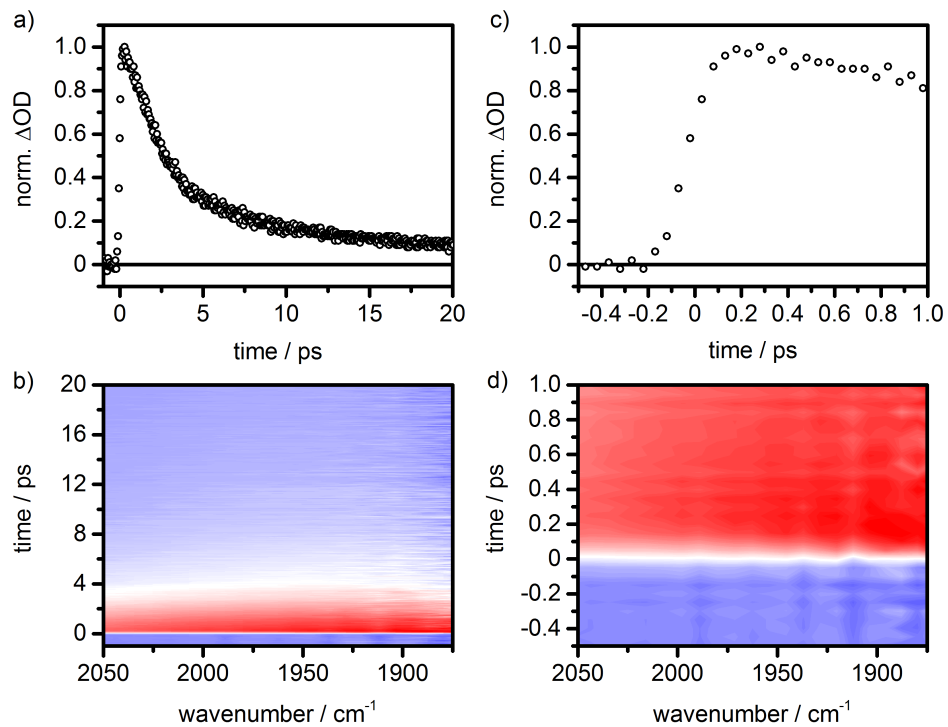


Figure 2.7: Spectro-temporal two-dimensional TVA data matrix of ZnSe excited at $\lambda_{\text{pump}} = 266$ nm and corresponding time profiles, (a and b) within the first 20 ps, (c and d) within 1 ps after photoexcitation.

In contrast to solid samples, the early-time transient signals of liquid probes are strongly superimposed by coherent artifacts. The origins of these coherent artifacts will be discussed in the following.

2.2 Coherent Artifacts and Data Analysis

As elaborated above, the temporal resolution of TVA data taken for solid samples relies solely – to first approximation – on the temporal width of the excitation pulses. For liquid samples, however, the early-time dynamics are strongly superimposed by a series of pump-induced coherent artifacts commonly known as transient lensing. The sum of these time-dependent processes effectively results in a transient gradient in the refractive index of the sample. As a consequence, as the probe beam propagates through the liquid sample, slight deflections and focusing leads to altered couplings of the probe into the detector.^[8–11]

The lensing phenomena originate from different interactions of the pump pulses with the liquid sample and are thus affecting the transient spectra on different timescales. For instance, excitation of sample molecules induces changes in the populations of the electronic ground state and the electronically excited states. Owing to a transient change in the associated dipole moments, the ensuing “population lens” will effectively perturb the refractive index of the sample in a time-dependent manner. Also, reorientation of solvent shells around the excited solutes (solvation lens) further contributes to a change in the refractive index. Moreover, excess energy dissipation to solvent molecules upon excitation above the electronic origin or subsequent non-radiative transitions from the initially excited state introduce local heating of the sample (thermal lens), which further affects the refractive index. Furthermore, depending on the intensity of the applied pulses, both solvent and solute molecules will align according to the electric field vector of the excitation (Kerr lens). Thus, the pump-induced anisotropy due to an optical electric field also contributes to the transient change in refractive index.

In order to minimize the transient lensing effects, which induce large-scale baseline offsets by pump-induced transient changes of the refractive index on the TVA spectra, reduced pump powers at loose focusing conditions and low sample concentrations are recommended. In practice, however, limited transmission in the mid-IR region for solvents requires rather high sample concentrations at thin sample volumes. Also, finite sample solubilities may require increased excitation powers. As a compromise, a balance between sample concentration and pump power has to be found for each sample depending on the particular prerequisites (solvent/solubility, absorption coefficient/concentration/volume thickness). Still, under normal conditions, the first transient spectra ($\Delta t \lesssim 1.0$ ps) will be subject to massive lensing effects, rendering these early-time transients invalid for data analysis. To account for pump-induced artifacts on longer timescales, the baseline correction implemented in the program package KOALA (Kinetics Observed After Light Absorption, University of Bristol)^[8] was used in this Thesis. KOALA allows for selection of up to five user-defined signal-free baseline regions to be fit with a unit, linear or quadratic function, which is subsequently subtracted from the experimental transient spectra.

For evaluation of the spectro-temporal data matrix, the first transient spectrum indicative of transient lensing features was chosen as the time when pump and probe pulses overlap in space and time within the sample cell (t_0 , *cf.* Fig. 2.1). After the corresponding spectral features ($\Delta t \leq 0.5$ to $\Delta t \leq 2.0$ ps) had faded, the observed bleached (negative) and transiently populated (positive) vibrational bands in the TVA spectra were fitted at every delay time to a sum of Gaussian functions in a global fashion according to

$$y = y_0 + \sum_i \frac{A_i}{w_i \sqrt{\pi/2}} \cdot \exp\left(-2 \cdot \frac{(\lambda - \lambda_i^c)^2}{w_i^2}\right). \quad (2.5)$$

Here, y_0 denotes the baseline of each transient spectrum, which is globally set to zero due to the baseline corrections in KOALA. The individual Gaussian functions are defined by their amplitudes A_i , widths w_i and central spectral positions λ_i^c . As the raw data obtained from the grating spectrograph are dispersed linearly in the wavelength regime, data analysis is also performed in the nanometer realm. For visual representation of the data, a conversion into the wavenumber regime is done. Due to the rather small spectral probe window of $\sim 250 \text{ cm}^{-1}$ in terms of energy, a Jacobian transformation^[12,13] may be dispensed towards these ends. Finally, the temporal evolution of the Gaussian amplitudes are fitted by a sum of exponentials in a global least-squares fashion to obtain kinetic time constants.

For even more robust evaluation of the TVA data, the amplitudes of related transient vibrational bands may be coupled by a time-independent factor f via $A_i = f_i \cdot A_j$. Coupling of related vibrational marker bands allows for description of distinct spectroscopic species by a sub-set of (coupled) Gaussian functions. As a result, the data analysis shifts from modeling individual vibrational marker bands towards time-resolved description of the underlying electronic states (*i.e.* ground-state recovery, decay and/or formation of excited states). In order to assign specific TVA marker bands to specific electronic states, quantum chemical vibrational mode calculations have been exploited in this Thesis. The powerful combination of determining experimental time constants and addressing them to specific electronic states on the grounds of their associated vibrational marker bands facilitates the understanding of the entire spectro-temporal evolution upon photoexcitation.

2.3 Assignment of Experimental Vibrational Bands

Ground-State Calculations

In order to assign experimental features to vibrational marker bands of the molecular species in different electronic states and to associate specific time constants with distinct kinetic processes, quantum chemical calculations have been performed. As a starting point, ground-state species were modeled at the level of density functional theory (DFT).

Density functional theory in the Kohn-Sham version models the effect of electron exchange and electron correlation as function of electron density. While generally exact, the true exchange-correlation functional remains elusive. Thus, the exchange-correlation functional is approached by means of density functional approximations (DFAs).^[14] As a result, a vast number of DFT-based methods has arisen over the years. In order to establish methodological clarity, the classification of different DFAs according to their underlying components – known as Jacob’s Ladder – subsumes the different DFAs under five sub-divisions (rung 1–5). As has been shown,^[15,16] performing calculations under higher rungs generally leads to more accurate results at the cost of higher computational time. Thus, rung 5 (double-hybrid functionals) calculations have been performed solely for thermochemical evaluations for the purposes of this work (*cf.* Chapter 4).

In order to assign experimentally observed vibrational features to ground-state species, DFAs of rung 4 (hybrid functionals) have been utilized in this work. In short, the molecular minimum structure was obtained by geometry optimization towards the steepest energy gradient. Subsequently, vibrational frequencies were extracted by the force constant matrix, *i.e.* the second derivatives of the energy with respect to position. Finally, the calculated harmonic vibrational frequencies were scaled^[17,18] by recommended factors of 0.94–0.99 to match the anharmonic experimental FTIR spectrum and the transient ground-state bleaches. For the molecules under investigation in this Thesis, best agreement with experimental data was found employing the rung 4 hybrid functionals M062X^[19] and B3LYP^[20] in conjunction with the 6-311+G** basis set.^[21–24] All rung 4 DFT calculations were performed using the Gaussian09 suite of programs.^[25]

Excited-State Calculations

Ground-state geometry optimizations and vibrational frequency calculations have also been performed at the MP2 (Møller-Plesset perturbation theory, truncated after the second term)^[26–29] level of theory, yielding comparable results. Subsequently, the minimum structure obtained from MP2 calculations was used as starting point for excited-state calculations. To evaluate the energetic orders of the excited electronic states from the Franck–Condon (FC) structure (MP2 minimum structure), vertical excitation energies (VEEs, single points) were calculated at the second-order approximate coupled-cluster (CC2) level of theory.^[30–35] CC2 was chosen since it is known to yield results of similar quality for electronically excited states as MP2 does for the electronic ground state.^[36]

Spawning on excited states from the FC structure, excited-state geometry optimizations and subsequent vibrational frequency calculations allowed for assignment of transiently populated states by their signatures in the mid-IR region. As for ground-state calculations, the harmonic excited-state vibrational modes were scaled^[37] by factors of 0.94–0.99. Al-

though performing robustly for the majority of calculations, CC2 struggles in the vicinity of regions on the potential energy hyper-surface (PEHS) with strong multi-configurational character like conical intersections. To overcome convergence failures in close proximity to such regions, second-order algebraic diagrammatic construction (ADC(2))^[38] calculations have been performed. While still remaining a single-reference method owing to the underlying Møller-Plesset electronic ground-state, ADC(2) performs more reliably at regions of the PEHS with strong electronic couplings due to a symmetric matrix as opposed to the non-symmetric Jacobian in CC2 calculations.^[39,40] Hence, the complete spectro-temporal evolution of the photo-initiated molecular dynamics can be followed in a state and structure sensitive way by tracking the spectro-temporal evolution of vibrational marker bands and assigning them on the grounds of quantum chemical calculations.

All MP2, CC2, and ADC(2) calculations in this Thesis were carried out in TurboMole7.0^[41] employing the (aug-)cc-pVDZ,^[42] def2-SVP,^[43] def2-TZVPP^[44] and def2-TZVPPD^[44–46] basis sets. For the correlation treatment and the description of excitation processes, all calculations employed the resolution of the identity (RI) approximation^[26,29,31–35,44,46–49] for the electron repulsion integrals.

Table 2.1: Calculated wavelength range for signal and idler generation in an OPA-BBO crystal pumped by the 800 nm laser fundamental alongside with the corresponding difference frequency for mid-IR generation in a DFG-AGS crystal.

signal / nm	idler / nm	mid-IR / nm	mid-IR / cm^{-1}
1200	2400	2400	4167
1210	2361	2482	4029
1220	2324	2568	3893
1230	2288	2659	3760
1240	2255	2756	3629
1250	2222	2857	3500
1260	2191	2965	3373
1270	2162	3079	3248
1280	2133	3200	3125
1290	2106	3329	3004
1300	2080	3467	2885
1310	2055	3614	2767
1320	2031	3771	2652
1330	2008	3941	2538
1340	1985	4123	2425
1350	1964	4320	2315
1360	1943	4533	2206
1370	1923	4765	2099
1380	1903	5018	1993
1390	1885	5295	1888
1400	1867	5600	1786
1410	1849	5937	1684
1420	1832	6311	1585
1430	1816	6729	1486
1440	1800	7200	1389
1450	1785	7733	1293
1460	1770	8343	1199
1470	1755	9046	1105
1480	1741	9867	1014
1490	1728	10836	923
1500	1714	12000	833

References

- [1] P. Hamm, R. A. Kaindl and J. Stenger, *Opt. Lett.*, 2000, **25**, 1798–1800.
- [2] F. Eickemeyer, R. A. Kaindl, M. Woerner, T. Elsaesser and A. M. Weiner, *Opt. Lett.*, 2000, **25**, 1472–1474.
- [3] R. A. Kaindl, M. Wurm, K. Reimann, P. Hamm, A. M. Weiner and M. Woerner, *J. Opt. Soc. Am. B*, 2000, **17**, 2086–2094.
- [4] N. Demirdöven, M. Khalil, O. Golonzka and A. Tokmakoff, *Opt. Lett.*, 2002, **27**, 433–435.
- [5] S. Backus, C. G. Durfee III, M. M. Murnane and H. C. Kapteyn, *Rev. Sci. Instrum.*, 1998, **69**, 1207–1223.
- [6] W. J. Tropf, M. E. Thomas and T. J. Harris, in *Handbook of Optics*, 2nd ed. M. Bass, ed. McGraw-Hill, New York, 1995, Vol. 2.
- [7] J. Bredenbeck and P. Hamm, *Rev. Sci. Instr.*, 2003, **74**, 3188–3189.
- [8] M. P. Grubb, A. J. Orr-Ewing and M. N. R. Ashfold, *Rev. Sci. Instr.*, 2014, **85**, 064104.
- [9] M. Terazima, *Chem. Phys. Lett.*, 1994, **230**, 87–92.
- [10] J. Yang and Y. Song, *Opt. Lett.*, 2009, **34**, 157–159.
- [11] M. Kopczynski, T. Lenzer, K. Oum, J. Seehusen, M. T. Seidel and V. G. Ushakov, *Phys. Chem. Chem. Phys.*, 2005, **7**, 2793–2803.
- [12] J. Mooney and P. Kambhampati, *J. Phys. Chem. Lett.*, 2013, **4**, 3316–3318.
- [13] J. Mooney and P. Kambhampati, *J. Phys. Chem. Lett.*, 2014, **5**, 3497–3497.
- [14] F. Jensen, in *Introduction to computational chemistry*, 2nd ed., ed. John Wiley & Sons Ltd., Chichester, 2007.
- [15] L. Goerigk, H. Kruse and S. Grimme, *ChemPhysChem*, 2011, **12**, 3421–3433.
- [16] L. Goerigk, A. Hansen, C. Bauer, S. Ehrlich, A. Najibi and S. Grimme, *Phys. Chem. Chem. Phys.*, 2017, **19**, 32184–32215.

- [17] M. L. Laury, S. E. Boesch, I. Haken, P. Sinha, R. A. Wheeler and A. K. Wilson, *J. Comput. Chem.*, 2011, **32**, 2339–2347.
- [18] M. L. Laury, M. J. Carlson and A. K. Wilson, *J. Comput. Chem.*, 2012, **33**, 2380–2387.
- [19] Y. Zhao and D. G. Truhlar, *Theor. Chem. Acc.*, 2008, **120**, 215–241.
- [20] A. D. Becke, *J. Chem. Phys.*, 1993, **98**, 5648–5652.
- [21] A. McLean and G. Chandler, *J. Chem. Phys.*, 1980, **72**, 5639–5648.
- [22] K. Raghavachari, J. Binkley, R. Seeger and J. Pople, *J. Chem. Phys.*, 1980, **72**, 650–654.
- [23] M. Frisch, J. Pople and J. Binkley, *J. Chem. Phys.*, 1984, **80**, 3265–3269.
- [24] T. Clark, J. Chandrasekhar, G. Spitznagel and P. Schleyer, *J. Comput. Chem.*, 1983, **4**, 294–301.
- [25] M. J. Frisch, G. W. Trucks, H. B. Schlegel, G. E. Scuseria, M. A. Robb, J. R. Cheeseman, G. Scalmani, V. Barone, B. Mennucci, G. A. Petersson, H. Nakatsuji, M. Caricato, X. Li, H. P. Hratchian, A. F. Izmaylov, J. Bloino, G. Zheng, J. L. Sonnenberg, M. Hada, M. Ehara, K. Toyota, R. Fukuda, J. Hasegawa, M. Ishida, T. Nakajima, Y. Honda, O. Kitao, H. Nakai, T. Vreven, J. A. Montgomery Jr., J. E. Peralta, F. Ogliaro, M. Bearpark, J. J. Heyd, E. Brothers, K. N. Kudin, V. N. Staroverov, T. Keith, R. Kobayashi, J. Normand, K. Raghavachari, A. Rendell, J. C. Burant, S. S. Iyengar, J. Tomasi, M. Cossi, N. Rega, J. M. Millam, M. Klene, J. E. Knox, J. B. Cross, V. Bakken, C. Adamo, J. Jaramillo, R. Gomperts, R. E. Stratmann, O. Yazyev, A. J. Austin, R. Cammi, C. Pomelli, J. W. Ochterski, R. L. Martin, K. Morokuma, V. G. Zakrzewski, G. A. Voth, P. Salvador, J. J. Dannenberg, S. Dapprich, A. D. Daniels, O. Farkas, J. B. Foresman, J. V. Ortiz, J. Cioslowski and D. J. Fox, *Gaussian 09, Revision D.01*, Gaussian Inc., Wallingford CT, 2013.
- [26] M. Häser and R. Ahlrichs, *J. Comput. Chem.*, 1989, **10**, 104–111.
- [27] F. Weigend and M. Häser, *Theor. Chim. Acta*, 1997, **97**, 331–340.
- [28] F. Weigend, M. Häser, H. Patzelt and R. Ahlrichs, *Chem. Phys. Lett.*, 1998, **294**, 143–152.
- [29] C. Hättig, A. Hellweg and A. Köhn, *Phys. Chem. Chem. Phys.*, 2006, **8**, 1159–1169.
- [30] A. Hellweg, S. Grün and C. Hättig, *Phys. Chem. Chem. Phys.*, 2008, **10**, 4119–4127.

- [31] R. Ahlrichs, *Phys. Chem. Chem. Phys.*, 2004, **6**, 5119–5121.
- [32] C. Hättig and A. Köhn, *J. Chem. Phys.*, 2002, **117**, 6939–6951.
- [33] A. Köhn and C. Hättig, *J. Chem. Phys.*, 2003, **119**, 5021–5036.
- [34] C. Hättig and F. Weigend, *J. Chem. Phys.*, 2000, **113**, 5154–5161.
- [35] O. Christiansen, H. Koch and P. Jørgensen, *Chem. Phys. Lett.*, 1995, **243**, 409–418.
- [36] M. Schreiber, M. R. Silva-Junior, S. P. A. Sauer and W. Thiel, *J. Chem. Phys.*, 2008, **128**, 134110.
- [37] D. H. Friese, L. Törk and C. Hättig, *J. Chem. Phys.*, 2014, **141**, 194106.
- [38] J. Schirmer, *Phys. Rev. A: At., Mol., Opt. Phys.*, 1982, **26**, 2395–2416.
- [39] A. Dreuw and M. Wormit, *WIREs Comput. Mol. Sci.*, 2015, **5**, 82–95.
- [40] D. Tuna, D. Lefrancois, Ł. Wolański, S. Gozem, I. Schapiro, T. Andruniów, A. Dreuw and M. Olivucci, *J. Chem. Theory Comput.*, 2015, **11**, 5758–5781.
- [41] TURBOMOLE V7.0 2015, a Development of University of Karlsruhe and Forschungszentrum Karlsruhe GmbH, 1989–2015, TURBOMOLE GmbH, since 2007; Available from <http://www.turbomole.com>.
- [42] T. H. Dunning, *J. Chem. Phys.*, 1989, **90**, 1007–1024.
- [43] A. Schäfer, H. Horn and R. Ahlrichs, *J. Chem. Phys.*, 1992, **97**, 2571.
- [44] F. Weigend and R. Ahlrichs, *Phys. Chem. Chem. Phys.*, 2005, **7**, 3297–3305.
- [45] A. Schäfer, C. Huber and R. Ahlrichs, *J. Phys. Chem.*, 1994, **100**, 5829.
- [46] D. Rappoport and F. Furche, *J. Chem. Phys.*, 2010, **133**, 134105.
- [47] F. Weigend and M. Häser, *Theor. Chem. Acc.*, 1997, **97**, 331–340.
- [48] F. Weigend, M. Häser, H. Patzelt and R. Ahlrichs, *Chem. Phys. Lett.*, 1998, **294**, 143–152.
- [49] A. Hellweg, S. A. Grün and C. Hättig, *Phys. Chem. Chem. Phys.*, 2008, **10**, 4119–4127.

Efficient Intersystem Crossing in 2-Aminopurine Riboside Probed by Femtosecond Time-Resolved Transient Vibrational Absorption Spectroscopy

HENDRIK BÖHNKE,^a KATHARINA RÖTTGER,^{a,b,‡} REBECCA A. INGLE,^{b,§} HUGO J. B. MARROUX,^{b,¶}
MATS BOHNSACK,^a ANDREW J. ORR-EWING^{*b} AND FRIEDRICH TEMPS^{*a}

^a Institute of Physical Chemistry, Christian-Albrechts-University Kiel, Olshausenstr. 40,
24098 Kiel, Germany.

^b School of Chemistry, University of Bristol, Cantock's Close, Bristol BS8 1TS, United
Kingdom.

[‡] Current address: Centre for Process Innovation, Wilton Centre, Wilton, Redcar TS10 4RF,
United Kingdom.

[§] Current address: École Polytechnique Fédérale de Lausanne, Laboratoire de Spectroscopie
Ultrarapide (LSU) and Lausanne Centre for Ultrafast Science (LACUS), ISIC, FSB, CH-1015
Lausanne, Switzerland.

[¶] Current address: Chemical Sciences Department, Lawrence Berkeley National Labora-
tory, 1 Cyclotron Road Berkeley CA 94720, USA.

* To whom correspondence should be addressed.

E-mail: temps@phc.uni-kiel.de; a.orr-ewing@bristol.ac.uk.

Published in Phys. Chem. Chem. Phys., 2018, 20, 20033-20042.

Reproduced by permission of the PCCP Owner Societies.

OWN CONTRIBUTIONS TO THIS PUBLICATION:

- Steady-state UV/vis, fluorescence and FTIR spectroscopy,
- Quantum chemical calculations for ground- and excited-state species,
- Transient femtosecond vibrational absorption spectroscopy,
- Analysis of experimental data and kinetic model simulations,
- Writing of the manuscript.

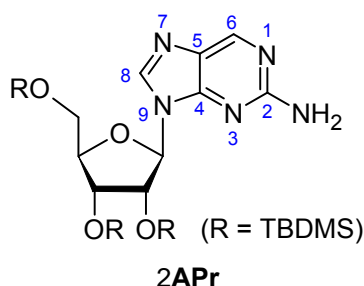
Abstract

The photophysical dynamics of 2-aminopurine riboside (**2APr**) in CHCl_3 have been studied following excitation at $\lambda_{\text{pump}} = 310 \text{ nm}$ by means of femtosecond transient vibrational absorption spectroscopy (TVAS) aided by quantum chemical density functional theory (DFT) and *ab initio* calculations. The experiments identified numerous vibrational marker bands in the regions of the NH_2 stretch and the 2AP ring vibrations which could be assigned to the bleach of the S_0 electronic ground state (GS) and to transient populations in the $^1\pi\pi^*$ and $^3\pi\pi^*$ excited electronic states. The temporal evolution of the transient vibrational bands shows that the decay of the $^1\pi\pi^*$ population is accompanied by a partial recovery of the GS and a concurrent population of the $^3\pi\pi^*$ state with a time constant of $\tau_2 = 740 \pm 15 \text{ ps}$. The ensuing electronic relaxation is concluded to proceed *via* the $^1n\pi^*$ state as intermediate state. The absence of observable transient vibrational bands of this state hints at an upper limit for its lifetime of $\tau < 100 \text{ ps}$. The triplet quantum yield is found to be $\phi_T = 0.42 \pm 0.07$.

3.1 Introduction

2-Aminopurine (2AP) is a highly fluorescent analogue of the canonical nucleobase adenine (\equiv 6-aminopurine, Ade)^[1–17] that base-pairs with thymine without substantial perturbation of the helical structure when incorporated into DNA.^[18–23] Free 2AP is known to exist in thermodynamic equilibrium in solution at room temperature in two tautomeric forms, 9H- and 7H-2AP,^[3,6,24–26] but tautomerization is blocked in the riboside (**2APr**; *cf.* Scheme 1) and 2'-deoxyriboside (2APdr) and their nucleotides, so that the N⁷-isomers can be neglected in common DNA and RNA research applications.

The 2AP chromophore features its first $^1\pi\pi^*$ electronic absorption band in the near ultraviolet (UV) at $\lambda \sim 310 \text{ nm}$, substantially red-shifted compared to Ade ($\lambda \sim 260 \text{ nm}$).^[1–3] This $^1\pi\pi^*$ transition has been investigated in some detail by gas phase spectroscopy in molecular beams^[27–36] and by theoretical studies, which focused especially on the fluorescence quenching mechanism.^[26,28,37–46] Highly unusually, isolated jet-cooled 2AP



Scheme 1 Chemical structure of 2-aminopurine riboside (2APr).

excited in the gas phase at 309 nm has a fluorescence lifetime of only 156 ps, but this value increases upon site-specific microhydration up to ~ 14.5 ns.^[34] Moreover, selective excitation of 2AP in water results in fluorescence with a lifetime of ~ 12 ns.^[5,6] Under other conditions, however, the fluorescence lifetimes and quantum yields are highly sensitive to the molecular environment.^[5,6,8–16,47–49] Accordingly, 2AP has been utilized to probe conformational dynamics,^[9,14,50–55] stacking/unstacking interactions,^[7–9,56–62] nucleotide binding and exchange,^[63,64] and charge transfer^[9,11,49,65–68] in DNA and RNA. The understanding of the radiationless electronic deactivation mechanisms causing quenching of the fluorescence of 2AP has nevertheless remained incomplete.^[32,34,42–46,48,49,59–61,66,69] In particular, measurements by Crespo-Hernández and co-workers using transient electronic absorption spectroscopy (TEAS) in acetonitrile, ethanol and aqueous solution have recently led to the discovery of an important triplet channel in the electronic deactivation of 2AP.^[70] A drawback of electronic absorption spectroscopy is, however, that direct information on chemical species and structures may be obscured by the broad appearance of the observed bands.

Here, we report on a study of the photophysical dynamics of **2APr** in chloroform (CHCl_3) after excitation at $\lambda_{\text{pump}} = 310$ nm by means of femtosecond time-resolved vibrational absorption spectroscopy (TVAS). Aided by density functional theory (DFT) and *ab initio* quantum chemical calculations for the assignment of the observed vibrational transients, our measurements provide chemical structure-specific information that maps the evolution from the photoexcited $^1\pi\pi^*$ state back to the electronic ground state (GS; S_0) and to the proposed long-lived first $^3\pi\pi^*$ state.

3.2 Methods

Time-Resolved Spectroscopy

The time-resolved UV pump–transient vibrational absorption measurements were performed with the spectrometer at the University of Bristol^[71] using sample concentrations of 25 mM and an optical pathlength of 100 μm . The use of CHCl_3 as solvent ensures high optical transmission of the solutions in the mid-infrared (mIR) spectrum, and adds the extra benefit that the dielectric constant of the environment is similar to that in the DNA double helix.^[72] The solubility of the **2APr** in CHCl_3 was enhanced by protection of the free OH positions of the sugar by *tert*-butyldimethylsilyl (TBDMS) groups (see SI) as done in previous work.^[73–76] The UV excitation pulses at $\lambda_{\text{pump}} = 310$ nm with duration of ~ 100 fs (full width at half maximum) were generated by a Coherent OPerA Solo optical parametric amplifier (OPA) pumped by 2.45 mJ per pulse from a Coherent Legend Elite HE+ regenerative amplifier running at 1 kHz and 800 nm with 40 fs duration. The pump pulses were attenuated to 100 nJ per pulse by a combination of a $\lambda/2$ waveplate and a wire-grid

polarizer and set to the magic angle condition (54.7°) with respect to the probe pulses. The broadband mIR probe pulses were supplied by difference frequency generation of the signal and idler from a second OPA, giving tunable pulses with $\sim 300\text{ cm}^{-1}$ bandwidth in the $1250\text{--}4000\text{ cm}^{-1}$ range. After passing through the sample, the mIR probe pulses were spectrally dispersed by a grating spectrograph (HORIBA Scientific, iHR320) and detected on a 128 pixel, liquid N_2 -cooled mercury cadmium telluride array (Infrared Associates). For transient measurements, the UV pump pulses were delayed using an aluminium retro-reflector mounted on a motorized delay stage and modulated at 0.5 kHz with an optical chopper wheel for pump-on/pump-off pairs of spectra.

Supporting time-resolved fluorescence measurements to determine the excited-state lifetime of **2APr** in CHCl_3 were performed using the up-conversion spectrometer in Kiel.^[77] Static ground-state vibrational spectra were measured on a Bruker IFS 66v Fourier-transform infrared (FTIR) spectrometer.

Computational Methods

Quantum chemical calculations were carried out to derive assignments for the characteristic vibrational marker bands observed in the TVA spectra to the GS and to the possible excited electronic states. Besides, they served to check the energetic order of the excited states above the GS at the Franck-Condon (FC) geometry. To save computer time, all calculations were run on 9-methyl 2-aminopurine (9Me-2AP) in place of **2APr**. Relaxed GS structures and vibrational frequencies were determined by DFT calculations with the M062X^[78] functional in combination with the 6-311+G** basis set^[79–82] using the Gaussian09 suite of programs.^[83] The calculated wavenumbers were scaled (*cf.* ref. 84 and 85) to obtain best agreement with the experimental (FTIR) data using factors of 0.955 and 0.94 below and above 2000 cm^{-1} , respectively. Complementary calculations were run using second-order Møller–Plesset perturbation theory (MP2) under the resolution of the identity (RI) approximation^[86–89] with the def2-TZVPPD^[90–92] basis set employing the Turbomole 7.0 program^[93] to obtain starting points for the excited states. Excited-state properties, including vertical excitation energies (VEEs), equilibrium structures and associated vibrational mode frequencies for the $^1\pi\pi^*$, $^1n\pi^*$ and $^3\pi\pi^*$ state minima, were then computed using the second-order approximation coupled-cluster (CC2) method in Turbomole 7.0 in the form of the RI-CC2 variant^[94–99] with the def2-TZVPPD basis set.^[90–92] The obtained vibrational wavenumbers in the excited states were scaled (*cf.* ref. 100) with factors of 0.99 and 0.94 below and above 2000 cm^{-1} , respectively, to obtain best agreement between the calculated and measured transient vibrational spectra.

3.3 Results

Static Spectra and Transient Fluorescence Spectroscopy

The UV absorption spectrum of **2APr** in CHCl_3 with its strong $^1\pi\pi^*$ band with maximum near ~ 310 nm and the static fluorescence spectrum upon excitation at this wavelength are displayed in Fig. 3.1 (a). The associated excited electronic state lifetime was determined by time-resolved fluorescence spectroscopy (TFLS) at a wavelength of $\lambda_{\text{FL}} = 410$ nm with the up-conversion experiment (Fig. 3.1 (b)). The obtained time profile features a delayed rise in $\tau_{1,\text{FL}} = 3.0 \pm 1.0$ ps followed by an exponential decay with a lifetime of $\tau_{2,\text{FL}} = 740 \pm 15$ ps. Quoted error limits refer to the 95% confidence interval here and below.

Computed Excitation Energies and Optimized Structures

The optimized structures for the GS and the $^1\pi\pi^*$, $^1n\pi^*$ and $^3\pi\pi^*$ states are given in Tables 3.1–3.4 in the SI. The computed VEEs (Table 3.5, SI and Fig. 3.2) agree with the known sequence of the $^1\pi\pi^*$, $^1n\pi^*$, $^3\pi\pi^*$ and $^3n\pi^*$ states, respectively, as S_1 , S_2 , T_1 and T_2 at the FC geometry.^[26,28,34,41–46] A subsequent structure optimization for the $^1\pi\pi^*$

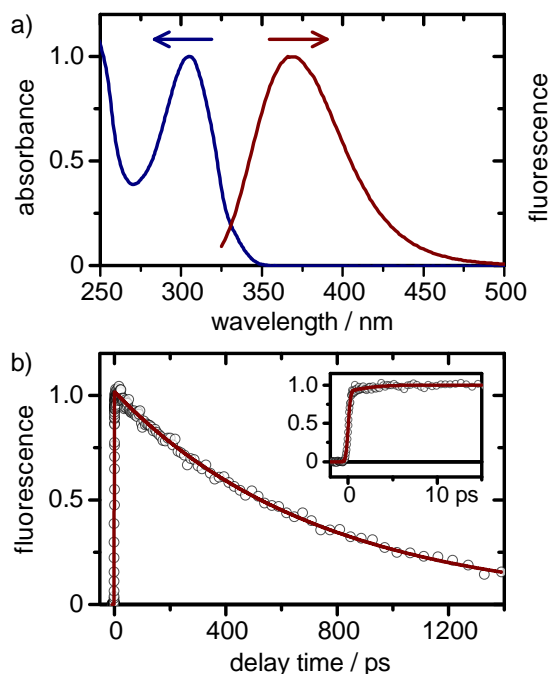


Figure 3.1: (a) UV absorption spectrum of **2APr** in CHCl_3 (left) and static fluorescence spectrum (right) from excitation at $\lambda_{\text{pump}} = 310$ nm. (b) Transient fluorescence–time profile measured at $\lambda_{\text{FL}} = 410$ nm after excitation at $\lambda_{\text{pump}} = 310$ nm. Open circles are data points, the solid red line is the least-squares best fit curve.

state converged to a local excited (LE) state minimum (referred to below as $S_{1,LE}$) on the S_1 potential energy hypersurface (PEHS). An attempt of a geometry optimization for the $^1n\pi^*$ state (S_2 at the FC structure, but S_1 in the global adiabatic minimum; *cf.* Fig. 3.2) at the RI-CC2/def2-TZVPPD level of theory failed, when starting from the FC point due to strong multiconfigurational character of the wavefunction along the energy gradient, but converged when taking the CASSCF/CASPT2 results of ref. 42 as initial structure. The global $^1n\pi^*$ (S_1) state minimum is separated from the above-mentioned local $^1\pi\pi^*$ state minimum by a conical intersection (CI) near a small potential energy barrier that is strongly dependent on the environment.^[28,34,41,42,44,45] The $^3\pi\pi^*$ configuration at the $^1n\pi^*$ potential energy minimum turned out to be nearly isoenergetic with this global S_1 minimum. The optimization of the $^3\pi\pi^*$ state confirmed it as the global minimum on the T_1 PEHS. Moreover, it is important that the $^3n\pi^*$ (T_2) state is positioned in energy well above the $^1\pi\pi^*$ ($S_{1,LE}$) local potential energy minimum.

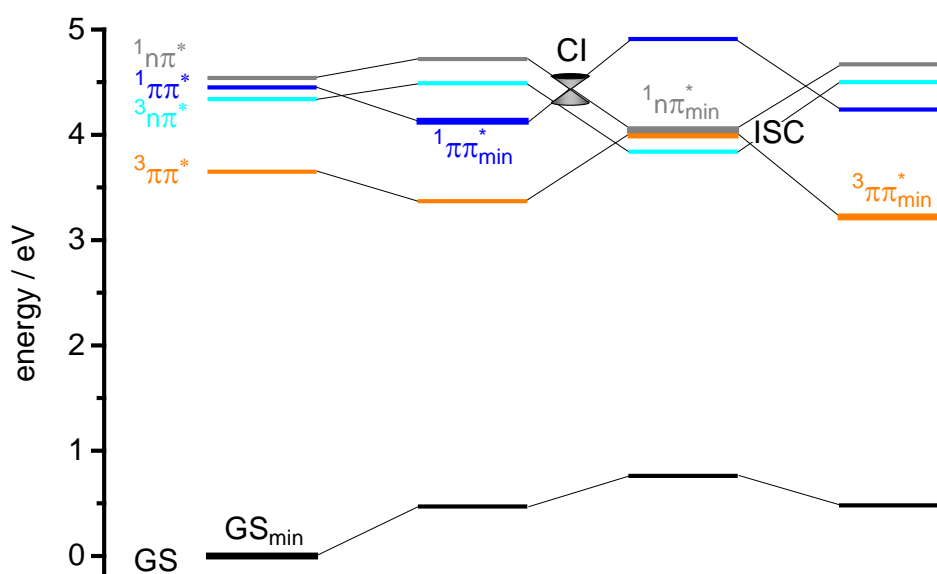


Figure 3.2: Energy diagram with the most important stationary points of the electronic states of 9Me-2AP calculated at the RI-MP2/def2-TZVPPD resp. RI-CC2/def2-TZVPPD levels of theory. The different columns show the computed energies relative to the optimized RI-MP2/def2-TZVPPD GS, the optimized $^1\pi\pi^*$ state, the optimized $^1n\pi^*$ state, and the optimized $^3\pi\pi^*$ state, respectively. The conical intersection between the $^1\pi\pi^*$ and $^1n\pi^*$ states and the intersystem crossing between the $^1n\pi^*$ and $^3\pi\pi^*$ states are indicated by CI and ISC.

Transient Vibrational Absorption Spectroscopy (TVAS)

The FTIR spectrum of **2APr** in CHCl_3 (Fig. 3.3 (a)) features two well-resolved vibrational bands at 3532 and 3424 cm^{-1} , which belong to the anti-symmetric (as) and symmetric (s) NH_2 stretch modes, respectively, and several partially superimposed bands in the region of the 2AP ring vibrations between 1650 and 1500 cm^{-1} . Comparison with the calculated vibrational wavenumbers for 9Me-2AP at the M062X/6-311+G** level of theory allows straightforward assignments of these bands (Fig. 3.3 (b)). The relevant normal modes and wavenumbers in the GS together with the corresponding calculated normal modes and wavenumbers for the $^1\pi\pi^*$ and $^3\pi\pi^*$ excited states for comparison with the transient vibrational spectra below are illustrated in Fig. 3.4.

With these premises, Fig. 3.5 displays the results of our transient vibrational absorption measurements on **2APr** after 310 nm excitation. Special attention is directed first to the characteristic NH_2 stretch modes between 3600 and 3200 cm^{-1} . According to our calculations (*cf.* Fig. 3.5 (a)), the wavenumbers of these vibrations in the $^1\pi\pi^*$ and $^3\pi\pi^*$ states appear red-shifted compared to the GS, and the $\text{NH}_2(\text{s})$ bands are stronger than the $\text{NH}_2(\text{as})$ bands. The observed TVA spectra in Fig. 3.5 (b) show two distinct positive bands red-shifted compared to the $\text{NH}_2(\text{s})$ stretch in the GS, one at 3356 (3342) cm^{-1} directly after photoexcitation and one at 3395 (3382) cm^{-1} showing a substantially delayed rise (calculated wavenumbers in parentheses). The observed wavenumbers agree very nicely with the expectations for the $^1\pi\pi^*$ and $^3\pi\pi^*$ states, respectively. Moreover, the experimental spectra

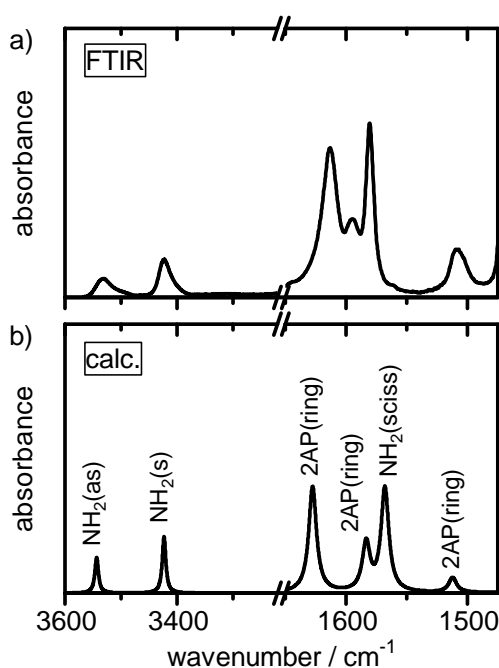


Figure 3.3: (a) Measured FTIR spectrum of **2APr** in CHCl_3 and (b) calculated (M062X/6-311+G**) vibrational spectrum of 9Me-2AP with assigned marker bands. The intensities in the NH_2 stretch region have been multiplied by a factor of two for clarity.

indicate two weak additional positive bands to lower wavenumber than the NH₂(as) stretch of the GS, at 3479 (3493) cm⁻¹ and at 3500 (3530) cm⁻¹. Here, the time evolutions are slightly obscured by interference with the two ground-state bleach (GSB) bands, but the observed positions again agree with the expectations for the ¹ππ* and ³ππ* states. The emerging temporal evolutions are indicated by arrows in the obtained global Gaussian band fit plots in Fig. 3.5 (c). In addition, the time evolutions of the main marker bands are layed out in the two-dimensional (2D) spectro-temporal absorption matrices of the change in optical density ΔOD after excitation as function of probe wavenumber and pump-probe time

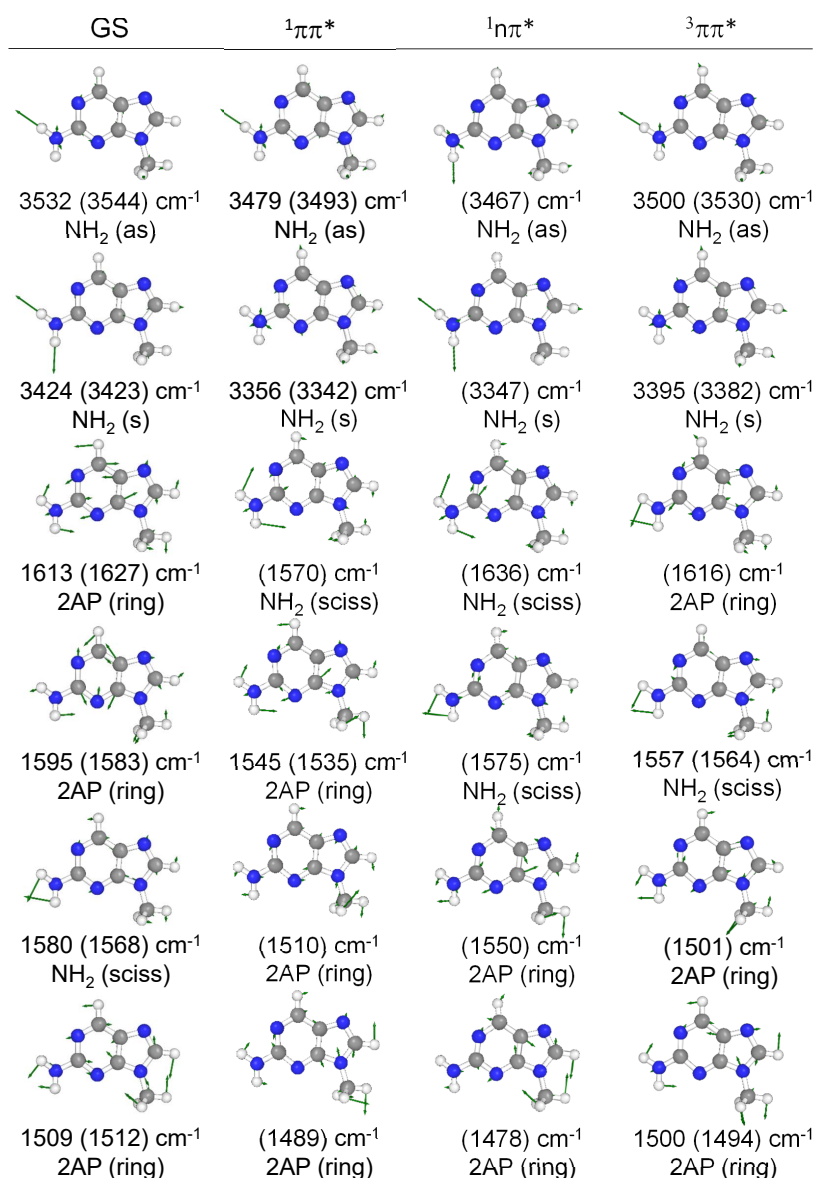


Figure 3.4: Observed and calculated vibrational marker modes of 2APr and 9Me-2AP, respectively, in the NH₂ stretch region and in the region of the 2AP ring vibrations in the GS and in the ¹ππ*, ¹nπ* and ³ππ* excited states. The wavenumbers given first are the experimental values from the FTIR spectrum for the GS or from the observed TVA spectra for the ¹ππ*, ¹nπ* and ³ππ* states. Values in parentheses are the respective scaled calculated wavenumbers for 9Me-2AP.

delay in Fig. 3.5 (e) and (f). As the positive transients slowly decay over time, the GSB signals partially recover. Additionally, the transients assigned to the $^3\pi\pi^*$ state grow in at later time delays. This applies very clearly, in particular, for the $\text{NH}_2(\text{s})$ band of the $^3\pi\pi^*$ state at 3395 cm^{-1} (see Fig. 3.5 (e) and (f)). Overall, the initial negative bleach signals and positive excited-state absorptions are well separated from the positive features growing in at late pump–probe delay times.

Likewise, the excited-state calculations predict new transient bands in the region of the 2AP ring vibrations between 1650 and 1475 cm^{-1} (Fig. 3.5 (a), right). However, the transient spectra in this region are partially superimposed by broad GS bleach bands, so that these experimental results are less conclusive (Fig. 3.5 (b) and (c), right). Nevertheless, all observed trends agree with those found in the NH_2 stretch spectra, and all bands could be fitted globally to either the GS, the $^1\pi\pi^*$ or the $^3\pi\pi^*$ state, depending on the band assignments. For example, a diffuse broad positive feature rises at $\sim 1545\text{ cm}^{-1}$ at early delay times, and then decays again as the intense bleach feature between ~ 1620 and 1570 cm^{-1} partially recovers, consistent with an assignment of the $\sim 1545\text{ cm}^{-1}$ feature to the calculated $^1\pi\pi^*$ state mode at 1535 cm^{-1} . Moreover, minor transient bands grow in at ~ 1640 and $\sim 1500\text{ cm}^{-1}$, hinting that they originate from the $^3\pi\pi^*$ state (Fig. 3.5 (b) and (c)).

Fig. 3.5 (c) and (f) show global band fits to all transient TVA spectra using sums of Gaussians at selected pump–probe delay times (Fig. 3.5 (c)) and the temporal evolutions of the amplitudes of those Gaussians in the investigated spectral regions (Fig. 3.5 (f)). The resulting time profiles of the GS and the $^1\pi\pi^*$ and $^3\pi\pi^*$ excited states are given in Fig. 3.5 (d). As can be seen, the data can be nicely described in a global fashion using two exponentials, with the same time constant values τ_1 and τ_2 as provided by the transient fluorescence measurements above (Fig. 3.1 (b)). After some fast initial process with

$$\tau_1 = 3.0 \pm 1.0\text{ ps},$$

the recovery of the population in the GS, the decay of the population in the intermediate $^1\pi\pi^*$ state, and the eventual rise of the population in the $^3\pi\pi^*$ state collectively take place with

$$\tau_2 = 740 \pm 15\text{ ps}.$$

For comparison, an unrestricted free floating fit of τ_1 and τ_2 to the TVA data gave a virtually identical result (albeit with significantly larger error limit) of $\tau_2 = 710 \pm 120\text{ ps}$ for the long time constant, while the first value came out consistently within the error limits ($\tau_1 \sim 8 \pm 5\text{ ps}$), but remained rather ill-determined.

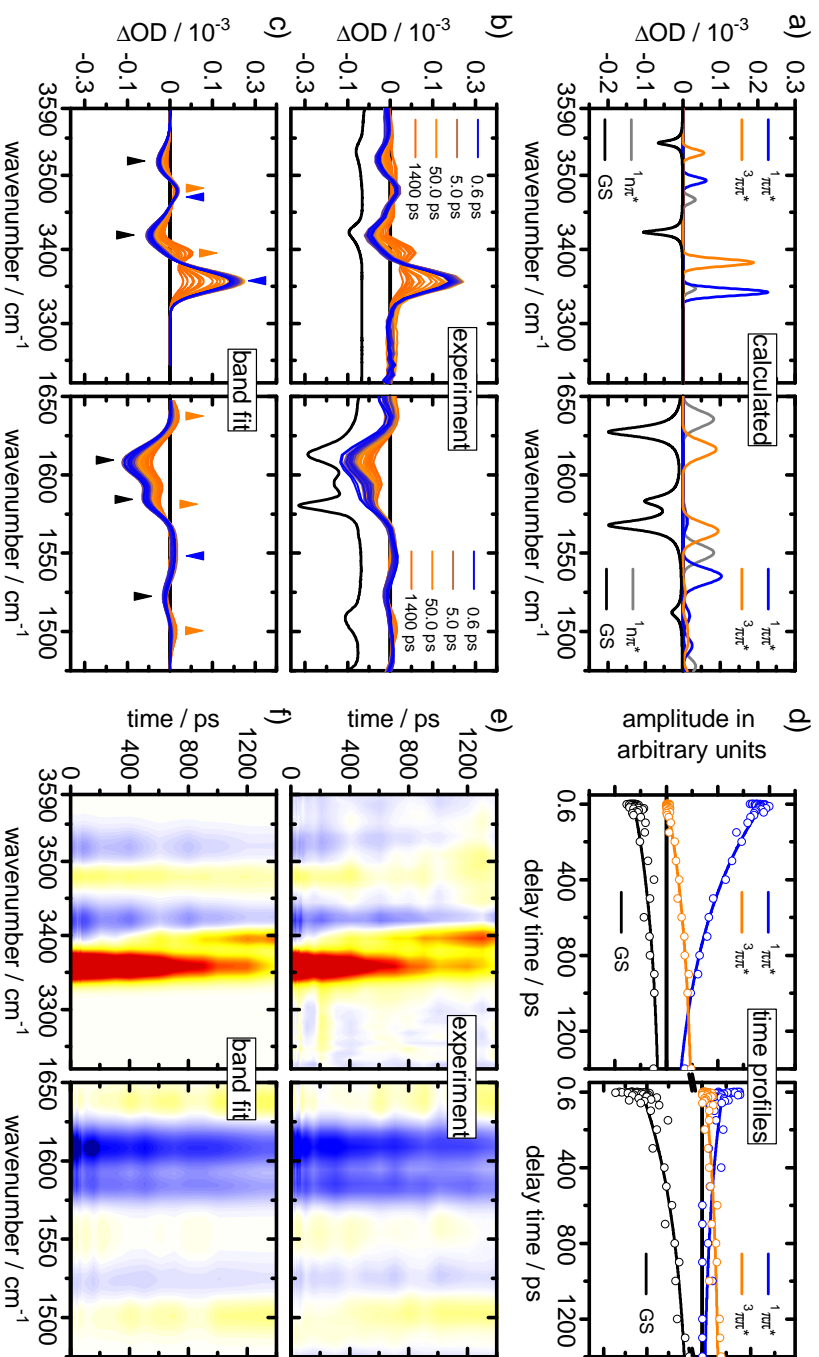


Figure 3.5: Results of the transient vibrational absorption (TVA) measurements on 2APr in CHCl_3 after excitation at $\lambda_{\text{pump}} = 310$ nm. In all panels, the data for the NH_2 stretch vibrations are shown on the left, and the data for the 2AP ring vibrations on the right. (a) Calculated vibrational spectra (9Me-2AP) for the GS (black), the photoexcited $^1\pi\pi^*$ state (blue), the $^1n\pi^*$ state (grey), and the $^3\pi\pi^*$ state (orange). Notice the weak band intensities for the $^1n\pi^*$ state in the NH_2 stretch region. (b) Experimental TVA spectra of 2APr after excitation at $\lambda_{\text{pump}} = 310$ nm at selected pump-probe delay times (black lines = negative FTIR traces for reference). (c) Global Gaussian band fits to the experimental TVA spectra, with arrows indicating decaying and rising transient vibrational bands belonging to the GS (black) and the $^1\pi\pi^*$ (blue) and $^3\pi\pi^*$ (orange) states. (d) Time profiles from the global band fits (open circles) and fitted multi-exponential fluorescence measurements (solid lines) for the GS (black) and the $^1\pi\pi^*$ (blue) and $^3\pi\pi^*$ (orange) states using the time constant values τ_1 and τ_2 provided by the transient probe wavenumber and pump-probe time delay. The false colour-coding from dark blue ($\Delta\text{OD} \leq -0.1 \times 10^{-3}$) to dark red ($\Delta\text{OD} \geq 0.1 \times 10^{-3}$) illustrates the temporal evolutions of the vibrational transients; (e) for the raw experimental data and (f) for the global Gaussian band fits.

Branching Ratio for GS Recovery and $^3\pi\pi^*$ Formation

Following the temporal evolution of the GS bleach bands in the TVA spectra provides immediate insight into the kinetics and efficiency of the recovery of the GS. In particular, the 2AP ring mode at 1613 cm^{-1} , which shows the behaviour most clearly, reveals a GS recovery yield of

$$\phi_{\text{GS}} = 0.58 \pm 0.07$$

by comparison of the initial bleach to the asymptotic late-time “permanent” bleach obtained from global exponential fits to the vibrational band amplitudes (Fig. 3.5 (d)). This value reflects the return of the molecules from the photoexcited $^1\pi\pi^*$ state to the GS by non-radiative electronic deactivation *via* internal conversion (IC) and, with a small contribution, radiative deexcitation (*i.e.* fluorescence). The error limits assigned to ϕ_{GS} are determined mainly by the uncertainty of the late-time bleach signal.

As the $^1\pi\pi^*$ excited-state signatures decay and the GS partially recovers, the new transient bands that arise in the TVA spectra reflect the buildup of the population in the $^3\pi\pi^*$ state. The quantum yield for triplet formation is therefore found to be given by

$$\phi_{\text{T}} = 0.42 \pm 0.07,$$

with error limits as for ϕ_{GS} . Practically the same value ($\phi_{\text{T}} = 0.43$) would be obtained by a comparison of the ratio of the computed RI-CC2 $\text{NH}_2(\text{s})$ band intensities in the $^3\pi\pi^*$ and $^1\pi\pi^*$ states to the intensity ratio of the measured final $^3\pi\pi^*$ and initial $^1\pi\pi^*$ TVA bands. The lifetime of the $^3\pi\pi^*$ state is known to be very long ($\tau > 1\ \mu\text{s}$)^[70] on the time scale of our experiments.

3.4 Discussion

Observed Electronically Excited States, Transient Vibrational Spectra and Time Constants

The above results paint a rather conclusive picture for the photophysical dynamics of 2AP^[101] in CHCl_3 that complements the recent time-resolved electronic absorption study of Crespo-Hernández and co-workers^[70] in acetonitrile, ethanol and aqueous solution by chemical structure-sensitive data based on well-resolved transient vibrational spectra. Accordingly, femtosecond laser excitation at $\lambda_{\text{pump}} = 310\text{ nm}$ prepares a wavepacket in the FC region of the optically bright first $^1\pi\pi^*$ state of the molecules. Driven by an effective potential energy gradient, the wavepacket rapidly leaves its region of birth to move into a local minimum on the $^1\pi\pi^*$ potential energy hypersurface (PEHS). The fast time component ($\tau_1 = 3.0\text{ ps}$) in our time-resolved fluorescence measurement that is also reflected as a build-

up time in the TVA spectra, and in good accordance with preceding work,^[10,48,70] is consequently assigned to this motion. The ensuing dynamics is accompanied by fast vibrational energy redistribution (IVR) in the photoexcited state, molecular rearrangement processes in the solvent shell, and vibrational energy transfer (VET) from the photoexcited molecules to the solvent.

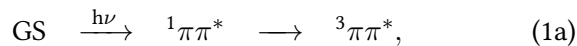
The local minimum on the $^1\pi\pi^*$ excited PEHS is the first state that is clearly identified and characterized by our TVA spectra. The global adiabatic minimum of the first singlet electronically excited (S_1) PEHS is nonetheless known to be of $^1n\pi^*$ nature. However, the first $^1n\pi^*$ state is optically dark and much higher in energy than $^1\pi\pi^*$ at the FC geometry; it therefore corresponds to S_2 at vertical excitation.^[26,28,39,41–43] Most importantly, the $^1n\pi^*$ global minimum is separated from the above-mentioned locally excited $^1\pi\pi^*$ ($S_{1,LE}$) minimum by a sizable potential energy barrier. The modulation of the height of this barrier has been identified as a main cause for the strongly environment-dependent fluorescence properties of 2AP.^[26,29,34,41] The second $^1\pi\pi^*$ excited state lies well outside the energy range of interest here.

The TVA spectra at early delay times consequently show two transient absorption bands at 3479 and 3356 cm^{-1} , which agree well with the computed positions of the anti-symmetric and symmetric NH_2 stretch modes at 3493 and 3342 cm^{-1} in the $^1\pi\pi^*$ ($S_{1,LE}$) local minimum. Additionally, the diffuse feature around $\sim 1545 \text{ cm}^{-1}$ in the region of the 2AP ring vibrations can be attributed to the computed $^1\pi\pi^*$ ($S_{1,LE}$) mode at 1535 cm^{-1} that is partially obscured by the strong, broad GS bleach signals in close proximity. The time profiles showing the decay of those vibrational marker bands of the $^1\pi\pi^*$ ($S_{1,LE}$) state mirror the temporal evolution seen by the transient fluorescence measurement. The time constant of $\tau_2 = 740 \pm 15 \text{ ps}$ is therefore identified as the effective lifetime of the $^1\pi\pi^*$ ($S_{1,LE}$) state.

The $^1\pi\pi^*$ ($S_{1,LE}$) population may either relax back to the electronic GS non-adiabatically *via* a conical intersection (CI)^[42,43] or proceed to a non-fluorescent state. Here, while the $^1\pi\pi^*$ state decays, our TVA spectra show both incomplete GSB recovery and a concurrent build-up of new transient vibrational bands. By comparison with our excited-state calculations, the experimentally observed late-time features unambiguously belong to the $^3\pi\pi^*$ state. This brings up the question for the underlying molecular mechanisms: In principle, the observed concurrent depopulation of $^1\pi\pi^*$ ($S_{1,LE}$) and population of $^3\pi\pi^*$ (T_1) with a common time constant of $\tau = 740 \text{ ps}$ might allow for two scenarios, direct ISC from $^1\pi\pi^*$ to $^3\pi\pi^*$ or ISC *via* $^1n\pi^*$ as an intermediate state.

Intersystem Crossing from $^1\pi\pi^*$ to $^3\pi\pi^*$

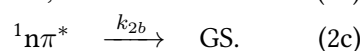
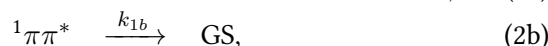
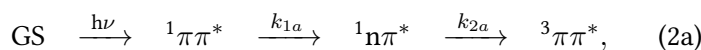
The observed TFLS and TVAS data imply the involvement of at least three electronic states in the deactivation mechanism of 2AP after $^1\pi\pi^*$ photoexcitation. A minimal kinetic scheme might thus be written as



By the El-Sayed rules,^[102,103] spin-orbit coupling in the $\pi\pi^*$ manifold should be weak and direct $^1\pi\pi^* \rightarrow ^3\pi\pi^*$ ISC is therefore expected to be slow, resulting in $^1\pi\pi^*$ lifetimes in the nanosecond range and beyond. Hence, our experimental 740 ps time constant associated with triplet formation appears to be too short for direct ISC in the $\pi\pi^*$ manifold. CASSCF/CASPT2 calculations^[42,43] on 2AP *in vacuo* suggested additional electronic deactivation channels for the $^1\pi\pi^*$ state, by which the lifetime of the $^1\pi\pi^*$ state could be shortened to the observed range, but then the quantum yield for triplet formation should be low. However, our experimentally obtained quantum yield for triplet formation of $\phi_T = 0.42 \pm 0.07$ shows that ISC proceeds very efficiently. Our result for ϕ_T in CHCl_3 is in good agreement with the TEAS measurements of Crespo-Hernández and co-workers,^[70] who found increasing triplet yields with decreasing solvent polarity, from $\phi_T \sim 0.1$ in water up to $\phi_T \sim 0.4$ in acetonitrile. Such high values are clearly not in agreement with a direct $^1\pi\pi^* \rightarrow ^3\pi\pi^*$ ISC mechanism on the grounds of El-Sayed's rules.

Strong spin-orbit coupling, fast ISC, and thereby a high triplet quantum yield are expected according to the El-Sayed rules between states of different electronic character.^[102,103] Here, we may eliminate a transition from the $^1\pi\pi^*$ ($S_{1,LE}$) to the $^3n\pi^*$ state as a plausible route, because the computed $^3n\pi^*$ energy lies well above the $^1\pi\pi^*$ ($S_{1,LE}$) local minimum. Moreover, the energy spacing between the $^3n\pi^*$ configuration with respect to the optimized $^3\pi\pi^*$ (T_1) minimum amounts to more than 1 eV (*cf.* Fig. 3.2). Further, although feasible on energetic grounds, a $^1n\pi^* \rightarrow ^3n\pi^*$ ISC transition would again be El-Sayed forbidden, and we would have to postulate an additional $^3n\pi^* \rightarrow ^3\pi\pi^*$ internal conversion step.

Instead, it appears likely that the $^3\pi\pi^*$ state is populated from $^1\pi\pi^*$ *via* the $^1n\pi^*$ state as intermediate. This route is supported by our calculations of the different excited electronic states for 9Me-2AP (*cf.* Fig. 3.2), which showed that the $^1n\pi^*$ state (computed at 4.04 eV) becomes virtually degenerate with the $^3\pi\pi^*$ state (computed at 4.01 eV) near the $^1n\pi^*$ minimum energy structure. A plausible scheme to explain the experimental findings can thus be written as



As already noted, the $^1n\pi^*$ state has been invoked in previous works to rationalize the increased fluorescence lifetimes of 2AP from the gas phase^[32,33,36] *via* microsolvated

2AP^[29,34,46] towards bulk solution.^[6,44,70] While the energetic positioning of the $^1\pi\pi^*$ state and the appearance of the UV absorption spectrum of 2AP are affected only little by varying solvent polarity,^[2,21] the $^1n\pi^*$ state is strongly destabilized in polar solvents like water. As a consequence, the potential energy barrier separating the photoexcited $^1\pi\pi^*$ state from the $^1n\pi^*$ state is substantially higher in water than in other environments.^[42–44] The correspondingly slower $^1\pi\pi^* \rightarrow ^1n\pi^*$ IC process that determines the lifetime of the fluorescent $^1\pi\pi^*$ state then results directly in the observed much higher fluorescence quantum yield of 2AP in water than *in vacuo*. Interestingly, Crespo-Hernández and co-workers also observed increasing triplet yields with decreasing fluorescence quantum yields.^[70] Furthermore, we note that similar El-Sayed allowed $^1\pi\pi^* \rightarrow ^1n\pi^* \rightarrow ^3\pi\pi^*$ dynamics have also been proposed for the plain prototypical chromophore purine^[104] and for some of the pyrimidine DNA bases.^[69,105–108]

Adopting the reaction scheme of eqn (2), one might expect experimental evidence for the intermediate $^1n\pi^*$ state by observation of transient vibrational modes of this state or by some other contribution to the observed kinetics. In fact, our calculations predict similar oscillator strengths in the region of the NH₂ (sciss) and 2AP (ring) vibrations in all electronic states (Fig. 3.5 (a), right). In particular, the well-separated 2AP (ring) mode calculated at 1550 cm⁻¹ in the $^1n\pi^*$ state is predicted to exhibit sufficient oscillator strength for use as a characteristic marker band. Still, our TVA spectra show no lasting absorption features around 1550 cm⁻¹ after the $^1\pi\pi^*$ decay. Likewise, the positive experimental feature at 1637 cm⁻¹ arises from the 2AP (ring) vibration in the $^3\pi\pi^*$ state (1616 cm⁻¹) superimposed by the GSB at 1613 cm⁻¹, rather than from the NH₂ (sciss) mode in the $^1n\pi^*$ state (1636 cm⁻¹). The NH₂ stretching modes of 2AP in the $^1n\pi^*$ state are calculated to be considerably weaker compared to the corresponding signatures in the $^1\pi\pi^*$ and $^3\pi\pi^*$ states (Fig. 3.5 (a), left). For this reason, the positive absorption at ~3450 cm⁻¹ in our TVA spectra towards late delay times is assigned to the broad symmetric NH₂ stretching mode in the $^3\pi\pi^*$ state, rather than to the $^1n\pi^*$ state. Indeed, the virtual lack of noticeable band shifts and the absence of any clear vibrational marker bands indicative for the $^1n\pi^*$ state in our experimental TVA data may only be rationalized by a short $^1n\pi^*$ lifetime relative to the observed $^1\pi\pi^*$ state.

Investigating this question further, Fig. 3.6 shows the results of kinetic model simulations of the populations of the different electronic states based on the reaction scheme defined in eqn (2) in comparison with the observed temporal evolutions of the TVA bands from Fig. 3.5 (d). In this model, the initially prepared $^1\pi\pi^*$ state decays to the adiabatically lower $^1n\pi^*$ state with rate coefficient $k_{1a} = 1/740$ ps, as was determined by the TFLS experiment. From there, the evolution continues to the $^3\pi\pi^*$ state with k_{2a} or to the GS with k_{2b} . A direct IC from $^1\pi\pi^*$ to the GS is disallowed at this stage, *i.e.* we set $k_{1b} = 0$ (see below for this transition). To explore the range of $^1n\pi^*$ lifetimes that would be compatible with the experimental results, we thus assumed $^1n\pi^*$ state decay rates k_2 of (a) 1/10 ps, (b) 1/50 ps, (c) 1/200 ps, and (d) 1/400 ps. The branching ratios between (2a) and (2b) are fixed in this scenario at $k_{2a}/k_2 = 0.42$ and $k_{2b}/k_2 = 0.58$, respectively, to correctly predict the experimentally observed quantum yields ϕ_T and ϕ_{GS} . The simulated time profiles with

those assumptions are given in Fig. 3.6. As shown, the experimental data for the GS and the $^3\pi\pi^*$ state are well described by the simulations with values of $k_2 = 1/10$ ps (Fig. 3.6 (a)) or $1/50$ ps (Fig. 3.6 (b)). Taking $k_2 = 1/200$ ps (Fig. 3.6 (c)) or $1/400$ ps (Fig. 3.6 (d)), however, the predicted sigmoidal time profiles for both states indicate a delayed recovery of the GS and delayed population of the $^3\pi\pi^*$ state, which clearly disagrees with the experimental data. For this reason, and for the absence of any transient features belonging to the $^1n\pi^*$ state in our TVA spectra, we infer an upper limit for the lifetime of the $^1n\pi^*$ state of $\tau < 100$ ps. This short upper limit compared with the rate-limiting lifetime of the $^1\pi\pi^*$ state is also corroborated by the emergence of a distinct isosbestic point between the $^1\pi\pi^*$ and $^3\pi\pi^*$ transient electronic absorption bands in the work of Crespo-Hernández and co-workers.^[70]

Ground-State Recovery and Overall Relaxation Scheme

Eventually, the measured TVA spectra reveal the recovery of the electronic GS with a yield of $\Phi_{\text{GS}} = 0.58 \pm 0.07$. In principle, the observed behaviour can arise from IC to the GS from the $^1\pi\pi^*$ or the $^1n\pi^*$ state or both, and – considering the almost ~ 1 ns lifetime – in part also from radiative processes (*i.e.* fluorescence). The $^3\pi\pi^*$ (T_1) state is far too long-lived to contribute to the observed GS recovery on the time scale of our experiment.^[70]

Following the reported quantum chemical calculations,^[28,32,42,43,46] 2AP exhibits two accessible conical intersections with the GS along the respective minimum energy pathways after $^1\pi\pi^*$ excitation. We therefore derived an electronic relaxation scheme for 2AP

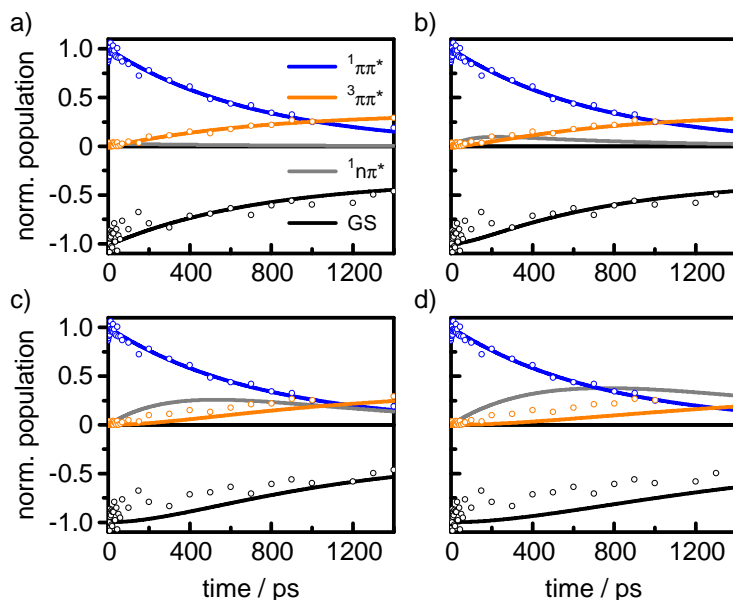


Figure 3.6: Comparison of kinetic model predictions (solid lines) for various $^1n\pi^*$ lifetimes with the observed temporal evolutions of the vibrational marker bands in the different electronic states (open circles), assuming $k_{1a} = 1/740$ ps, $k_{1b} = 0$, $k_{2a}/k_{2b} = \Phi_T/\Phi_{\text{GS}}$, and (a) $k_2 = 1/10$ ps, (b) $k_2 = 1/50$ ps, (c) $k_2 = 1/200$ ps, (d) $k_2 = 1/400$ ps.

after $^1\pi\pi^*$ photoexcitation as depicted in Fig. 3.7. The CIs predicted by the quantum chemical calculations are of $^1n\pi^*/\text{GS}$ character along the puckered N^1C^6 bond and of $^1\pi\pi^*/\text{GS}$ character along the puckered N^3C^2 bond. However, as already stated, the strong dependence of the fluorescence lifetime of the $^1\pi\pi^*$ state on solvent polarity and molecular environment and the long fluorescence lifetime of 2AP in solution, especially in bulk water, reflect a corresponding potential energy barrier en route to the decisive CI between the $^1\pi\pi^*$ and $^1n\pi^*$ states. This is also reflected in our calculated energy diagram of the excited states in Fig. 3.2. As the TVA data show, the GS recovery takes place with virtually the same 740 ps time constant as found for the $^1\pi\pi^*$ deactivation and the $^3\pi\pi^*$ formation. Hence, the $^1\pi\pi^* \rightarrow ^1n\pi^*$ IC process with $\tau = 740$ ps seems to be the overall rate-limiting step. Since the GS recovery exhibits that same time constant, it likely takes place mainly from the $^1n\pi^*$ state. By the same token, the $^1\pi\pi^*/\text{GS}$ CI is concluded to be higher in energy than the $^1\pi\pi^*/^1n\pi^*$ CI so that the direct $^1\pi\pi^* \rightarrow \text{GS}$ electronic deactivation pathway in solution falls behind the $^1\pi\pi^* \rightarrow ^1n\pi^* \rightarrow \text{GS}$ route.

Although GS recovery *via* the $^1n\pi^*/\text{GS}$ CI clearly predominates, a small contribution by direct deactivation from the $^1\pi\pi^*$ state up to $k_{1b}/k_1 \sim 10\text{--}20\%$ *via* the cited $^1\pi\pi^*/\text{GS}$ CI along the puckered N^3C^2 bond cannot be excluded on the basis of the experimental data. For a contribution of $k_{1b}/k_1 > 20\%$, one would have to assume a similarly strong energetic influence by the molecular environment on the $^1\pi\pi^*/\text{GS}$ CI as for the $^1\pi\pi^*/^1n\pi^*$ CI to rationalize the well-established strong solvation dependence of the 2AP fluorescence properties.^[26,29,34,41] Hence, we conclude that the direct deactivation from $^1\pi\pi^*$ to the GS plays relatively little role. Further, no evidence was found for a contribution to the dynamics by the $^3n\pi^*$ (T_2) state, which has a calculated vertical excitation energy close to that of the $^1\pi\pi^*$ state (*cf.* SI), but lies well above the optimized $^1\pi\pi^*$ ($S_{1,\text{LE}}$) and $^3\pi\pi^*$ (T_1) minima.

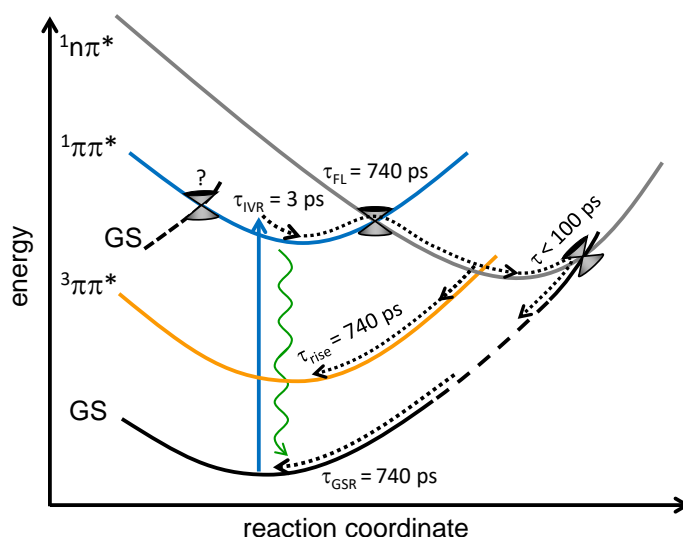


Figure 3.7: Sketch of the proposed electronic deactivation pathways in 2AP after $^1\pi\pi^*$ excitation showing the efficient ISC route to the $^3\pi\pi^*$ state and the IC route to the electronic GS *via* the intermediate $^1n\pi^*$ state.

3.5 Conclusions

In conclusion, we have investigated the photophysical dynamics of 2-aminopurine riboside in CHCl_3 solution by femtosecond time-resolved transient vibrational absorption spectroscopy aided by quantum chemical DFT and *ab initio* calculations of the ground- and excited-state normal mode vibrations. The excited electronic state lifetime was determined by femtosecond fluorescence up-conversion measurements. After excitation of the molecules to the $^1\pi\pi^*$ optically bright state at $\lambda_{\text{pump}} = 310$ nm, we observe an initial fast relaxation with $\tau_1 = 3.0 \pm 1.0$ ps that reflects the motion of the prepared wavepacket away from its Franck-Condon region into a $^1\pi\pi^*$ local minimum ($S_{1,\text{LE}}$) on the first excited singlet electronic potential energy surface (S_1), as well as fast internal vibrational redistribution and reorientation dynamics in the solvent shell. With the subsequent decay of the $^1\pi\pi^*$ population, we observe a partial recovery of the electronic ground state and a concurrent population of the $^3\pi\pi^*$ (T_1) state with a time constant $\tau_2 = 740 \pm 15$ ps. Two possible relaxation pathways towards the electronic ground state and the $^3\pi\pi^*$ state were discussed. While a contribution by direct ISC within the $\pi\pi^*$ manifold cannot be ruled out, the dynamics likely proceed *via* internal conversion from the $^1\pi\pi^*$ ($S_{1,\text{LE}}$) state to the adiabatic global $^1n\pi^*$ (S_1) potential energy minimum followed by El-Sayed allowed ISC to the $^3\pi\pi^*$ (T_1) state with a quantum yield of $\phi_{\text{T}} = 0.42 \pm 0.07$. With a lifetime of $\tau(^1\pi\pi^*) = 740$ ps, the $^1\pi\pi^* \rightarrow ^1n\pi^*$ IC process is proposed as rate-limiting step. The $^1n\pi^*$ state has a lifetime of $\tau(^1n\pi^*) < 100$ ps as an upper limit.

Acknowledgments

The laser system and research at the University of Bristol have been supported by ERC Advanced Grant CAPRI 290966. The group at the University of Kiel has been supported by the Deutsche Forschungsgemeinschaft through the Collaborative Research Centre 677 “Function by Switching”. KR has received support by DFG grant RO 4952/1-1. HJBM and RAI were supported by EPSRC Doctoral Training Grant awards.

Notes and References

- [1] D. C. Ward, E. Reich and L. Stryer, *J. Biol. Chem.*, 1969, **244**, 1228–1237.
- [2] J. Smagowicz and K. L. Wierzchowski, *J. Lumin.*, 1974, **8**, 210–232.
- [3] C. Santhosh and P. Mishra, *Spectrochim. Acta, Part A*, 1991, **47**, 1685–1693.
- [4] C. R. Guest, R. A. Hochstrasser, L. C. Sowers and D. P. Millar, *Biochemistry*, 1991, **30**, 3271–3279.
- [5] E. L. Rachofsky, E. Seibert, J. T. Stivers, R. Osman and J. B. A. Ross, *Biochemistry*, 2001, **40**, 957–967.
- [6] R. Neely, S. Megennis, D. Dryden and A. Jones, *J. Phys. Chem. B*, 2004, **108**, 17606–17610.
- [7] J. M. Jean and K. B. Hall, *Proc. Natl. Acad. Sci. U. S. A.*, 2001, **98**, 37–41.
- [8] J. M. Jean and K. B. Hall, *Biochemistry*, 2004, **43**, 10277–10284.
- [9] J. M. Jean and B. P. Krueger, *J. Phys. Chem. B*, 2006, **110**, 2899–2909.
- [10] S. K. Pal, J. Peon and A. H. Zewail, *Chem. Phys. Lett.*, 2002, **363**, 57–63.
- [11] S. K. Pal, L. Zhao, T. Xia and A. H. Zewail, *Proc. Natl. Acad. Sci. U. S. A.*, 2003, **100**, 13746–13751.
- [12] O. J. G. Somsen, L. B. Keukens, M. N. de Keijzer, A. van Hoek and H. van Amerongen, *ChemPhysChem*, 2005, **6**, 1622–1627.
- [13] O. J. Somsen, A. van Hoek and H. van Amerongen, *Chem. Phys. Lett.*, 2005, **402**, 61–65.
- [14] A. C. Jones and R. K. Neely, *Q. Rev. Biophys.*, 2015, **48**, 244–279.
- [15] L. Zhao and T. Xia, *J. Am. Chem. Soc.*, 2007, **129**, 4118–4119.
- [16] T. Gelot, P. Tourón-Touceda, O. Creégut, J. Léonard and S. Haacke, *J. Phys. Chem. A*, 2012, **116**, 2819–2825.
- [17] W. Xu, K. Min and E. T. Kool, *Nature*, 2017, **9**, 1043–1055.

- [18] L. C. Sowers, G. V. Fazakerley, R. Eritjat, B. E. Kaplant, M. F. Goodman and S. W. Benson, *Proc. Natl. Acad. Sci. U. S. A.*, 1986, **83**, 5434–5438.
- [19] T. M. Nordlund, S. Andersson, L. Nilsson, R. Rigler, A. Gråslund and L. W. Mclaughlin, *Biochemistry*, 1989, **28**, 9095–9103.
- [20] M. Kawai, M. J. Lee, K. O. Evans and T. M. Nordlund, *J. Fluoresc.*, 2001, **11**, 23–32.
- [21] K. Evans, D. Xu, Y. Kim and T. M. Nordlund, *J. Fluoresc.*, 1992, **2**, 209–216.
- [22] N. P. Johnson, W. A. Baase and P. H. von Hippel, *Proc. Natl. Acad. Sci. U. S. A.*, 2004, **101**, 3426–3431.
- [23] A. Dallmann, L. Dehmel, T. Peters, C. Mügge, C. Griesinger, J. Tuma and N. Ernsting, *Angew. Chem., Int. Ed.*, 2010, **49**, 5989–5992.
- [24] R. Ramaekers, L. Adamowicz and G. Maes, *Eur. Phys. J. D*, 2002, **20**, 375–388.
- [25] A. Broo and A. Holmén, *Chem. Phys.*, 1996, **211**, 147–161.
- [26] R.-X. He, X.-H. Duan and X.-Y. Li, *Phys. Chem. Chem. Phys.*, 2006, **8**, 587–591.
- [27] E. Nir, K. Kleinermanns, L. Grace and M. de Vries, *J. Phys. Chem. A*, 2001, **105**, 5106–5110.
- [28] K. A. Seefeld, C. Plützer, D. Löwenich, T. Häber, R. Linder, K. Kleinermanns, J. Tatchen and C. M. Marian, *Phys. Chem. Chem. Phys.*, 2005, **7**, 3021–3026.
- [29] K. Feng, G. Seefeld and K. Kleinermanns, *ChemPhysChem*, 2009, **10**, 886–889.
- [30] R. K. Sinha, S. Lobsiger and S. Leutwyler, *J. Phys. Chem. A*, 2011, **116**, 1129–1136.
- [31] R. K. Sinha, S. Lobsiger, M. Trachsel and S. Leutwyler, *J. Phys. Chem. A*, 2011, **115**, 6208–6217.
- [32] S. Lobsiger, R. K. Sinha, M. Trachsel and S. Leutwyler, *J. Chem. Phys.*, 2011, **134**, 114307.
- [33] M. A. Trachsel, S. Lobsiger, T. Schaär and S. Leutwyler, *J. Chem. Phys.*, 2014, **140**, 044331.

- [34] S. Lobsiger, S. Blaser, R. K. Sinha, H.-M. Frey and S. Leutwyler, *Nat. Chem.*, 2014, **6**, 989–993.
- [35] S. Smolarek, A. M. Rijs, W. J. Buma and M. Drabbels, *Phys. Chem. Chem. Phys.*, 2010, **12**, 15600–15606.
- [36] C. Canuel, M. Mons, F. Piuze, B. Tardivel, I. Dimicoli and M. Elhanine, *J. Chem. Phys.*, 2005, **122**, 074316.
- [37] A. Holmén, B. Nordén and B. Albinsson, *J. Am. Chem. Soc.*, 1997, **119**, 3114–3121.
- [38] A. Broo, *J. Phys. Chem. A*, 1998, **102**, 526–531.
- [39] J. M. Jean and K. B. Hall, *J. Phys. Chem. A*, 2000, **104**, 1930–1937.
- [40] B. Mennucci, A. Toniolo and T. Jacopo, *J. Phys. Chem. A*, 2001, **105**, 4749–4757.
- [41] E. L. Rachofsky, J. B. A. Ross, M. Krauss and R. Osman, *J. Phys. Chem. A*, 2001, **105**, 190–197.
- [42] S. Perun, A. L. Sobolewski and W. Domcke, *Mol. Phys.*, 2006, **104**, 1113–1121.
- [43] L. Serrano-Andrés, M. Merchán and A. C. Borin, *Proc. Natl. Acad. Sci. U. S. A.*, 2006, **103**, 8691–8696.
- [44] V. Ludwig, M. S. do Amaral, Z. M. da Costa, A. C. Borin, S. Canuto and L. Serrano-Andrés, *Chem. Phys. Lett.*, 2008, **463**, 201–205.
- [45] J. Liang and S. Matsika, *J. Am. Chem. Soc.*, 2011, **133**, 6799–6808.
- [46] M. Barbatti and H. Lischka, *Phys. Chem. Chem. Phys.*, 2015, **17**, 15452–15459.
- [47] E. Rachofsky, R. Osman and J. Ross, *Biochemistry*, 2001, **40**, 946–956.
- [48] O. F. Larsen, I. H. van Stokkum, M.-L. Groot, J. T. Kennis, R. van Grondelle and H. van Amerongen, *Chem. Phys. Lett.*, 2003, **371**, 157–163.
- [49] O. F. A. Larsen, I. H. M. van Stokkum, F. L. de Weerd, M. Vengris, C. T. Aravindakumar, R. van Grondelle, N. E. Geacintov and H. van Amerongen, *Phys. Chem. Chem. Phys.*, 2004, **6**, 154–160.

- [50] S. M. Law, R. Eritja, M. F. Goodman and K. J. Breslauer, *Biochemistry*, 1996, **35**, 12329–12337.
- [51] K. Liebert, A. Hermann, M. Schlickerrieder and A. Jeltsch, *J. Mol. Biol.*, 2004, **341**, 443–454.
- [52] R. K. Neely and A. C. Jones, *J. Am. Chem. Soc.*, 2006, **128**, 15952–15953.
- [53] B. J. Lee, M. Barch, E. W. Castner, J. Völker and K. J. Breslauer, *Biochemistry*, 2007, **46**, 10756–10766.
- [54] N. N. Degtyareva, M. J. Reddish, B. Sengupta and J. T. Petty, *Biochemistry*, 2009, **48**, 2340–2346.
- [55] M. Li, Y. Sato, S. Nishizawa, T. Seino, K. Nakamura and N. Teramae, *J. Am. Chem. Soc.*, 2009, **131**, 2448–2449.
- [56] S. J. O. Hardman and K. C. Thompson, *Biochemistry*, 2006, **45**, 9145–9155.
- [57] E. Y. M. Bonnist and A. C. Jones, *ChemPhysChem*, 2008, **9**, 1121–1129.
- [58] H.-N. Nguyen, L. Zhao, C. W. Gray, D. M. Gray and T. Xia, *Biochemistry*, 2011, **50**, 8989–9001.
- [59] D. A. Smith, L. F. Holroyd, T. van Mourik and A. C. Jones, *Phys. Chem. Chem. Phys.*, 2016, **18**, 14691–14700.
- [60] J. Liang, Q. L. Nguyen and S. Matsika, *Photochem. Photobiol. Sci.*, 2013, **12**, 1387–1400.
- [61] J. M. Remington, A. M. Philip, M. Hariharan and B. Kohler, *J. Chem. Phys.*, 2016, **145**, 155101.
- [62] T. van Mourik and S. W. L. Hogan, *Struct. Chem.*, 2016, **27**, 145–158.
- [63] W. Frey, L. Sowers, D. Millar and S. Benkovic, *Biochemistry*, 1995, **34**, 9185–9192.
- [64] C. Hariharan, L. B. Bloom, S. A. Helquist, E. T. Kool and L. J. Reha-Kranz, *Biochemistry*, 2006, **45**, 2836–2844.
- [65] S. Kelley and J. Barton, *Science*, 1999, **283**, 375–380.

- [66] T. Fiebig, C. Wan and A. H. Zewail, *ChemPhysChem*, 2002, **3**, 781–788.
- [67] J. Genereux, S. Wuerth and J. Barton, *J. Am. Chem. Soc.*, 2011, **133**, 3863–3868.
- [68] J. Genereux and J. Barton, *Chem. Rev.*, 2010, **10**, 1642–1662.
- [69] R. González-Luque, T. Climent, I. González-Ramírez, M. Merchán and L. Serrano-Andrés, *J. Chem. Theory Comput.*, 2010, **6**, 2103–2114.
- [70] C. Reichardt, C. Wen, R. A. Vogt and C. E. Crespo-Hernández, *Photochem. Photobiol. Sci.*, 2013, **12**, 1341–1350.
- [71] G. M. Roberts, H. J. B. Marroux, M. P. Grubb, M. N. R. Ashfold and A. J. Orr-Ewing, *J. Phys. Chem. A*, 2014, **118**, 11211–11225.
- [72] K. Siriwong, A. Voityuk, M. Newton and N. Rösch, *J. Phys. Chem. B*, 2003, **107**, 2595–2601.
- [73] N. K. Schwalb and F. Temps, *J. Am. Chem. Soc.*, 2007, **129**, 9272–9273.
- [74] N. K. Schwalb, T. Michalak and F. Temps, *J. Phys. Chem. B*, 2009, **113**, 16365–16376.
- [75] K. Röttger, H. J. B. Marroux, M. P. Grubb, P. M. Coulter, H. Böhnke, A. S. Henderson, M. C. Galan, F. Temps, A. J. Orr-Ewing and G. M. Roberts, *Angew. Chem., Int. Ed.*, 2015, **54**, 14719–14722.
- [76] K. Röttger, H. J. B. Marroux, H. Böhnke, D. T. J. Morris, A. T. Voice, F. Temps, G. M. Roberts and A. J. Orr-Ewing, *Faraday Discuss.*, 2016, **194**, 683–708.
- [77] N. K. Schwalb and F. Temps, *J. Phys. Chem. A*, 2009, **113**, 13113–13123.
- [78] Y. Zhao and D. G. Truhlar, *Theor. Chem. Acc.*, 2008, **120**, 215–241.
- [79] A. McLean and G. Chandler, *J. Chem. Phys.*, 1980, **72**, 5639–3648.
- [80] K. Raghavachari, J. Binkley, R. Seeger and J. Pople, *J. Chem. Phys.*, 1980, **72**, 650–654.
- [81] M. Frisch, J. Pople and J. Binkley, *J. Chem. Phys.*, 1984, **80**, 3265–3269.
- [82] T. Clark, J. Chandrasekhar, G. Spitznagel and P. Schleyer, *J. Comput. Chem.*, 1983, **4**, 294–300.

- [83] M. J. Frisch, G. W. Trucks, H. B. Schlegel, G. E. Scuseria, M. A. Robb, J. R. Cheeseman, G. Scalmani, V. Barone, B. Mennucci, G. A. Petersson, H. Nakatsuji, M. Caricato, X. Li, H. P. Hratchian, A. F. Izmaylov, J. Bloino, G. Zheng, J. L. Sonnenberg, M. Hada, M. Ehara, K. Toyota, R. Fukuda, J. Hasegawa, M. Ishida, T. Nakajima, Y. Honda, O. Kitao, H. Nakai, T. Vreven, J. A. Montgomery Jr., J. E. Peralta, F. Ogliaro, M. Bearpark, J. J. Heyd, E. Brothers, K. N. Kudin, V. N. Staroverov, T. Keith, R. Kobayashi, J. Normand, K. Raghavachari, A. Rendell, J. C. Burant, S. S. Iyengar, J. Tomasi, M. Cossi, N. Rega, J. M. Millam, M. Klene, J. E. Knox, J. B. Cross, V. Bakken, C. Adamo, J. Jaramillo, R. Gomperts, R. E. Stratmann, O. Yazyev, A. J. Austin, R. Cammi, C. Pomelli, J. W. Ochterski, R. L. Martin, K. Morokuma, V. G. Zakrzewski, G. A. Voth, P. Salvador, J. J. Dannenberg, S. Dapprich, A. D. Daniels, O. Farkas, J. B. Foresman, J. V. Ortiz, J. Cioslowski and D. J. Fox, *Gaussian 09, Revision D.01*, Gaussian Inc., Wallingford CT, 2013.
- [84] M. L. Laury, S. E. Boesch, I. Haken, P. Sinha, R. A. Wheeler and A. K. Wilson, *J. Comput. Chem.*, 2011, **32**, 2339–2347.
- [85] M. L. Laury, M. J. Carlson and A. K. Wilson, *J. Comput. Chem.*, 2012, **33**, 2380–2387.
- [86] M. Häser and R. Ahlrichs, *J. Comput. Chem.*, 1989, **10**, 104–111.
- [87] F. Weigend and M. Häser, *Theor. Chim. Acta*, 1997, **97**, 331–340.
- [88] F. Weigend, M. Häser, H. Patzelt and R. Ahlrichs, *Chem. Phys. Lett.*, 1998, **294**, 143–152.
- [89] C. Hättig, A. Hellweg and A. Köhn, *Phys. Chem. Chem. Phys.*, 2006, **8**, 1159–1169.
- [90] A. Schäfer, C. Huber and R. Ahlrichs, *J. Phys. Chem.*, 1994, **100**, 5829–5835.
- [91] F. Weigend and R. Ahlrichs, *Phys. Chem. Chem. Phys.*, 2005, **7**, 3297–3305.
- [92] D. Rappoport and F. Furche, *J. Chem. Phys.*, 2010, **133**, 134105.
- [93] R. Ahlrichs, M. Bär, M. Häser, H. Horn and C. Kölmel, *Chem. Phys. Lett.*, 1989, **162**, 165–169.
- [94] A. Hellweg, S. Grün and C. Hättig, *Phys. Chem. Chem. Phys.*, 2008, **10**, 4119.
- [95] R. Ahlrichs, *Phys. Chem. Chem. Phys.*, 2004, **6**, 5119–5121.
- [96] C. Hättig and A. Köhn, *J. Chem. Phys.*, 2002, **117**, 6939–6951.

- [97] A. Köhn and C. Hättig, *J. Chem. Phys.*, 2003, **119**, 5021–5036.
- [98] C. Hättig and F. Weigend, *J. Chem. Phys.*, 2000, **113**, 5154–5161.
- [99] O. Christiansen, H. Koch and P. Jørgensen, *Chem. Phys. Lett.*, 1995, **243**, 409–418.
- [100] D. H. Friese, L. Törk and C. Hättig, *J. Chem. Phys.*, 2014, **141**, 194106.
- [101] As the ribose moiety is not involved in the observed dynamics, we shall refer to our title compound simply as 2AP from here on, rather than **2APr**.
- [102] M. A. El-Sayed, *J. Chem. Phys.*, 1963, **38**, 2834–2838.
- [103] C. M. Marian, F. Schneider, M. Kleinschmidt and J. Tatchen, *Eur. Phys. J. D*, 2002, **20**, 357–367.
- [104] C. E. Crespo-Hernández, L. Martínez-Fernández, C. Rauer, C. Reichardt, S. Mai, M. Pollum, P. Marquetand, L. González and I. Corral, *J. Am. Chem. Soc.*, 2015, **137**, 4368–4381.
- [105] P. M. Hare, C. E. Crespo-Hernández and B. Kohler, *J. Phys. Chem. B*, 2006, **110**, 18641–18650.
- [106] P. M. Hare, C. E. Crespo-Hernández and B. Kohler, *Proc. Natl. Acad. Sci. U. S. A.*, 2007, **104**, 435–440.
- [107] W.-M. Kwok, C. Ma and D. L. Phillips, *J. Am. Chem. Soc.*, 2008, **130**, 5131–5139.
- [108] M. Etinski, T. Fleig and C. M. Marian, *J. Phys. Chem. A*, 2009, **113**, 11809–11816.

3.6 Supplementary Information

Synthesis of the TBDMS-Protected 2-Aminopurine Riboside

To a solution of 2-aminopurine riboside (1.0 g, 3.75 mmol) and imidazole (2.4 g, 35.7 mmol) in anhydrous DMF (9.1 mL) at room temperature, TBDMSCl (2.7 g, 17.9 mmol) was added. This mixture was stirred (72 h) under argon atmosphere, concentrated *in vacuo* and then dissolved in ethyl acetate (50 mL). The organic phase was washed with water (3 x 10 mL), dried over sodium sulfate and concentrated. Column chromatography (ethyl acetate) yielded 2',3',5'-tri-O-(*tert*-butyldimethylsilyl)-2-aminopurine riboside (1.3 g, 60%) as a colourless solid; $R_f = 0.5$ (ethyl acetate).

^1H NMR (200 MHz, CDCl_3) δ /ppm: 8.54 (1H, s, C₆H), 8.07 (1H, s, C₈H), 5.82 (1H, d, $J = 4.7$ Hz, H-1'), 4.96 (2H, br s, NH₂), 4.36 (1H, t, $J = 4.5$ Hz, H-2'), 4.16 (1H, t, $J = 4.2$ Hz, H-3'), 3.98 (1H, td, $J = 3.7$ and 2.7 Hz, H-4'), 3.86 (1H, dd, $J = 11.4$ and 3.6 Hz, H-5a'), 3.65 (1H, dd, $J = 11.4$ and 2.5 Hz, H-5b'), 0.82 (9H, br s, C(CH₃)₃), 0.80 (9H, br s, C(CH₃)₃), 0.69 (9H, br s, C(CH₃)₃), 0.01 (3H, br s, CH₃), 0.00 (3H, br s, CH₃), -0.03 (3H, br s, CH₃), -0.04 (3H, br s, CH₃), -0.15 (3H, br s, CH₃), -0.31 (3H, br s, CH₃);

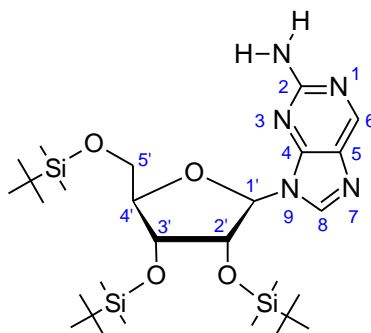
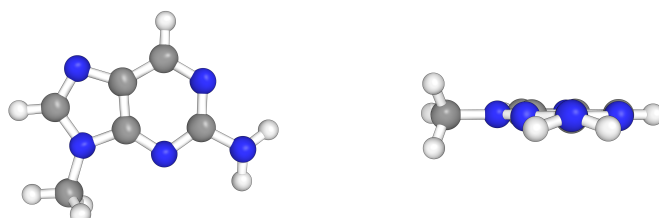


Figure 3.8: Atom numbering of the *tert*-butyldimethylsilyl (TBDMS) protected 2AP riboside.

Calculated Relaxed Structures of 9Me-2AP in its Electronic Ground State and in the Excited $^1\pi\pi^*$, $^1n\pi^*$ and $^3\pi\pi^*$ States

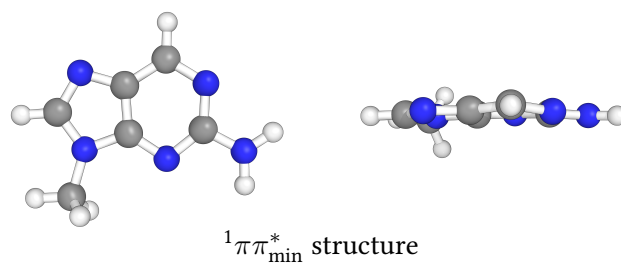
Table 3.1: Cartesian coordinates for the optimized structure of 9Me-2AP in the ground electronic state at the M062X / 6-311+G** level of theory.



GS_{min} structure

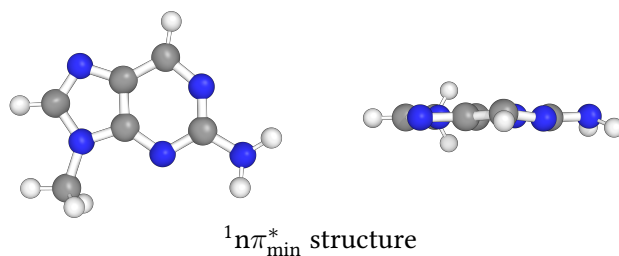
atom	X / Å	Y / Å	Z / Å
N	-0.69320	-1.03900	0.00060
C	0.34970	-0.22120	-0.00100
C	0.31360	1.18120	-0.00240
C	-0.95970	1.73860	0.00290
N	-2.03410	0.96170	0.00150
C	-1.85510	-0.37750	-0.00580
N	1.59810	1.69900	0.00040
C	2.36050	0.64780	0.00250
N	1.67530	-0.55330	0.00180
H	-1.11940	2.81270	0.01160
N	-2.99710	-1.12920	-0.05580
H	3.44180	0.65980	0.00340
H	-2.91240	-2.10160	0.18870
H	-3.85320	-0.65580	0.18040
C	2.21420	-1.89860	0.00030
H	1.89960	-2.43100	0.89840
H	1.86010	-2.44150	-0.87650
H	3.30140	-1.83810	-0.02430

Table 3.2: Cartesian coordinates for the optimized structure of 9Me-2AP in the $^1\pi\pi^*$ state at the RI-CC2 / def2-TZVPPD level of theory.



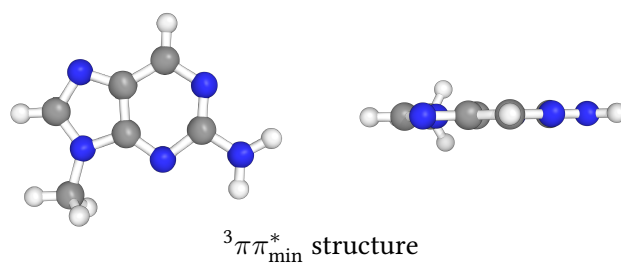
atom	X / Å	Y / Å	Z / Å
N	-0.6562444	-1.1182982	0.1111756
C	0.3573914	-0.2259930	-0.0008329
C	0.2834734	1.1912144	0.0131290
C	-1.0273705	1.7959580	0.1063167
N	-2.0888953	0.9192461	-0.0562148
C	-1.8319814	-0.4059632	0.0199180
N	1.5268826	1.7303292	-0.0140708
C	2.3614054	0.6657137	-0.0286302
N	1.7085567	-0.5244508	0.0042642
H	-1.2099263	2.8508940	-0.0384058
N	-2.9307944	-1.1934377	-0.0027764
H	3.4380297	0.7240685	-0.0604848
H	-2.8161521	-2.1920352	0.0822797
H	-3.8385390	-0.7602593	-0.0828668
C	2.2693932	-1.8610778	-0.0124458
H	1.8477662	-2.4385732	0.8071348
H	2.0334696	-2.3543297	-0.9533518
H	3.3473353	-1.7853059	0.1043620

Table 3.3: Cartesian coordinates for the optimized structure of 9Me-2AP in the ${}^1n\pi^*$ state at the RI-CC2 / def2-TZVPPD level of theory.



atom	X / Å	Y / Å	Z / Å
N	0.7591675	1.0328498	0.0983895
C	-0.3593971	0.2541879	0.0186917
C	-0.4280358	-1.1535798	-0.0195987
C	0.8219126	-1.8484561	0.0868728
N	1.8931881	-0.9620037	-0.0028839
C	1.9369106	0.3418791	0.0626625
N	-1.7226981	-1.5685262	-0.0839128
C	-2.4406973	-0.4448457	-0.0699292
N	-1.6493661	0.6881991	-0.0028390
H	0.9941271	-2.8860471	-0.1547364
N	3.1153345	1.0410013	0.1505593
H	-3.5151616	-0.3746327	-0.1150172
H	3.0315869	1.9907233	-0.1823126
H	3.9239397	0.5484749	-0.1973232
C	-2.0775083	2.0728501	0.0291940
H	-1.7208623	2.5516489	0.9389091
H	-1.6827989	2.6058708	-0.8336895
H	-3.1638486	2.0953993	0.0066393

Table 3.4: Cartesian coordinates for the optimized structure of 9Me-2AP in the ${}^3\pi\pi^*$ state at the RI-CC2 / def2-TZVPPD level of theory.



atom	X / Å	Y / Å	Z / Å
N	1.0624523	0.4041203	0.0219492
C	-0.2124401	0.0419362	-0.0039726
C	-0.7619187	-1.2827166	-0.0214820
C	0.1883963	-2.3790443	-0.0097117
N	1.5172251	-2.0511483	0.0170865
C	1.8656677	-0.7821404	0.0304138
N	-2.0923527	-1.2473049	-0.0464860
C	-2.4134637	0.1009184	-0.0452770
N	-1.3009713	0.8843804	-0.0205292
H	-0.0986897	-3.4185371	-0.0202750
N	3.1796651	-0.4684388	0.0563222
H	-3.4119704	0.5022228	-0.0627829
H	3.4489715	0.4995711	0.0676276
H	3.8616740	-1.2079979	0.0656308
C	-1.2227590	2.3324041	-0.0089999
H	-0.7261819	2.6648923	0.8999588
H	-0.6518287	2.6728589	-0.8699752
H	-2.2314759	2.7340238	-0.0494974

Calculated Electronic Excitation Energies for 9Me-2AP

Table 3.5: Calculated vertical excitation energies (VEEs) for 9Me-2AP at the minimum energy structure of the GS and calculated energies at the minimum energy structures of the $^1\pi\pi^*$, $^1n\pi^*$ and $^3\pi\pi^*$ excited states at the RI-MP2 / def2-TZVPPD (GS) resp. RI-CC2 / def2-TZVPPD (excited states) levels of theory.

	GS _{min}		$^1\pi\pi^*_{\text{min}}$	$^1n\pi^*_{\text{min}}$	$^3\pi\pi^*_{\text{min}}$
	VEE / eV ^b	$f^{a,b}$	E / eV ^b	E / eV ^b	E / eV ^b
GS	0.00	-	0.47 (0.48)	0.76 (0.84)	0.48
$^3\pi\pi^*$	3.65 (3.58)	-	3.37 (3.32)	4.01 (3.74)	3.22 (2.91)
$^3n\pi^*$	4.34 (4.33)	-	4.49	3.84	4.50
$^1\pi\pi^*$	4.45 (4.35)	0.1458 (0.1374)	4.13 (4.02)	4.91 (4.84)	4.24
$^1n\pi^*$	4.54 (4.55)	0.0025 (0.0031)	4.72 (4.68)	4.04 (4.01)	4.67

^a Oscillator strength, ^b Values in parentheses from ref. 1.

References

- [1] S. Lobsiger, R. K. Sinha, M. Trachsel and S. Leutwyler, *J. Chem. Phys.*, 2011, **134**, 114307.

Electronic Relaxation Dynamics of UV-Photoexcited 2-Aminopurine–Thymine Base Pairs in Watson–Crick and Hoogsteen Conformations

HENDRIK BÖHNKE,^a KATHARINA RÖTTGER,^{a,b,‡} REBECCA A. INGLE,^{b,§} HUGO J. B. MARROUX,^{b,¶}
MATS BOHNSACK,^a NINA K. SCHWALB,^{a,†} ANDREW J. ORR-EWING^{*b} AND FRIEDRICH TEMPS^{*a}

^a Institute of Physical Chemistry, Christian-Albrechts-University Kiel, Olshausenstr. 40, 24098 Kiel, Germany.

^b School of Chemistry, University of Bristol, Cantock's Close, Bristol BS8 1TS, United Kingdom.

[‡] Current address: Centre for Process Innovation, Wilton Centre, Wilton, Redcar TS10 4RF, United Kingdom.

[§] Current address: École Polytechnique Fédérale de Lausanne, Laboratoire de Spectroscopie Ultrarapide (LSU) and Lausanne Centre for Ultrafast Science (LACUS), ISIC, FSB, CH-1015 Lausanne, Switzerland.

[¶] Current address: Chemical Sciences Department, Lawrence Berkeley National Laboratory, 1 Cyclotron Road Berkeley CA 94720, USA.

[†] Current address: Bayer AG, Consumer Health Division, 51368 Leverkusen, Germany.

* To whom correspondence should be addressed.

E-mail: temps@phc.uni-kiel.de; a.orr-ewing@bristol.ac.uk.

Reprinted with permission from *J. Phys. Chem. B*, **2019**, *123*, 2904–2914.

Copyright 2019 American Chemical Society.

OWN CONTRIBUTIONS TO THIS PUBLICATION:

- Steady-state UV/vis, fluorescence and FTIR spectroscopy,
- Quantum chemical calculations for ground- and excited-state species,
- Transient femtosecond vibrational absorption spectroscopy,
- Analysis of experimental data,
- Writing of the manuscript.

Abstract

The fluorescent analogue 2-aminopurine (2AP) of the canonical nucleobase adenine (6-aminopurine) base-pairs with thymine (T) without disrupting the helical structure of DNA. It therefore finds frequent use in molecular biology for probing DNA and RNA structures and conformational dynamics. However, detailed understanding of the processes responsible for fluorescence quenching remains largely elusive on a fundamental level. Although attempts have been made to ascribe decreased excited-state lifetimes to intrastrand charge-transfer and stacking interactions, possible influences from dynamic interstrand H-bonding have been widely ignored. Here, we investigate the electronic relaxation of UV-excited 2AP·T in Watson–Crick (WC) and Hoogsteen (HS) conformations. Although the WC conformation features slowed-down, monomer-like electronic relaxation in $\tau \sim 1.6$ ns toward ground-state recovery and triplet formation, the dynamics associated with 2AP·T in the HS motif exhibit faster deactivation in $\tau \sim 70$ ps. As recent research has revealed abundant transient interstrand H-bonding in the Hoogsteen motif for duplex DNA, the established model for dynamic fluorescence quenching may need to be revised in the light of our results. The underlying supramolecular photophysical mechanisms are discussed in terms of a proposed excited-state double-proton transfer as an efficient deactivation channel for recovery of the HS species in the electronic ground state.

4.1 Introduction

2-Aminopurine (2AP) is a fluorescent analogue of the canonical nucleobase adenine that base-pairs with thymine (T) with little perturbation of the helical structure when incorporated into DNA.^[1–7] Since its fluorescence lifetime is highly sensitive to the molecular microenvironment,^[8–15] it is widely used in DNA and RNA studies as a weakly perturbing probe for monitoring solvation^[9] and conformational dynamics,^[12,13,16,17] base stacking/unstacking interactions,^[11,12,18–20] nucleotide binding and exchange,^[21] and charge-transfer processes.^[22–24] Photoexcitation at $\lambda = 310$ nm selectively addresses the 2AP chromophore owing to the red shift of its first $^1\pi\pi^*$ electronic absorption band in the ultraviolet (UV) compared to the spectra of the canonical nucleobases. However, understanding the complex electronic relaxation mechanisms in photoexcited oligonucleotides continues to present challenges due to competing intrastrand deactivation dynamics induced *via* charge-transfer and stacking interactions, including exciton and excimer formation, and interstrand de-excitation *via* H-bonded base pairs.^[25–30] Moreover, as recently discovered, duplex DNA also contains transient Hoogsteen base pairs as additional structural motifs to enhance functional versatility beyond the Watson–Crick limitations,^[31,32] further complicating the dynamics of photoexcited DNA, especially when containing 2AP.

Here, we report on the electronic deactivation pathways in purely H-bonded 2AP·T base pairs in Watson–Crick (WC) and Hoogsteen (HS) conformations after selective UV

photoexcitation of the 2AP chromophore. Our investigations used femtosecond transient vibrational absorption spectroscopy (TVAS), a method sensitive not only to the molecular structure but also to the characters of the excited electronic states. To assure sufficient concentrations of 2AP·T, we studied the *tert*-butyldimethylsilyl (TBDMS)-protected nucleoside of 2AP and the respective protected 2'-deoxynucleoside of T in chloroform (CHCl₃) solution. For simplicity, the free 2AP riboside, the free T 2'-deoxyriboside, and their H-bonded pairs are henceforth referred to as 2AP, T, T·T and 2AP·T, respectively.

4.2 Methods

Time-Resolved Spectroscopy

Time-resolved measurements upon UV excitation were performed using 25 mM equimolar sample concentrations of 2AP and T at an optical pathlength of 100 μm . CHCl₃ was chosen as the solvent as it features a dielectric environment similar to that in the DNA double helix^[33] and ensures a high optical transmission in the mid-infrared (mIR) spectrum. To enable sufficient solubility of 2AP and T in such an apolar solvent, the riboside OH groups of the nucleoside and 2'-deoxynucleoside, respectively, were protected by bulky, apolar *tert*-butyldimethylsilyl (TBDMS) groups. Association constants for heterodimer formation ($K_{2\text{AP}\cdot\text{T}}$) and homodimer formation ($K_{\text{T}\cdot\text{T}}$) were determined by concentration-dependent static ground-state vibrational spectroscopy (*cf.* Fig. 4.1) using a Bruker IFS 66v Fourier transform infrared (FTIR) spectrometer.

Time-resolved transient vibrational absorption measurements of UV-photoexcited molecules were performed at the University of Bristol.^[34] Excitation pulses at $\lambda_{\text{pump}} = 310 \text{ nm}$ with a duration of $\sim 100 \text{ fs}$ (full width at half-maximum) were generated by a Coherent OPerA Solo optical parametric amplifier (OPA) pumped by 2.45 mJ per pulse from a Coherent Legend Elite HE+ regenerative amplifier running at 1 kHz and 800 nm with 40 fs duration. The pump pulses were attenuated to 100 nJ per pulse (2AP) and 200 nJ per pulse (2AP + T) by a combination of a $\lambda/2$ waveplate and a wire-grid polarizer and set to the magic angle condition (54.7°) with respect to the probe pulses. The doubled excitation energy for the measurements of the 2AP + T mixture relative to the measurements of the free monomer accounts for the lower effective excited-state concentration of free 2AP in the mixture ($\sim 50\%$). Thus, no further weighting was necessary for the subtraction of the TVA spectra of 2AP from the spectra of the 2AP + T mixture (see later). Broadband mIR probe pulses were supplied by difference frequency generation of the signal and idler from a second OPA, giving tunable pulses with $\sim 300 \text{ cm}^{-1}$ bandwidth in the 1250–4000 cm^{-1} range. After passing through the sample, the mIR probe pulses were spectrally dispersed in a grating spectrograph (HORIBA Scientific, iHR320) and detected on a 128 pixel, liquid-N₂-cooled mercury cadmium telluride array (Infrared Associates).

For transient measurements, the UV pump pulses were delayed using an aluminum retro-reflector mounted on a motorized delay stage and modulated at 0.5 kHz with an optical chopper wheel for pump-on/pump-off pairs of spectra.

The supplementary time-resolved fluorescence measurements to determine the excited-state lifetimes of 2AP·T in CHCl_3 were performed using the up-conversion setup in Kiel.^[35]

Computational Methods

Quantum chemical calculations were carried out to derive the energetic order of the excited electronic states above the Frank–Condon (FC) geometry of the ground state (GS) and to assign the characteristic vibrational marker bands observed in the FTIR and time-resolved TVA spectra. To save computer time, the protected riboside residue was substituted by a methyl group in all calculations. Relaxed GS structures and vibrational frequencies were determined by density functional theory (DFT) calculations with the M062X functional^[36] in combination with the 6-311+G** basis set^[37–40] using the Gaussian 09 suite of programs^[41] for free 2AP, free T, T·T homodimers, and 2AP·T heterodimers. The calculated wavenumbers were scaled^[42,43] to obtain the best agreement with the experimental data using factors of 0.955 and 0.94 below and above 2000 cm^{-1} , respectively, as done before for the 2AP monomer. The relative energies of the different species were obtained by DFT calculations at the B2PLYP-D3(BJ)^[44]/def2-QZVP^[45] level of theory employing the Turbomole 7.0 program.^[46] The B2PLYP-D3(BJ) double-hybrid method was chosen because it has recently been shown in a series of benchmark calculations^[44,47,48] to provide more accurate results than the common B3LYP functional.

Complementary calculations were run using second-order Møller–Plesset perturbation theory (MP2) under the resolution of the identity (RI) approximation^[49–52] with the def2-TZVPPD basis set^[53–55] to obtain starting points for the excited states. Vertical excitation energies (VEEs) were then computed using the second-order approximation coupled-cluster (CC2) method in Turbomole 7.0 in the form of the RI-CC2^[56–61] variant with the def2-TZVPPD basis set. Excited-state properties such as equilibrium structures and associated vibrational mode frequencies for the $^1\pi\pi^*$ and $^3\pi\pi^*$ state minima were computed for free 2AP.^[62] The obtained vibrational wavenumbers in the excited states were scaled with factors of 0.99 and 0.94 below and above 2000 cm^{-1} , respectively,^[63] to obtain the best agreement between the calculated and measured transient vibrational spectra. To mimic the vibrational spectra in the region of ring vibrations in the electronically excited states of 2AP·T, the calculated spectra for free 2AP were scaled to match the observed transient features with a factor of 0.975. Geometry relaxations and VEEs at frozen N–H distances in the 2AP·T dimers in the WC and HS conformations were carried out under the resolution of the identity approximation at the MP2 (GS) and ADC(2)^[64] ($^1\pi\pi^*$) levels of theory employing the def2-SVP basis set.^[53]

4.3 Results

Association Equilibria between 2AP, T, T·T and 2AP·T

H-bonded 2AP·T co-exists in concentration-dependent equilibria with free 2AP, free T and T·T dimers in CHCl₃ solution. As illustrated in Fig. 4.1, characteristic vibrational marker bands of 2AP, T, T·T and 2AP·T were identified in measured Fourier transform infrared (FTIR) spectra and assigned aided by quantum chemical calculations. Investigation of the spectral region from 3600 to 3150 cm⁻¹ in Fig. 4.1 reveals vibrational bands at 3532 (3544) cm⁻¹ and 3424 (3423) cm⁻¹ associated with the antisymmetric and symmetric NH₂ stretching modes of 2AP (calculated values in parentheses), respectively, both in the spectra of 2AP and the 2AP + T mixture. Also, the 2AP + T mixture shows vibrational modes of T at 3398 (3397) cm⁻¹ and 3201 (3181) cm⁻¹ associated with the NH stretching mode of free T and homodimeric T·T, respectively. By following these vibrational marker bands in concentration-dependent studies, we determined the specific association constants $K_{T·T} = 2.1 \pm 0.7 \text{ M}^{-1}$ for the equilibrium between T and T·T,^[65] and $K_{2AP·T} = 60 \pm 17 \text{ M}^{-1}$ for the equilibrium between 2AP, T and 2AP·T. No evidence was found for significant self-association of 2AP in the investigated concentration range. Also, justified by the choice of CHCl₃ as the solvent, no indications of stacked chromophores were obtained in the FTIR and UV/vis spectra (Figs. 4.1 and 4.3). With these premises, taking the association constants $K_{T·T}$ and $K_{2AP·T}$, the percentage amount of H-bonded 2AP·T in a mixture of 2AP and T can readily be calculated. In a mixture of 2AP + T at initial concentrations of $c_0(2AP) = c_0(T) = 25 \text{ mM}$ as used in all time-resolved dynamics measurements in this work, the molar fractions of the constituents are calculated as $x_{2AP·T} = 0.29$, $x_{2AP} = 0.36$, $x_T = 0.34$, and $x_{T·T} = 0.01$. Thus, we calculate the free bases 2AP and T, and heterodimeric 2AP·T to be the dominating species in our sample solutions, whereas homodimeric T·T contributes only insignificantly to the FTIR spectra owing to the low association constant for self-association of T.

To gain further insight into the structural diversity of the subset of heterodimeric 2AP·T, we employed quantum chemical calculations at the B2PLYP-D3(BJ)/def2-QZVP level of theory (corresponding to 0 K dissociation energies without zero-point energy or solvent correction). As depicted in Fig. 4.2, our calculations revealed very similar binding energies for the 2AP·T dimer in the Watson–Crick (WC), reverse-Watson–Crick (rWC), Hoogsteen (HS), and reverse-Hoogsteen (rHS) conformations, thus hinting at a rather diverse distribution of H-bonded 2AP·T dimers in WC and HS conformations. As has been shown elsewhere,^[66] the Wobble conformation of 2AP·T is energetically less favored and therefore neglected here. Note that rather crude gas-phase computations neglecting solvent effects, zero-point energies, and steric effects of the TBDMS residue can provide only limited information on the actual distribution of H-bonded species. However, the charac-

terization of exact thermodynamic distributions within the 2AP + T mixture is beyond the scope of this work. Still, justified by the emergence of distinct time constants for electronic deactivation in our time-resolved measurements below, our calculations tentatively hint at a rather heterogeneous distribution of WC and HS conformations at room temperature in CHCl_3 solution. Because they were indistinguishable in our experiments due to their structural similarities, the WC and rWC conformations on the one hand and the HS and rHS conformations on the other will be referred to simply as WC and HS conformations, respectively.

Fortunately, the rather complex distribution of free 2AP, free T and dimeric 2AP·T species gets significantly reduced for time-resolved experiments by selective photoexcitation of the 2AP chromophore both in free 2AP and within the 2AP·T framework. As can be seen from the UV absorption spectra of 2AP, T and the 2AP + T mixture in Fig. 4.3a, only the 2AP chromophore is excited at $\lambda_{\text{pump}} = 310$ nm. Accordingly, calculated vertical excitation energies revealed no significant red shift of the optically bright electronic transitions of the T moiety upon H-bonding with 2AP (*cf.* Fig. 4.3b and Supporting Information Table 4.1). As elaborated above, the 2AP + T mixture consists of 2AP (36%), T (34%), T·T (1%), and 2AP·T (29%) in the electronic ground state. Assuming unchanged electronic transitions of 2AP upon H-bonding with T, this would translate to $\sim 55\%$ photoexcited 2AP and $\sim 45\%$ photoexcited 2AP·T. However, the first excited $^1\pi\pi^*$ state of the 2AP moiety within the

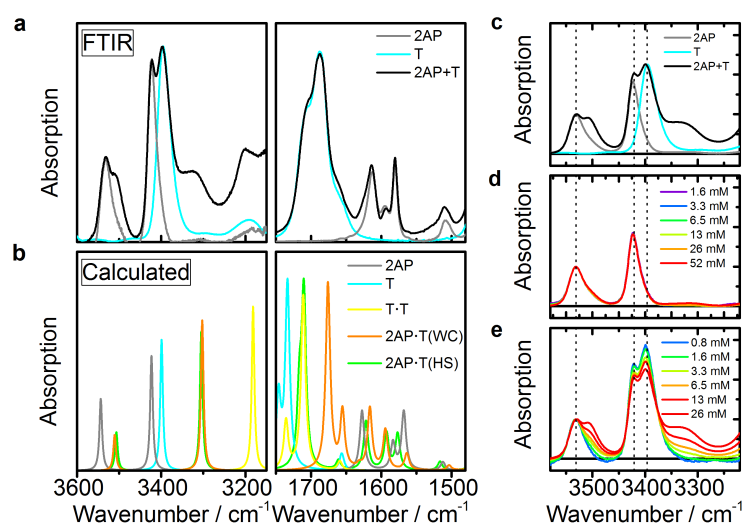


Figure 4.1: FTIR spectra of 2AP, T and the 2AP + T mixture; computed vibrational modes; and association constants. (a) FTIR spectra of 2AP (gray), T (cyan), and a mixture of 2AP and T (2AP + T, black) in CHCl_3 solution. (b) Calculated (M062X/6-311+G**) vibrational spectra of 2AP (gray), T (cyan), homodimeric T·T (yellow), and heterodimeric 2AP·T in the Watson–Crick (WC, orange) and in the Hoogsteen (HS, green) conformation. For clarity, only the most stable T·T dimer (-55.4 kJ/mol) is shown and the spectra for rWC and rHS are omitted. (c) FTIR spectra of free 2AP, free T and the 2AP + T mixture to highlight the characteristic 2AP·T dimer marker bands in the NH_2 stretching region. (d) Normalized FTIR spectra of free 2AP at different concentrations to exclude self-association. (e) FTIR spectra of equimolar mixtures of 2AP and T at different concentrations to obtain the association constant of H-bonded 2AP·T dimers.

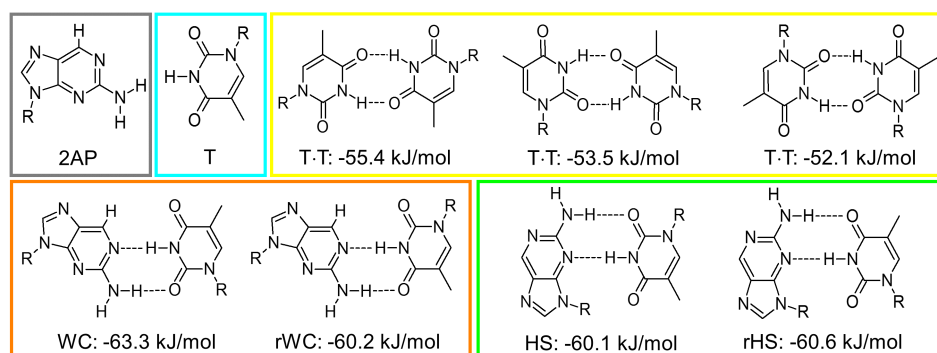


Figure 4.2: Molecular species present in the 2AP + T mixture. Monomeric, homodimeric and heterodimeric molecular species in the mixture of 2AP and T in CHCl_3 solution with calculated (0 K, isolated dimer) binding energies at the B2PLYP-D3(BJ)/def2-QZVP level of theory for the minimum energy structures obtained at the M062X/6-311+G** level of theory. The riboside residue (-R) was substituted by a methyl group in all calculations.

2AP·T framework is computed to exhibit a red shift for both WC and HS conformations at comparable oscillator strengths (*cf.* Table 4.1). Thus, excitation at 310 nm leads to $\sim 50\%$ photoexcited free 2AP and $\sim 50\%$ photoexcited base-paired 2AP·T (WC and HS). Hence, contributions by free T and dimeric $\text{T}\cdot\text{T}^{[65]}$ to the dynamics signals in the time-resolved measurements are safely negligible.

Time-Resolved Measurements

As the first test for dimer-specific electronic relaxation pathways in H-bonded 2AP·T, Fig. 4.3 shows time-resolved experimental fluorescence decay curves after 310 nm photoexcitation of solutions of free 2AP (Fig. 4.3c) and 2AP + T (Fig. 4.3d). For free 2AP, the measurement reveals minor initial Franck–Condon (FC) and solvational relaxation dynamics on a time scale of

$$\tau_{\text{solv}} = 3.0 \pm 1.0 \text{ ps}$$

followed by depopulation of the prepared optically bright $^1\pi\pi^*$ state with a time constant of

$$\tau_{2\text{AP}} = 740 \pm 15 \text{ ps.}$$

Since the 2AP + T solution consists of effectively $\sim 50\%$ photoexcited free 2AP, the time-resolved fluorescence data consequentially exhibit a sizable signature of $\tau_{2\text{AP}}$ as well. However, the observed temporal evolution of the fluorescence clearly features two additional time constants,

$$\tau_{1,2\text{AP}\cdot\text{T}} = 44 \pm 10 \text{ ps}$$

and

$$\tau_{2,2\text{AP}\cdot\text{T}} = 1.9_{-1.9}^{+6} \text{ ns,}$$

in addition to the contribution by free 2AP. Thus, despite the moderate ($\sim 50\%$) excited-state fraction of dimeric 2AP·T species in the 2AP + T mixture, the observed temporal fluorescence profiles clearly reveal new dynamics that can arise only from H-bonded 2AP·T in either the WC or HS conformations or both.

As neither transient fluorescence nor transient electronic absorption spectroscopy provides sufficient chemical structure specificity, we use transient vibrational absorption spectroscopy in combination with quantum chemical vibrational mode calculations as methods of choice for identifying the 2AP·T species and electronic states involved in the dynamics. The results are displayed in Figures 4.4 and 4.5.

We first isolate the features related to the free chromophore in the 2AP + T mixture after UV excitation. Toward these ends, we turn to our recent work on the electronic deactivation of 2AP in CHCl_3 ^[62] and a preceding study by Reichardt *et al.*^[67] In short, the relaxation pathways of free 2AP were identified from the temporal evolutions of a number of characteristic vibrational marker bands in the electronic ground and excited states. The spectral region of the NH_2 stretching vibrations proved to be especially valuable (*cf.*

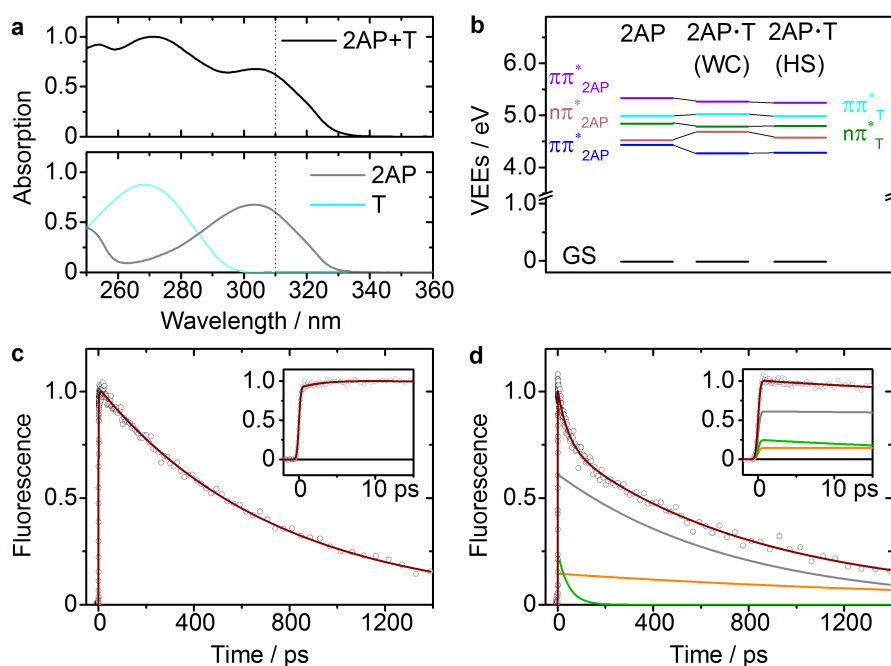


Figure 4.3: Electronic absorptions and time-resolved fluorescence of 2AP, T and 2AP·T. (a) UV absorption spectra of 2AP (gray), T (cyan) and a mixture of 2AP and T (2AP + T, black) in CHCl_3 solution. (b) Calculated vertical excitation energies (VEEs) at the RI-CC2/def2-TZVPPD level of theory for free 2AP and H-bonded Watson-Crick (WC) and Hoogsteen (HS) 2AP·T dimers at the RI-MP2/def2-TZVPPD-optimized ground-state structures. (c) Transient fluorescence-time profile of free 2AP measured at $\lambda_{\text{FL}} = 410$ nm after photoexcitation at $\lambda_{\text{pump}} = 310$ nm. Open circles are data points, the solid line is the least-squares best fit curve with $\tau = 740$ ps. (d) Transient fluorescence-time profile of the 2AP + T mixture measured at $\lambda_{\text{FL}} = 410$ nm after excitation at $\lambda_{\text{pump}} = 310$ nm. The solid black line is the least-squares best fit curve with components of $\tau_{1,2\text{AP}\cdot\text{T}} = 44$ ps (green), $\tau_{2\text{AP}} = 740$ ps (gray) and $\tau_{2,2\text{AP}\cdot\text{T}} = 1.9$ ns (orange).

Figure 4.4a. At early times after excitation, the TVA spectra feature two negative bands at 3532 and 3424 cm^{-1} associated with the bleached antisymmetric (as) and symmetric (s) NH_2 stretching modes, respectively, in the electronic ground state (GS; see Fig. 4.5). Positive transients showing up at 3479 and 3356 cm^{-1} are indicative for the $\text{NH}_2(\text{as})$ and $\text{NH}_2(\text{s})$ stretching modes, respectively, in the photoexcited $^1\pi\pi^*$ state. Concurrent with the $^1\pi\pi^*$ state depopulation and GS recovery, a transfer to the $^3\pi\pi^*$ state is witnessed by the rise of transient vibrational bands at 3500 and 3395 cm^{-1} at later times. Summarizing the conclusions for free 2AP, depopulation of the photoexcited $^1\pi\pi^*$ state is initiated by a fast population transfer to the lower-lying, short-lived, $^1n\pi^*$ state, for which an upper limit for its lifetime of $\tau \leq 100$ ps was estimated. From there, the excited molecules evolve partly to recover the GS (58% in CHCl_3) and partly *via* intersystem crossing to the $^3\pi\pi^*$ state (42%). The rate-limiting step in the mechanism that gives rise to the observed 740 ps time constant τ_{2AP} is the $^1\pi\pi^*/^1n\pi^*$ internal conversion.^[62]

TVA data were analyzed by fitting the experimental marker bands in different electronic states to a sum of Gaussian functions in a global fashion. Showcasing data analysis of TVA spectra for free 2AP in the spectral region of NH_2 stretching vibrations in Fig. 4.4a, a sum of six Gaussians, indicated by colored arrows, was used to model the experimentally observed features. In the region from 3600 to 3200 cm^{-1} , the transient spectra are described by two negative, yet recovering, Gaussians at 3532 (3544) cm^{-1} and 3424 (3423) cm^{-1} associated with initial ground-state bleaching and subsequent incomplete recovery (calculated values in parentheses). Additionally, the transient TVA spectra were described by a pair of Gaussians at 3479 (3493) cm^{-1} and 3356 (3342) cm^{-1} corresponding to the initially excited $^1\pi\pi^*$ state. Finally, the transient spectra were modeled by an additional pair of Gaussians at 3500 (3530) cm^{-1} and 3395 (3382) cm^{-1} to account for the rise of transient features toward late delay times associated with $^3\pi\pi^*$ formation. To gain insight into the temporal evolution of the fitted transient marker bands, the associated Gaussian amplitudes at various delay times can be plotted as individual time profiles. Aided by quantum chemical calculations, however, Gaussian amplitudes of related vibrational marker bands have been coupled by a time-independent factor throughout the description of the temporal evolution of the TVA spectra. Thus, the overall spectral shape of distinct spectroscopic species is described by subsets of coupled Gaussian functions. As a result, data analysis shifts from a temporal description of individual bands toward the time-resolved description of the dynamics of underlying electronic states, effectively reducing the number of time profiles and stabilizing the fitting procedure significantly in the process. Hence, Fig. 4.4a features three effective time profiles [ground-state recovery (GSR) (gray), $^1\pi\pi^*$ decay (blue), and $^3\pi\pi^*$ formation (red)] for the description of the spectral region from 3600 to 3200 cm^{-1} . Furthermore, the spectral region from 1650 to 1475 cm^{-1} has been modeled accordingly. In a final step, accounting for all time profiles in all spectral regions, the temporal evolutions of all (coupled) Gaussian amplitudes were fitted biexponentially in a global, least-squares fashion to yield the time constants $\tau_{\text{solv}} = 8.0 \pm 5.0$ ps and $\tau_{2AP} = 710 \pm 120$ ps in good agreement with our time-resolved emission measurements (3.0 ± 1.0 and 740 ± 15 ps).

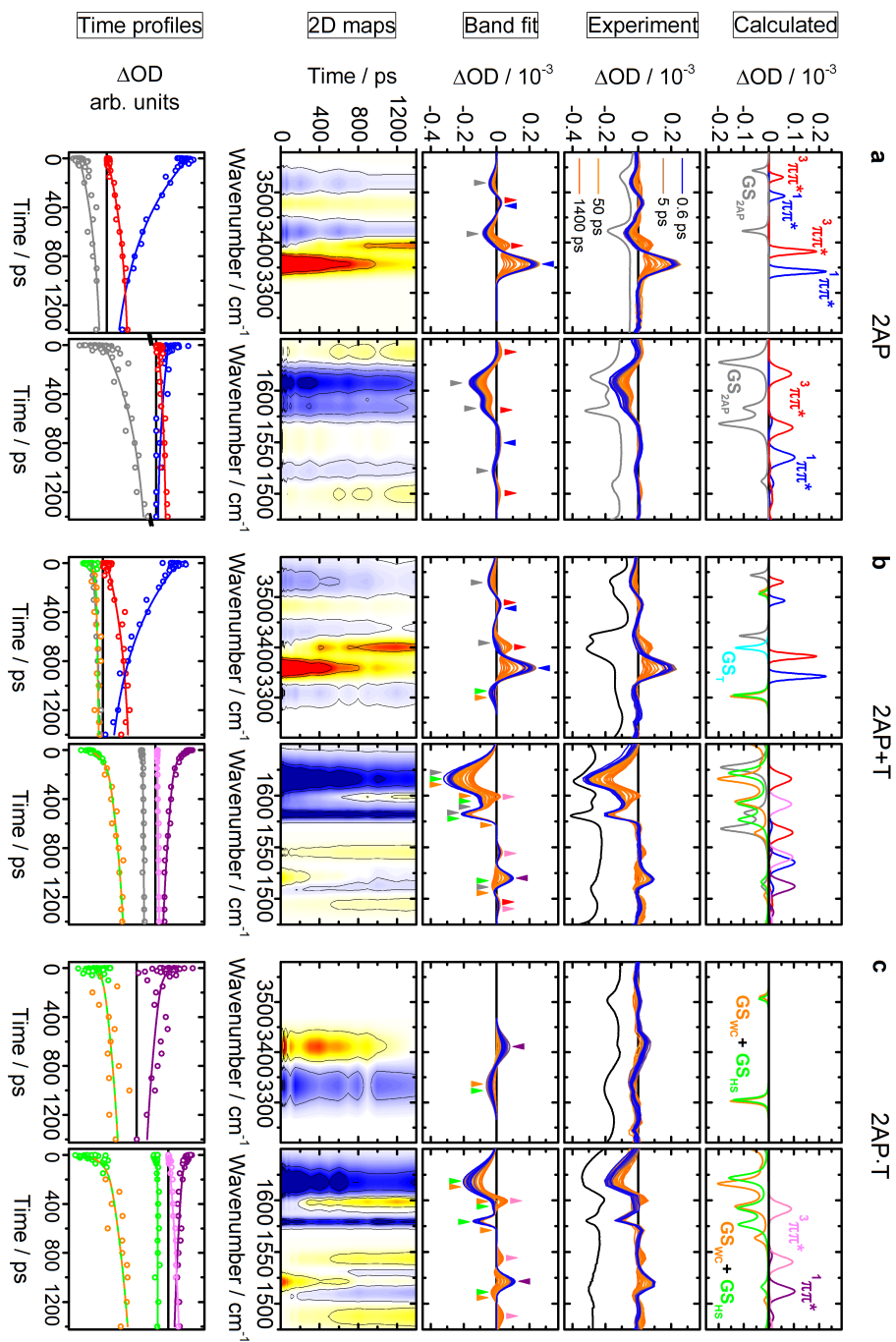


Figure 4.4: Transient vibrational absorption spectroscopic results: Comparison of the TVA spectra for free 2AP (2AP, a), a mixture of 2AP and T (2AP + T, b) and the difference of 2AP + T and 2AP to highlight pure dimer dynamics (2AP-T, c). Calculated: Computed ground-state vibrational spectra of free 2AP (gray), free T (cyan) and H-bonded 2AP-T in the Watson-Crick (WC, orange) and the Hoogsteen (HS, green) conformations as well as excited-state vibrational spectra in the $1\pi\pi^*$ (2AP: blue, 2AP-T: purple) and $3\pi\pi^*$ (2AP: red, 2AP-T: pink) states. Experimental: Time-resolved TVA spectra after 310 nm photoexcitation at selected pump-probe delay times (gray/black lines = inverted FTIR traces for reference). Band fits: Global Gaussian band fits to the experimental TVA spectra, with arrows indicating decaying and rising transient vibrational bands. 2D maps: Spectro-temporal representations of the fitted data. Negative signals are shown in blue, and red colours refer to positive TVA signals. Time profiles: Corresponding temporal evolutions of Gaussian amplitudes of the global fit results to the TVA data and the associated result of an exponential global fit to the Gaussian amplitudes with up to four time constants (see the text).

With these premises, we turn to the spectro-temporal evaluation of the 2AP + T mixture. Although many of the additional vibrational signatures in the TVA spectra after photoexcitation of the 2AP + T mixture (shown in Fig. 4.4b) are superimposed by transients of free 2AP, close inspection of the data readily reveals substantial contributions that have to be attributed to 2AP·T dimer species. Particular attention is directed at the features at 3309, 1620–1580, and 1520 cm^{-1} . Here, the bleach at 3309 cm^{-1} observed after excitation of 2AP + T is absent in the TVA spectra of free 2AP (Fig. 4.4a). Also, the complex pattern around 1620–1580 cm^{-1} in the 2AP + T spectra is of very different shape and intensity than for 2AP. Additionally, the pronounced positive peak at 1520 cm^{-1} in the TVA spectra of 2AP + T is virtually absent in the spectra of free 2AP.

To highlight the identification of specific marker bands of 2AP·T species, Fig. 4.6 shows the global fit result of a sum of Gaussian functions to the TVA spectra of the 2AP + T mixture. Similar to data evaluation of free 2AP, the transient spectra in the region from 3600 to 3200 cm^{-1} are described by pairs for bleached ground-state recovery (gray), $^1\pi\pi^*$ decay (blue), and $^3\pi\pi^*$ formation (red) as marker bands for the antisymmetric and symmetric NH_2 stretching vibrations in different electronic states of free 2AP. Notably, however, the TVA spectra feature an additional bleaching signal at 3309 cm^{-1} , in strikingly good agreement with our calculated bound NH_2 stretching vibration of 2AP·T species

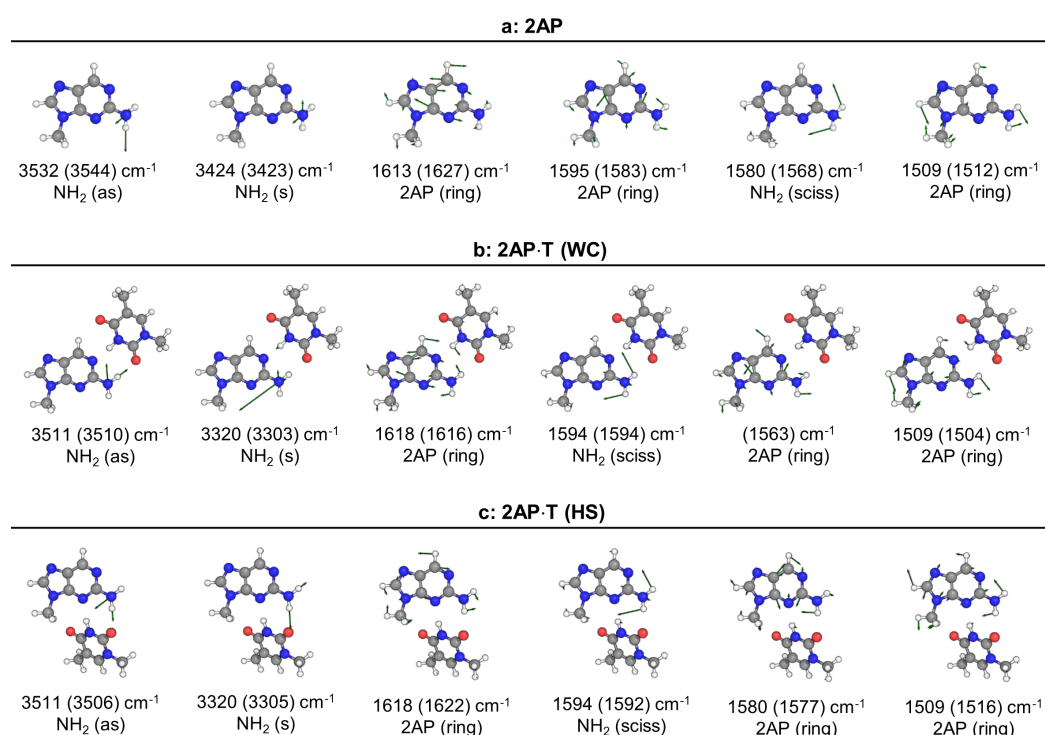


Figure 4.5: Computed vibrational ground-state modes of free 2AP and the 2AP·T dimers in the Watson–Crick and Hoogsteen conformations. Calculated ground-state vibrational marker bands of free 2AP (a) and the 2AP·T dimer in the Watson–Crick (WC, b) and Hoogsteen (HS, c) conformations. The experimental vibrational wavenumbers are from FTIR spectra and ground-state bleaching signals in the TVA spectra; the calculated wavenumbers are given in parentheses. The riboside residue in both chromophores was substituted by a methyl group in all calculations.

both in the WC (3303 cm^{-1} , orange) and HS (3305 cm^{-1} , green) conformation. Due to the strong overlap of these marker bands, the bleaching signal in the TVA data was modeled with a single Gaussian function. However, as further illustrated in Fig. 4.6, the temporal evolution of this band proceeds in a biexponential manner within $\tau_{1,2AP\cdot T} \approx 70\text{ ps}$ and $\tau_{2,2AP\cdot T} \approx 1.6\text{ ns}$. The same time constants, exclusive to $2AP\cdot T$ species within the $2AP + T$ mixture, have also been identified in the region of ring vibrations from 1650 to 1475 cm^{-1} . Due to strongly overlapping vibrational marker bands (*cf.* calculated vibrational spectra in Figs. 4.1, 4.4, and 4.5) in this spectral region, however, the transient spectra were modeled by a sum of eight Gaussian functions: four bleached signals at 1618 , 1594 , 1580 , and 1509 cm^{-1} ; one Gaussian for $^1\pi\pi^*$ decay at 1519 cm^{-1} ; and three Gaussians for $^3\pi\pi^*$ formation at 1600 , 1545 , and 1495 cm^{-1} . Evaluation of the temporal evolution of these bands (*cf.* Figs. 4.4 and 4.6) revealed kinetic contributions from both free $2AP$ and $2AP\cdot T$ dimers. For instance, bleach-recovery of the TVA bands at 1618 ($1627/1616/1622\text{ cm}^{-1}$), 1594 ($1583/1594/1592\text{ cm}^{-1}$) and 1509 ($1512/1504/1516\text{ cm}^{-1}$) proceeds in a triexponential fashion within τ_{2AP} , $\tau_{1,2AP\cdot T}$, and $\tau_{2,2AP\cdot T}$ (calculated vibrations of free $2AP/WC/HS$ in parentheses, *cf.* Fig. 4.5). However, the bleached band at 1580 cm^{-1} is described by only biexponential recovery within τ_{2AP} and $\tau_{1,2AP\cdot T}$. Furthermore, in line with our time-resolved emission measurements, the marker band for the $2AP\cdot T$ excited $^1\pi\pi^*$ state (purple) at 1519 cm^{-1} decays biexponentially within $\tau_{1,2AP\cdot T}$ and $\tau_{2,2AP\cdot T}$. Triplet formation (pink) at 1600 , 1545 , and 1495 cm^{-1} proceeds monoexponentially within $\tau_{2,2AP\cdot T}$, and is overlapped with contributions for $^3\pi\pi^*$ formation of free $2AP$ (red) only at 1495 cm^{-1} in agreement with our TVA measurements of free $2AP$ alone.

To extract even minor contributions of $2AP\cdot T$ dynamics superimposed by transient signals of free $2AP$, the TVA spectra of free $2AP$ (Fig. 4.4a) were subtracted from the spectra recorded for the $2AP + T$ mixture (Fig. 4.4b). The isolated transient marker bands of $2AP\cdot T$

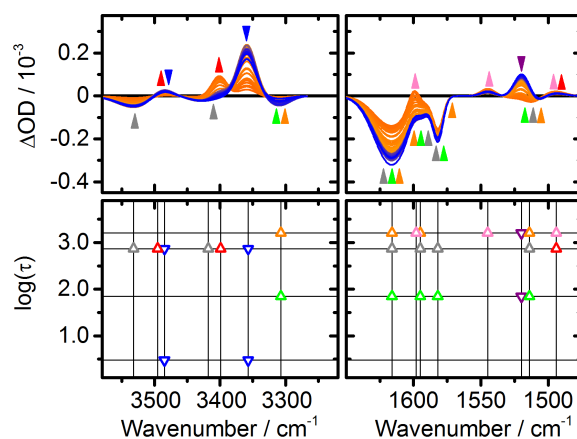


Figure 4.6: Two-dimensional spectro-temporal plot of TVA data. Vibrational marker bands for the $2AP + T$ mixture (*cf.* Fig. 4.4b) are represented according to their associated wavenumbers and time constants. Free $2AP$: Gray triangles represent ground-state recovery (GSR), $^1\pi\pi^*$ dynamics is shown in blue, and red triangles indicate $^3\pi\pi^*$ formation. Dimeric $2AP\cdot T$: GSR is color-coded as orange (Watson–Crick, WC) and green (Hoogsteen). Purple triangles refer to $^1\pi\pi^*$ dynamics of dimeric $2AP\cdot T$, and pink triangles assign $^3\pi\pi^*$ formation of the WC pair.

dimers are displayed in Fig. 4.4c. As elaborated above, the excited-state population of 2AP within the 2AP + T mixture is estimated to be $\sim 50\%$. As data acquisition was accomplished using doubled excitation energies for the 2AP + T mixture with respect to the monomer measurements (*cf.* Methods), no further scaling in the generation of 2AP·T spectra was applied. The resulting “pure” transient vibrational 2AP·T spectra were subsequently modeled by a sum of two Gaussian functions in the NH_2 stretching region and a sum of eight Gaussians in the region of ring vibrations. Ground-state recovery of overlapping 2AP·T (WC/HS, orange/green) bleach signals at 3320 ($3303/3305$) cm^{-1} , 1618 ($1616/1622$) cm^{-1} , 1594 ($1594/1592$) cm^{-1} and 1509 ($1504/1516$) cm^{-1} unwinds biexponentially within $\tau_{1,2\text{AP}\cdot\text{T}}$ and $\tau_{2,2\text{AP}\cdot\text{T}}$. Notably, recovery of the bleached band at 1580 (1577) cm^{-1} is determined exclusively by the fast constant $\tau_{1,2\text{AP}\cdot\text{T}}$. Furthermore, excited $^1\pi\pi^*$ state (purple) vibrations at 3411 and 1519 cm^{-1} decay in a biexponential manner within $\tau_{1,2\text{AP}\cdot\text{T}}$ and $\tau_{2,2\text{AP}\cdot\text{T}}$. Finally, $\tau_{2,2\text{AP}\cdot\text{T}}$ is found as the monoexponential rising component in the marker bands of the $^3\pi\pi^*$ state (pink) at 1599 , 1544 , and 1487 cm^{-1} .

Taking all spectral regions and time-resolved measurements into account, the encoded temporal information in our TVA data was extracted by a global least-squares fitting analysis of all time profiles (2AP, 2AP + T, and 2AP·T) given in Fig. 4.4 in the bottom row using up to four exponentials to yield the time constants

$$\begin{aligned}\tau_{\text{solv}} &= 3 \text{ ps (fixed)} \\ \tau_{2\text{AP}} &= 740 \text{ ps (fixed)} \\ \tau_{1,2\text{AP}\cdot\text{T}} &= 68 \pm 15 \text{ ps} \\ \tau_{2,2\text{AP}\cdot\text{T}} &= 1.6 \pm 0.4 \text{ ns}\end{aligned}$$

in satisfactory agreement with the time constants from the time-resolved fluorescence measurements above. The values for τ_{solv} and $\tau_{2\text{AP}}$ were fixed in this analysis at the above results for free 2AP, whereas $\tau_{1,2\text{AP}\cdot\text{T}}$ and $\tau_{2,2\text{AP}\cdot\text{T}}$ were taken as free-floating parameters. As opposed to the model-free analysis of our time-resolved fluorescence data, even the longest time constant $\tau_{2,2\text{AP}\cdot\text{T}}$ comes out to be rather well determined by the coupling of related transient vibrational marker bands on the grounds of quantum chemical calculations, significantly stabilizing the fitting routine. Description of all time profiles in a global fit analysis further supports the reliability of time constants when compared to single individual time trace analyses. In the following, the distinct values of $\tau_{1,2\text{AP}\cdot\text{T}} \sim 70$ ps and $\tau_{2,2\text{AP}\cdot\text{T}} \sim 1.6$ ns will be attributed to the HS and WC conformations of 2AP·T, respectively.

4.4 Discussion

The combined kinetic results from our time-resolved measurements are corroborated by the computed normal mode vibrations (*cf.* Fig. 4.5) that enable us to assign all observed vibrational bands and to interpret the entire spectro-temporal evolution encoded in our TVA spectra. In contrast to the antisymmetric and symmetric NH₂ modes of free 2AP, which are observed as distinct features in the electronic ground state at 3532 (3544) cm⁻¹ and 3424 (3423) cm⁻¹ (calculated values in parentheses), respectively, the corresponding vibrational modes associated with the 2AP·T dimers, observed at 3511 and 3320 cm⁻¹, are subject to spectral broadening caused by H-bonding and overlapping bands of both the WC (calculated at 3510 and 3303 cm⁻¹) and HS (3506 and 3305 cm⁻¹) conformations. Although the bleach signals of the free (f) NH₂ stretching modes of 2AP·T (WC and HS) at 3511 cm⁻¹ are too weak to be detected in the transient spectra, the corresponding vibrations in the ¹ππ* excited state show up as positive absorptions at 3411 cm⁻¹ directly after excitation and decay in a biexponential manner with τ_{1,2AP·T} and τ_{2,2AP·T}. Accordingly, this band is assumed to be a superposition of the WC and HS conformations. It follows the trend for a red shift of the absorption in the ¹ππ* state relative to the GS as also found for free 2AP. Likewise, the bleached 2AP·T band at 3320 cm⁻¹ arises from the superimposed bound (b) NH₂ stretching vibrations of 2AP·T in the WC (3303 cm⁻¹) and HS (3305 cm⁻¹) conformations. Recovery to the GS of this superimposed band proceeds biexponentially with τ_{1,2AP·T} and τ_{2,2AP·T}. The associated ¹ππ* excited-state vibration is expected to be red-shifted in absorption and to have moved out of the detection window in Fig. 4.4. Another characteristic absorption associated with the ¹ππ* state is present at 1519 cm⁻¹ in the region of the ring vibrations directly after excitation, which also decays in a biexponential manner with τ_{1,2AP·T} and τ_{2,2AP·T}. The biexponential decay of the ¹ππ* state with τ_{1,2AP·T} and τ_{2,2AP·T} is in good agreement with the results of the time-resolved fluorescence experiments; thus the fast picosecond time constant components obtained in the fluorescence (44 ± 10 ps) and vibrational absorption (68 ± 15 ps) experiments are considered to arise from the same species within the error limits. Furthermore, the overlapping 2AP·T(WC/HS) bleach signals at 1618 (1616/1622) cm⁻¹, 1594 (1594/1592) cm⁻¹ and 1509 (1504/1516) cm⁻¹ recover biexponentially with τ_{1,2AP·T} and τ_{2,2AP·T} as well. Most importantly, however, the recovery of the characteristic bleached band at 1580 (1577) cm⁻¹ is determined by the fast τ_{1,2AP·T} = 68 ps time constant only. Based on the specifics of the electronic relaxation pathways (see below), we attribute this band to H-bonded 2AP·T in the HS conformation. In fact, the association with a specific 2AP·T conformation of this rather well-separated vibrational marker band at 1580 (1577) cm⁻¹ along with its domination by τ_{1,2AP·T} led us to attribute the fast time constant τ_{1,2AP·T} to the electronic deactivation of the ¹ππ* state of the HS conformation of 2AP·T and, *vice versa*, the slow time constant τ_{2,2AP·T} to the deactivation of the ¹ππ* state of 2AP·T in the WC conformation.

Combining the information from our time-resolved fluorescence and vibrational absorption measurements, we propose the overall scheme for the electronic relaxation dynamics of 2AP·T in the WC and HS conformations sketched in Fig. 4.7: after UV excitation of the 2AP moiety in the 2AP·T(WC) base pair, the molecule rapidly relaxes from the initial FC geometry to the $^1\pi\pi^*$ potential-energy minimum. According to our excited-state calculations, the structure of the 2AP moiety in the WC dimer resembles the $^1\pi\pi^*$ minimum energy structure of free 2AP to a high extent. The rather flat structure of the WC dimer is slightly broken by the six-membered ring puckering at the C⁶ position of the 2AP chromophore similar to free 2AP.^[62] Thus, H-bonding of the 2AP moiety with T in the WC conformation exerts only a small effect on the structure of the 2AP chromophore in the $^1\pi\pi^*$ excited state. The energies of the different electronic states, on the other hand, and their crossings are more strongly affected. As has recently been shown,^[14] the $^1\pi\pi^*$ lifetime of 2AP is significantly increased upon H-bonding due to an increased energy of the $^1n\pi^*$ state and the associated $^1\pi\pi^*/^1n\pi^*$ conical intersection. Congruently, we observe the increased fluorescence lifetime of the 2AP moiety by H-bonding with T in the WC motif to $\tau_{2AP\cdot T(WC)} = 1.6$ ns, substantially longer than the lifetime of free 2AP ($\tau_{2AP} = 740$ ps). Due to the structural similarity, however, the ensuing dynamics of 2AP·T(WC) is expected to follow similar pathways as in free 2AP. Hence, we expect a transient population of a short-lived $^1n\pi^*$ state that acts as an intermediate state for both efficient GS recovery and $^3\pi\pi^*$ formation. In line with these considerations, we observe the 1.6 ns time constant in the ground-state recovery time profiles of the bleaching signals at 3320, 1618, 1594, and 1509 cm⁻¹ and as the rising component in the marker bands of the $^3\pi\pi^*$ state at 1599, 1544, and 1487 cm⁻¹. The experimentally observed vibrational bands associated with 2AP·T(WC) in the $^3\pi\pi^*$ state coincide strikingly well with the frequency-shifted calculated spectrum for the triplet vibrations of free 2AP in the region of the ring vibrations, again highlighting the similarity between free 2AP and the 2AP moiety in the 2AP·T(WC) base pair.

In contrast to that of 2AP·T(WC), the structure of the 2AP moiety in the HS network in the excited $^1\pi\pi^*$ state gets more strongly distorted by H-bonding with T. According to our excited-state calculations as shown in Fig. 4.7, partial planarity of the 2AP moiety in the 2AP·T(HS) conformation is maintained due to the effect of interbase H-bonding. At the same time, however, the steric influence of the bulky residue at the 9-position in 2AP pushes the chromophore away from planarity. As a result, the 2AP moiety in the HS 2AP·T conformation appears to be bent along the C⁶/N³ axis in the $^1\pi\pi^*$ state. According to our time-resolved experiments, this distorted species finds an efficient route for electronic de-excitation to the GS in ~ 68 ps ($\tau_{2AP\cdot T(HS)}$). Interestingly, this time constant contributes to the decay of the bright $^1\pi\pi^*$ and to the recovery of the GS vibrations of 2AP·T(HS), but not as a rising component in triplet formation. Hence, we attribute $\tau_{2AP\cdot T(HS)}$ to direct repopulation of the electronic ground state from the initially excited $^1\pi\pi^*$ state.

Exploring Deactivation Pathways of 2AP·T in the Hoogsteen Conformation

Since our chemical structure and electronic state-sensitive time-resolved results enabled us to distinguish between the distinct deactivation dynamics of 2AP·T in the WC and HS forms, the focus moves to the reason for the much faster electronic deactivation in the HS configuration. Here, the possibility of excited-state proton transfer has lately gained much attention as an efficient way for electronic deactivation in H-bonded nucleobases. For example, excited-state proton transfer accounts for highly efficient electronic deactivation in the G·C Watson–Crick base pair,^[35,68] whereas no comparable evidence for such a process was found for the A·T pair in the Watson–Crick conformation.^[69] To explore the possibility of excited-state proton transfer in the 2AP·T base pair forms, Fig. 4.8 maps the energies of various electronic states along an extended N–H distance in the 2AP moiety of 2AP·T. Starting from the ground-state minimum structure, Fig. 4.8 maps the electronic energy of the GS (RI-MP2/def2-SVP) at extended, frozen N–H distances. For all calculations, only the N–H bond distance of 2AP was frozen at discrete values, whereas all other degrees of freedom were allowed to relax unrestrictedly. As illustrated by insets in Fig. 4.8, elongation of the N–H distance results in single-proton transfer from 2AP to T and spontaneous transfer of the central intermolecularly bonded proton from T to 2AP (double-proton transfer, DPT) both in the electronic GS and excited $^1\pi\pi^*$ state of 2AP·T in both the WC and HS conformations. In the electronic ground state (black solid circles), however, this process is associated with a sizable energy barrier. Also, as the DPT species is rendered unstable, DPT is not expected in the GS on the grounds of our calculations. For every optimized ground-state structure, the energies of higher excited states upon

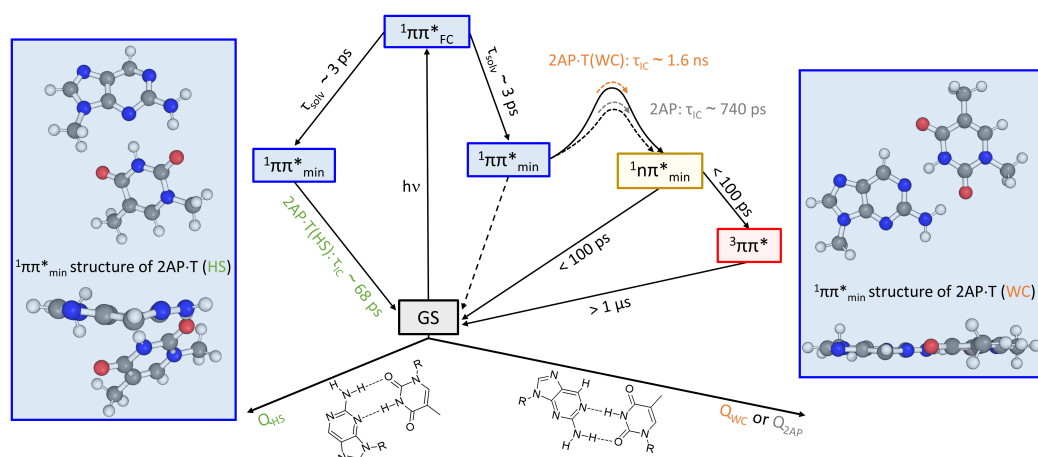


Figure 4.7: Schematic depiction of the proposed electronic deactivation pathways after UV excitation for free 2AP, 2AP·T in the Watson–Crick (WC), and 2AP·T in the Hoogsteen (HS) conformations. The excited-state $S_1(^1\pi\pi^*)$ minimum structures of 2AP·T in the WC (right) and HS (left) conformations were calculated at the RI-CC2/def2-SVP level of theory.

vertical excitation are plotted in colored open circles. Neither crossing of excited states nor the occurrence of charge-transfer states could be observed along the N–H bond distance coordinate for 2AP·T in the WC and HS forms.

Analogous restricted excited-state geometry optimizations in the first excited $^1\pi\pi^*$ state at extended N–H distances have been performed at the RI-ADC(2)/def2-SVP level of theory as shown as solid blue squares in Fig. 4.8. Accordingly, spawning from the Franck–Condon region on the excited $^1\pi\pi^*$ potential surface, excited-state PT is associated with a moderate energy barrier. As opposed to the GS, however, the DP-transferred species is expected to be stable in the excited $^1\pi\pi^*$ state according to our calculations. Hence, excited-state DPT is possible for 2AP·T in both the WC and HS motifs. Yet, the rather flat potential-energy surface would probably impede the occurrence of distinct vibrational marker bands in our TVA spectra. Most importantly, however, Fig. 4.8 additionally maps the potential energy of the GS (open squares) corresponding to relaxed excited-state structures. Accordingly, the potential energy of the GS is dramatically affected by excited-state DPT in the HS form.

Hence, in line with recent findings on the grounds of quantum chemical calculations,^[70] excited-state proton transfer is not expected as an efficient way for electronic deactivation within the WC conformation of 2AP·T. Surprisingly, however, our calculations predict a conical intersection as an efficient electronic de-excitation pathway in the HS conformation that connects the $^1\pi\pi^*$ state with the electronic GS at a double-proton-transferred species after overcoming a small potential-energy barrier induced by single-proton transfer. Following the scenario sketched in Fig. 4.8, the excited-state HS population is expected to evolve to the GS, once the excited-state barrier is overcome, whereas the WC form features no such deactivation pathways. Back in the GS, the original HS conformation likely recovers, as the proton-transferred species is unstable in the GS. At this point, we emphasize that efficient electronic deactivation along a double-proton-transfer coordinate followed by recovery of the original HS species in the GS is consistent with our time-resolved measurements. Still, highly efficient electronic deactivation to the GS within $\tau_{\text{HS}} \sim 68$ ps may be possible, in principle, along other coordinates. In fact, given the highly bent structure of the HS form in the excited $^1\pi\pi^*$ state, chemical intuition suggests a conical intersection along a ring-puckered mode in close vicinity to the excited-state minimum structure. Thus, more elaborate quantum chemical calculations are desirable to elucidate the pathways for electronic deactivation in the 2AP·T(HS) dimer.

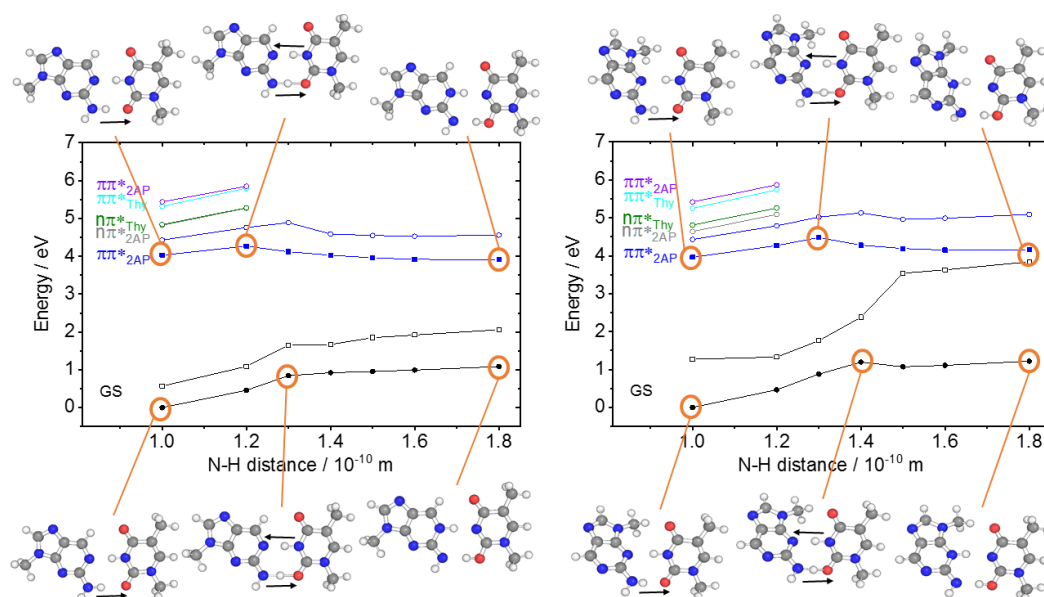


Figure 4.8: Potential-energy curves along the H-atom transfer coordinate for 2AP·T in the Watson–Crick (WC, left) and Hoogsteen (HS, right) conformations. Open circles represent vertical RI-ADC(2)/def2-SVP energies relative to restricted RI-MP2/def2-SVP ground-state optimizations (solid black circles). Squares indicate the respective energies relative to restricted S_1 excited-state RI-ADC(2)/def2-SVP optimizations. Virtually the same results were found for rWC and rHS conformations.

4.5 Conclusions

We have investigated distinct electronic relaxation pathways in H-bonded 2AP·T dimers in the Watson–Crick (WC) and Hoogsteen (HS) conformations after UV photoexcitation, by time-resolved fluorescence and transient vibrational absorption spectroscopy methods aided by quantum chemical calculations. When compared to free 2AP, H-bonding with T exerts little effect on the structure of the 2AP chromophore in the WC form. Hence, similar to that of free 2AP, electronic deactivation of the initially excited $^1\pi\pi^*$ state proceeds to a short-lived intermediate state of $^1n\pi^*$ character, followed partially by recovery of the electronic ground state and partially by crossing to the $^3\pi\pi^*$ state. However, the energetic barrier for the internal conversion to the $^1n\pi^*$ state is raised by the H-bonding in 2AP·T(WC). Thus, the $^1\pi\pi^*$ lifetime is increased from $\tau_{2AP} = 740$ ps to $\tau_{2AP\cdot T(WC)} \sim 1.6$ ns. In contrast, the structure of the 2AP moiety in the HS base pair is distorted in the $^1\pi\pi^*$ excited state. The distorted structure opens up new pathways for electronic deactivation. In particular, direct recovery is observed from the initially excited $^1\pi\pi^*$ state to the electronic ground state in $\tau_{2AP\cdot T(HS)} \sim 68$ ps. Although other electronic de-excitation coordinates cannot be ruled out, the observed dynamics is in accordance with a calculated double-proton-transfer process in the photoexcited $^1\pi\pi^*$ state of the 2AP·T(HS) base pair. As most of the vibrational marker bands for 2AP·T in the Watson–Crick and Hoogsteen conformations overlap and the relative ratio of both conformations can only be estimated to be roughly the same, statements about quantum yields remain tentative. Still, as the

fast time constant $\tau_{\text{HS}} \sim 68$ ps is not found as a rising component in the marker bands associated with the $^3\pi\pi^*$ state, we conclude that the significant contribution to triplet formation stems from 2AP·T in the Watson–Crick conformation with a quantum yield similar to that in free 2AP (*i.e.*, $\sim 42\%$).

Commonly, 2AP is used as an intrinsic fluorescent probe to report on conformational motifs in duplex DNA. Typically, 2AP-containing DNA duplexes feature fluorescence decay times of $\tau_1 < 100$ ps, $\tau_2 \sim 0.5$ ns, $\tau_3 \sim 2$ ns and $\tau_4 \sim 10$ ns. Quenching of excited-state lifetimes is widely attributed to charge-transfer and intrastrand stacking interactions. However, we note that τ_1 and τ_3 coincide strikingly well with our $\tau_{2\text{AP}\cdot\text{T}(\text{HS})}$ and $\tau_{2\text{AP}\cdot\text{T}(\text{WC})}$ values, respectively, obtained from the study of the dynamics of purely H-bonded 2AP·T dimers. As recent research highlights the abundance of transient HS motifs in duplex DNA, our results suggest extending the established picture for dynamic fluorescence quenching of 2AP by also incorporating dynamic interstrand H-bonding effects.

Acknowledgments

The laser system and research at the University of Bristol were supported by ERC Advanced Grant CAPRI 290966. The group at the University of Kiel has been supported by the Deutsche Forschungsgemeinschaft through the Collaborative Research Centre 677 “Function by Switching”. K.R. received support by the DFG grant RO 4952/1-1. H.J.B.M. and R.A.I. were supported by EPSRC Doctoral Training Grant awards.

References

- [1] D. C. Ward, E. Reich and L. Stryer, *J. Biol. Chem.*, 1969, **244**, 1228–1237.
- [2] C. R. Guest, R. A. Hochstrasser, L. C. Sowers and D. P. Millar, *Biochemistry*, 1991, **30**, 3271–3279.
- [3] M. Kawai, M. J. Lee, K. O. Evans and T. M. Nordlund, *J. Fluoresc.*, 2001, **11**, 23–32.
- [4] L. C. Sowers, G. V. Fazakerley, R. Eritjat, B. E. Kaplant, M. F. Goodman and S. W. Benson, *Proc. Natl. Acad. Sci. U.S.A.*, 1986, **83**, 5434–5438.
- [5] T. M. Nordlund, S. Andersson, L. Nilsson, R. Rigler, A. Gråslund and L. W. Mclaughlin, *Biochemistry*, 1989, **28**, 9095–9103.
- [6] N. P. Johnson, W. A. Baase and P. H. von Hippel, *Proc. Natl. Acad. Sci. U.S.A.*, 2004, **101**, 3426–3431.
- [7] A. Dallmann, L. Dehmel, T. Peters, C. Mügge, C. Griesinger, J. Tuma and N. Ernsting, *Angew. Chem., Int. Ed.*, 2010, **49**, 5989–5992.
- [8] E. Rachofsky, R. Osman and J. Ross, *Biochemistry*, 2001, **40**, 946–956.
- [9] S. K. Pal, L. Zhao, T. Xia, and A. H. Zewail, *Proc. Natl. Acad. Sci. U.S.A.* 2003, **100**, 13746–13751.
- [10] R.K. Neely, S. W. Megennis, D. T. S. Dryden and A. C. Jones, *J. Phys. Chem. B*, 2004, **108**, 17606–17610.
- [11] O. J. G. Somsen, A. van Hoek and H. van Amerongen, *Chem. Phys. Lett.* 2005, **402**, 61–65.
- [12] T. Gelot, P. Tourón-Touceda, O. Crégut, J. Léonard and S. Haacke, *J. Phys. Chem. A*, 2012, **116**, 2819–2825.
- [13] A. C. Jones and R. K. Neely, *Q. Rev. Biophys.* 2015, **48**, 244–279.
- [14] S. Lobsiger, S. Blaser, R. K. Sinha, H.-M. Frey and S. Leutwyler, *Nat. Chem.*, 2014, **6**, 989–993.

- [15] M. Barbatti and H. Lischka, *Phys. Chem. Chem. Phys.* 2015, **17**, 15452–15459.
- [16] R. K. Neely and A. C. Jones, *J. Am. Chem. Soc.* 2006, **128**, 15952–15953.
- [17] N. N. Degtyareva, M. J. Reddish, B. Sengupta, and J. T. Petty, *Biochemistry*, 2009, **48**, 2340–2346.
- [18] J. M. Jean and K. B. Hall, *Proc. Natl. Acad. Sci.*, 2001, **98**, 37–41.
- [19] J. M. Jean and B. P. Krueger, *J. Phys. Chem. B* 2006, **110**, 2899–2909.
- [20] E. Y. M. Bonnist, and A. C. Jones, *ChemPhysChem* 2008, **9**, 1121–1129.
- [21] C. Hariharan, L. B. Bloom, S. A. Helquist, E. T. Kool, and L. J. Reha-Kranz, *Biochemistry*, 2006, **45**, 2836–2844.
- [22] S. Kelley and J. Barton, *Science*, 1999, **283**, 375–380.
- [23] J. Genereux, S. Wuerth and J. Barton, *J. Am. Chem. Soc.*, 2011, **133**, 3863–3868.
- [24] J. Genereux and J. Barton, *Chem. Rev.*, 2010, **10**, 1642–1662.
- [25] C. E. Crespo-Hernández, B. Cohen, P. M. Hare and B. Kohler, *Chem. Rev.*, 2004, **104**, 1977–2019.
- [26] N. K. Schwalb and F. Temps, *Science*, 2008, **322**, 243–245.
- [27] C. T. Middleton, K. de La Harpe, C. Su, Y. K. Law, C. E. Crespo-Hernández and B. Kohler, *Annu. Rev. Phys. Chem.*, 2009, **60**, 217–239.
- [28] V. A. Spata, W. Lee and S. Matsika, *J. Phys. Chem. Lett.*, 2016, **7**, 976–984.
- [29] W. J. Schreier, P. Gilch and W. Zinth, *Annu. Rev. Phys. Chem.*, 2015, **66**, 497–519.
- [30] P. Marquetand, J. Nogueira, S. Mai, F. Plasser and L. González, *Molecules*, 2017, **221**, 49.
- [31] E. N. Nikolova, E. Kim, A. A. Wise, P. J. O'Brien, I. Andricioaei, and H. M. Al-Hashimi, *Nature*, 2011, **470**, 498–502.
- [32] D. Chakraborty and D. J. Wales, *J. Phys. Chem. Lett.*, 2018, **9**, 229–241.

- [33] K. Siriwong, A. Voityuk, M. Newton and N. Rösch, *J. Phys. Chem. B*, 2003, **107**, 2595–2601.
- [34] G. M. Roberts, H. J. B. Marroux, M. P. Grubb, M. N. R. Ashfold and A. J. Orr-Ewing, *J. Phys. Chem. A*, 2014, **118**, 11211–11225.
- [35] N. K. Schwalb and F. Temps, *J. Am. Chem. Soc.*, 2007, **129**, 9272–9273.
- [36] Y. Zhao and D. G. Truhlar, *Theor. Chem. Acc.*, 2008, **120**, 215–241.
- [37] A. D. McLean and G. S. Chandler, *J. Chem. Phys.*, 1980, **72**, 5639–5648.
- [38] R. Krishnan, J. S. Binkley, R. Seeger and J. A. Pople, *J. Chem. Phys.*, 1980, **72**, 650–654.
- [39] M. J. Frisch, J. A. Pople, and J. S. Binkley, *J. Chem. Phys.*, 1984, **80**, 3265–3269.
- [40] T. Clark, J. Chandrasekhar, G. W. Spitznagel and P. von Ragué Schleyer, *J. Comput. Chem.*, 1983, **4**, 294–300.
- [41] M. J. Frisch, G. W. Trucks, H. B. Schlegel, G. E. Scuseria, M. A. Robb, J. R. Cheeseman, G. Scalmani, V. Barone, B. Mennucci, G. A. Petersson, H. Nakatsuji, M. Caricato, X. Li, H. P. Hratchian, A. F. Izmaylov, J. Bloino, G. Zheng, J. L. Sonnenberg, M. Hada, M. Ehara, K. Toyota, R. Fukuda, J. Hasegawa, M. Ishida, T. Nakajima, Y. Honda, O. Kitao, H. Nakai, T. Vreven, J. A. Montgomery Jr., J. E. Peralta, F. Ogliaro, M. Bearpark, J. J. Heyd, E. Brothers, K. N. Kudin, V. N. Staroverov, T. Keith, R. Kobayashi, J. Normand, K. Raghavachari, A. Rendell, J. C. Burant, S. S. Iyengar, J. Tomasi, M. Cossi, N. Rega, J. M. Millam, M. Klene, J. E. Knox, J. B. Cross, V. Bakken, C. Adamo, J. Jaramillo, R. Gomperts, R. E. Stratmann, O. Yazyev, A. J. Austin, R. Cammi, C. Pomelli, J. W. Ochterski, R. L. Martin, K. Morokuma, V. G. Zakrzewski, G. A. Voth, P. Salvador, J. J. Dannenberg, S. Dapprich, A. D. Daniels, O. Farkas, J. B. Foresman, J. V. Ortiz, J. Cioslowski and D. J. Fox, *Gaussian 09, Revision D.01*, Gaussian Inc., Wallingford CT, 2013.
- [42] M. L. Laury, S. E. Boesch, I. Haken, P. Sinha, R. A. Wheeler and A. K. Wilson, *J. Comput. Chem.*, 2011, **32**, 2339–2347.
- [43] M. L. Laury, M. J. Carlson and A. K. Wilson, *J. Comput. Chem.*, 2012, **33**, 2380–2387.
- [44] S. Grimme, *J. Chem. Phys.*, 2006, **124**, 034108.
- [45] F. Weigend, F. Furche and R. Ahlrichs, *J. Chem. Phys.*, 2003, **119**, 12753.

- [46] TURBOMOLE V7.0 2015, a Development of University of Karlsruhe and Forschungszentrum Karlsruhe GmbH, 1989–2015, TURBOMOLE GmbH, since 2007; Available from <http://www.turbomole.com>.
- [47] T. Schwabe and S. Grimme, *Phys. Chem. Chem. Phys.*, 2007, **9**, 3397–3406.
- [48] L. Goerigk, H. Kruse and S. Grimme, *ChemPhysChem*, 2011, **12**, 3421–3433.
- [49] M. Häser and R. Ahlrichs, *J. Comput. Chem.*, 1989, **10**, 104–111.
- [50] F. Weigend and M. Häser, *Theor. Chem. Acc.*, 1997, **97**, 331–340.
- [51] F. Weigend, M. Häser, H. Patzelt and R. Ahlrichs, *Chem. Phys. Lett.*, 1998, **294**, 143–152.
- [52] C. Hättig, A. Hellweg and A. Köhn, *Phys. Chem. Chem. Phys.*, 2006, **8**, 1159–1169.
- [53] A. Schäfer, H. Horn and R. Ahlrichs, *J. Chem. Phys.*, 1992, **97**, 2571.
- [54] F. Weigend and R. Ahlrichs, *Phys. Chem. Chem. Phys.*, 2005, **7**, 3297–3305.
- [55] D. Rappoport and F. Furche, *J. Chem. Phys.*, 2010, **133**, 134105.
- [56] A. Hellweg, S. A. Grün and C. Hättig, *Phys. Chem. Chem. Phys.*, 2008, **10**, 4119–4127.
- [57] R. Ahlrichs, *Phys. Chem. Chem. Phys.*, 2004, **6**, 5119–5121.
- [58] C. Hättig and A. Köhn, *J. Chem. Phys.*, 2002, **117**, 6939–6951.
- [59] A. Köhn and C. Hättig, *J. Chem. Phys.*, 2003, **119**, 5021–5036.
- [60] C. Hättig and F. Weigend, *J. Chem. Phys.*, 2000, **113**, 5154–5161.
- [61] O. Christiansen, H. Koch and P. Jørgensen, *Chem. Phys. Lett.*, 1995, **243**, 409–418.
- [62] H. Böhnke, K. Röttger, R. A. Ingle, H. J. B. Marroux, M. Bohnsack, A. J. Orr-Ewing and F. Temps, *Phys. Chem. Chem. Phys.*, 2018, **20**, 20033–20042.
- [63] D. H. Friese, L. Törk and C. Hättig, *J. Chem. Phys.*, 2014, **141**, 194106.
- [64] J. Schirmer, *Phys. Rev. A.*, 1982, **26**, 2395–2416.

- [65] K. Röttger, H. J. B. Marroux, H. Böhnke, D. T. J. Morris, A. T. Voice, F. Temps, G. M. Roberts and A. J. Orr-Ewing, *Faraday Discuss.*, 2016, **194**, 683–708.
- [66] O. O. Brovarets', H. Pérez-Sánchez and D. M. Hovorun, *RSC Adv.*, 2016, **6**, 99546–99557.
- [67] C. Reichardt, C. Wen, R. A. Vogt and C. E. Crespo-Hernández, *Photochem. Photobiol. Sci.*, 2013, **12**, 1341–1350.
- [68] K. Röttger, J. J. B. Marroux, M. P. Grubb, P. M. Coulter, H. Böhnke, A. S. Henderson, M. C. Galan, F. Temps, A. J. Orr-Ewing and G. M. Roberts, *Angew. Chem., Int. Ed.*, 2015, **54**, 14719–14722.
- [69] K. Röttger, H. J. B. Marroux, A. F. M. Chemin, E. Elsdon, T. A. A. Oliver, S. T. G. Street, A. S. Henderson, M. C. Galan, A. J. Orr-Ewing and G. M. Roberts, *J. Phys. Chem. B*, 2017, **121**, 4448–4455.
- [70] G. D. Bull and K. C. Thompson, *Biochemistry*, 2018, **57**, 4547–4561.

4.6 Supplementary Information

Table 4.1: Vertical Excitation Energies (VEEs) Calculated at the RI-CC2/def2-TZVPPD Level of Theory for RI-MP2/def2-TZVPPD Optimized Ground-State Structures of Free 2AP and H-bonded Watson–Crick (WC) and Hoogsteen (HS) 2AP·T Dimers, Respectively. Oscillator Strengths are given in Parentheses.

	2AP and T	2AP·T(WC)	2AP·T(HS)
$\pi\pi^*$ (2AP)	4.45 eV (0.1458)	4.29 eV (0.1602)	4.30 eV (0.1275)
$n\pi^*$ (2AP)	4.54 eV (0.0025)	4.70 eV (0.0018)	4.59 eV (0.0021)
$n\pi^*$ (T)	4.86 eV (0.0000)	4.80 eV (0.0000)	4.81 eV (0.0001)
$\pi\pi^*$ (T)	5.01 eV (0.2331)	5.04 eV (0.1529)	5.00 eV (0.1793)
$\pi\pi^*$ (2AP)	5.35 eV (0.0138)	5.28 eV (0.0359)	5.26 eV (0.0059)

Ultrafast Dynamics of the ESIPT Photoswitch *N*-(3-Pyridinyl)-2-Pyridine- Carboxamide

HENDRIK BÖHNKE,^{a,‡} JULIA BAHRENBURG,^{a,‡} XIAONAN MA,^{a,§} KATHARINA RÖTTGER,^{a,¶}
CHRISTIAN NÄTHER,^b MICHAŁ F. RODE,^c ANDRZEJ L. SOBOLEWSKI^c AND FRIEDRICH TEMPS^{*a}

^a Institute of Physical Chemistry, Christian-Albrechts-University Kiel, Olshausenstr. 40,
24098 Kiel, Germany.

^b Institute of Inorganic Chemistry, Christian-Albrechts-University Kiel, Olshausenstr. 40,
24098 Kiel, Germany.

^c Institute of Physics, Polish Academy of Science, al. Lotników 32/46, 02-668 Warsaw,
Poland.

[‡] Both authors contributed equally to this work.

[§] Present address: Institute of Physical and Theoretical Chemistry, Julius-Maximilians-
University Würzburg, Am Hubland, 97074 Würzburg, Germany.

[¶] Present address: Centre for Process Innovation, Wilton Centre, Wilton, Redcar TS10 4RF,
United Kingdom.

* To whom correspondence should be addressed. E-mail: temps@phc.uni-kiel.de.

Published in Phys. Chem. Chem. Phys., **2018**, *20*, 2646-2655.

Reproduced by permission of the PCCP Owner Societies.

OWN CONTRIBUTIONS TO THIS PUBLICATION:

- Steady-state FTIR spectroscopy,
- Quantum chemical calculations for ground-state species,
- Transient femtosecond vibrational absorption spectroscopy,
- Analysis of experimental data,
- Writing of the TVAS section for the manuscript.

Abstract

Molecular switches based on proton transfer that are photochromic and can be interconverted by light at different wavelengths back and forth between two thermodynamically stable tautomeric states in solution at room temperature are rare to date. We report on a study of the ultrafast conversion of the bistable proton transfer switch *N*-(3-pyridinyl)-2-pyridinecarboxamide (NPPCA) to a corresponding iminol after photoexcitation at $\lambda_{\text{pump}} \approx 265$ nm by means of femtosecond time-resolved broad-band and single-colour transient electronic absorption spectroscopy (TEAS), transient fluorescence spectroscopy (TFLS), and transient vibrational absorption spectroscopy (TVAS) in acetonitrile solution. The interpretation of the data was accompanied by *ab initio* quantum chemical calculations of the excited electronic states and the vibrational frequencies of the reactant and product in their ground electronic state. The TEAS experiments provided four time constants, $\tau_1 = 0.09 \pm 0.01$ ps, $\tau_2 = 0.61 \pm 0.01$ ps, $\tau_3 = 5.10 \pm 0.80$ ps, and $\tau_4 = 20.0 \pm 1.0$ ps. The first two agree well with the measured TFLS lifetimes, $\tau_{1,\text{TFL}} < 0.18$ ps and $\tau_{2,\text{TFL}} = 0.50 \pm 0.01$ ps. τ_1 is related to the relaxation of the initially excited Franck–Condon (FC) state of the pyridinecarboxamide, followed by the excited-state intramolecular proton transfer (ESIPT) step to the neighbouring pyridine. The subsequent return of the molecules to the electronic ground state takes place within τ_2 , mediated by a conical intersection (CI) at a twisted configuration of the pyridinecarboxamide moiety. The main components in all TEAS time profiles feature a rise with τ_2 and a decay with τ_4 and describe subsequent molecular transformations in the electronic ground state. τ_3 is ascribed to vibrational cooling of the molecules. The final iminol exhibits a permanent UV absorption at $\lambda = 247$ nm, where its absorbance is stronger than that of the carboxamide reactant. The iminol structure is unambiguously identified by the TVA spectra, which show the build-up of corresponding vibrational bands with $\tau_{4,\text{TVA}} = 23 \pm 2$ ps after the initial bleach of the reactant vibrational bands, in excellent agreement with the TEAS data. Its lifetime is > 10 ns.

5.1 Introduction

Excited-state intramolecular proton transfer (ESIPT) processes are key steps in many complex biological and artificial reaction systems.^[1–10] Moreover, they belong to the fastest chemical reactions known. On the time scales down to ~ 10 – 50 fs in favourable examples,^[11–20] the probability of competing side reactions is practically eliminated. Due to the resulting exceptional stabilities against ultraviolet (UV) radiation, ESIPT compounds allow for record numbers of repeatable photoswitching cycles. These properties have led to important applications as sunscreen agents and UV photostabilizers in organic materials and coatings.^[10,21–23] Following the photo-induced proton transfer in the excited state (normally S_1), the molecules usually return to their S_0 ground electronic state by ultrafast radiationless internal conversion (IC). The reaction cycle is subsequently closed by fast pro-

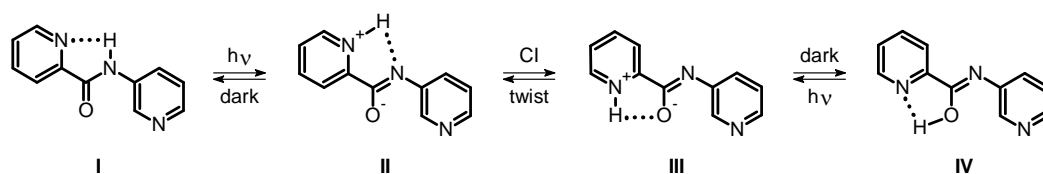


Figure 5.1: Reaction scheme of the bistable ESIPT switch *N*-(3-pyridinyl)-2-pyridinecarboxamide (NPPCA, I) upon UV photoexcitation.

ton back-transfer, through which the molecules return to their initial configuration where they are ready to absorb another UV photon.^[1,2] The formation of stable photoproducts is undesired for photostabilizers, the potential energy barriers for proton back-transfer in the S_0 state should therefore be low. The hydroxybenzotriazole-based Tinuvin P, for example, one of the most common photostabilizers for varnishes and adhesives, has an overall excited-state lifetime of only ~ 200 fs and shows proton back-transfer in the S_0 state in ≤ 1 ps.^[24–26] Moreover, its dynamics is nearly unchanged in polymer environments, a very important property for its use as photostabilizer.

For advanced applications, *e.g.* as fluorescence sensors, photonic elements, or optical memory and logic devices, however, suitable ESIPT molecules should be thermodynamically bistable and photoswitchable from one form to another reversibly by light at different wavelengths. Towards these ends, a novel photochemical scheme has recently been proposed,^[27,28] whereby the absorption of a photon triggers a proton transfer (PT) in the excited electronic state from a donor group to an intermediate proton “crane”, which then performs a large-amplitude rotamerization and transformation through a conical intersection (CI) to the S_0 state, before the proton is dropped at an acceptor site some distance away from the donor. The net result is a long-range proton transport along the molecular scaffold. In this case, a sufficiently high potential energy barrier in the electronic ground state is desirable to prevent fast thermally activated intramolecular proton back-transfer. By photoexcitation of the PT product, however, the reaction may be driven in the reverse direction to recover the ESIPT switch in its initial form. An example, for which a related crane-mediated PT has been demonstrated, is 7-hydroxy-8-(morpholinomethyl)quinoline.^[29,30] However, the adiabatic nature of the PT pathway in the S_1 state precludes a photo-initiated reverse reaction of this molecule,^[28] leaving only a thermal back-isomerization route.

Here, we report on a comprehensive study of the ultrafast photo-induced dynamics of *N*-(3-pyridinyl)-2-pyridinecarboxamide (NPPCA), which has been proposed as a potential new bistable photochromic ESIPT switch following the above scheme.^[31] As sketched in Fig. 5.1, the amide nitrogen acts as proton donor, the adjacent pyridine plays the role of the proton crane, and the carbonyl oxygen is the final proton acceptor. Accordingly, photoexcitation of the stable initial carboxamide I induces an ESIPT from the amide-N to the neighbouring pyridine-N. The resulting intermediate II evolves on the excited potential energy surface (PES) by twisting around the pyridine–carboxamide single bond towards a conical intersection (CI) that mediates the internal conversion of the molecule to the

S_0 electronic ground state. The torsional motion continues on S_0 to the intermediate **III**, from where it is followed by the final PT step to the iminol product **IV**, or the molecule on S_0 returns *via* structure **II** to its initial state **I** by proton back-transfer. Both **II** and **III** are unstable intermediates in the electronic ground state.

To shed light onto this complex photochemical reaction sequence, the ensuing mechanisms have first been explored by *ab initio* quantum chemical calculations at the second-order Møller-Plesset (MP2), second-order coupled cluster (CC2) and algebraic diagrammatic construction of second order (ADC(2)) levels of theory. The dynamics of the molecules were then examined experimentally in acetonitrile (ACN) solution following UV photoexcitation to the first $^1\pi\pi^*$ electronic state by means of femtosecond time-resolved broad-band and single-colour transient electronic absorption spectroscopy (TEAS), transient fluorescence spectroscopy (TFLS) and transient vibrational absorption spectroscopy (TVAS). Special attention was directed at the ultrafast ESIPT step from the initial carboxamide **I** to the excited intermediate structure **II**, the radiationless electronic relaxation through the CI, and the subsequent transformation of the molecules on the S_0 PES to the final product **IV**. Eventually, the iminol structure of **IV** was verified by TVAS.

5.2 Methods

Computational Methods

The equilibrium structures of the molecules in their stable forms in the electronic ground state and in the lowest excited $^1\pi\pi^*$ and $^1n\pi^*$ states were computed using the MP2 and the ADC(2) methods, respectively. The ADC(2) method^[32] offers a description of electronically excited states with similar quality as MP2 does for electronic ground states. The optimization and reaction pathway calculations were performed using the cc-pVDZ basis set,^[33] which is known to be adequate for the description of the geometry of organic molecules. For calculating the electronic excitation energies of the stable conformers, the cc-pVDZ basis was augmented with diffuse functions. Vertical electronic absorption spectra were calculated using the CC2 method^[34,35] and the aug-cc-pVDZ^[33] basis set at the MP2/cc-pVDZ optimized geometry. Vibrational frequencies for the reactant and product molecules were obtained using the resolution of the identity variant of MP2/aug-cc-pVDZ and by density functional theory (DFT) calculations at the B3LYP/6-311+G**, B3LYP-D3/6-311+G**, CAM-B3LYP/6-311+G**, M062X/6-311+G** and PBE0/6-311+G** levels, using scaling factors for the harmonic frequencies between 0.985 and 0.95. All MP2, CC2 and ADC(2) calculations were carried out with the TURBOMOLE^[36] program package, all DFT calculations with the Gaussian09^[37] suite.

Time-Resolved Measurements

NPPCA was synthesized as described in the literature^[38] and recrystallized from ethanol. The purity of the product (> 99%) was checked by one- and two-dimensional NMR spectroscopy in deuterated acetonitrile (dACN) and D₂O. Additionally, an X-ray diffraction structure was obtained.

The TEA and TFL spectrometers in our laboratory have been described previously.^[39–41] The main measurements were performed in anhydrous acetonitrile (ACN, supplied by Sigma-Aldrich and dried over molecular sieve) employing sample concentrations of 6 mM (TEAS) and 0.3 mM (TFLS) in 1 mm pathlength all-quartz (Hellma Analytics) flow cuvettes. All solutions were prepared in a glove box purged with dry air. Some additional measurements were run in ultrapure H₂O. Excitation pulses at $\lambda_{\text{pump}} = 264$ nm were delivered by frequency-doubled home-built non-collinear optical parametric amplifiers (NOPAs) pumped by a 1 kHz regeneratively amplified 775 nm Ti:Sa laser (Clark MXR CPA 2001) and focused into the sample cells by dichroic mirrors. Pulse energies were reduced to ≤ 150 nJ (TEAS) and ≤ 100 nJ (TFLS). Supercontinuum probe pulses for TEAS in the range $\lambda_{\text{probe}} = 350\text{--}750$ nm were generated in CaF₂, split into signal and reference beam paths and focused into the sample cell, where the probe was spatially overlapped with the pump pulses. The transmitted light was dispersed in a prism spectrograph and detected by two fast frame transfer CCD cameras. Single-colour probe pulses at $\lambda_{\text{probe}} = 247$ nm were obtained simultaneously from another frequency-doubled NOPA, split again into signal and reference, and detected by two matched photodiodes. Each pump–probe delay scan was repeated three times. Signals due to pump-induced cross-phase modulation (XPM), multiphoton absorption (MPA) and solvated electron absorption (SEA) in H₂O were measured independently for the pure solvents and subtracted in the usual way.^[39,42] The instrument response function (IRF) allowed for an experimental time resolution of $\Delta t \sim 50$ fs.

Transient fluorescence–time profiles were taken at three selected wavelengths, $\lambda_{\text{FL}} = 340$, 430 and 500 nm, using the up-conversion technique by type I sum frequency generation with the 775 nm Ti:Sa gate pulses. The up-converted light passed a double monochromator and was detected as function of pump–gate delay time on a photomultiplier connected to a gated photon counter. Each run was repeated twice. Background signals from impurities or unwanted coherent effects were ruled out by scans of the neat solvent. The time resolution determined by the pump-gate cross correlation was of the order of $\Delta t \sim 130$ fs.

The TVAS experiments were performed in dACN employing sample concentrations of 1.2 mM in a home-built 0.5 mm flow cell with CaF₂ windows similar to that of ref. 43 using loosely focused excitation pulses of ~ 1.3 μJ energy at $\lambda_{\text{pump}} = 266$ nm by frequency tripling the output of a 90 fs, 1 kHz Ti:Sa laser (Coherent Libra HE) at 800 nm. Tunable infrared (IR) probe pulses between $\lambda_{\text{probe}} = 2.5$ and 11 μm were provided by difference frequency generation in AgGaS₂^[44,45] between the signal and idler of a two-stage 800 nm-pumped OPA and detected after dispersion in a grating spectrograph on a 2×32 pixel

HgCdTe detector (Infrared Associates). Transient spectra were collected in windows of $\sim 200\text{--}300\text{ cm}^{-1}$ width as function of pump–probe delay time after the decay of initial transient lensing and local solvent equilibration artefacts in $\Delta t \sim 0.8\text{ ps}$. Required base line corrections were made using the KOALA program.^[46] The temporal information in the spectra was evaluated globally by Gaussian band fitting. Vibrational assignments were made by comparison with calculated vibrational frequencies.

5.3 Results

Minimum Energy Structures in the Electronic Ground State

The photochemically relevant structures **I–IV** of the NPPCA photoswitch have been sketched in Fig. 5.1. The obtained X-ray diffraction structure (see SI, Fig. 5.7 and Tables 5.2–5.4) confirms the carboxamide form **I** with a distinct pre-orientation of the proton donating N–H unit towards the adjacent pyridine nitrogen that indicates the intramolecular hydrogen bonding. The calculated structures for **I** and **IV** are shown in Fig. 5.8 (SI, see also Tables 5.5 and 5.6). The planar carboxamide **I** is the most stable form according to the MP2/cc-pVDZ calculations. The second minimum, denoted as **IV** in Fig. 5.1, corresponds to the eventual proton transfer product, which has *trans*-iminol structure and is less stable than the global minimum structure **I** by $\sim 0.54\text{ eV}$. **IV** is again planar in the region around the intramolecular hydrogen bond, although the lone pyridine moiety is rotated from planarity by $\sim 33^\circ$. The calculations also showed a *cis*-iminol form (denoted as **V** in the following) at $\sim 0.8\text{ eV}$ above the global minimum **I** and two rotamers, the carboxamide-*r* form **VI** at $\sim 0.46\text{ eV}$ and the *trans*-iminol-*r* form **VII** at $\sim 1.15\text{ eV}$ above **I** (SI, Table 5.7). All computational results, including some additional information, are summarized in Fig. 5.10 (SI).

The intermediate structures **II** and **III** are relevant for the photochemistry of the molecule, but are not stable on the electronic ground state PES. **II** relaxes spontaneously to **I**, and **III** to **IV**. Most importantly, **I** and **IV** are separated by a high potential energy barrier of $\sim 2\text{ eV}$ on the S_0 PES and are thus not thermally interconvertible at room temperature.

UV/VIS Absorption Spectra and Computed Excited States

The measured static UV/VIS spectrum of NPPCA is shown in Fig. 5.2. The strong absorption peaking at $\lambda = 276\text{ nm}$ in ACN and 275 nm in H_2O belongs to the lowest $^1\pi\pi^*$ transition, which carries the bulk of the oscillator strength. Excitation at $\lambda_{\text{pump}} = 264\text{--}266\text{ nm}$ leads exclusively to population of this state. The shorter wavelength absorption band at $\lambda = 224\text{ nm}$ in both solvents belongs to a second $^1\pi\pi^*$ transition (see below).

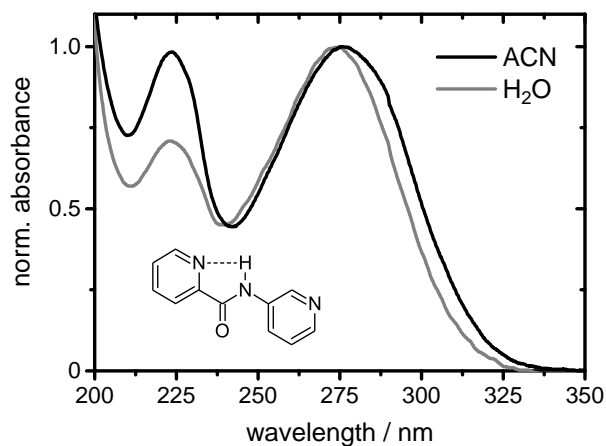


Figure 5.2: UV/VIS absorption spectra of NPPCA in acetonitrile (ACN, black) and water (H₂O, grey). The spectra were normalised at $\lambda = 275$ nm for better comparison.

Table 5.1: Calculated vertical excitation energies for structures **I** and **IV** with respect to their S_0 state minima, and oscillator strengths and dipole moments of the excited states at the CC2/aug-cc-pVDZ level of theory for the MP2/cc-pVDZ ground state optimized geometries.

Structure	Electronic state	$\Delta E/eV$	f^a	$\mu/Debye^b$
I	S_0	0.00	-	4.3
	$n\pi^*$	4.32	0.000	1.7
	$\pi\pi^*$	4.52	0.407	4.6
	$\pi\pi^*$	4.77	0.044	4.0
	$\pi\pi^*$	5.01	0.030	3.2
	$n\pi^*$	5.09	0.006	3.3
	$n\pi^*$	5.13	0.000	2.4
	$\pi\pi^*$	5.59	0.268	9.2
	$\pi\pi^*$	6.06	0.097	3.2
	$\pi\pi^*$	6.06	0.043	9.7
	IV	S_0	0.54 ^{c)}	-
$\pi\pi^*$		4.30	0.777	2.2
$n\pi^*$		4.51	0.002	2.7
$\pi\pi^*$		4.80	0.019	3.8
$n\pi^*$		4.82	0.0003	0.5
$\pi\pi^*$		4.98	0.037	2.3
$n\pi^*$		5.13	0.004	3.0
$\pi\pi^*$		5.61	0.026	4.1
$\pi\pi^*$		5.94	0.102	1.6
$\pi\pi^*$		6.08	0.001	7.4

a) Calculated oscillator strengths of the excited states.

b) Calculated dipole moments of the excited states in Debye.

c) Relative energy of the S_0 state of **IV** relative to **I**.

The computed vertical excitation energies (VEEs) and the oscillator strengths and dipole moments of the excited states for tautomers **I** and **IV** at the CC2/aug-cc-pVDZ level of theory are listed in Table 5.1. Additional data for some of the other structures at the CC2/cc-pVDZ level can be found in Table 5.7 (SI). According to the calculations, the lowest energy $^1\pi\pi^*$ excited state of the carboxamide **I** has a CC2/aug-cc-pVDZ VEE of 4.52 eV (274 nm). Its adiabatic excitation energy (AEE), that is the excited-state energy in its optimized geometry relative to the energy of the optimized ground-state global minimum, is 3.75 eV (CC2/cc-pVDZ value). The CI connecting the first $^1\pi\pi^*$ excited state to the S_0 ground electronic state can be reached directly along a barrierless pathway. The first $^1n\pi^*$ state has a VEE of 4.32 eV (CC2/aug-cc-pVDZ) and an AEE of 3.53 eV (CC2/cc-pVDZ). The experimentally observed shorter-wavelength absorption maxima at 224 nm and 200 nm in Fig. 5.2 correspond well to the calculated VEEs for the S_4 ($^1\pi\pi^*$) and S_5 ($^1\pi\pi^*$) states of 5.59 eV and 6.06 eV, respectively. The calculated UV absorption spectrum in Fig. 5.9 (SI) is in excellent agreement with the experimental one.

The first $^1\pi\pi^*$ excited state of the iminol PT product **IV** has a VEE of 4.30 eV (288 nm). Thus, the onset of the UV absorption of **IV** is substantially red-shifted compared to the carboxamide **I** (*cf.* Fig. 5.9, SI), suggesting true UV photochromic behaviour. Moreover, the first $^1\pi\pi^*$ transition of the iminol is predicted by the calculations to have a considerably larger oscillator strength ($f = 0.777$) than the first $^1\pi\pi^*$ transition of the initial carboxamide **I** ($f = 0.407$).

Transient Electronic Absorption and Fluorescence Spectroscopy (TEAS and TFLS)

The measured spectro-temporal transient electronic absorption map showing the change in optical density ΔOD for NPPCA in ACN after excitation at $\lambda_{\text{pump}} = 264$ nm is displayed in Fig. 5.3 (a). As seen, it features a number of distinctive, time-dependent, spectral bands. The transient spectra at selected delay times in Figs. 5.3 (b and c) reveal the encoded dynamics in further detail. The data first show a negative signal near time-zero between $\lambda_{\text{probe}} = 420\text{--}540$ nm from stimulated emission (SE), which is filled in within ~ 100 fs (Fig. 5.3 (a)). Positive excited-state absorption (ESA) bands appear around $\lambda_{\text{probe}} = 350, 450, 600$ and 730 nm. The most prominent feature is the strong ESA at around $\lambda_{\text{probe}} = 450$ nm, which shows a delayed rise growing out of the initially negative SE signal followed by a much slower decay in ~ 20 ps. Another notable feature is a relatively long-lived absorption band near ~ 750 nm (*cf.* Fig. 5.3 (c)).

For comparison, Fig. 5.3 (d) depicts the very different transient absorption map for NPPCA in H_2O . Here, we see positive and negative spectral features at virtually the same probe wavelengths as for ACN, but the observed lifetimes are much shorter. In particular, the long-living strong absorption in ACN around $\lambda_{\text{probe}} = 450$ nm is completely missing in H_2O . The same applies to the weaker long-living absorption around 750 nm. Since an

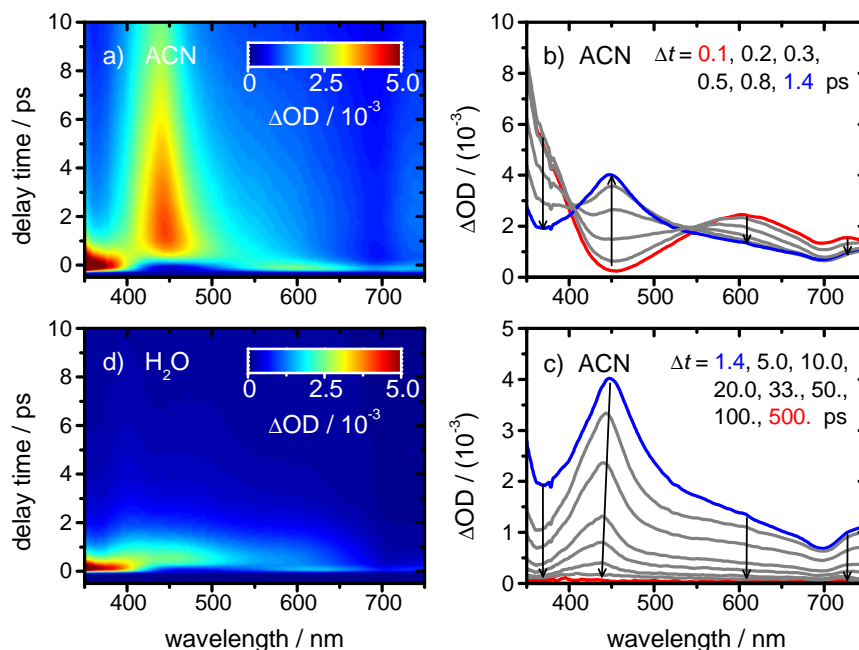


Figure 5.3: (a) Spectro-temporal map of the change in optical density ΔOD for NPPCA in ACN after excitation at $\lambda_{\text{pump}} = 264$ nm. (b and c) Transient absorption spectra at delay times from 0.1 to 1.4 ps (b) and 1.4 to 500 ps (c) after the pump pulse. The arrows indicate the temporal evolution of the spectra. (d) Transient absorption map after excitation at $\lambda_{\text{pump}} = 264$ nm for NPPCA in H_2O . The transient absorption maps are displayed in panels (a) and (d) for clarity only up to $\Delta t = 10$ ps, but were recorded up to $\Delta t = 1$ ns.

intramolecular proton transfer and (stepwise) production of **IV** is expected only in aprotic solvents, like ACN, and not in the protic H_2O , the 450 nm and 750 nm absorption features in ACN strongly hint at some intermediate PT state(s) or product(s). The analysis of the time profiles and predominating time constants for NPPCA in ACN follows right below, the corresponding results in H_2O are given in the SI (*cf.* Fig. 5.11–5.13).

The time histories of the absorption features in ACN are displayed in Fig. 5.4. The curves were obtained by integration of the transient absorptions over the respective spectral bands. The evaluation of the integrated spectral band profiles has the advantage that the bands may, at least in principle, be identified with certain excited states or intermediates in the reaction mechanism. The obtained decay curves were subsequently analyzed in a global fashion by non-linear least squares fitting using a sum of four exponentials for each of the windows from $\lambda_{\text{probe}} = 710\text{--}750$ nm, 600–650 nm (not shown), 430–480 nm, and 350–380 nm and for the single-colour measurement performed at $\lambda_{\text{probe}} = 247$ nm. The fitting yielded the four time constants values (with 2σ error limits) of

$$\tau_1 = 0.09 \pm 0.01 \text{ ps,}$$

$$\tau_2 = 0.61 \pm 0.05 \text{ ps,}$$

$$\tau_3 = 5.10 \pm 0.80 \text{ ps,}$$

$$\tau_4 = 20.0 \pm 1.00 \text{ ps.}$$

The decay-associated spectra from a complementary singular value decomposition (SVD) analysis belonging to these time constant values are given in Fig. 5.14 (SI).

Additional transient fluorescence measurements were performed to assess the photo-physical processes behind these data taking place in the electronically excited state. Two exemplary fluorescence–time profiles, recorded at $\lambda_{\text{FL}} = 340$ and at $\lambda_{\text{FL}} = 500$ nm, are shown in Figs. 5.4 (e and f). The analysis of those data gave time constants (with 2σ error limits) of

$$\tau_{1,\text{TFL}} = 0.18 \pm 0.01 \text{ ps},$$

$$\tau_{2,\text{TFL}} = 0.50 \pm 0.01 \text{ ps}.$$

The above time constant values project a rather complex picture for the dynamics of the photoexcited molecules. Nevertheless, the transient electronic spectroscopy data can be tentatively interpreted with some certainty even without the TVAS data, which will be added to our consideration afterwards:

1. The lifetimes of $\tau_1 = 0.09$ ps and $\tau_2 = 0.61$ ps, which were observed partially in SE ($\lambda_{\text{probe}} = 430\text{--}480$ and $350\text{--}380$ nm) and partially in ESA ($\lambda_{\text{probe}} = 710\text{--}750$, $600\text{--}650$ and $350\text{--}380$ nm), correlate well with the two fluorescence decay times. The value of $\tau_{1,\text{TFL}}$ determined by the fluorescence measurements should actually be taken as an IRF-determined upper limit in view of the time resolution of the TFLS experiment (*i.e.*, $\tau_{1,\text{TFL}} < 0.18$ ps). The relative amplitude of this component decreases rapidly with increasing emission wavelength. The time profile at $\lambda_{\text{FL}} = 340$ nm is almost completely determined by the fast component, whereas that at $\lambda_{\text{FL}} = 500$ nm can be fully described using $\tau_{2,\text{TFL}}$ only. The value of τ_1 is therefore assigned to the departure of the initially excited wavepacket from the Franck–Condon (FC) region, followed by the ultrafast ESIPT from the amide-N to the neighbouring pyridine-N. The value of τ_2 can safely be accepted as the lifetime of the excited electronic state, which is determined by the transformation of the excited molecules through the CI to the S_0 ground state.
2. The assignment of the transient components with $\tau_3 = 5.1$ ps is less obvious. Time constant values of this magnitude are typical for vibrational cooling dynamics of molecules of similar size after their return from the photoexcited to the ground electronic state in ACN solution.^[47] Such cooling processes appear less prominent by the relatively small amplitudes in the present case than with other molecules.^[48–50] This argument will be taken up again below in the Discussion. The respective transients in Fig. 5.4 are always overshadowed by stronger decay components associated with τ_4 , so that possible rising features with τ_3 remain hidden.
3. Most importantly, the main components (beyond the ultrashort τ_1 and τ_2) in all transient absorption traces at $\lambda_{\text{probe}} > 400$ nm and in the single-colour trace at $\lambda_{\text{probe}} = 247$ nm, exhibit a decay time of $\tau_4 = 20.0 \pm 1.0$ ps after an initial rise in

~ 0.6 ps. At $\lambda_{\text{probe}} = 247$ nm (Fig. 5.4), τ_4 is also taken into account to describe the rise of the transient absorption to the observed final steady state value. As this time constant predominates in the absorption–time profiles in all probe windows above 400 nm and at 247 nm, and as the 0.6 ps rise time nicely reflects the excited electronic state lifetime $\tau_{2,\text{TFL}}$ inferred from the fluorescence measurements, the respective transient absorption features likely belong to configurations **II** and/or **III** in the electronic ground state. Time constant τ_4 is therefore attributed to the (slower) transformations of the molecules in S_0 from structure **II** back to **I** and, in particular, from structure **III** to the final PT product **IV**.

4. In addition to the component decaying with τ_4 , the absorption–time profile at $\lambda_{\text{probe}} = 247$ nm also features a persistent positive absorption signal with a relative amplitude of $\sim 12\%$ that does not decay to zero within our temporal detection window. Although UV absorption spectra are not too sensitive to the involved chemical species owing to the broad and unspecific nature of the observed bands, the likely structure to which this long-lived absorption is assignable is the iminol **IV**. Considering the involved species, the carboxamide is expected to give a negative contribution (bleach) to the observed final signal, and the iminol a positive one (product absorption). The computed UV absorption spectra in Fig. 5.9 (SI) suggest a small advantage for the carboxamide at the wavelength in question, but the experiment which detects the net effect appears to indicate that the iminol wins. Obviously, it has to be kept in mind here that the appearance of the computed spectra depends on the assumed Gaussian band shape functions, which is unknown for **IV**, and that the computed oscillator strengths for **I** and **IV** have considerable room for error. The formation of **IV** is unambiguously confirmed by the TVA spectra below.
5. The estimated limit for the lifetime of the long-lived product of >10 ns is far longer than for “normal” ESIPT molecules.
6. The time profiles at $\lambda_{\text{probe}} = 710\text{--}750$, $430\text{--}480$ and $350\text{--}380$ nm also indicate very minor long-lived components (grey) with amplitudes $< 4\%$ (*cf.* Fig. 5.4). Fit attempts without those contributions were not satisfactory, but their physical origin remains debatable. They may belong to a minor pathway involving $n\pi^*$ states, to slow processes in the electronic ground state, or plainly to experimental artefacts, such as a background drift.
7. Last but not least, the transient absorption data for NPPCA in H_2O (Fig. 5.3 (d) and Fig. 5.11–5.13, SI) confirm the absence of time constant τ_4 and therefore the iminol **IV** in the protic environment.

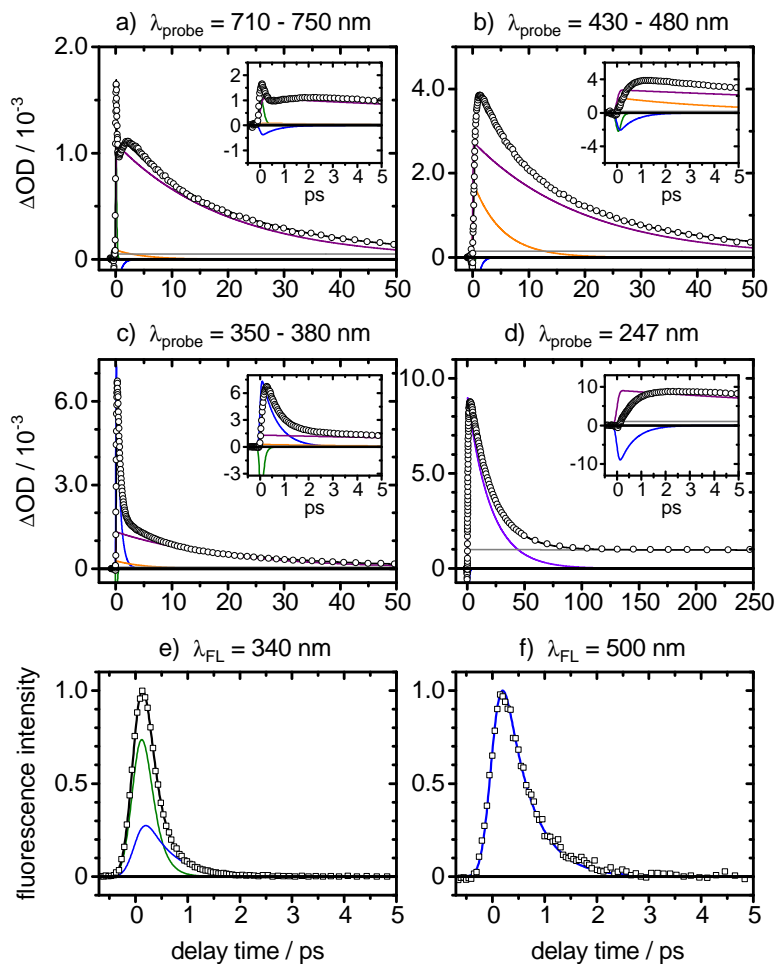


Figure 5.4: (a–d) Transient absorption–time profiles of NPPCA in ACN after excitation at $\lambda_{\text{pump}} = 264$ nm in four selected probe windows (a: 710–750 nm, b: 430–480 nm, c: 350–380 nm, d: 247 nm). Open symbols denote the experimental data, solid black lines the overall least-squares fit curves. The different contributions are indicated by coloured lines (olive: τ_1 , blue: τ_2 , red: τ_3 , purple: τ_4 , grey: constant offset). The insets show the same data on a shorter time scale up to $\Delta t = 5$ ps. The data in the window from 600–650 nm were very similar to those in the 710–750 nm window and are not shown here to save space. (e and f) Fluorescence–time profiles of NPPCA in ACN after excitation at $\lambda_{\text{pump}} = 264$ nm at two emission wavelengths (e: $\lambda_{\text{FL}} = 340$ nm, f: $\lambda_{\text{FL}} = 500$ nm). Open symbols are data points, solid lines give the least-squares fit curves (olive: $\tau_{1,\text{TFL}}$, blue: $\tau_{2,\text{TFL}}$).

Transient Vibrational Absorption Spectroscopy (TVAS)

The proposed mechanistic pathways and the involved states and species were finally verified by making use of the structural sensitivity of transient vibrational absorption spectroscopy. Comparison of calculated vibrational spectra for the ground-state species **I** and **IV** at the RI-MP2/aug-cc-pVDZ level of theory and a measured Fourier-transform infrared (FTIR) spectrum of NPPCA led to the identification of several prominent vibrational marker modes. As illustrated in Fig. 5.15 and 5.16 (SI), the carboxamide **I** features its NH stretch vibration with a calculated frequency of 3323 cm^{-1} , the prominent CO stretch vibration at 1698 cm^{-1} and two modes with predominantly NH bend character at 1586 and 1537 cm^{-1} . The proposed iminol product **IV**, on the other hand, is expected to show its OH stretch vibration at 3317 cm^{-1} , the (mixed) CN stretch/OH bend vibration around 1679 cm^{-1} as well as additional mixed, mostly OH bend vibrations around 1480 and 1372 cm^{-1} . The respective vibrational frequencies were confirmed by RI-MP2/aug-cc-pVDZ *ab initio* and B3LYP/6-311+G**, B3LYP-D3/6-311+G**, M062X/6-311+G**, CAM-B3LYP/6-311+G** and PBE0/6-311+G** DFT calculations (Fig. 5.17, SI).

TVAS measurements investigating those marker vibrations were carried out focusing on the spectral range from ~ 1400 to 1700 cm^{-1} . The spectra in the NH/OH stretch region were very broad and therefore less informative. The overall results along with corresponding global band fits and along with the calculated (RI-MP2/aug-cc-pVDZ) vibrational spectra for species **I** and **IV** for comparison are presented in Fig. 5.5 (a). The complete transient spectra from 1400 to 1700 cm^{-1} were spliced together from corresponding records over three individually measured smaller windows, for which the globally fitted spectra along with globally fitted mono-exponential functions to their amplitudes are displayed in Fig. 5.5 (b–d). Because the early dynamics in the excited electronic state after the UV pump pulse cause diffuse broadening and large-scale shifting of the vibrational bands, the first transients shown in Fig. 5.5 refer to $\Delta t = 1.8\text{ ps}$ after the pump pulse, *i.e.* after the supposed ultrafast deactivation of the molecules to the ground electronic state.

As can be seen, the transient vibrational spectra in Fig. 5.5 feature incompletely recovering bleach signals, signatures of decaying intermediate species, and product absorptions rising in time to constant final values. Most importantly, the observed spectra at long pump–probe delay times ($\Delta t \geq 100\text{ ps}$) reflect the calculated spectra for species **I** and **IV** over the entire spectral range strikingly well. In particular, the partial bleach recovery of the CO stretch band at 1690 cm^{-1} (calculated frequency: 1698 cm^{-1}) and the rise of the CN stretch/OH bend vibration at 1670 cm^{-1} (calculated frequency: 1679 cm^{-1}) clearly show the time evolution of the carboxamide **I** and the formation of the iminol product **IV**, respectively. The same is true for the assigned other vibrational signatures of **I** and **IV**. The positive going transient features, on the other hand, centered at ~ 1655 , 1550 , 1478 and 1403 cm^{-1} can be assigned to intermediates species, *e.g.* tentatively to **II** and/or **III**, which decay back to zero on similar time scales as the product bands grow in.

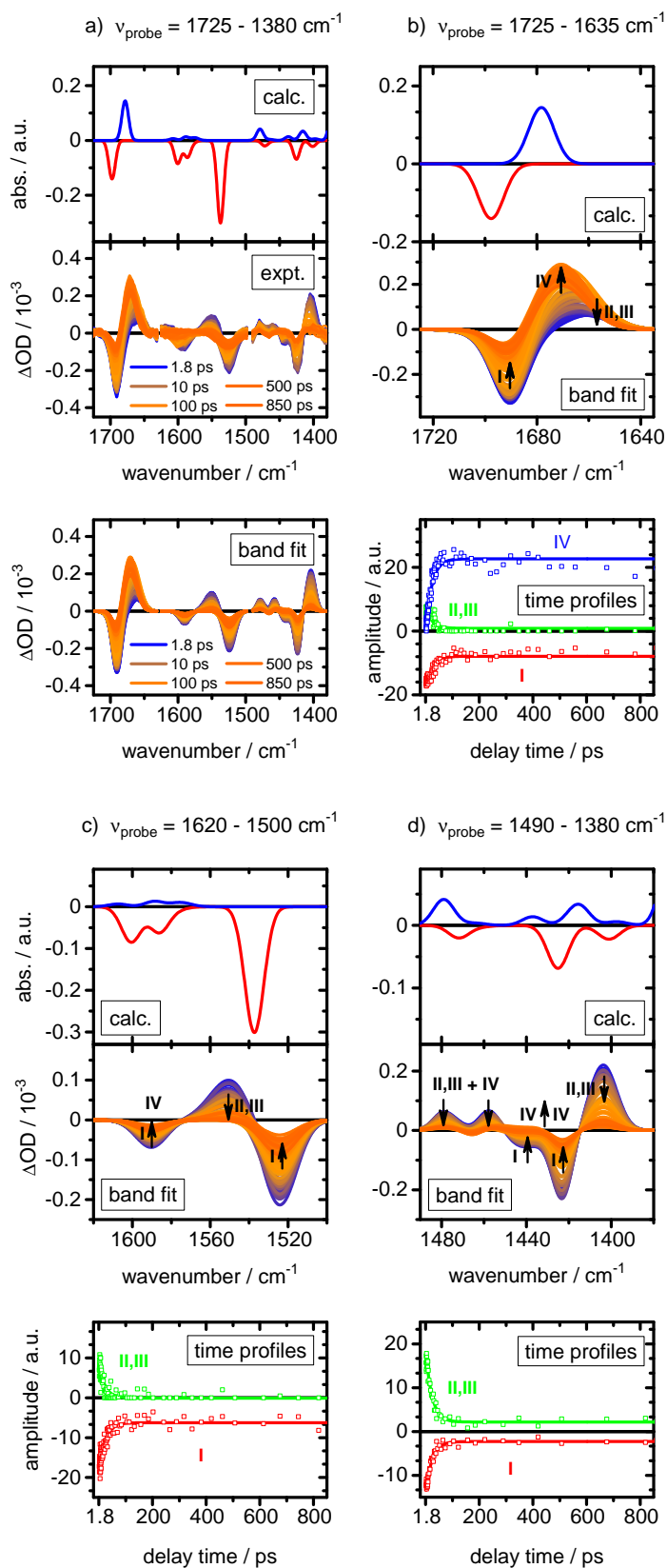


Figure 5.5: (a) Measured transient vibrational absorption spectra following excitation of NPPCA in ACN at $\lambda_{\text{pump}} = 266$ nm along with calculated vibrational frequencies for **I** (negative, red) and **IV** (positive, blue) and a global band fit. (b–d) Temporal evolution of the globally fitted bands in the probe windows from (b) 1725–1635 cm^{-1} , (c) 1620–1500 cm^{-1} and (d) 1490–1390 cm^{-1} . Open symbols are data points, solid lines give the least-squares fit curves (red: structure **I**, green: structures **II** and **III**, blue: structure **IV**).

A global analysis yielded an associated lifetime (with 2σ error) for the observed processes in the TVA spectra of

$$\tau_{4,\text{TVA}} = 23 \pm 2 \text{ ps.}$$

Moreover, taking the ratio of the final to the initial bleach amplitude of the prominent carboxamide CO stretch band at 1690 cm^{-1} (*cf.* Fig. 5.5 (a)), an estimate can be derived for the quantum yield of the iminol product of

$$\phi(\text{IV}) \sim 0.40 \pm 0.07.$$

5.4 Discussion

The above transient fluorescence, electronic absorption, and vibrational absorption data, taken together with the quantum chemical calculations, provide detailed insight into the ultrafast photo-induced dynamics of the NPPCA switch. The observed reaction steps are illustrated in Fig. 5.6.

Irradiation of the electronic ground state carboxamide tautomer **I** at $\lambda_{\text{pump}} \approx 265 \text{ nm}$ projects a wavepacket into the FC region of the first excited ${}^1\pi\pi^*$ state (S_2 at vertical excitation). In principle, this state (which we will refer to as **I**^{*} to indicate the structure and electronic excitation) can relax to the slightly lower ${}^1n\pi^*$ (S_1) state, or perform the supposed ESIPT on the ${}^1\pi\pi^*$ PES to give tautomer **II**^{*}. On the $n\pi^*$ PES, as shown by the computational results summarized in Fig. 5.10 (SI), the wavepacket would have to surmount an energy barrier for the PT of $\Delta E \sim 0.27 \text{ eV}$. On the $\pi\pi^*$ PES, however, **II**^{*} and the $\pi\pi^*/S_0$ CI, through which the molecules can return to the electronic ground state, are accessible without significant energy barriers, making this the preferred route. Hence,

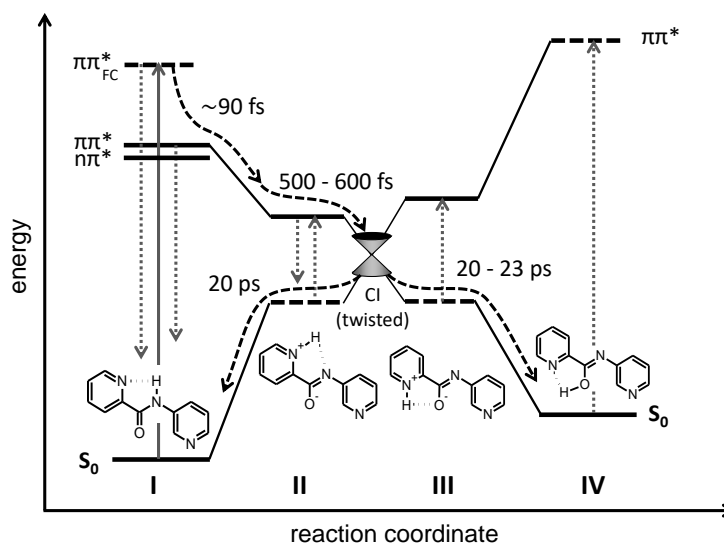


Figure 5.6: Proposed photo-induced proton transfer scheme in the NPPCA ESIPT switch by combination of the experimental and computational (CC2 and ADC(2)) results.

the observed fluorescence and ESA components decaying with $\tau_1 = 0.09$ ps are associated with the rapid departure of the excited wavepacket from the FC region of the $^1\pi\pi^*$ PES, and the actual ESIPT step on the $^1\pi\pi^*$ PES from **I*** to **II***.

The second time constant ($\tau_2 \sim 0.5$ – 0.6 ps) is attributed to subsequent structural relaxation of **II*** and, most importantly, to the barrierless nonadiabatic transition from **II*** through the $\pi\pi^*/S_0$ CI found at a twisted configuration of the pyridine crane to the electronic ground state of **II**. The observed ~ 0.6 ps ESA lifetime is nicely confirmed by the time-resolved fluorescence results, where the value of 0.50 ps is the longest observed lifetime component. The kinetics of the ESIPT step from **I*** to **II*** should thus be described by this time constant.

In agreement with these results, the early-time transient vibrational absorption spectra of the excited molecules are subject to major spectral broadening and spectral shifts (not shown in Fig. 5.5), which reflect the above ultrafast (sub-picosecond) relaxation and PT dynamics. A good picosecond after completion of the electronic deactivation through the CI, however, the observed bleach features in the TVA spectra resemble the calculated vibrational spectrum of tautomer **I** rather strikingly (*cf.* Fig. 5.5, $\Delta t = 1.8$ ps).

The slightly longer third experimental time constant $\tau_3 = 5.1$ ps has the typical magnitude for vibrational cooling of the initially vibrationally “hot” molecules after their return through the CI to the electronic ground state.^[47] Compared with the electronic deactivation of other molecules, where a very large amount of vibrational energy is dumped into the S_0 state virtually instantaneously by the nonadiabatic transition through the CI, the amount of vibrational energy set free in NPPCA by the transition from state **II*** to states **II** and **III** is much lower, however, because the latter structures are at higher energies on the S_0 PES. Overall, the vibrational energy is set free only gradually, as the reaction continues on the S_0 PES more slowly ($\tau_4 \sim 20$ ps) to the iminol **IV**. Thus, the low amplitude of the vibrational cooling components with τ_3 in the TEAS data and the virtual lack of corresponding transients with τ_3 in the TVAS data is not surprising at all.

The predominant fourth time constant, $\tau_4 = 20$ ps, was observed only in absorption and not in fluorescence. Hence, it is associated with the eventual dynamics on the S_0 PES. This conclusion is supported qualitatively and quantitatively by the TVAS results ($\tau_{4,TVA} = 23$ ps). The two processes coming into mind are (*i*) the intramolecular proton back-transfer *via* **II** to the initial carboxamide structure **I** completing the efficient electronic deactivation similarly as in other ESIPT molecules, and (*ii*) the formation *via* **III** of the iminol product **IV** by the final PT from the pyridine crane to the carbonyl oxygen. Here, it is important to notice that several of the TEA time profiles, especially the data at $\lambda_{\text{probe}} = 710$ – 750 nm and 247 nm, feature a ~ 0.6 ps rise time, just as may be expected from the observed ~ 0.5 – 0.6 ps excited-state electronic deactivation time, before the subsequent final decay dynamics with the 20 ps lifetime. As the energy difference between the excited and ground states of **II** and **III** is only of the order of 1 eV, and even though **II** and **III** are not stable minima on the S_0 PES, the observed TEA band at $\lambda_{\text{probe}} > 700$ nm likely corresponds to absorption from intermediate structures close to **II** and/or **III**. As already mentioned, the permanent residual electronic absorption at $\lambda_{\text{probe}} = 247$ nm is readily

rationalized by the calculated larger oscillator strength of the first $\pi\pi^*$ transition of **IV** ($f = 0.777$) compared to **I** ($f = 0.407$).

Eventually, the formation of the iminol product **IV** is shown by the transient vibrational spectra, especially by the comparison of the observed late-time TVA spectrum to calculated spectra (Fig. 5.17, SI). That the time constant inferred from the TVA experiment is slightly longer than indicated by the TEA data (23 vs. 20 ps) is explained by the fact that the broad electronic absorption band samples a range of vibrational states above $v = 0$, which need some time for vibrational relaxation to $v = 0$, while the vibrational absorption measurement detects essentially just the $v = 0$ to 1 transition. Vibrational absorptions by intermediates **II/III** gave rise to transient positive bands in the observed spectra. In accordance with TEAS results, however, the signatures of **II/III** decay with $\tau \sim 20$ ps to either partially repopulate **I** or to form the photoproduct **IV**. A presence of long-lived $^1n\pi^*$ or triplet states could be ruled out by vibrational frequency calculations for those states, which did not match the measured TVA spectra.

Unambiguous evidence for **IV** is given by the rise of the prominent C=N band at 1670 cm^{-1} (cf. Fig. 5.5 (b)), which appears red-shifted to the C=O bleach of **I** as predicted by the vibrational frequency calculations. The resemblance of the positive going bands in the transient vibrational spectra with the calculated frequencies of **IV** after decay of the intermediate features of **II/III** is indeed very satisfactory (SI, Fig. 5.17). We emphasize again that no comparable products or long-lived (~ 20 ps) transients were observed in the measurements of NPPCA in H_2O , where intramolecular PT is disfavoured by the ubiquitous hydrogen bonds from the solute to the surrounding water molecules.

Pertaining to photoswitching applications of NPPCA, the estimated quantum yield for the formation of **IV** of $\phi \sim 0.40 \pm 0.07$ should suffice well. Moreover, the apparent lifetime of **IV** clearly exceeds the few nanosecond range, as no decay was discernible at all within our experimental observation time of ~ 1 ns. The resulting lower limit of $\tau \gtrsim 10$ ns is far longer than for “normal” ESIPT molecules (and of a similar order as the value of van der Loop *et al.* for 7-hydroxy-8-(morpholinomethyl)quinoline^[30]). Considering the calculated potential energy barrier height for unimolecular thermal back isomerization of **IV** to **I** of around ~ 2 eV, the iminol PT product should indeed be stable in the dark for many hours, days, or longer, such that we may suggest the carboxamide–iminol system as kinetically bistable. In practice, in solution at room temperature, however, the effective lifetime of **IV** may be determined by slow (diffusion-controlled) bimolecular back-conversion, possibly catalyzed by trace amounts of H_2O . For switching applications, the elimination of intermolecular proton back-transfer processes thus requires very strict exclusion of traces of water and suppression of bimolecular proton exchange reactions between the tautomer states. Both those aims may be accomplished in matrix or polymer environments, if necessary at lower temperature. Last but not least, the calculated UV spectra of **IV** and **I** differ substantially from each other (cf. Fig. 5.9, SI) to suggest true photochromic behaviour. The first $\pi\pi^*$ transition of **IV** was predicted by the *ab initio* calculations to have a larger oscillator strength ($f = 0.777$) than the first $\pi\pi^*$ transition of **I** ($f = 0.407$). In particular, however, the calculated UV absorption spectra indicate that a selective photoexcitation

of **IV** over **I** may be accomplished at $\lambda = 290\text{--}310$ nm. Eventually, to answer remaining questions on bistability, photochromaticity, and reverse photoswitchability, we are in the process of designing a nanosecond flash photolysis experiment to measure the UV absorption spectrum and lifetime of **IV** and to generate higher steady-state concentrations of **IV** using a 266 nm Nd:YAG laser, as prerequisite for looking at the reverse ESIPT from **IV** to **I**. Further, plenty of room is left for improvements of the system by chemical modification at the two pyridine rings.

5.5 Conclusion

In conclusion, we have presented an experimental and computational study of the photo-induced dynamics of the bistable excited-state intramolecular proton transfer (ESIPT) switch *N*-(3-pyridinyl)-2-pyridinecarboxamide (NPPCA) in solution in ACN by means of femtosecond time-resolved fluorescence up-conversion, transient electronic absorption and transient vibrational absorption spectroscopy after excitation at $\lambda_{\text{pump}} = 265$ nm. The interpretation of the data was supported by *ab initio* excited-state calculations. The results clearly hint at a stepwise proton transfer reaction from the thermally stable carboxamide tautomer **I** to the desired iminol tautomer **IV**. A global analysis of the absorption-time profiles yielded four time constants, $\tau_1 = 0.09 \pm 0.01$ ps, $\tau_2 = 0.61 \pm 0.05$ ps, $\tau_3 = 5.10 \pm 0.80$ ps and $\tau_4 = 20.0 \pm 1.00$ ps. The two fast time constants were also found in the fluorescence data, whereas τ_4 was confirmed by the time-resolved vibrational absorption measurements ($\tau_{4,\text{TVL}} = 23$ ps). Time constant τ_1 was assigned to the relaxation of the initially excited Franck–Condon state of the carboxamide tautomer **I**^{*}, followed by the subsequent ultrafast ESIPT to the intermediate structure **II**^{*}. The value of τ_2 is associated with the practically barrierless nonadiabatic electronic deactivation of **II**^{*} to the ground state **II** via the $\pi\pi^*/S_0$ conical intersection at a twisted configuration of the pyridine crane moiety. The ESIPT process from **I**^{*} to **II**^{*} is therefore completed in $\sim 0.5\text{--}0.6$ ps. The main decay time $\tau_4 = 20\text{--}23$ ps seen in the transient electronic and vibrational absorption experiments belongs to states **II** and **III** in the S_0 electronic ground state, where the final proton transfer takes place to the iminol product **IV**. Several of the absorption traces feature a delayed rise time in 0.5 ps as expected for the observed deactivation time of the excited electronic state. The persistent electronic absorption at $\lambda_{\text{probe}} = 247$ nm provided initial evidence for the proposed stepwise formation of **IV**. Eventually, the formation of **IV** with an estimated quantum yield of $\phi \sim 0.40$ could be followed directly by the rise of its characteristic C=N stretch vibration concurrent with the depopulation of the intermediate species **II/III** and the partial refilling of the C=O bleach of **I**. The obtained overall picture fits well with the proposed theoretical concept for the design of bistable ESIPT switches.^[27,28] In this context, our present work may be a helpful case study.

Acknowledgments

The support of the work of HB, JB, KR and FT by the Deutsche Forschungsgemeinschaft through the Collaborative Research Centre 677 “Function by Switching” is gratefully acknowledged. XM thanks the Alexander von Humboldt foundation for a postdoctoral fellowship. KR has received additional support by a DFG research fellowship. CN thanks the DFG for continued support. The work of MFR and ALS has been supported by the National Science Centre of Poland and the ICM Warsaw.

References

- [1] S. J. Formosinho and L. G. Arnaut, *J. Photochem. Photobiol., A*, 1993, **75**, 21–48.
- [2] A. Douhal, F. Lahmani and A. H. Zewail, *Chem. Phys.*, 1996, **207**, 477–498.
- [3] T. Elsaesser and H. J. Bakker, *Ultrafast hydrogen bonding dynamics and proton transfer processes in the condensed phase*, Kluwer Academic Publishers, Dordrecht, 2002.
- [4] K.-L. Han and G.-J. Zhao, *Hydrogen bonding and transfer in the excited state*, Wiley, Chichester, UK, 2011, vol. 1 & 2.
- [5] J. E. Kwon and S. Y. Park, *Adv. Mater.*, 2011, **23**, 3615–3642.
- [6] J. Zhao, S. Ji, Y. Chen, H. Guo and P. Yang, *Phys. Chem. Chem. Phys.*, 2012, **14**, 8803–8817.
- [7] A. P. Demchenko, K.-C. Tang and P.-T. Chou, *Chem. Soc. Rev.*, 2013, **42**, 1379–1408.
- [8] V. I. Tomin, A. P. Demchenko and P.-T. Chou, *J. Photochem. Photobiol., C*, 2015, **22**, 1–18.
- [9] H.-W. Tseng, J.-Y. Shen, T.-Y. Kuo, T.-S. Tu, Y.-A. Chen, A. P. Demchenko and P.-T. Chou, *Chem. Sci.*, 2016, **7**, 655–665.
- [10] L. A. Baker, S. E. Greenough and V. G. Stavros, *J. Phys. Chem. Lett.*, 2016, **7**, 4655–4665.
- [11] J. L. Herek, S. Pedersen, L. Bañares and A. H. Zewail, *J. Chem. Phys.*, 1992, **97**, 9046–9061.
- [12] S. Lochbrunner, A. J. Wurzer and E. Riedle, *J. Chem. Phys.*, 2000, **112**, 10699–10702.
- [13] S. Ameer-Beg, S. M. Ormson, R. G. Brown, P. Matousek, M. Towrie, E. T. J. Nibbering, P. Foggi and F. V. R. Neuwahl, *J. Phys. Chem. A*, 2001, **105**, 3709–3718.
- [14] S. Lochbrunner, T. Schultz, M. Schmitt, J. P. Shaffer, M. Z. Zgierski and A. Stolow, *J. Chem. Phys.*, 2001, **114**, 2519–2522.
- [15] K. Stock, T. Bizjak and S. Lochbrunner, *Chem. Phys. Lett.*, 2002, **354**, 409–416.
- [16] S. Lochbrunner, A. J. Wurzer and E. Riedle, *J. Phys. Chem. A*, 2003, **107**, 10580–10590.

- [17] C. Schrieffer, M. Barbatti, K. Stock, A. J. A. Aquino, D. Tunega, S. Lochbrunner, E. Riedle, R. de Vivie-Riedle and H. Lischka, *Chem. Phys.*, 2008, **347**, 446–461.
- [18] C. H. Kim and T. Joo, *Phys. Chem. Chem. Phys.*, 2009, **11**, 10266–10269.
- [19] M. Higashi and S. Saito, *J. Phys. Chem. Lett.*, 2011, **2**, 2366–2371.
- [20] J. Lee, C. H. Kim and T. Joo, *J. Phys. Chem. A*, 2013, **117**, 1400–1405.
- [21] J. Pospíšil and S. Nešpurek, *Prog. Polym. Sci.*, 2000, **25**, 1261–1335.
- [22] M. Zayat, P. Garcia-Parejo and D. Levy, *Chem. Soc. Rev.*, 2007, **36**, 1270–1281.
- [23] R. Kumasaka, A. Kikuchi and M. Yagi, *Photochem. Photobiol.*, 2014, **90**, 727–733.
- [24] M. Wiechmann, H. Port, F. Laermer, W. Frey and T. Elsaesser, *Chem. Phys. Lett.*, 1990, **165**, 28–34.
- [25] M. Wiechmann, H. Port, W. Frey, F. Laermer and T. Elsaesser, *J. Phys. Chem.*, 1991, **95**, 1918–1923.
- [26] A. L. Sobolewski, W. Domcke and C. Hättig, *J. Phys. Chem. A*, 2006, **110**, 6301–6306.
- [27] A. L. Sobolewski, *Phys. Chem. Chem. Phys.*, 2008, **10**, 1243–1247.
- [28] L. Lapinski, M. J. Nowak, J. Nowacki, M. F. Rode and A. L. Sobolewski, *ChemPhysChem*, 2009, **10**, 2290–2295.
- [29] C. J. Jalink, W. M. van Ingen, A. H. Huizer and C. A. G. Varma, *J. Chem. Soc., Faraday Trans.*, 1991, **87**, 1103–1108.
- [30] T. H. van der Loop, F. Ruesink, S. Amirjalayer, H. J. Sanders, W. J. Buma and S. Woutersen, *J. Phys. Chem. B*, 2014, **118**, 12965–12971.
- [31] J. Bahrenburg, M. F. Rode, A. L. Sobolewski and F. Temps, in *Ultrafast Phenomena*, ed. K. Yamanouchi, S. Cundiff, R. de Vivie-Riedle, M. Kuwata-Gonokami and L. DiMauro, Springer, 2014, vol. 19, pp. 399–402.
- [32] J. Schirmer, *Phys. Rev. A: At., Mol., Opt. Phys.*, 1982, **26**, 2395–2416.
- [33] T. H. Dunning, *J. Chem. Phys.*, 1989, **90**, 1007–1024.

- [34] O. Christiansen, H. Koch and P. Jørgensen, *Chem. Phys. Lett.*, 1995, **243**, 409–418.
- [35] C. Hättig and F. Weigend, *J. Chem. Phys.*, 2000, **113**, 5154.
- [36] R. Ahlrichs, M. Bär, M. Häser, H. Horn and C. Kölmel, *Chem. Phys. Lett.*, 1989, **162**, 165–169.
- [37] M. J. Frisch, G. W. Trucks, H. B. Schlegel, G. E. Scuseria, M. A. Robb, J. R. Cheeseman, G. Scalmani, V. Barone, B. Mennucci, G. A. Petersson, H. Nakatsuji, M. Caricato, X. Li, H. P. Hratchian, A. F. Izmaylov, J. Bloino, G. Zheng, J. L. Sonnenberg, M. Hada, M. Ehara, K. Toyota, R. Fukuda, J. Hasegawa, M. Ishida, T. Nakajima, Y. Honda, O. Kitao, H. Nakai, T. Vreven, J. A. Montgomery Jr., J. E. Peralta, F. Ogliaro, M. Bearpark, J. J. Heyd, E. Brothers, K. N. Kudin, V. N. Staroverov, T. Keith, R. Kobayashi, J. Normand, K. Raghavachari, A. Rendell, J. C. Burant, S. S. Iyengar, J. Tomasi, M. Cossi, N. Rega, J. M. Millam, M. Klene, J. E. Knox, J. B. Cross, V. Bakken, C. Adamo, J. Jaramillo, R. Gomperts, R. E. Stratmann, O. Yazyev, A. J. Austin, R. Cammi, C. Pomelli, J. W. Ochterski, R. L. Martin, K. Morokuma, V. G. Zakrzewski, G. A. Voth, P. Salvador, J. J. Dannenberg, S. Dapprich, A. D. Daniels, O. Farkas, J. B. Foresman, J. V. Ortiz, J. Cioslowski and D. J. Fox, *Gaussian 09, Revision D.01*, Gaussian Inc., Wallingford CT, 2013.
- [38] J. Anand, N. C. Singha and D. N. Sathyanarayana, *J. Mol. Struct.*, 1997, **412**, 221–229.
- [39] K. Röttger, R. Siewertsen and F. Temps, *Chem. Phys. Lett.*, 2012, **536**, 140–146.
- [40] T. Pancur, N. K. Schwalb, F. Renth and F. Temps, *Chem. Phys.*, 2005, **313**, 199–212.
- [41] N. K. Schwalb and F. Temps, *J. Phys. Chem. A*, 2009, **113**, 13113–13123.
- [42] M. Lorenc, M. Ziolk, R. Naskrecki, J. Karolczak, J. Kubicki and A. Maciejewski, *Appl. Phys. B: Lasers Opt.*, 2002, **74**, 19–27.
- [43] J. Bredenbeck and P. Hamm, *Rev. Sci. Instrum.*, 2003, **74**, 3188–3189.
- [44] R. A. Kaindl, M. Wurm, K. Reimann, P. Hamm, A. M. Weiner and M. Woerner, *J. Opt. Soc. Am. B*, 2000, **17**, 2086–2094.
- [45] P. Hamm, R. A. Kaindl and J. Stenger, *Opt. Lett.*, 2000, **25**, 1798–1800.
- [46] M. P. Grubbs, A. J. Orr-Ewing and M. N. R. Ashfold, *Rev. Sci. Instrum.*, 2014, **85**, 064104.

- [47] S. Kovalenko, R. Schanz, H. Hennig and N. Ernsting, *J. Chem. Phys.*, 2001, **115**, 3256–3273.
- [48] J. Bahrenburg, K. Röttger, R. Siewertsen, F. Renth and F. Temps, *Photochem. Photobiol. Sci.*, 2012, **11**, 1210–1219.
- [49] R. Siewertsen, F. Renth and F. Temps, *Phys. Chem. Chem. Phys.*, 2009, **11**, 5952–5961.
- [50] R. Siewertsen, F. Strübe, J. Mattay, F. Renth and F. Temps, *Phys. Chem. Chem. Phys.*, 2011, **13**, 3800–3808.

5.6 Supplementary Information

Crystal Structure Data

Crystal structure determination was carried out using an Imaging Plate Diffraction System (IPDS-2) from STOE & CIE. The structure was solved using SHELXS-97 and refined against F^2 using SHELXL-2014. All non-hydrogen atoms were refined anisotropic. The C–H and N–H H atoms were located in a different map but were positioned with idealized geometry and refined isotropically with $U_{\text{iso}}(\text{H}) = 1.2 U_{\text{eq}}(\text{C})$ using a riding model. An ORTEP plot of NPPCA with labeling and displacement ellipsoids is given in Fig. 5.7. Selected crystal data and details of the refinement can be found in Table 5.2, selected bond lengths and angles are given in Table 5.3 and hydrogen bonds in the crystal structure are presented in Table 5.4.

CCDC 1556507 contains the supplementary crystallographic data for this paper. These data can be obtained free of charge from the Cambridge Crystallographic Data Centre *via* http://www.ccdc.cam.ac.uk/data_request/cif.

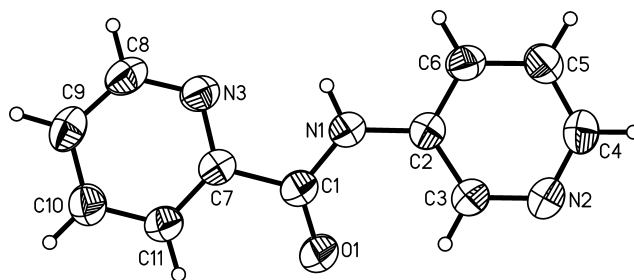


Figure 5.7: ORTEP plot of NPPCA with labeling and displacement ellipsoids drawn at the 50% probability level indicating a pre-orientation due to intramolecular N–H···N hydrogen bonding (C2–N1–C1–C7 : $178.8(2)^\circ$; dihedral angle between the 6-membered rings: $6.24(1)^\circ$; $\text{H1}\cdots\text{N3}$: 2.27 \AA , $\text{N1–H1}\cdots\text{N3}$: 110.4°).

Table 5.2: Crystal data and structure refinement parameters for NPPCA.

Empirical formula	C ₁₁ H ₉ N ₃ O
Formula weight	199.21 g/mol
Temperature	293(2) K
Wavelength	0.71073 Å
Crystal system	Monoclinic
Space group	P2 ₁ /n
Unit cell dimensions	a = 5.7147(4) Å, $\alpha = 90^\circ$ b = 8.3019(6) Å, $\beta = 94.120(5)^\circ$ c = 20.1261(14) Å, $\gamma = 90^\circ$
Volume	952.37(12) Å ³
Z	4
Density (calculated)	1.389 Mg/m ³
Absorption coefficient	0.094 mm ⁻¹
F(000)	416
Crystal size	0.3 x 0.2 x 0.2 mm ³
Theta range for data collection	2.029 to 26.002°
Index ranges	$-6 \leq h \leq 7$, $-10 \leq k \leq 10$, $-24 \leq l \leq 24$
Reflections collected	10738
Independent reflections	1875 [R(int) = 0.0639]
Observed reflections	1508
Completeness to theta = 25.242°	99.7%
Refinement method	Full-matrix least-squares on F ²
Data / restraints / parameters	1875 / 0 / 137
Goodness-of-fit on F ²	1.082
Final R indices [I > 2σ(I)]	R1 = 0.0456, wR2 = 0.0985
R indices (all data)	R1 = 0.0631, wR2 = 0.1058
Extinction coefficient	0.031(7)
Largest diff. peak and hole	0.130 and -0.135 e.Å ⁻³

Table 5.3: Bond lengths and angles for NPPCA.

bond	distance / Å	bond	angle / °
C(1)-O(1)	1.227(2)	O(1)-C(1)-N(1)	124.44(15)
C(1)-N(1)	1.356(2)	O(1)-C(1)-C(7)	121.08(15)
C(1)-C(7)	1.497(2)	N(1)-C(1)-C(7)	114.47(14)
N(1)-C(2)	1.407(2)	C(1)-N(1)-C(2)	127.91(14)
C(2)-C(6)	1.381(2)	C(6)-C(2)-C(3)	117.76(15)
C(2)-C(3)	1.385(2)	C(6)-C(2)-N(1)	118.52(14)
C(3)-N(2)	1.333(2)	C(3)-C(2)-N(1)	123.72(15)
N(2)-C(4)	1.328(2)	N(2)-C(3)-C(2)	123.36(17)
C(4)-C(5)	1.372(3)	C(4)-N(2)-C(3)	117.80(16)
C(5)-C(6)	1.378(2)	N(2)-C(4)-C(5)	122.99(16)
C(7)-N(3)	1.339(2)	C(4)-C(5)-C(6)	118.93(16)
C(7)-C(11)	1.373(2)	C(5)-C(6)-C(2)	119.12(16)
N(3)-C(8)	1.327(2)	N(3)-C(7)-C(11)	123.40(15)
C(8)-C(9)	1.378(3)	N(3)-C(7)-C(1)	117.75(14)
C(9)-C(10)	1.372(3)	N(3)-C(7)-C(1)	117.75(14)
C(10)-C(11)	1.375(2)	C(11)-C(7)-C(1)	118.83(14)
		C(8)-N(3)-C(7)	116.50(15)
		N(3)-C(8)-C(9)	124.16(16)
		C(10)-C(9)-C(8)	118.21(16)
		C(9)-C(10)-C(11)	118.87(17)
		C(7)-C(11)-C(10)	118.80(16)

Table 5.4: Hydrogen bond lengths and angles between acceptor A and donor D in the NPPCA crystal structure.

D-H...A	d(D-H) / Å	d(H...A) / Å	d(D...A)	∠(D-H-A) / °
N(1)-H(1)...N(3)	0.86	2.27	2.690(2)	110.4
C(3)-H(3)...O(1)	0.93	2.27	2.875(2)	122.1
C(6)-H(6)...O(1)#1	0.93	2.53	3.216(2)	130.7
C(9)-H(9)...N(2)#2	0.93	2.63	3.428(2)	144.5

Calculated Ground Structures for Tautomers I and IV

Examination of the ground-state PEHS at the MP2/cc-pVDZ level of theory yielded four local minima next to the global minimum of **I** (trans-carboxamide) at the indicated energies:

1. trans-iminol (**IV**): 0.54 eV,
2. cis-iminol (**V**): 0.80 eV,
3. trans-carboxamide rotamer (**VI**): 0.46 eV,
4. trans-iminol rotamer (**VII**): 1.15 eV.

The calculated structures for the two tautomeric forms **I** and **IV** at the RI-MP2/aug-cc-pVDZ level of theory are displayed in Fig. 5.8, the respective cartesian coordinates are listed in Tables 5.5–5.6. Structure **V** is solely accessible upon excitation of **IV**. Structures **VI** and **VII** are unfavoured due to the lack of intramolecular hydrogen bonds. Structures **II** and **III** are unstable on the ground-state PEHS. Thus, the relevant ground-state structures upon $\pi\pi^*$ excitation at $\lambda_{\text{pump}} = 266 \text{ nm}$ are **I** and **IV**.

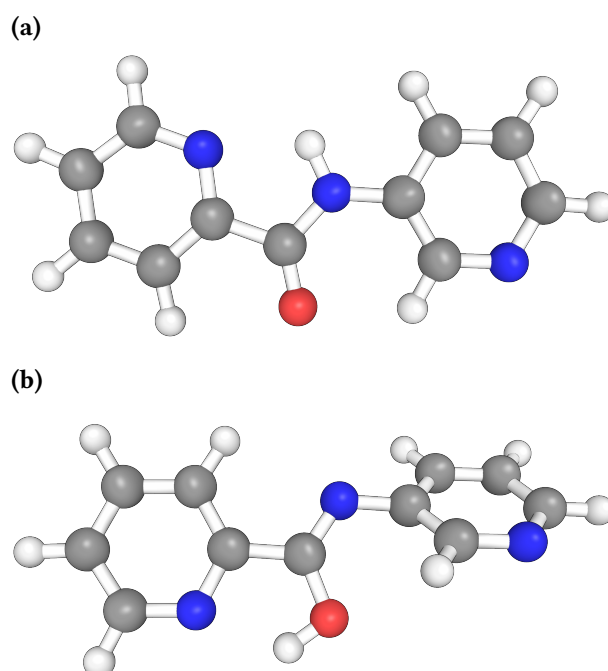


Figure 5.8: Calculated structures of NPPCA in (a) form **I** and (b) form **IV** at the RI-MP2/aug-cc-pVDZ level of theory.

Table 5.5: Cartesian coordinates for the optimized structure of **I** at the RI-MP2/aug-cc-pVDZ level of theory.

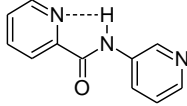
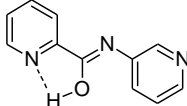
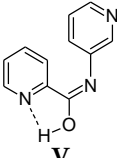
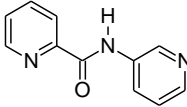
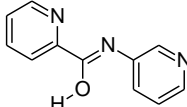
atom	X / Å	Y / Å	Z / Å
C	-3.2552498	1.4074652	-0.0001088
C	-4.3779865	0.5598759	0.0001076
C	-4.1763963	-0.8318847	0.0001231
C	-2.8610469	-1.3207577	-0.0000577
C	-1.8048061	-0.3916027	-0.0001076
N	-1.9844740	0.9522004	-0.0001861
H	-5.0269817	-1.5192319	0.0003015
H	-3.3772861	2.4950371	-0.0002739
H	-5.3843110	0.9866909	0.0003071
H	-2.6276162	-2.3874744	-0.0002697
C	-0.3826230	-0.9010829	-0.0000001
O	-0.1260407	-2.1111191	0.0001056
N	0.5362934	0.1167777	-0.0000197
H	0.1094561	1.0447313	0.0000321
C	2.6693224	1.2362960	-0.0000335
C	1.9377759	0.0289066	-0.0000588
C	2.6542971	-1.1939771	-0.0000650
C	4.6913422	-0.0830269	0.0000713
H	2.1209626	-2.1438636	-0.0001448
H	2.1433616	2.1972100	-0.0001167
H	5.7826823	-0.1659935	0.0001306
N	4.0058526	-1.2466018	0.0000138
C	4.0675888	1.1781375	0.0000661
H	4.6658832	2.0932877	0.0001837

Table 5.6: Cartesian coordinates for the optimized structure of **IV** at the RI-MP2/aug-cc-pVDZ level of theory.

atom	X / Å	Y / Å	Z / Å
C	-3.7409332	1.4198357	0.2731449
C	-4.5700137	0.3718899	-0.1706472
C	-3.9759963	-0.8170417	-0.6270241
C	-1.8511297	0.0139658	-0.2302467
H	-4.5883134	-1.6524992	-0.9790830
H	-4.1734214	2.3569520	0.6345498
H	-5.6585812	0.4702044	-0.1640342
C	-0.3911439	-0.2751950	-0.3012480
N	0.4629101	0.6312486	0.0478478
C	2.7101127	1.3437559	-0.5110000
C	1.8481500	0.3503541	-0.0044916
C	2.4289087	-0.8320616	0.5160451
C	4.5665938	-0.1139609	0.0181629
H	1.7911570	-1.6096873	0.9458570
H	2.2876391	2.2789586	-0.8899148
H	5.6392601	-0.3314880	0.0379583
N	3.7579978	-1.0656058	0.5394596
C	4.0907540	1.0981773	-0.5134762
H	4.7926920	1.8376262	-0.9093020
N	-2.6389003	-1.0019971	-0.6586392
C	-2.3505979	1.2417103	0.2440542
H	-1.6489803	2.0110279	0.5725796
O	-0.0809844	-1.5073746	-0.7725247
H	-0.9522796	-1.9190953	-0.9779275

Calculated Excitation Energies and UV Spectra

Table 5.7: Vertical excitation energies of **I**, **IV**, **V**, **VI** and **VII** at the CC2/ cc-pVDZ level of theory for MP2/cc-pVDZ optimized geometries relative to the global minimum of **I**.

 <p style="text-align: center;">I</p>				 <p style="text-align: center;">IV</p>				 <p style="text-align: center;">V</p>			
state	$\Delta E/eV$	f	$\mu/Debye$	state	$\Delta E/eV$	f	$\mu/Debye$	state	$\Delta E/eV$	f	$\mu/Debye$
S ₀	0.00	-	4.2	S ₀	0.54	-	5.2	S ₀	0.80	-	5.2
nπ*	4.44	0.001	1.6	ππ*	4.45	0.745	2.1	ππ*	3.98	0.041	5.6
ππ*	4.70	0.394	3.9	nπ*	4.62	0.002	2.4	ππ*	4.67	0.064	2.2
ππ*	4.93	0.056	3.2	ππ*	4.93	0.016	3.9	ππ*	4.84	0.124	2.8
ππ*	5.13	0.025	3.4	nπ*	4.93	0.001	0.2	nπ*	5.09	0.007	4.4
nπ*	5.24	0.006	3.3	ππ*	5.11	0.054	2.1	ππ*	5.10	0.021	2.4
nπ*	5.28	0.000	2.8	nπ*	5.26	0.003	3.1		5.23	0.001	2.7
ππ*	5.86	0.225	10.4	ππ*	5.82	0.023	5.3		5.28	0.010	3.3
ππ*	6.30	0.214	3.2	ππ*	6.18	0.108	1.8	ππ*	5.53	0.089	2.9
ππ*	6.35	0.006	2.7	ππ*	6.43	0.062	7.4		5.65	0.006	2.6
								ππ*	5.86	0.147	3.9
 <p style="text-align: center;">VI</p>				 <p style="text-align: center;">VII</p>							
state	$\Delta E/eV$	f	$\mu/Debye$	state	$\Delta E/eV$	f	$\mu/Debye$				
S ₀	0.46	-	3.9	S ₀	1.15	-	6.6				
S ₁	4.67	0.002	0.7	S ₁	4.46	0.316	4.0				
S ₂	4.89	0.112	4.7	S ₂	4.76	0.070	4.7				
S ₃	5.01	0.027	2.1	S ₃	4.90	0.040	1.9				
S ₄	5.13	0.134	1.2	S ₄	4.99	0.009	6.2				
S ₅	5.18	0.118	1.7	S ₅	5.04	0.007	4.0				
S ₆	5.23	0.123	3.2	S ₆	5.11	0.003	3.7				
S ₇	5.27	0.004	5.0								
S ₈	5.54	0.002	5.5								
S ₉	6.04	0.016	12.3								
S ₁₀	6.14	0.042	9.3								

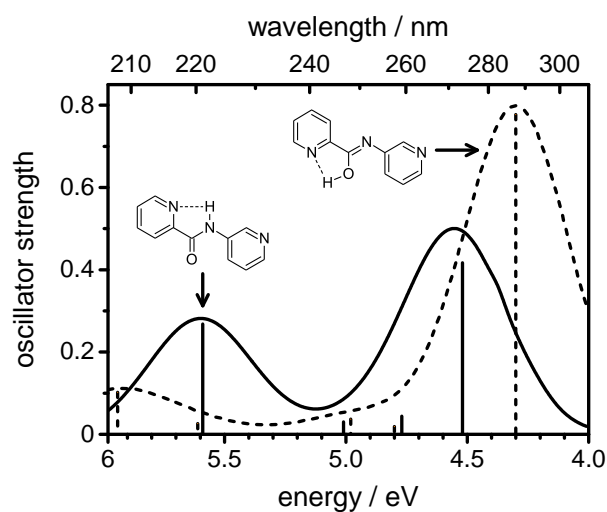


Figure 5.9: Calculated UV/VIS spectra of NPPCA in forms I (solid black line) and IV (dashed black line) at the CC2/aug-cc-pVDZ level of theory.

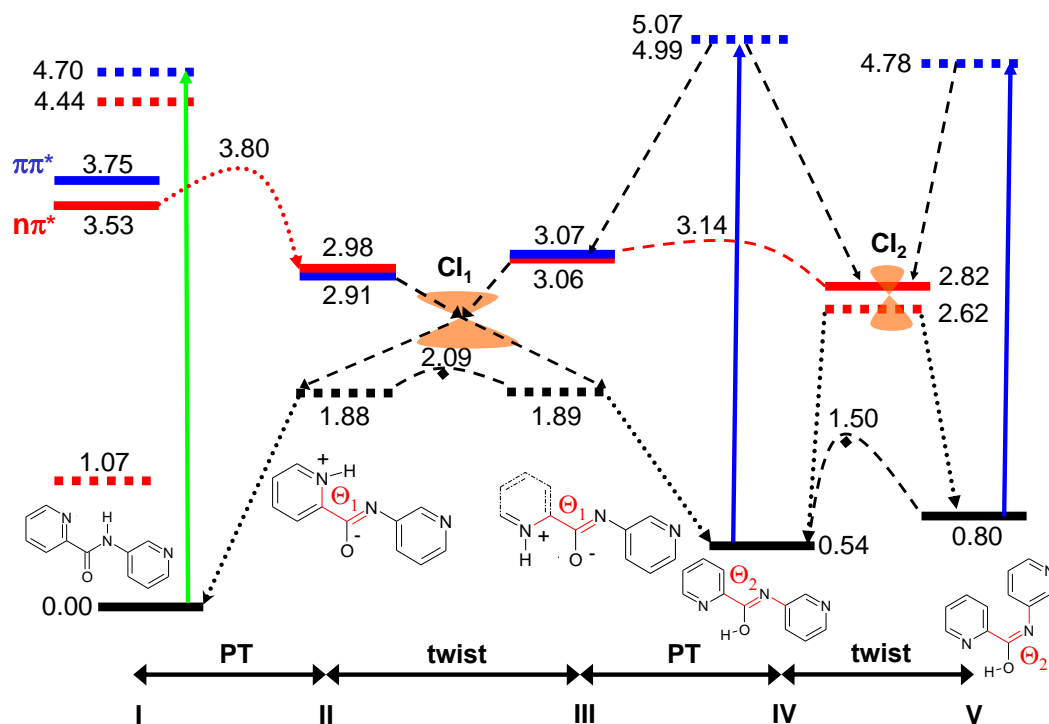


Figure 5.10: Computational results pertaining to the ground-state and excited-state potential energy surfaces for NPPCA.

Time Profiles and Decay Time Constants for NPPCA in Water

TEAS measurements for NPPCA in water, where all hydrogen bonding sites are occupied by H₂O molecules so that intramolecular proton transfer to **IV** is unlikely, showed fast transient absorption decays without long-lived 20 ps lifetime components. A comparison of measured transient absorption–time profiles in ACN and H₂O at two probe wavelengths is shown in Fig. 5.11.

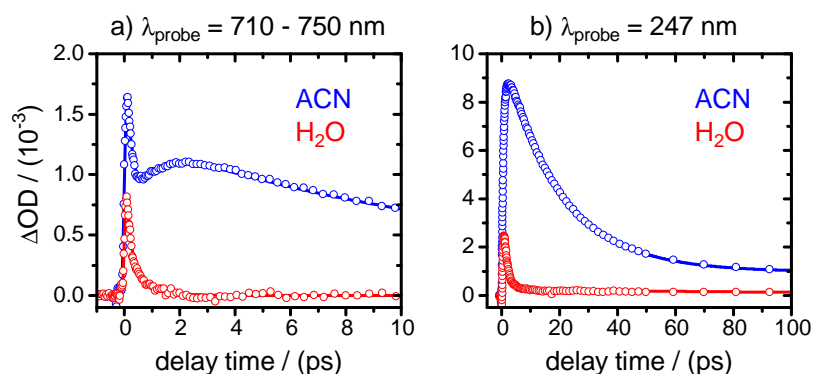


Figure 5.11: Comparison of the transient absorption-time profiles of NPPCA in ACN (blue) and H₂O (red) at (a) $\lambda_{\text{probe}} = 710\text{--}750$ nm and (b) $\lambda_{\text{probe}} = 247$ nm after photoexcitation at $\lambda_{\text{pump}} = 264$ nm. The measurements in ACN and H₂O were made directly one after the other, so that a direct comparison of the data is possible.

Figure 5.12 shows a set of absorption and fluorescence decay time profiles for NPPCA in H₂O after integration over the distinct transient absorption bands in the spectro-temporal absorption map of Fig. 5.3 (d). A simultaneous least-squares fit to the absorption data yielded the following three time constant values:

$$\tau_1 = 0.08 \pm 0.01 \text{ ps,}$$

$$\tau_2 = 0.30 \pm 0.02 \text{ ps,}$$

$$\tau_3 = 1.32 \pm 0.05 \text{ ps.}$$

The fluorescence decay time profiles were found to be described by

$$\tau_{1,\text{TFL}} = 0.15 \pm 0.02 \text{ ps,}$$

$$\tau_{2,\text{TFL}} = 0.46 \pm 0.05 \text{ ps.}$$

The results were confirmed by singular value decomposition (SVD) analysis. The obtained decay-associated spectra and SVD time profiles are displayed in Fig. 5.13 (H₂O) and Fig. 5.14 (ACN).

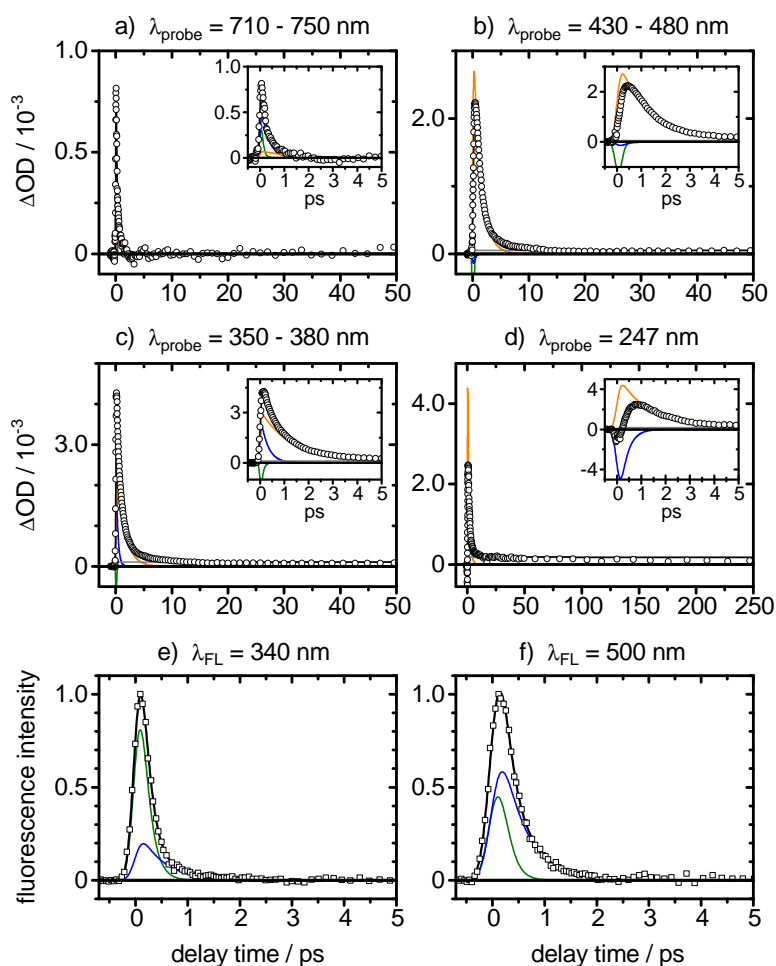


Figure 5.12: (a–d) Transient absorption–time profiles of NPPCA in H₂O after excitation at $\lambda_{\text{pump}} = 264$ nm in four selected probe windows ((a) 710–750 nm, (b) 430–480 nm, (c) 350–380 nm, (d) 247 nm). (e–f) Fluorescence–time profiles of NPPCA in H₂O after excitation at $\lambda_{\text{pump}} = 264$ nm at two emission wavelengths ((e) $\lambda_{\text{FL}} = 340$ nm, (f) $\lambda_{\text{FL}} = 500$ nm).

SVD Analysis of the Transient Absorption Matrix for NPPCA in Water

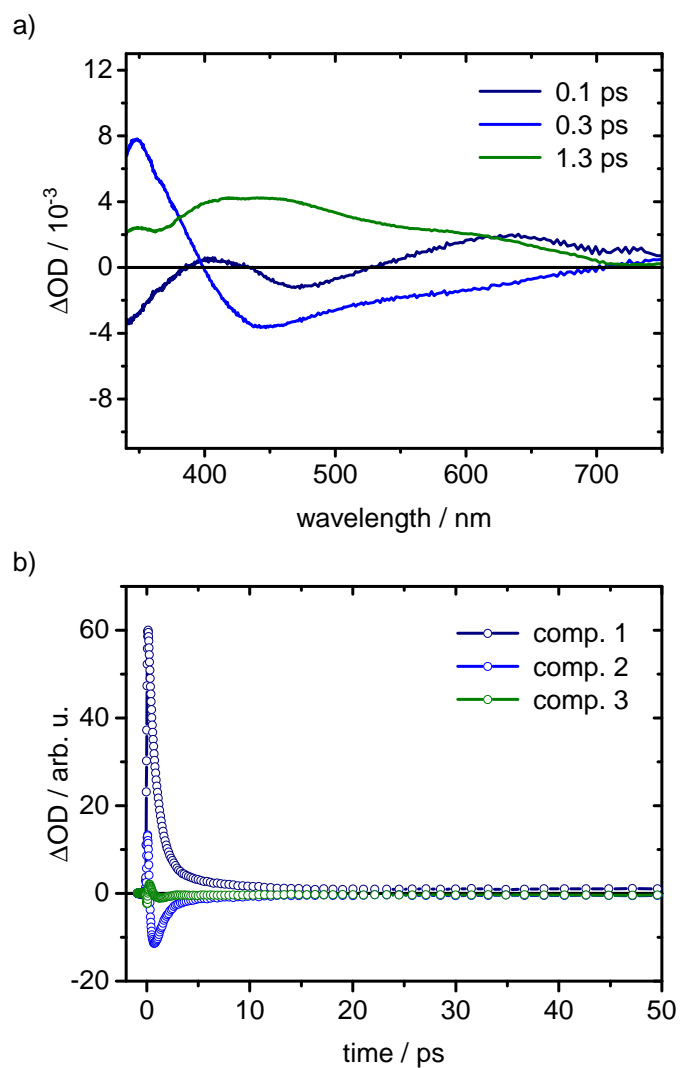


Figure 5.13: (a) Decay-associated spectra and (b) SVD time profiles for NPPCA in H₂O.

SVD Analysis of the Transient Absorption Matrix for NPPCA in ACN

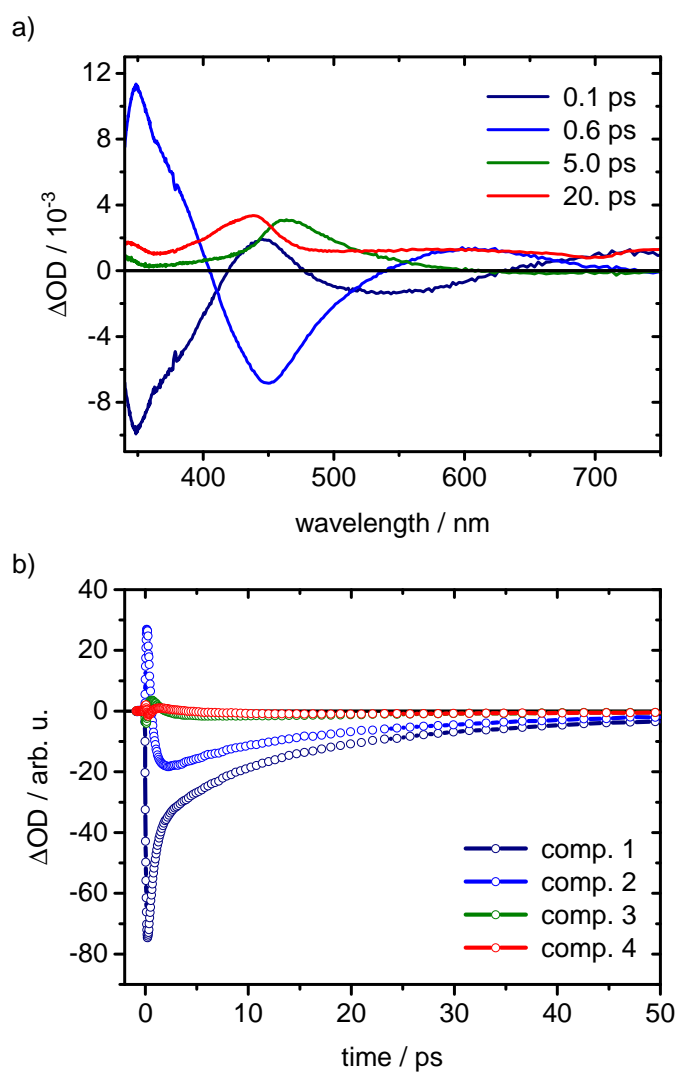


Figure 5.14: (a) Decay-associated spectra and (b) SVD time profiles for NPPCA in ACN.

Comparison of Experimental and Calculated Vibrational Spectra

FTIR spectra were recorded at a nominal resolution of 1 cm^{-1} on a Bruker IFS66v spectrometer equipped with a with liquid nitrogen-cooled MCT detector. The sample compartment was continuously purged with dry air containing $< 1\text{ ppm}$ water vapour and $< 1\text{ ppm}$ CO_2 . The CaF_2 cell had an optical path length of $100\text{ }\mu\text{m}$ to allow for measurements from $600\text{--}5000\text{ cm}^{-1}$.

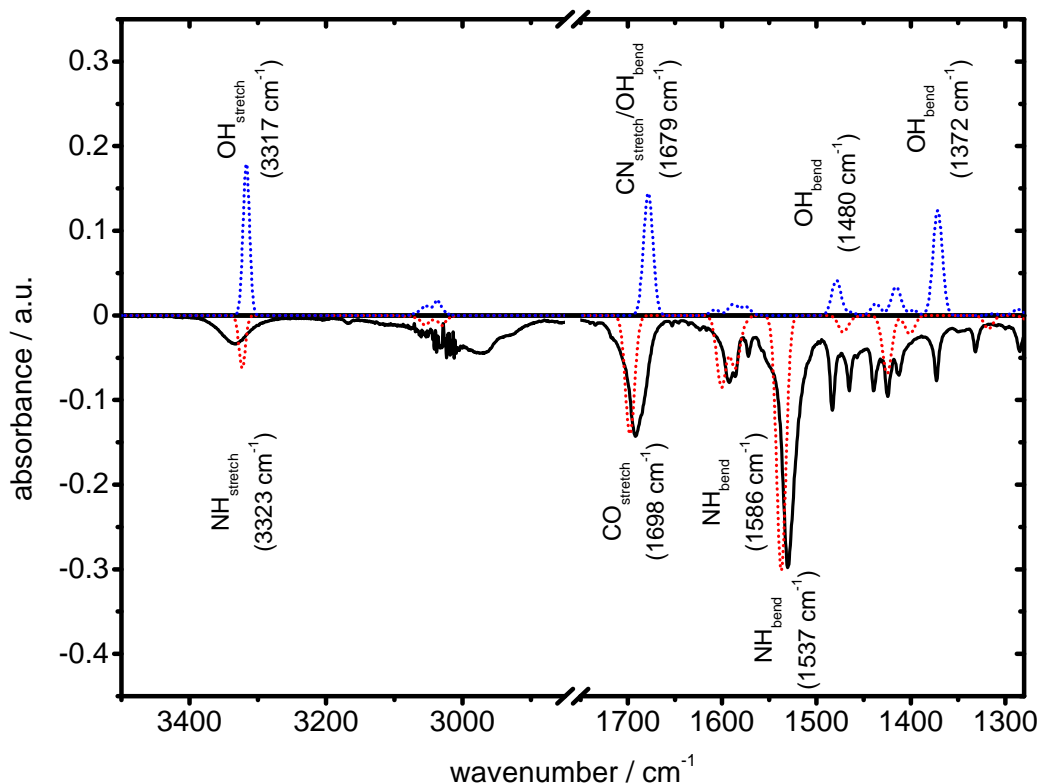


Figure 5.15: FTIR spectrum of NPPCA (I) in CHCl_3 (negative solid black line) compared with calculated RI-MP2/aug-cc-pVDZ vibrational spectra for I (negative dotted red line) and IV (positive dotted blue line) using scaling factors of 0.985 below 1800 cm^{-1} and 0.945 above 1800 cm^{-1} . The respective vibrational modes are illustrated in Fig. 5.16.

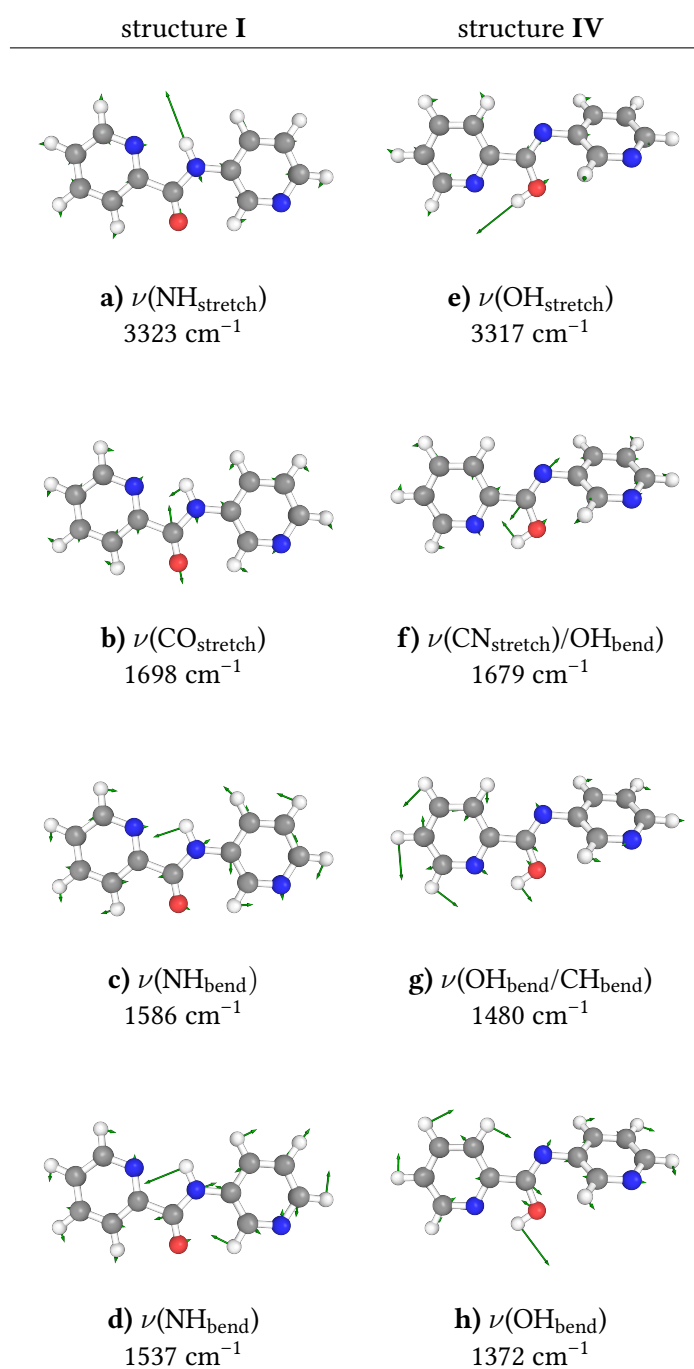


Figure 5.16: Vibrational marker modes of the electronic ground state species **I** and **IV** calculated at the RI-MP2/aug-cc-pVDZ level of theory. Wavenumbers are given after applying scaling factors of 0.985 below 1800 cm^{-1} and 0.945 above 1800 cm^{-1} .

Comparison of a late-time TVA Spectrum to Calculated Vibrational Spectra for Structures I and IV

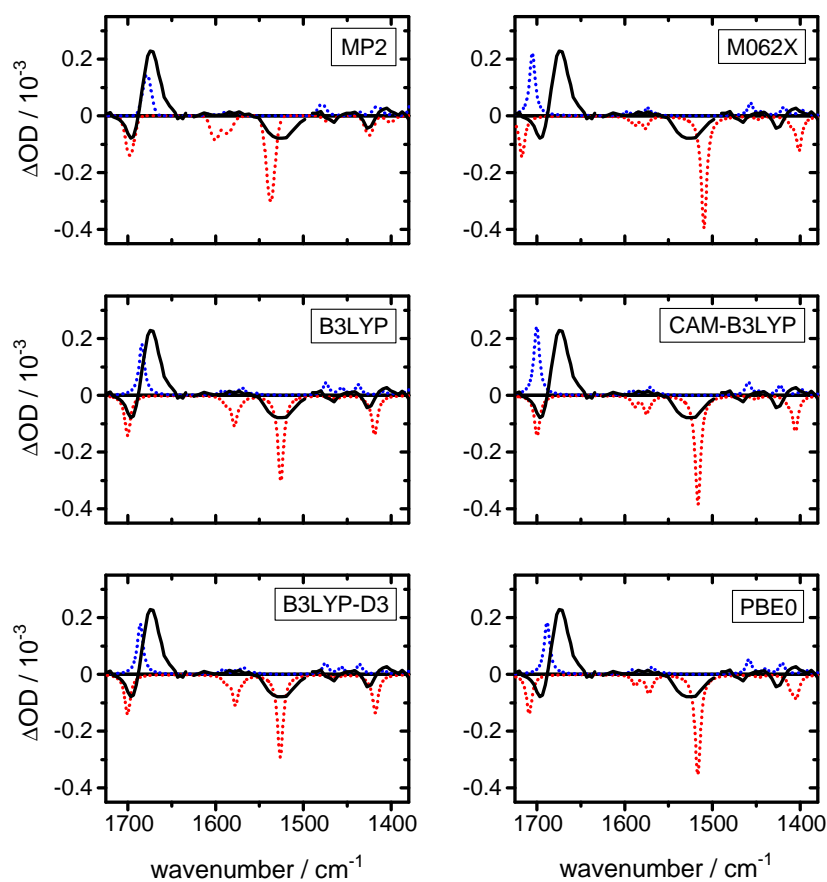


Figure 5.17: Comparison of the measured TVA spectrum at $\Delta t = 850$ ps (black solid lines) with calculations for **I** shown in the negative direction (red dotted lines) and for **IV** shown in the positive direction (blue dotted lines). The calculations were performed at the RI-MP2/aug-cc-pVDZ, B3LYP/6-311+G**, B3LYP-D3/6-311+G**, M062X/6-311+G**, CAM-B3LYP/6-311+G** and PBE0/6-311+G** levels of theory using scaling factors of 0.985, 0.975, 0.975, 0.95, 0.95 and 0.955, respectively.

5.7 Additional Information

In order to further improve bi-stability, chemical modification of NPPCA could be applied in future studies. For instance, as illustrated in Fig. 5.18, the reaction pathway established for NPPCA could be extended by an additional stabilizing H-bonded species **V** in the ground state. Preliminary vibrational mode calculations at the RI-MP2/aug-cc-pVDZ level of theory for the ground-state structures **I**, **IV** and **V** shown in Fig. 5.19 hint at good chances to distinguish between the transient conformations and to identify the respective species by their characteristic vibrational marker bands *via* TVAS measurements.

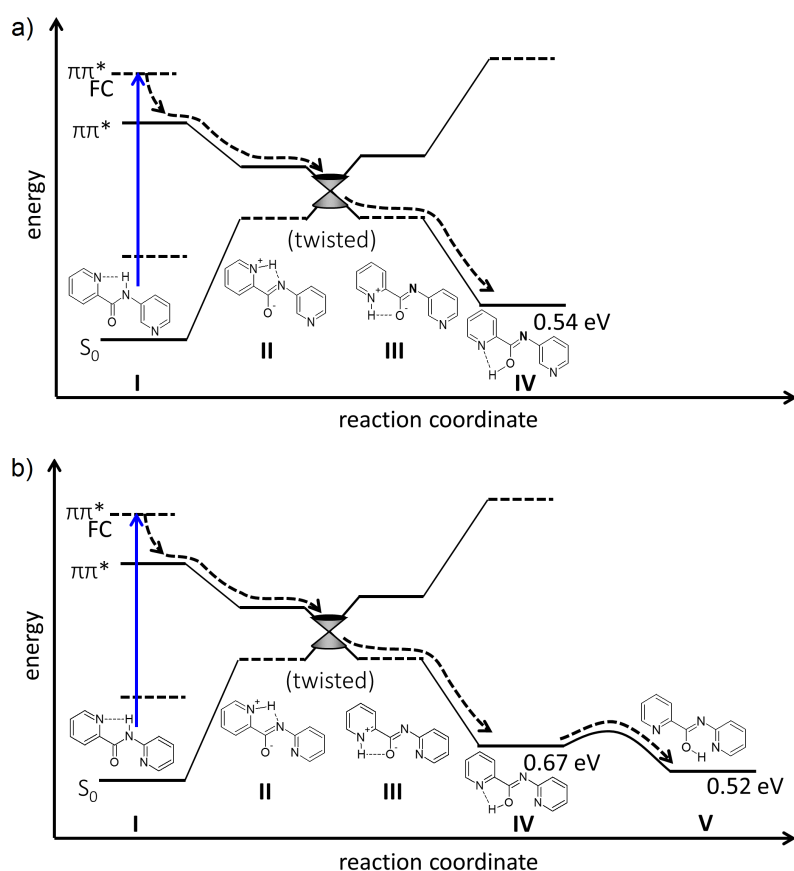


Figure 5.18: Schematic reaction pathways (a) of NPPCA from forms **I** to **IV** and (b) for the next generation ESIPT switch NPPCA2 with an additional ground-state species **V** in order to stabilize the photoproduct.

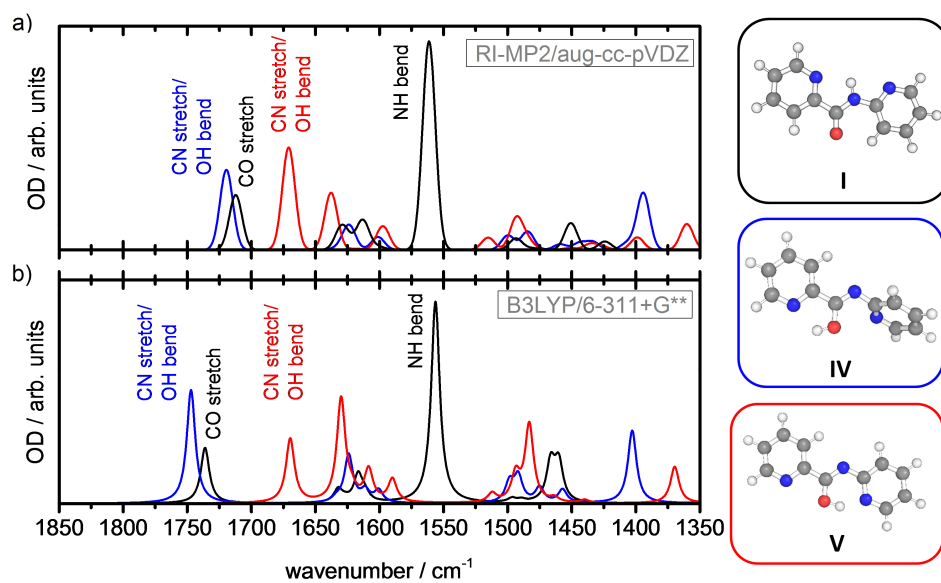


Figure 5.19: Calculated (unscaled) vibrational spectra for the stable ground-state species I (black), IV (blue) and V (red) for the next generation ESIPT switch NPPCA2 at the (a) RI-MP2/aug-cc-pVDZ and (b) B3LYP/6-311+G** levels of theory.

Is Excited-State Proton Transfer Involved in the Electronic Deactivation of 2-Acetylpyrrole?

HENDRIK BÖHNKE, CARSTEN SCHRÖDER, SEBASTIAN SCHATZ, SEBASTIAN MEGOW, DENNIS BANK, TIM RAEKER, BERND HARTKE AND FRIEDRICH TEMPS*

Institute of Physical Chemistry, Christian-Albrechts-University Kiel, Olshausenstr. 40, 24098 Kiel, Germany.

* To whom correspondence should be addressed. E-mail: temps@phc.uni-kiel.de.

Manuscript in preparation.

OWN CONTRIBUTIONS TO THIS MANUSCRIPT:

- Steady-state UV/vis and FTIR spectroscopy,
- Quantum chemical calculations for ground- and excited-state species,
- Transient femtosecond vibrational absorption spectroscopy,
- Analysis of experimental TVA data,
- Writing of the manuscript.

Abstract

The photo-induced electronic relaxation and reaction dynamics of 2-acetylpyrrole (2AcPy) and its N-methyl analogue 2-acetyl-1-methylpyrrole (Me2AcPy) have been investigated by a combination of femtosecond time-resolved emission and absorption techniques following $S_2(\pi\pi^*)$ excitation. In acetonitrile (ACN) solution, featuring monomeric 2AcPy exclusively, the excited-state population relaxes from the initially populated $^1\pi\pi^*$ state towards a lower-lying $S_1(n\pi^*)$ state within $\tau \approx 4$ ps. This long-lived $^1n\pi^*$ state survives on the two nanosecond scope of our time-resolved experiment and is believed to ultimately drive the majority of the excited-state population towards a triplet state. Comparison of the transient signatures of 2AcPy with Me2AcPy revealed virtually the same deactivation pathways. Slight indications for an excited-state intramolecular proton transfer (ESIPT) process in the 2AcPy $S_1(n\pi^*)$ state as a pathway of minor significance have been found as well. Additional spectro-temporal signatures in cyclohexane solution have been attributed to kinetics associated with 2AcPy homo-dimers. The experimental findings were corroborated by *ab initio* and *semi*-empirical quantum chemical calculations.

6.1 Introduction

Many biologically relevant molecules like chlorophylls, bacteriochlorophylls and heme consist of condensed substituted pyrrole sub-units. Due to its small size, extensive computational and experimental studies have been reported on the photo-physics of pyrrole and methyl-substituted derivatives.^[1–9] However, little is known about the photo-dynamics of carbonyl-substituted pyrroles. While many aliphatic ketones are known to undergo Norrish type I or II reactions,^[10–16] keto-substituted aromatic systems feature an altered photo-physical behavior: For aromatic and N-heterocyclic aromatic carbonyl compounds a low-lying $n\pi^*$ state has been reported to mediate an efficient intersystem crossing (ISC) towards the triplet state.^[17–19] For 2-acetylpyrrole (2AcPy, Fig. 6.1 (a)) and its N-methyl analogue 2-acetyl-1-methylpyrrole (Me2AcPy, Fig. 6.1 (b)), for example, nanosecond laser flash photolysis experiments found significant quantum yields for intersystem crossing towards a triplet state upon direct population of the $S_1(n\pi^*)$ state.^[20]

The conformational equilibria of 2AcPy and Me2AcPy are dependent on solvent polarity and have been discussed controversially by different authors.^[20–24] For nonpolar solvents, combined infrared and NMR spectroscopy results supported by theoretical calculations^[21] recently found hydrogen-bonded homo-dimeric structures of 2AcPy, which are also known to exist in the solid phase.^[23,24] However, monomeric structures are expected to prevail in polar solvents.^[21] For monomeric 2AcPy and Me2AcPy in acetonitrile solution, intrinsic triplet state lifetimes of 7.7 μ s and 5.9 μ s, respectively, have been reported.^[20]

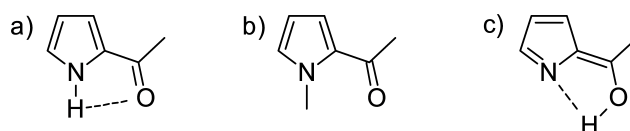


Figure 6.1: Chemical structures of (a) 2-acetylpyrrole (2AcPy), (b) 2-acetyl-1-methylpyrrole (Me2AcPy) and (c) 2-(1-hydroxy-ethyleniden)-pyrrole (2HEP), the H-transferred product of 2AcPy.

Moreover, an excited-state intramolecular proton transfer (ESIPT) mechanism within the $n\pi^*$ state has recently been proposed for 2AcPy.^[22] The H-transferred product structure is shown in Fig. 6.1 (c).

Here, we report on the relaxation dynamics of 2AcPy and Me2AcPy in acetonitrile solution upon $S_2(\pi\pi^*)$ excitation monitored by a combination of femtosecond time-resolved emission and absorption techniques to elucidate the early events of electronic deactivation prior to intersystem crossing towards the triplet manifold. Experimental results are supported by quantum chemical *ab initio* calculations at the RI-SCS-MP2/def2-TZVPP and RI-SCS-CC2/def2-TZVPP levels of theory as well as *semi*-empirical calculations employing a floating-occupation configuration interaction (FOCI) setup, which were carried out at Kiel University by the Hartke group. The deactivation dynamics of monomeric 2AcPy are compared to the kinetic processes observed for dimeric 2AcPy in cyclohexane solution. Note that the results reported in this Chapter are of preliminary nature.

6.2 Methods

2-Acetylpyrrole (2AcPy) and 2-acetyl-1-methylpyrrole (Me2AcPy) were purchased from Sigma Aldrich and used without further purification. For IR experiments, deuterated dry solvents were bought from Deutero. Dry solvents of spectroscopic grade used for absorption and fluorescence experiments were purchased from Merck. Great care was taken to keep the samples from ambient humidity throughout sample preparation and measurements by working strictly under dry atmospheres.

IR spectra were recorded on an IFS 66v FTIR spectrometer (Bruker) using a liquid nitrogen-cooled MCT detector. For continuous flushing of the sample compartment, compressed dry air (< 1 ppm H₂O, < 1 ppm CO₂) was taken from a purge gas generator (PG 85 L, cmc-Instruments). A CaF₂ cell with a path length of 100 μm was used for measurements over a spectral range from 5000–600 cm^{-1} with a spectral resolution of 1 cm^{-1} . UV/vis spectra were obtained from a UV-2401PC spectrophotometer (Shimadzu) using a quartz cell with a path length of 1 mm (Hellma Analytics). Fluorescence spectra were recorded on a FluoroMax-4 spectrofluorometer (Horiba Jobin Yvon) using quartz cells of 1 cm path length (Hellma Analytics).

Time-Resolved Fluorescence Spectroscopy

The employed femtosecond time-resolved broadband fluorescence (Kerr gating) setup^[25] was supplied with 710 μJ per pulse from a Ti:Sa laser (Libra HE, Coherent) with pulse lengths of 90 fs at 800 nm. 50% of the energy were delayed *via* a translation stage (M-521.DG, Physik Instrumente) equipped with a retroreflector (OW-25-1PS, LaserComponents) and focused into a Kerr medium after attenuation to 120 μJ per pulse by a neutral density filter. Subsequently, the polarization plane was rotated by 45° with respect to the pump pulses by a $\lambda/2$ wave plate. The other half of the laser fundamental was used to deliver excitation pulses at a center wavelength of 266 nm with a bandwidth of 5 nm at 250 nJ per pulse *via* a home-built non-collinear optical parametric amplifier (NOPA) with subsequent temporal compression and frequency doubling (SHG). The excitation pulses were focused into a home-built flow cell equipped with quartz windows ($d = 0.2$ mm, diameter 15 mm, Korth Kristalle) and a PTFE spacer of 1 mm thickness. A gear pump equipped with organic solvent resistant tubing (Reglo-Z analog, Ismatec) was employed to flow the sample solution continuously through the cell. Fluorescence was collimated and focused by Cassegrainian optics (reflective microscope objective, $f = 13.0$ mm, model 50105-02) into the Kerr medium after passing a polarizer (WP25L-UB, Thorlabs) which was set to the magic angle condition with respect to the excitation pulses. Carbon tetrachloride served as Kerr medium in a second home-built flow cell. A gear pump (Reglo-Z analog, Ismatec) equipped with an organic solvent resistant pump head (Z-186 with PSS gears, Ismatec) and PTFE tubing was used to flow the sample solution of 1.4 mM concentration continuously through the cell. After passing the Kerr medium and a second polarizer orthogonal to the first one, fluorescence was re-collimated by a Cassegrainian and finally sent into a grating spectrograph (2150i, Acton) connected to an iCCD camera (PI-MAX, Princeton Instruments).

Time-Resolved Vibrational Absorption Spectroscopy

The time-resolved transient vibrational absorption setup (TVAS) described in this work (Chapter 2) was supplied by 900 μJ per pulse from the same Ti:Sa amplifier. 300 μJ per pulse were used to generate excitation pulses of 1.3 μJ per pulse at 266 nm using a commercially available kit for third harmonic generation (FKE-800-100, EksmaOptics) and set to the magic angle condition with respect to the probe pulses. The excitation pulses were delayed by a translation stage (M-521.DG, Physik Instrumente) equipped with a retroreflector (protected Al, Edmund Optics) and passed an optical chopper (MC2000, Thorlabs) equipped with a 10 shot blade (MC1F10, Thorlabs) that blocked every second pulse for sample-background pairs. The remaining 600 μJ per pulse of the laser fundamental were used to obtain tunable mid-IR probe pulses from $4000\text{--}800\text{ cm}^{-1}$ with a bandwidth of $\sim 200\text{ cm}^{-1}$ and an energy of ~ 150 nJ per pulse. Tunable mid-IR pulses were obtained by a home-built two-stage

BBO-OPA (BBO, $\theta = 27^\circ$, $\phi = 30^\circ$, 6 mm x 6 mm x 4 mm, GWU-Lasertechnik) which was pumped with the laser fundamental of 800 nm. The idler (1.7–2.4 μm) and amplified signal (1.2–1.5 μm) near-IR pulses were mixed in a difference frequency generation realized in an AgGaS₂ crystal (AGS, $\theta = 39^\circ$, $\phi = 45^\circ$, 5 mm x 5 mm x 1.5 mm, TOPAG Lasertechnik) to obtain the desired mid-IR pulses. The UV excitation pulses and mid-IR probe pulses were focused into a home-built sample flow cell inspired by Bredenbeck *et al.*^[26] equipped with O-rings (Chemraz, Greene, Tweed & Co. GmbH), a PTFE spacer ($d = 0.5$ mm) and CaF₂ windows ($d = 2$ mm, 25 mm diameter, Korth Kristalle). A gear pump equipped with organic solvent resistant tubes (Reglo-Z analog, Ismatec) was employed to flow the sample solution of 2.7 mM concentration continuously through the cell. Finally, the mid-IR probe pulses were directed through a computer-controlled grating spectrometer (iHR320, Horiba Yvon Jobin) onto a liquid nitrogen cooled 32 pixel MCT detector, which was read out by a boxcar-type integrator system (FPAS-6416, Infrared Systems Development).

Time-Resolved Electronic Absorption Spectroscopy

The employed experiment for time-resolved transient electronic absorption spectroscopy (TEAS)^[27–30] was supplied by 500 μJ per pulse of the output of a Ti:Sa laser (Clark-MXR CPA 2001) delivering pulses at 775 nm with 150 fs pulse duration. Excitation pulses were obtained in a home-built non-collinear optical parametric amplifier (NOPA) followed by temporal compression and second harmonic generation, resulting in pulses at 266 nm with a bandwidth of 4 nm. For generation of broadband probe pulses, ~ 70 μJ per pulse of the laser fundamental passed a delay stage (M-531.DG, Physik Instrumente) equipped with a retroreflector (CVI Melles Griot) prior to attenuation to ~ 2 μJ per pulse by an absorptive neutral density filter and a combination of a $\lambda/2$ wave plate and a polarizer. The pulses were focused into a CaF₂ plate ($d = 2$ mm, Korth Kristalle), which was rasterized vertically and horizontally to generate the broadband probe pulses. The pulses were split into probe and reference by using the front and rear reflections of a planar glass plate. The excitation pulses were set to magic angle polarization with respect to the probe pulses using a $\lambda/2$ wave plate. An optical chopper (MC2000, Thorlabs) equipped with a 10 shot blade (MC1F10, Thorlabs) was used to cut out every second laser pulse, thus enabling the measurement of background signals without excitation. The transmitted broadband pulses were dispersed in a prism spectrograph and detected by two full-frame transfer back-thinned CCD cameras (Entwicklungsbüro Stresing, Berlin). The sample solutions of 1.4 mM concentration were pumped through a home-built flow cell which was equipped with two quartz windows ($d = 0.2$ mm, diameter 15 mm, Korth Kristalle) and a PTFE spacer of 100 μm thickness. A gear pump (Reglo-Z analog, Ismatec) equipped with an organic solvent resistant pumphead (Z-186 with PPS gears, Ismatech) and PTFE tubes was employed to flow the sample solution continuously through the cell.

Computational Methods

Ground-state equilibrium structures and vibrational frequencies of 2AcPy and Me2AcPy were computed using the second-order Møller-Plesset perturbation theory (MP2) under the resolution of the identity (RI) approximation and the spin-component scaling (SCS) modification (RI-SCS-MP2)^[31–35] with a def2-TZVPP basis set.^[36] Vertical excitation energies (VEEs), excited-state equilibrium structures and excited-state vibrational frequencies of 2AcPy and Me2AcPy were calculated using the second-order approximate coupled-cluster method in the same variant (RI-SCS-CC2).^[37–42] All computed vibrational spectra were scaled using a factor of 0.965 throughout. Line spectra were broadened with Gaussian functions of 5 cm⁻¹ standard deviation. These theoretical results were obtained employing the TurboMole 7.0 program package^[43].

Additionally, a *semi*-empirical configuration-interaction (CI) setup to scan multiple potential energy surfaces (PES) with respect to the CO bond length was chosen. Generally, as *semi*-empirical methods alone are not suitable for calculations of electronically excited states, they need to be coupled to a method which yields such information. In this work, this is achieved by the floating-occupation interaction (FOCI)^[44] ansatz which generates excited Slater determinants from the *semi*-empirical reference wavefunction. This procedure is implemented in a development version of MOPAC by Granucci and Persico.^[45] The parameters for the calculation, *i.e.* the Hamiltonian and CI space size, were taken from a scan of all possible combinations comparing the results against CASSCF reference data^[22] as shown in Table 1 (*cf.* SI). Best results were obtained from an AM1 Hamiltonian^[46] and an active space of 12 electrons in 12 orbitals with 103 Slater determinants, corresponding to all single and symmetric double excitations from the reference wavefunction. The ability of FOCI-AM1 to be in agreement with higher level calculations and experiment was previously shown for azobenzene-based compounds.^[47,48] The performed scan along the CO bond is fully relaxed in all other degrees of freedom and followed the ground state gradient.

6.3 Results and Discussion

Computational Results

Calculated vertical excitation energies, transition characters and oscillator strengths for 2AcPy, Me2AcPy and 2HEP are listed in Table 6.1 and pictured in Fig. 6.2 alongside with the experimental UV/vis absorption spectra of 2AcPy and Me2AcPy in ACN solution. While the calculated vertical excitation energies *in vacuo* naturally differ from those obtained in the liquid phase, the energetic order presented in Fig. 6.2 reflects the features in the absorption spectra of 2AcPy and Me2AcPy in accordance with calculated and experimental values reported elsewhere.^[20,22] Thus, excitation at 266 nm predominantly populates the optically bright $S_2(\pi\pi^*)$ state in both 2AcPy and Me2AcPy. Following excitation to the $^1\pi\pi^*$ state, the excited-state population is expected to evolve towards the adiabatically lower $^1n\pi^*$ state *via* internal conversion. As can be seen from the calculated molecular orbitals involved in the $n\pi^*$ excitation in Fig. 6.2 (c), the $S_1(n\pi^*)$ state is characterized by a node along the carbonyl group, indicative for a substantial weakening of the CO band character in the excited state.

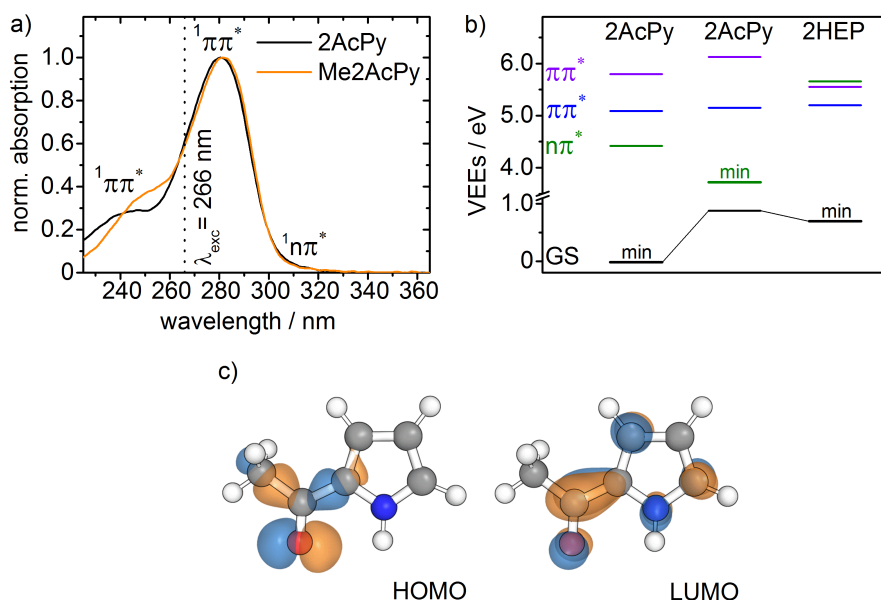
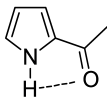
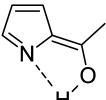
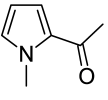


Figure 6.2: (a) Steady-state UV/vis absorption spectra of 2AcPy (black) and Me2AcPy (orange) in ACN solution. The experimental features are assigned to electronic transitions of $^1n\pi^*$ and $^1\pi\pi^*$ character based on computed vertical excitation energies (VEEs). (b) VEEs seen from the ground-state equilibrium structure of 2AcPy. Relative potential energies are given for the $^1n\pi^*$ -state minimum structure and back at the 2HEP ground-state geometry after ESIPT. (c) Molecular orbitals involved in the $S_1(n\pi^*)$ excited-state configuration of 2AcPy.

Table 6.1: Vertical excitation energies (VEEs) of 2AcPy, 2HEP and Me2AcPy at the RI-SCS-CC2/def2-TZVPP level of theory for RI-SCS-MP2/def2-TZVPP optimized geometries. The values for the ESIPT product 2HEP refer to potential energies relative to the global minimum of 2AcPy.

	 2AcPy			 2HEP			 Me2AcPy		
	state	VEE/eV	<i>f</i>	state	VEE/eV	<i>f</i>	state	VEE/eV	<i>f</i>
GS min.	S ₀	0.00	-	S ₀	0.70	-	S ₀	0.00	-
	¹ nπ*	4.42	0.000213	¹ ππ*	5.20	0.281652	¹ nπ*	4.45	0.000224
	¹ ππ*	5.09	0.297875	¹ ππ*	5.55	0.217753	¹ ππ*	5.27	0.258357
	ππ*	5.80	0.094423	¹ nπ*	5.66	0.001805	ππ*	5.94	0.129407
nπ* min.	S ₀	0.88							
	¹ nπ*	3.72							
	¹ ππ*	5.15							
	¹ ππ*	6.13							

Potential energy surface (PES) scans along the CO bond length employing the *semi*-empirical FOCI method are shown in Fig. 6.3 for 2AcPy and Me2AcPy. These calculations hint at a conical intersection (CI) connecting the S₂ and S₁ excited states in close proximity to the ground-state equilibrium CO distance. Thus, an ultrafast relaxation from the originally excited ¹ππ* state to the lower-lying ¹nπ* state is proposed by these calculations. Once relaxed to the ¹nπ* state, the wavepacket is expected to be trapped and believed to only rarely overcome the considerable activation barrier towards lower-lying triplet states also reported elsewhere.^[16] Hence, the ¹nπ* state is expected to survive on the nanosecond timescale of our time-resolved experiments. The proposed relaxation pathway is predicted to be virtually the same for 2AcPy and Me2AcPy.

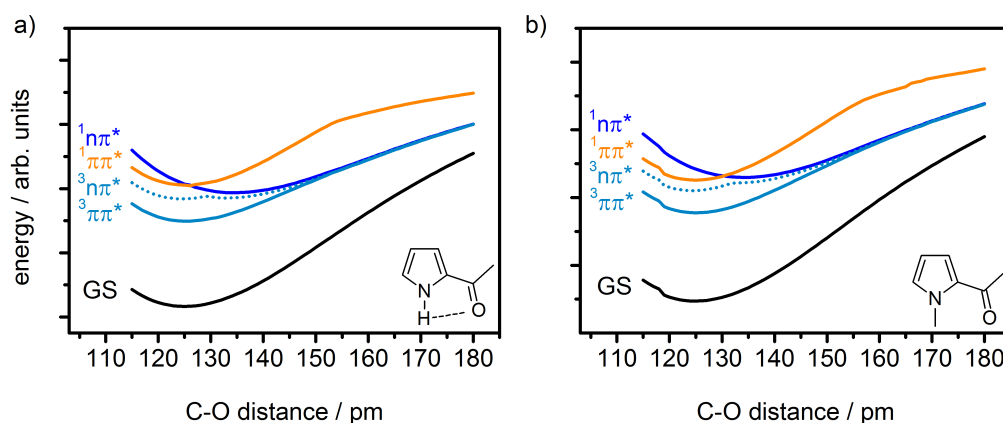


Figure 6.3: Potential energy surface scan along the CO bond length as a crucial parameter on the ¹nπ* dynamics for (a) 2AcPy and (b) Me2AcPy employing the semi-empirical FOCI setup.

Calculated vibrational spectra at the RI-SCS-MP2/def2-TZVPP and RI-SCS-CC2/def2-TZVPP levels of theory for the electronic ground state and the excited $^1n\pi^*$ state, respectively, are presented in Fig. 6.4. While the region of ring vibrations around $1500\text{--}1300\text{ cm}^{-1}$ appears dense in all electronic states and is thus expected to be challenging for TVA data analysis, the CO stretching region appears rather lucid around 1600 cm^{-1} . As highlighted in Fig. 6.4, the proposed ESIPT photoproduct of 2AcPy (2HEP) is expected to feature a pronounced vibrational band of CC stretch character in very close proximity to the CO stretching band of 2AcPy at 1650 cm^{-1} , shifted by only 4 cm^{-1} according to our calculations.

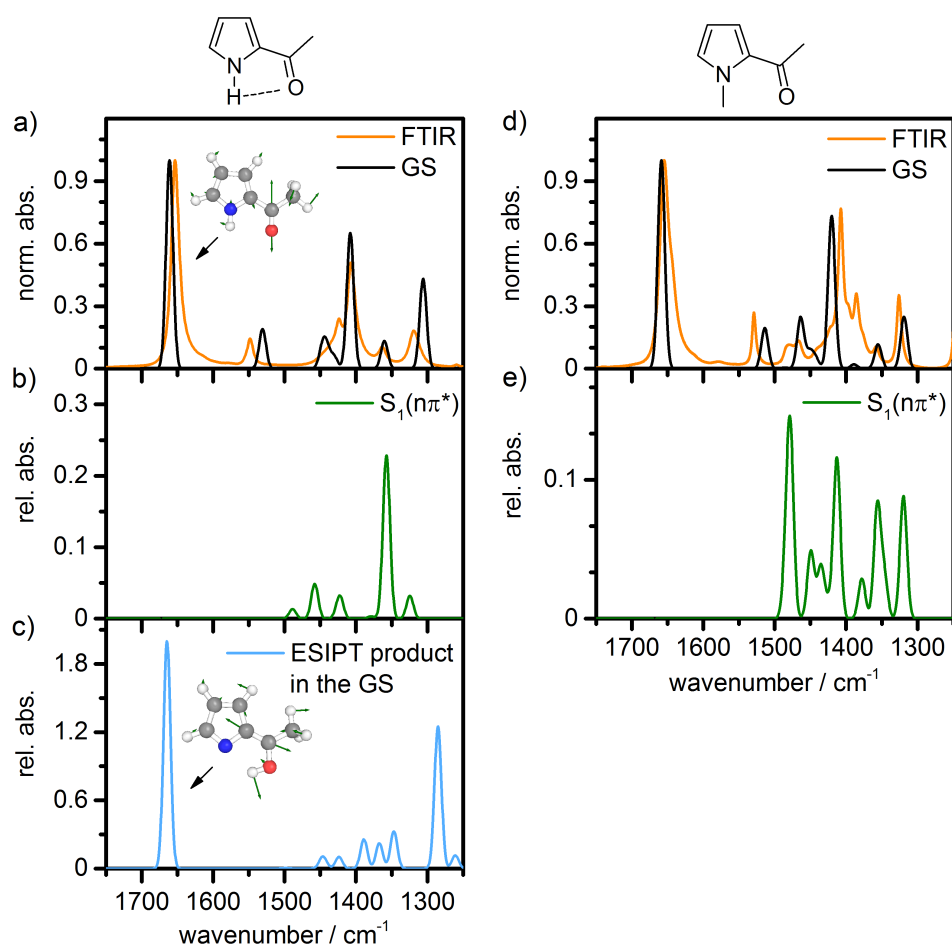


Figure 6.4: Vibrational marker bands of 2AcPy and Me2AcPy in various electronic states. (a) Comparison of the steady-state FTIR spectrum of 2AcPy in ACN solution with calculated frequencies in the ground state (GS). (b) Computed vibrational marker bands of 2AcPy in the relaxed $S_1(n\pi^*)$ state, (c) calculated vibrational modes of 2HEP, the proposed ESIPT photoproduct of 2AcPy in the electronic ground state. (d) Comparison of the steady-state FTIR spectrum of Me2AcPy with the calculated vibrational modes in the ground state. (e) Calculated spectrum for the relaxed first excited $S_1(n\pi^*)$ state of Me2AcPy.

Time-Resolved Electronic Absorption Spectroscopy

The measured femtosecond time-resolved transient electronic absorption (TEA) spectra of 2AcPy and Me2AcPy in acetonitrile solution recorded by Sebastian Megow and Dennis Bank are shown in Fig. 6.5. At early delay times, the TEA spectra of both 2AcPy and Me2AcPy are governed by stimulated emission (SE) around 350 nm superimposed by a distinct excited-state absorption (ESA), which is attributed to the $S_2(\pi\pi^*)$ state. As the SE decays upon leaving of the Franck–Condon region, the ESA band rises to its maximum within the first 250 fs after photoexcitation (blue arrows). Subsequently, a broad ESA grows in (red arrows) as the $\pi\pi^*$ absorption decays (orange arrows) on the ps timescale. This successor state is ascribed to the $S_1(n\pi^*)$ state and remains virtually unchanged beyond $\Delta t = 6$ ps for the rest of our experimental time frame of 2 ns. Still, exclusive to 2AcPy, some minor evolutions at late delay times can be observed in the ESA of the $^1n\pi^*$ state around 500 nm, which will be discussed with respect to a possible ESIPT process below.

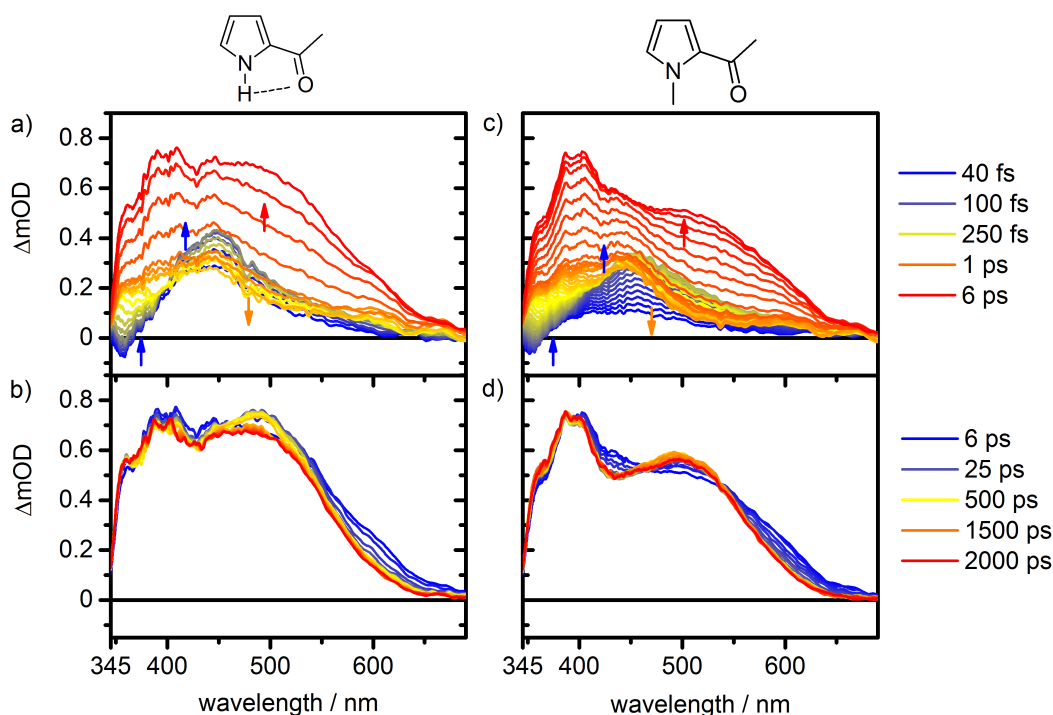


Figure 6.5: Transient electronic absorption spectra of (a and b) 2AcPy and (c and d) Me2AcPy at different delay times after 266 nm excitation to the $S_2(\pi\pi^*)$ state.

Time-Resolved Fluorescence Spectroscopy

Complementary time-resolved fluorescence measurements have been performed by Sebastian Schatz employing the described Kerr-gating technique. Both, 2AcPy and Me2AcPy feature an ultrafast decay component within the instrument response function of $\tau \leq 200$ fs. In agreement with the timescale of stimulated emission in our TEA data, the associated deactivation process is ascribed to a relaxation out of the Franck–Condon region in the $S_2(\pi\pi^*)$ state. Additionally, a second lifetime of $\tau_{\text{fluo}} \sim 4$ ps is found in the fluorescence time profiles. Supported by the rise time of the broad ESA in the transient TEA spectra, this time constant is associated with the decay of the $^1\pi\pi^*$ state to the dark $S_1(n\pi^*)$ state. No long-lived time constant and no red-shifted fluorescence indicative for emission of an ESIPT species as reported previously for 2AcPy in a nonpolar solvent^[22] was found in acetonitrile.

Time-Resolved Vibrational Absorption Spectroscopy

In addition to the time-resolved electronic measurements described above, TVAS measurements were performed. To gain insight into the structural motifs involved in the photo-induced dynamics, we followed the vibrational signature of 2AcPy and Me2AcPy in the CO stretching region around 1600 cm^{-1} and the region of the ring vibrations around $1500\text{--}1300\text{ cm}^{-1}$ after UV excitation. Since the latter is densely packed with bleach features superimposed by adjacent positive bands, sufficient baselining of the data covering the total spectral range proved to be challenging. The transient TVA spectra of 2AcPy and Me2AcPy in ACN solution along with the associated temporal evolution of the most significant features are illustrated in Fig. 6.6.

Obtained from integration over the spectral regions visualized in Fig. 6.6, the kinetic time profiles feature an incomplete recovery of the bleach signal within

$$\tau_{2\text{AcPy, VC}} = 10 \pm 1 \text{ ps}$$

and

$$\tau_{\text{Me2AcPy, VC}} = 4 \pm 1 \text{ ps}$$

for 2AcPy and Me2AcPy, respectively. This time constant is ascribed to vibrational cooling back in the electronic ground state after direct ultrafast radiationless decay of the S_2 state to the GS in the vicinity of the Franck–Condon structure.

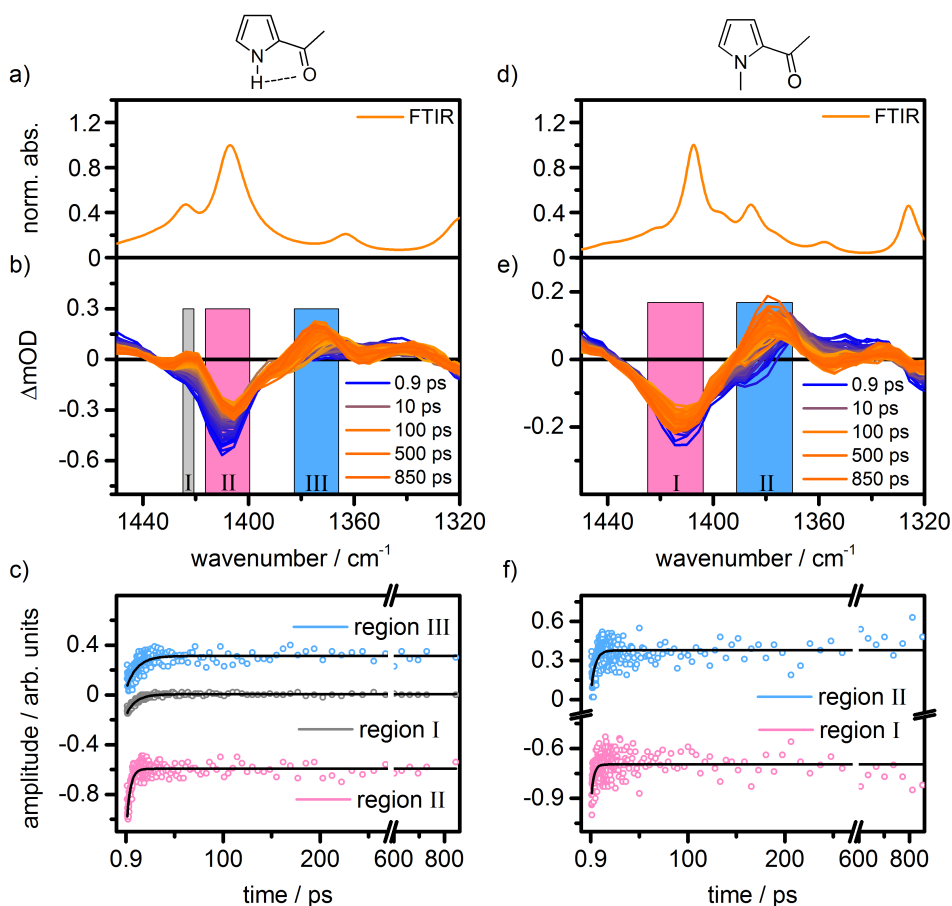


Figure 6.6: Transient vibrational absorption spectra of 2AcPy and Me2AcPy in the region of the ring vibrations. (a) Steady-state FTIR spectrum, (b) transient TVA spectra and (c) time profiles for 2AcPy. (d) Steady-state FTIR spectrum, (e) transient TVA spectra and (f) time profiles for Me2AcPy. Regions integrated for kinetic time profiles are highlighted in colored boxes.

Furthermore, a positive feature grows in with

$$\tau_{2\text{AcPy, rise}} = 4 \pm 1 \text{ ps}$$

and

$$\tau_{\text{Me2AcPy, rise}} = 3 \pm 1 \text{ ps}$$

in the TVA spectra of 2AcPy and Me2AcPy, respectively. This time constant is in good agreement with $\tau_{\text{fluo}} \sim 4 \text{ ps}$ which was found in the time-resolved emission experiment and is ascribed to the evolution of the $^1\pi\pi^*$ state towards the $^1n\pi^*$ state. It also reflects the spectro-temporal evolution of the TEA spectra within the first several picoseconds.

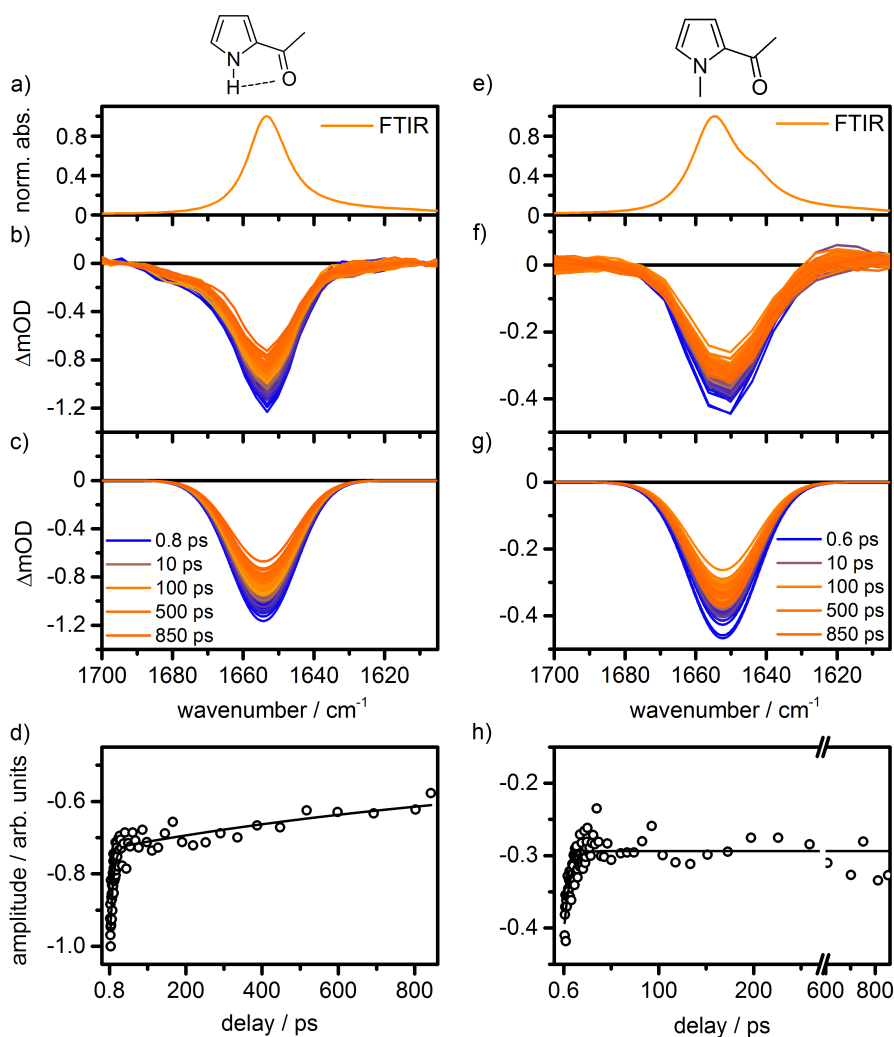


Figure 6.7: Transient vibrational absorption spectra of 2AcPy and Me2AcPy in the region of CO and CC stretch vibrations. (a) Steady-state FTIR spectrum, (b) transient TVA spectra, (c) globally fitted data and (d) time profiles of 2AcPy. (e) Steady-state FTIR spectrum, (f) transient TVA spectra, (g) globally fitted data and (h) time profiles of Me2AcPy.

Additionally, TVA spectra in the CO stretching region were recorded and fitted globally with a Gaussian function as shown in Fig. 6.7. In accordance with the kinetic profiles in the region of the ring vibrations, a time constant for the observed incomplete bleach recovery was found to be

$$\tau_{2\text{AcPy, VC}} = 8 \pm 2 \text{ ps}$$

and

$$\tau_{\text{Me2AcPy, VC}} = 6 \pm 2 \text{ ps}$$

for 2AcPy and Me2AcPy, respectively. In this spectral region, no distinct vibrational marker bands of excited electronic states, photoproduct species or hot ground-state absorptions could be observed. Exclusive for 2AcPy, however, the time profile for ground-state recovery of the vibrational marker band at 1655 cm^{-1} features an additional time constant in the nanosecond regime. This spectral feature will be discussed in terms of an obscured marker

band due to ESIPT below.

The combined results of our time-resolved measurements can be summarized in an interim conclusion as follows: Excitation at 266 nm predominantly populates the optically bright $S_2(\pi\pi^*)$ state of 2AcPy and Me2AcPy. Upon bifurcation of the wavepacket from the Franck–Condon region, a fraction of the excited-state population ($\sim 50\%$) deactivates by ultrafast radiationless internal conversion back to the GS and recovers the v_0 ground-state vibrational marker bands following vibrational cooling in $\tau_{VC} \approx 4 - 10$ ps. The remaining excited-state fraction evolves towards the $\pi\pi^*$ minimum structure within a few hundred femtoseconds. Subsequently, the excited-state population evolves from the $S_2(\pi\pi^*)$ state to the lower-lying $S_1(n\pi^*)$ state within $\tau \sim 4$ ps. Our calculations suggest a conical intersection connecting the $^1\pi\pi^*$ and $^1n\pi^*$ excited states at an extended CO bond length in close proximity of the ground-state equilibrium distance (*cf.* Fig. 6.3). The $^1n\pi^*$ state survives on the two nanosecond time range of our experiments and is believed to ultimately drive the majority of the excited-state population to a triplet state, probably of $^3\pi\pi^*$ character according to El-Sayed's rules.^[49,50] Indeed, high quantum yields for intersystem crossing to the triplet manifold were reported upon direct excitation of the $^1n\pi^*$ state for 2AcPy and Me2AcPy in acetonitrile solution elsewhere.^[20] As can also be seen in Fig. 6.3, once trapped in the minimum of the transient $^1n\pi^*$ state, energetic degeneracy for efficient intersystem crossing towards the triplet manifold is associated with a sizable energy barrier along an extended CO bond length. Thus, the nanosecond lifetime of the $^1n\pi^*$ state is ascribed to a significant activation barrier which needs to be overcome.

Besides, an excited-state intramolecular proton transfer was recently proposed for 2AcPy.^[22] Although no unambiguous spectral features of such a process could be observed in our experiments, slight indications for excited-state proton transfer could be isolated from comparison of subtle differences in the transient evolution of 2AcPy and Me2AcPy as will be discussed in the following.

Indications for ESIPT in the $S_1(n\pi^*)$ State of 2AcPy

ESIPT involving an activation barrier of 25.1 kcal/mol has been proposed for 2AcPy in the S_1 state on the grounds of quantum chemical calculations.^[22] At first glance, no unambiguous evidence for such a process was found in our time-resolved experiments. However, since the electronic character of the PES is expected to remain mainly unchanged during the ESIPT process, pronounced changes in the specific signature of the transient TEA spectra are not expected. Still, comparing our TEA spectra of 2AcPy and Me2AcPy reveals minor spectro-temporal evolutions at late delay times exclusive for 2AcPy.

In order to further elucidate the possible ESIPT in 2AcPy we turn to our structure-sensitive TVA data. As already discussed above, the relaxation dynamics of 2AcPy and Me2AcPy appear to be virtually the same during deactivation towards the $S_1(n\pi^*)$ state. As such, the spectro-temporal evolution of the TVA spectra of 2AcPy reflects the dynamic processes of Me2AcPy in the spectral region of the ring vibrations to a high extent (*cf.* Fig. 6.6). Judging from the vibrational frequency calculations in Fig. 6.4, however, no significant contributions of ESIPT species are expected in the investigated spectral region as the marker bands of the ESIPT species 2HEP are computed to show little absorption in this spectral region. Yet, as opposed to the spectral region under investigation in Fig. 6.6, strong vibrational contributions of ESIPT species to the TVA data are expected in the spectral region probed in Fig. 6.7 on the grounds of our quantum chemical calculations (*cf.* Fig. 6.4). Most intriguingly, while the bleached signature of 2AcPy approaches a constant plateau in the region of the ring vibrations (Fig. 6.6), it features an additional contribution to an apparent recovery of the bleached CO stretching mode in the nanosecond regime (Fig. 6.7, $\tau \sim 1250$ ps). This additional contribution is absent in Me2AcPy, which is incapable of ESIPT. Also, as this bleach-associated nanosecond component is present solely in one spectral region, it cannot reflect a true refilling of the ground state of 2AcPy. Judging from our vibrational frequency calculations, the vibrational signature of the CC stretching mode in the proposed H-transferred species (1659 cm^{-1}) is expected to overlap almost entirely with the bleached CO stretching band of 2AcPy (1655 cm^{-1} , *cf.* Fig. 6.4). Hence, we attribute the apparent contribution to the bleach recovery in the CO stretching region of 2AcPy to the formation of this ESIPT species on the nanosecond timescale. The lack of corresponding features for the ESIPT species in other spectral regions or electronically excited states is ascribed to lower vibrational absorption coefficients and presumably low quantum yields for the ESIPT process due to a significant activation barrier in the excited state as was previously proposed.^[22] In fact, judging from our calculations in Fig. 6.2 (b), the formation of 2HEP appears energetically unfavoured. On the same grounds, considering the small oscillator strengths for $^1n\pi^*$ states, the lack of fluorescence from the proton-transferred species in the excited state may be explained. To ascertain an ESIPT process with low quantum yields, it would be helpful to measure TVA spectra in the region of the NH/OH stretching vibrations.

Relaxation Dynamics of Homo-Dimeric 2AcPy

In cyclohexane (CHX) solution, 2AcPy exists in a temperature-dependent equilibrium between monomeric and dimeric structures. As illustrated in Fig. 6.8 (a), monomeric 2AcPy – indicated by the CO stretching mode at 1665 cm^{-1} – dominates at high temperatures. In contrast, the vibrational marker band of dimeric 2AcPy at 1645 cm^{-1} marks the significant share of homo-dimers at lower and ambient temperatures. At room temperature, significant amounts of both monomeric and dimeric 2AcPy are present in cyclohexane solution. Note, that the CO stretching vibration of free 2AcPy is shifted from 1655 cm^{-1} in ACN to 1665 cm^{-1} in CHX, indicating a significant influence of the polar solvent within the intramolecular H-bonding network in ACN.

As can be seen from Fig. 6.8, irradiation at 266 nm excites both monomeric and dimeric 2AcPy. The transient vibrational absorption spectra, the global fit result of a sum of Gaussian functions to the TVA data and the corresponding time profiles are shown in Fig. 6.8 (c–e). At early delay times, a broad positive absorption band, superimposed by the bleached signals of monomeric and dimeric 2AcPy, is observed. The decay of this transient feature is characterized by

$$\tau_1 = 0.76 \pm 0.12\text{ ps.}$$

Further complementary time-resolved measurements need to be conducted to assess this transient feature to real kinetic processes or transient lensing artifacts. The monomer-associated bleached mode at 1665 cm^{-1} recovers with

$$\tau_2^{\text{monomer}} = 3.8 \pm 0.6\text{ ps}$$

to a constant negative offset. Most notably, opposed to measurements in ACN, monomeric 2AcPy in CHX does not show any indications for an ESIPT process on the nanosecond timescale from the time profile of the bleach recovery. In comparison with the monomer dynamics, the bleach recovery of dimeric 2AcPy is significantly prolonged to

$$\tau_2^{\text{dimer}} = 23 \pm 7\text{ ps.}$$

Furthermore, a positive transient feature at 1630 cm^{-1} rises with

$$\tau = 5.8 \pm 0.6\text{ ps}$$

towards a permanent positive absorption at late delay times. Further quantum chemical calculations are required for assignment of this marker band to a transient excited-state absorption or to photoproduct formation back in the electronic ground state.

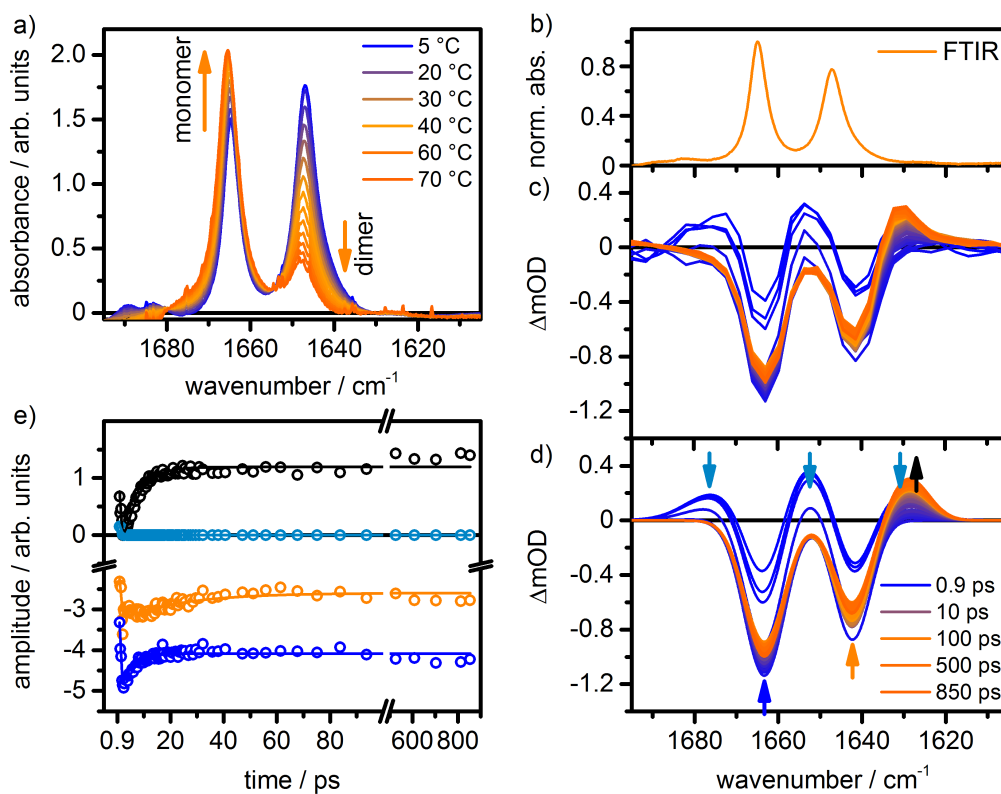


Figure 6.8: (a) Temperature-dependent FTIR spectra of 2AcPy in cyclohexane solution. (b) Steady-state FTIR spectrum, (c) transient TVA spectra and (d) globally fitted data of 2AcPy in cyclohexane solution upon 266 nm excitation. (e) Time profiles of the features in the corresponding TVA spectra. The time traces are color-coded with respect to the colored arrows from (d).

6.4 Conclusion

In conclusion, we have reported on the ultrafast relaxation dynamics of 2-acetylpyrrole (2AcPy) and its N-methyl analogue 2-acetyl-1-methylpyrrole (Me2AcPy) employing a combination of time-resolved emission and absorption techniques supported by *ab initio* and *semi*-empirical calculations. The results suggest an ultrafast relaxation from the initially excited $S_2(\pi\pi^*)$ state to the lower-lying $S_1(n\pi^*)$ state within $\tau \sim 4$ ps. The long-lived $n\pi^*$ state survives on the 2 ns scope of our experiments and is believed to ultimately drive the majority of the excited-state population to a triplet state in accordance with measurements reported on the ns-to- μ s timescale.^[20] Assuming a low quantum yield process, indications for an excited-state intramolecular proton transfer (ESIPT) in the $n\pi^*$ state as proposed previously^[22] have been found for monomeric 2AcPy in acetonitrile solution. Yet, such indications are absent in measurements in cyclohexane solution. Instead, we have revealed additional kinetic processes, which could be ascribed to homo-dimeric deactivation dynamics. All processes require further investigation.

Acknowledgement

Financial support by the DFG through project A7 of the Collaborative Research Centre 677 – Function by Switching is gratefully acknowledged.

References

- [1] G. M. Roberts, C. A. Williams, H. Yu, A. S. Chatterley, J. D. Young, S. Ullrich and V. G. Stavros, *Faraday Discuss.*, 2013, **163**, 95–116.
- [2] G. Wu, S. P. Neville, O. Schalk, T. Sekikawa, M. N. R. Ashfold, G. A. Worth and A. Stolow, *J. Chem. Phys.*, 2015, **142**, 074302.
- [3] G. Wu, S. P. Neville, O. Schalk, T. Sekikawa, M. N. R. Ashfold, G. A. Worth and A. Stolow, *J. Chem. Phys.*, 2016, **144**, 014309.
- [4] V. Ovejas, R. Montero, M. Fernández-Fernández and A. Longarte, *J. Phys. Chem. A*, 2015, **119**, 3355–3365.
- [5] L. Blancafort, V. Ovejas, R. Montero, M. Fernández-Fernández and A. Longarte, *J. Phys. Chem. Lett.*, 2016, **7**, 1231–1237.
- [6] J. Wei, A. Kuczmann, J. Riedel, F. Renth and F. Temps, *Phys. Chem. Chem. Phys.* 2003, **5**, 315–320.
- [7] J. Wei, J. Riedel, A. Kuczmann, F. Renth and F. Temps, *Faraday Discuss.* 2004, **127**, 267–282.
- [8] A. Sobolweski, W. Domcke, C. Dedonder-Lardeux and C. Jouvet, *Phys. Chem. Chem. Phys.* 2002, **4**, 1093–1100.
- [9] P. A. Mullen and M. K. Orloff, *J. Chem. Phys.* 1969, **51**, 2276–2278.
- [10] R. G. W. Norrish, H. G. Crone and O. D. Saltmarsh, *J. Chem. Soc.* 1934, **0**, 1456–1464.
- [11] H. Okabe, *Photochemistry of Small Molecules*, Wiley, 1978.
- [12] C. E. Wayne and R. P. Wayne, *Photochemistry*, Oxford University Press, 1996.
- [13] Y. Haas, *Photochem. Photobiol. Sci.*, 2004, **3**, 6–16.
- [14] W. Horspool and D. Armesto, *Organic Photochemistry: A Comprehensive Treatment*, Ellis Horwood Limited: Chichester, England, 1992, 160–200.
- [15] O. Hüter and F. Temps, *J. Chem. Phys.* 2016, **145**, 214312.

- [16] O. Hüter, N. Helle and F. Temps, *ChemRxiv* 12-03-2019.
- [17] S. T. Park, J. S. Feenstra and A. H. Zewail, *J. Chem. Phys.*, 2006, **124**, 174707.
- [18] M. Baba, *J. Phys. Chem. A*, 2011, **115**, 9514–9519.
- [19] W.-H. Fang, *Accounts in Chemical Research*, 2008, **41**, 452–457.
- [20] M. Ikegami and T. Arai, *Photochem. Photobiol. Sci.*, 2003, **2**, 418–423.
- [21] L. C. Ducati, C. B. Braga, R. Rittner, C. F. Tormena, *Spectrochim. Acta A*, 2013, **116**, 196–203.
- [22] N. Singla and P. Chowdhury, *Chem. Phys. Lett.*, 2014, **612**, 25–32.
- [23] E. A. Camarillo, H. Flores, P. Amador and S. Bernès, *Acta Cryst.*, 2007, **63**, 2593–2594.
- [24] J. C. Viljoen and A. M. Heyns, *Spectr. Lett.*, 1987, **20**, 765–776.
- [25] S. Wang, S. Schatz, M. C. Stuhldreier, H. Böhnke, J. Wiese, C. Schröder, T. Raeker, B. Hartke, J. K. Keppler, K. Schwarz, F. Renth and F. Temps, *Phys. Chem. Chem. Phys.* 2017, **19**, 30683–30694.
- [26] J. Bredenbeck and P. Hamm, *Rev. Sci. Instr.*, 2003, **74**, 3188–3189.
- [27] K. Röttger, F. D. Sönnichsen and F. Temps, *Photochem. Photobiol. Sci.* 2013, **12**, 1466–1473.
- [28] R. Siewertsen, F. Strübe, J. Mattay, F. Renth and F. Temps, *Phys. Chem. Chem. Phys.* 2011, **13**, 3800–3808.
- [29] R. Siewertsen, F. Renth, F. Temps and F. D. Sönnichsen, *Phys. Chem. Chem. Phys.* 2009, **11**, 5952–5961.
- [30] F. Renth, M. Foca, A. Petter and F. Temps, *Chem. Phys. Lett.* 2006, **428**, 62–67.
- [31] M. Häser and R. Ahlrichs, *J. Comput. Chem.*, 1989, **10**, 104–111.
- [32] F. Weigend and M. Häser, *Theor. Chem. Acta*, 1997, **97**, 331–340.
- [33] F. Weigend, M. Häser, H. Patzelt and R. Ahlrichs, *Chem. Phys. Lett.*, 1998, **294**, 143–152.

- [34] S. Grimme, *J. Chem. Phys.*, 2003, **118**, 9095.
- [35] C. Hättig, A. Hellweg and A. Köhn, *Phys. Chem. Chem. Phys.*, 2006, **8**, 1159–1169.
- [36] F. Weigend and R. Ahlrichs, *Phys. Chem. Chem. Phys.*, 2005, **7**, 3297–3305.
- [37] O. Christiansen, H. Koch and P. Jørgensen, *Chem. Phys. Lett.*, 1995, **243**, 409–418.
- [38] C. Hättig and F. Weigend, *J. Chem. Phys.*, 2000, **113**, 5154–5161.
- [39] C. Hättig and A. Köhn, *J. Chem. Phys.*, 2002, **117**, 6939–6951.
- [40] A. Köhn and C. Hättig, *J. Chem. Phys.*, 2003, **119**, 5021–5036.
- [41] R. Ahlrichs, *Phys. Chem. Chem. Phys.*, 2004, **6**, 5119–5121.
- [42] A. Hellweg, S. A. Grün and C. Hättig, *Phys. Chem. Chem. Phys.*, 2008, **10**, 4119–4127.
- [43] Turbomole v7.0 2015, a development of University of Karlsruhe and Forschungszentrum Karlsruhe GmbH, 1989-2007, Turbomole GmbH, since 2007; available from <http://www.turbomole.com>.
- [44] G. Granucci and A. Toniolo, *Chem. Phys. Lett.*, 2000, **325**, 79–85.
- [45] J. J. P. Stewart, *J. Comput. Aided Molec. Des.*, 1990, **4**, 1–103.
- [46] M. J. S. Dewar, E. G. Zoebisch, E. F. Healy and J. J. P. Stewart, *J. Am. Chem. Soc.*, 1985, **107**, 3902–3909.
- [47] N. O. Carstensen, J. Sielk, J. B. Schoenborn, G. Granucci and B. Hartke, *J. Chem. Phys.*, 2010, **133**, 124305.
- [48] T. Raeker, N. O. Carstensen and B. Hartke, *J. Phys. Chem. A*, 2012, **116**, 11241–11248.
- [49] M. A. El-Sayed, *J. Chem. Phys.*, 1963, **38**, 2834–2838.
- [50] C. M. Marian, F. Schneider, M. Kleinschmidt and J. Tatchen, *Eur. Phys. J. D*, 2002, **20**, 357–367.

6.5 Supplementary Information

Table 6.2: Results of the meta-optimization for important points on the PES of 2AcPy. The CASSCF(4,6) reference values are taken from Ref. [1]. The best semi-empirical setup is the AM1 Hamiltonian in combination with a 12,12 active space and a CIS.5 excitation level. All values are listed in eV

	AM1 (12,12) CIS.5	CASSCF (4,6)
C-AP S0S1	3.58	4.10
C-AP S0S2	4.20	4.59
C-AP S0S3	4.58	5.13
C-AP S1S0	3.29	3.30
C-AP S2S0	4.17	4.39
C-AP S3S0	4.58	4.91
C-T S0	0.17	0.16
T-AP S0S1	3.52	4.01
T-AP S0S2	4.20	4.61
T-AP S0S3	4.58	5.14
T-AP S1S0	3.17	3.11
T-AP S2S0	4.14	4.60
T-AP S3S0	4.57	5.03
C-Z S0	0.70	0.69
C-Z S1	0.01	0.27
Z-AP S1S0	2.12	2.57
Z-AP S2S0	3.16	3.41
Z-AP S3S0	3.70	3.90

[1] N. Singla and P. Chowdhury, *Chem. Phys. Lett.*, 2014, **612**, 25–32.

Ultrafast Electronic Deactivation and Reaction Dynamics of 3-Hydroxypicolinic Acid

HENDRIK BÖHNKE,^a KATHARINA RÖTTGER,^{a,b,‡} REBECCA A. INGLE,^{b,§} HUGO J. B. MARROUX,^{b,¶}
MATS BOHNSACK,^a ANDREW J. ORR-EWING^{*b} AND FRIEDRICH TEMPS^{*a}

^a Institute of Physical Chemistry, Christian-Albrechts-University Kiel, Olshausenstr. 40,
24098 Kiel, Germany.

^b School of Chemistry, University of Bristol, Cantock's Close, Bristol BS8 1TS, United
Kingdom.

[‡] Current address: Centre for Process Innovation, Wilton Centre, Wilton, Redcar TS10 4RF,
United Kingdom.

[§] Current address: École Polytechnique Fédérale de Lausanne, Laboratoire de Spectroscopie
Ultrarapide (LSU) and Lausanne Centre for Ultrafast Science (LACUS), ISIC, FSB, CH-1015
Lausanne, Switzerland.

[¶] Current address: Chemical Sciences Department, Lawrence Berkeley National Labora-
tory, 1 Cyclotron Road Berkeley CA 94720, USA.

* To whom correspondence should be addressed.

E-mail: temps@phc.uni-kiel.de; a.orr-ewing@bristol.ac.uk.

Manuscript in preparation.

OWN CONTRIBUTIONS TO THIS MANUSCRIPT:

- Steady-state UV/vis, fluorescence and FTIR spectroscopy,
- Quantum chemical calculations for ground- and excited-state species,
- Transient femtosecond vibrational absorption spectroscopy,
- Time-correlated single photon counting measurements,
- Analysis of experimental data,
- Writing of the manuscript.

Abstract

Bi-stable photochromic molecular switches based on excited-state intramolecular proton transfer (ESIPT) have raised substantial attention due to their huge application potential in data storage and photo-protection. Recently, intramolecular double proton transfer was proposed for interconversion of two stable ground-state species of 3-hydroxypicolinic acid (3HPA) on the grounds of quantum chemical *ab initio* calculations. In order to elucidate the electronic deactivation and reaction pathways experimentally, we employed transient vibrational absorption spectroscopy (TVAS) – a method sensitive to both molecular structure and the nature of the electronic states. Here, we report on the photo-induced electronic deactivation and reaction dynamics of 3HPA in CHCl_3 solution upon excitation at $\lambda_{\text{pump}} = 310$ nm. The proposed ultrafast ESIPT process towards formation of an H-transferred ground-state photoproduct could not be observed. Instead, we have scrutinized a consecutive deactivation pathway including time constants on the picosecond-to-nanosecond timescale. As inferred from time-resolved TVA data and time-resolved fluorescence measurements, an optically bright $^1\pi\pi^*$ state with a lifetime of $\tau_1 \approx 50$ ps is populated by the photoexcitation. While a fraction of the excited-state population gets trapped in this state, electronic deactivation proceeds towards an optically dark state, possibly of $^1n\pi^*$ character. Concurrent to decay of this dark state, a third transient state rises in with $\tau_2 \approx 410$ ps and survives on the nanosecond scope of our time-resolved experiments. Accordingly, small-amplitude contributions in fluorescence data ($\tau_3, \text{UPC} \approx 1.5$ ns and $\tau_3, \text{TCSPC} \approx 3.9$ ns) hint at processes on the nanosecond timescale. However, assessment of the nanosecond time constant either to the decay of the long-lived successor state or rather to deactivation processes of the trapped fraction in the initial bright $^1\pi\pi^*$ state remains elusive. From the bleaching signals, no recovery of ground-state species could be identified on the picosecond-to-nanosecond timescale.

7.1 Introduction

Excited-state intramolecular proton transfer (ESIPT) processes belong to the fastest chemical reactions known. With effective reaction times down to just a few tens of femtoseconds, ESIPT unfolds on the ultrafast timescale.^[1–10] As the possibility of undesired side-reactions is virtually eliminated on these timescales, combination of ESIPT processes with twist-associated efficient electronic deactivation *via* conical intersections towards recovery of the electronic ground state enables unrivalled photostability. As a result, compounds featuring ESIPT-associated electronic deactivation pathways demonstrate huge application potential as photo-stabilizers and sunscreen agents.^[11–14]

Once efficient repopulation of the electronic ground state is accompanied by the formation of a structural isomer of the initially excited molecular species in significant amounts, such compounds may be regarded as molecular ESIPT switches. Besides high

quantum yields for structural interconversion, an important prerequisite for molecular ES IPT switches is sufficient stability of at least two structural isomers accompanied by altered UV/vis absorption spectra for selective excitation of one species.

Recently, an excited-state intramolecular double proton transfer for interconversion between two such stable photochromic tautomers was proposed for 3-hydroxypicolinic acid (3HPA). The transient species illustrated in Fig. 7.1 are characterized by two tautomeric pairs: While protonation and deprotonation of the hydroxy group is referred to as **Enol/Oxo**, deprotonation and protonation of the aromatic nitrogen is denoted as **Imino/Amino**. In principle, photoexcitation of the **EI** species may result in photo-formation of the **OA** form by transient double proton transfer. On the grounds of quantum chemical calculations however, the exact route for photo-reaction *via* either the transient **OI** or **EA** species, remains elusive.^[15,16] Thus, we employed time-resolved transient vibrational absorption spectroscopy – a method sensitive to molecular structure and the involved electronic states – for investigation of the electronic deactivation of 3HPA in CHCl_3 solution.

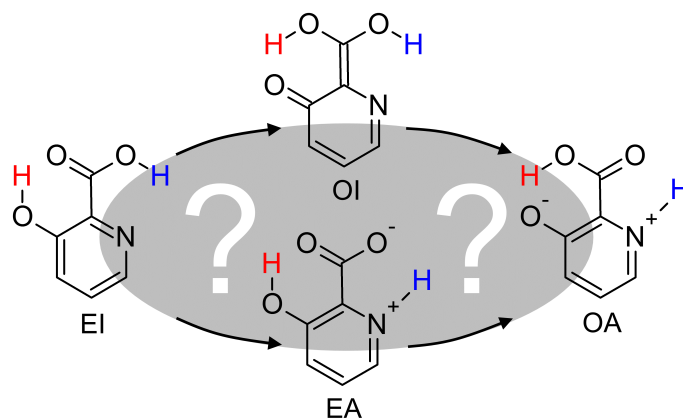


Figure 7.1: Schematic reaction route from the **EI** towards the **OA** form by intramolecular double proton transfer *via* possible **OI/EA** transient species as proposed by Ref. [15,16].

7.2 Methods

Time-Resolved Spectroscopy

Time-resolved UV pump–transient vibrational absorption measurements were performed with the spectrometer at the University of Bristol^[17] using sample concentrations of 1 mM and an optical pathlength of 600 μm . UV excitation pulses at $\lambda_{\text{pump}} = 310 \text{ nm}$ with duration of $\sim 100 \text{ fs}$ (full width at half maximum) were generated by a Coherent OPerA Solo optical parametric amplifier (OPA) pumped by 2.45 mJ per pulse from a Coherent Legend Elite HE+ regenerative amplifier running at 1 kHz and 800 nm with 40 fs duration. Pump pulses were attenuated to 200 nJ per pulse by a combination of a $\lambda/2$ waveplate and a wire-grid polarizer and set to the magic angle condition (54.7°) with respect to the probe pulses. Broadband mid-IR probe pulses were supplied by difference frequency generation of signal and idler pulses from a second OPA, giving tunable pulses with $\sim 300 \text{ cm}^{-1}$ bandwidth in the $1250\text{--}4000 \text{ cm}^{-1}$ range. After passing through the sample, mid-IR probe pulses were spectrally dispersed by a grating spectrograph (HORIBA Scientific, iHR320) and detected on a 128 pixel, liquid N_2 -cooled mercury cadmium telluride array (Infrared Associates). For transient measurements, UV pump pulses were delayed using an aluminium retro-reflector mounted on a motorized delay stage and modulated at 0.5 kHz with an optical chopper wheel for pump-on/pump-off pairs of spectra.

Supporting time-resolved fluorescence measurements to determine the excited-state lifetime of 3HPA in CHCl_3 were performed using the up-conversion spectrometer in Kiel.^[18] Additionally, time-correlated single photon counting measurements (TCSPC, FluoroTime200, PicoQuant) have been performed to robustly resolve temporal components in the nanosecond regime. IR spectra were recorded on an IFS 66v FTIR spectrometer (Bruker) using a liquid nitrogen cooled MCT detector. For continuous flushing of the sample compartment, compressed air was scavenged from atmospheric water vapor ($< 1 \text{ ppm}$) and CO_2 ($< 1 \text{ ppm}$) with a purge gas generator (PG 85 L, cmc-Instruments). A CaF_2 cell with a path length of 100 μm was used for measurements recording a spectral range of $600\text{--}5000 \text{ cm}^{-1}$ with a spectral resolution of 1 cm^{-1} . UV/vis spectra were obtained from a UV-2401PC spectrophotometer by Shimadzu using a quartz cell with a path length of 1 mm (Hellma Analytics). Fluorescence spectra were recorded on a FluoroMax-4 spectrofluorometer (Horiba Jobin Yvon) using quartz cells of 1 cm path length (Hellma Analytics).

Computational Methods

Quantum chemical calculations were carried out to derive assignments for the characteristic vibrational marker bands observed in the TVA spectra to the GS and to the possible excited electronic states of different tautomeric forms of 3HPA. Relaxed GS structures and vibrational frequencies were determined by DFT calculations with the M062X^[19] functional in combination with the aug-cc-pVDZ basis set^[21] using the Gaussian09 suite of programs.^[22] The calculated wavenumbers were scaled (*cf.* Ref. [22,23]) to obtain best agreement with the experimental (FTIR) data using factors of 0.95. Complementary calculations were run using second-order Møller–Plesset perturbation theory (MP2) under the resolution of the identity (RI) approximation^[24–27] with the aug-cc-pVDZ basis set employing the Turbomole 7.0 program^[28] to obtain starting points for the excited states. Excited-state properties, including vertical excitation energies (VEEs), equilibrium structures and associated vibrational mode frequencies for the $^1\pi\pi^*$, $^1n\pi^*$ and $^3\pi\pi^*$ state minima, were then computed using the second-order approximation coupled-cluster (CC2) method in Turbomole 7.0 in the form of the RI-CC2 variant^[29–34] with the aug-cc-pVDZ basis set for the **EI** and **OA** forms of 3HPA. Where CC2 calculations failed to converge, additional ADC(2) calculations^[35] were performed. However, the obtained vibrational wavenumbers in the excited $^1\pi\pi^*$, $^1n\pi^*$ and $^3\pi\pi^*$ states of **EI** and **OA** did not resemble the measured transient vibrational spectra. Thus, more elaborate quantum chemical calculations are required to assign the transient vibrational marker bands to molecular species in distinct electronic states.

7.3 Results and Discussion

Tautomeric Equilibrium of 3HPA

According to *ab initio* calculations in the gas phase, the two tautomeric ground-state species of 3HPA – **EI** and **OA** – are separated by a moderate energy barrier of 0.34 eV.^[15,16] Furthermore, the less stable **OA** species is expected to feature a $^1\pi\pi^*$ absorption band at 3.37 eV, significantly red-shifted compared to the thermodynamically stable **EI** form at 4.35 eV. In order to check for tautomeric purity in the liquid phase, Fig. 7.2 (a) shows a set of UV/vis absorption spectra of 3HPA in various solvents. While the absorption spectra in acetonitrile (ACN) and ethanol (EtOH) comprise a diffuse shoulder around 350 nm, possibly indicative for either the $^1n\pi^*$ absorption of the **EI** species or signature of the $^1\pi\pi^*$ absorption of the **OA** form, the absorption spectrum in CHCl_3 appears to feature only the pure $^1\pi\pi^*$ band of the stable **EI** form. However, as the excited $^1\pi\pi^*$ state of the rather polar **OA** species may be stabilized in polar solvents, the associated absorption

band is expected to be blue-shifted compared to gas phase predictions and might thus be superimposed by the absorption band of the **EI** form.

For further inspection, Fig. 7.2 (b) illustrates the experimental FTIR spectrum of 3HPA in CHCl_3 alongside with calculated vibrational frequencies for the **EI** and **OA** ground-state species. As can be seen, the majority of the vibrational bands in the FTIR spectrum can be explained by **EI**-related modes. However, to account for the entire experimental spectrum, particularly around 1600 cm^{-1} and 1540 cm^{-1} , minor contributions of the **OA** form have to be assumed to be present in CHCl_3 solution. Further, the FTIR spectrum reveals significant amounts of water, indicated by asterisks in Fig. 7.2 (b) (*cf.* Ref. [36]). The contamination of the solution is caused by intake of water trapped in the crystalline framework of the sample rather than by atmospheric impurities. Thus, despite working strictly under dried atmospheres and performing multiple re-crystallization cycles, a considerable amount of water contamination could not be avoided. Unfortunately, however, the presence of water molecules in the sample aggravates a distinction between intermolecular and intramolecular H-transfer processes, complicating the interpretation of transient data. In fact, the presence of water molecules in our sample solution likely precludes intramolecular proton transfer processes upon photoexcitation as intermolecular H-transfer with H_2O molecules is facilitated.

Time-Resolved Data

The transient vibrational absorption spectra obtained for 3HPA in CHCl_3 solution upon excitation at $\lambda_{\text{pump}} = 310\text{ nm}$ are presented in Fig. 7.2 (c–e) at different times after excitation. In accordance with the steady-state FTIR spectrum, the transient spectra feature ground-state bleache signals at 1730 cm^{-1} , 1600 cm^{-1} and 1540 cm^{-1} . No bleaching is observed at 1675 cm^{-1} , again highlighting the origin of this band from water contamination. Also, directly after photoexcitation, the first TVA spectrum at $\Delta t = 1\text{ ps}$ comprises a positive absorption at 1638 cm^{-1} . As this band decays to a positive, non-zero value with a time constant of

$$\tau_{1, \text{TVA}} = 50 \pm 24\text{ ps},$$

a second band grows in at 1603 cm^{-1} . As this vibrational mode decays within

$$\tau_{2, \text{TVA}} = 410 \pm 120\text{ ps},$$

a concurrent build-up of two vibrational bands at 1678 cm^{-1} and 1555 cm^{-1} is observed.

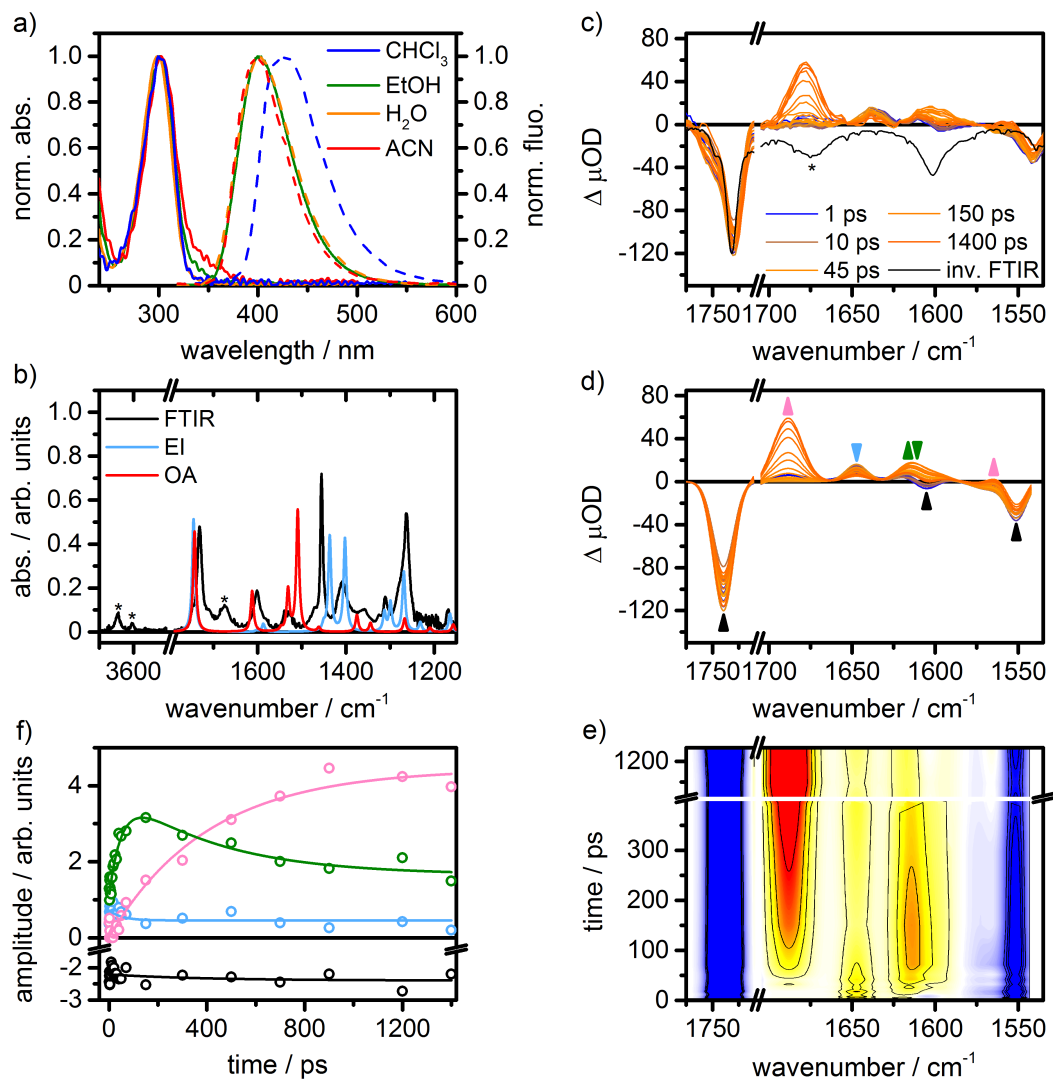


Figure 7.2: Experimental data of 3-hydroxypicolinic acid. (a) Steady-state UV/vis and static fluorescence spectra in various solvents. (b) Experimental FTIR spectrum in CHCl₃ (black) alongside with the calculated ground-state vibrational spectra of 3HPA in the EI (blue) and OA (red) form. Features assigned with an asterisk correspond to vibrational bands of water contaminations. (c) Experimental transient vibrational absorption spectra in CHCl₃ solution and (d) associated global fits to a sum of Gaussian functions. (e) Two-dimensional spectro-temporal representation of the fitted data. (f) Time profiles of the TVA marker bands.

These TVA data were corroborated by time-resolved fluorescence measurements using the up-conversion technique (Mats Bohnsack, unpublished results) and time-correlated single photon counting measurements (TCSPC, data not shown). The fluorescence measurements revealed

$$\tau_{1, \text{UPC}} = 48 \pm 3 \text{ ps} \quad \tau_{1, \text{TCSPC}} \approx 37 \text{ ps}$$

and

$$\tau_{3, \text{UPC}} = 1500 \pm 600 \text{ ps} \quad \tau_{3, \text{TCSPC}} \approx 3900 \text{ ps}$$

as time constants for deactivation of the fluorescing electronic states.

In order to assign the transient marker bands in the TVA spectra to distinct molecular structures in various electronic states, *ab initio* excited-state calculations were performed. Surprisingly, however, the computed vibrational wavenumbers in the excited $^1\pi\pi^*$, $^1n\pi^*$ and $^3\pi\pi^*$ states of the **EI** and **OA** species did not resemble the measured transient vibrational spectra. Note, however, that the water contamination of the sample aggravates the identification of the molecular identities. At this point, it remains unclear, whether the observed vibrational marker bands are associated with transient species upon intramolecular H-transfer or rather belong to intermolecular transfer processes with H₂O contaminations.

Still, although more elaborate excited-state *ab initio* quantum chemical calculations are required to assign the observed vibrational marker bands to distinct molecular species in different electronic states, incorporation of the time constants obtained from our time-resolved UPC and TCSPC fluorescence measurements with the clear consecutive kinetics observed in our TVAS data allows for the following statements, which are illustrated in Fig. 7.3:

1. Judging from the steady-state UV/vis and FTIR spectra in Fig. 7.2 (a–b), 3-hydroxypicolinic acid exists predominantly in the **EI** form in CHCl₃ solution. Thus, in agreement with gas phase calculations,^[15,16] photoexcitation at $\lambda_{\text{pump}} = 310 \text{ nm}$ initially populates the S₁($\pi\pi^*$) excited state of the **EI** form.
2. Although ESIPT processes are expected on the ultrafast timescale, no hints for such dynamic processes were found in our time-resolved TVAS and UPC experiments. Still, ultrafast kinetics on timescales below the experimental IRF of $\sim 150 \text{ fs}$ cannot be excluded on the grounds of limited temporal information on the early dynamic processes directly after photoexcitation. In any case, the first TVA spectrum at $\Delta t = 1 \text{ ps}$ features a vibrational marker band at 1638 cm^{-1} that decays within $\tau_{1, \text{TVAS}} = 50 \text{ ps}$. As this time constant is also found in time-resolved fluorescence measurements ($\tau_{1, \text{UPC}} = 48 \text{ ps}$, $\tau_{1, \text{TCSPC}} \approx 37 \text{ ps}$), the nature of this state can safely be assigned to a bright excited state of $^1\pi\pi^*$ character. Remarkably, however, as illustrated in Fig. 7.2 (c–f), the vibrational marker band of this $^1\pi\pi^*$ state decays towards a permanent positive offset. Thus, a significant fraction ($\sim 50\%$) of the initially excited population is believed to be trapped in this state.

3. As can be seen in Fig. 7.2 (e–f), the excited-state population proceeds in a clear consecutive manner from the bright $^1\pi\pi^*$ towards a successor state with a vibrational marker band at 1603 cm^{-1} . The time profile of this band is characterized by $\tau_{1,\text{TVAS}} = 50\text{ ps}$ as a rise time and $\tau_{2,\text{TVAS}} = 410\text{ ps}$ for subsequent electronic deactivation. Since $\tau_{2,\text{TVAS}}$ is not found in the fluorescence–time profiles, this state is considered optically dark, possibly of $^1n\pi^*$ character.
4. Finally, as this dark state decays, the TVA spectra feature two marker bands at 1678 cm^{-1} and 1555 cm^{-1} , which rise in with $\tau_{2,\text{TVAS}} = 410\text{ ps}$. The fate of this state remains elusive due to the limited time window for probing the molecular dynamics ($\Delta t \leq 1.4\text{ ns}$). Since the late-time marker bands do not correspond to any calculated signatures of ground-state species, they are expected to be associated with a long-lived excited electronic state, possibly of triplet character. Notably, time-resolved fluorescence revealed additional excited-state lifetimes in the nanosecond regime ($\tau_{3,\text{UPC}} = 1.5\text{ ns}$, $\tau_{3,\text{TCSPC}} \approx 3.9\text{ ns}$). Whether these time constants are related to the trapped fraction in the bright $^1\pi\pi^*$ state or associated to the decay of the final state observable in TVAS remains inconclusive.
5. All observed transient dynamic processes follow a strict consecutive pattern in the excited-state manifolds. From the ground-state bleach, no recovery of the initially excited EI ground-state species can be inferred on the picosecond-to-nanosecond timescale.

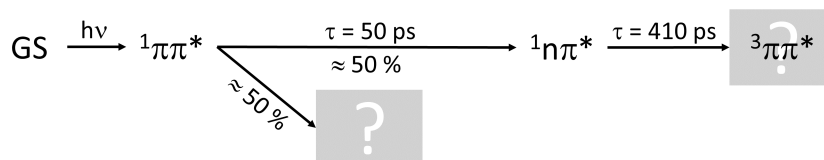


Figure 7.3: Consecutive reaction scheme of photo-excited 3HPA constructed from the time-resolved fluorescence and TVA data.

7.4 Conclusion

In conclusion, the photo-induced electronic deactivation and reaction dynamics of 3-hydroxypicolinic acid in CHCl_3 solution after excitation at $\lambda_{\text{pump}} = 310 \text{ nm}$ has been investigated. The proposed ultrafast excited-state intramolecular proton transfer process towards formation of an H-transferred ground-state species could not be observed. Instead, we have scrutinized a consecutive deactivation pathway including time constants in the picosecond-to-nanosecond timescale. As inferred from time-resolved transient vibrational absorption data and time-resolved fluorescence measurements, a bright $^1\pi\pi^*$ state with a lifetime of $\tau_1 = 50 \text{ ps}$ is populated after photoexcitation. While a fraction of the population gets trapped in this state, electronic deactivation proceeds towards an optically dark state, possibly of $^1n\pi^*$ character. As this dark state decays, a third transient state gets populated within $\tau_2 = 410 \text{ ps}$. Small-amplitude contributions in the fluorescence data ($\tau_{3, \text{UPC}} = 1.5 \text{ ns}$ and $\tau_{3, \text{TCSPC}} \approx 3.9 \text{ ns}$) hint at processes on the nanosecond timescale, which may be associated with the decay of the final successor state or to deactivation processes of the trapped fraction in the bright $^1\pi\pi^*$ state. From the ground-state bleaching signals, no recovery of the initially excited **EI** species could be witnessed within the scope of the 1.4 ns time window of our TVA experiment. Assignment of vibrational marker bands to distinct molecular species in different electronic states either to transient species within an ESIPT pathway or rather to excited-state species upon intermolecular transfer processes with H_2O contaminations remains elusive to this point, unfortunately.

References

- [1] J. L. Herek, S. Pedersen, L. Bañares and A. H. Zewail, *J. Chem. Phys.*, 1992, **97**, 9046–9061.
- [2] S. Lochbrunner, A. J. Wurzer and E. Riedle, *J. Chem. Phys.*, 2000, **112**, 10699–10702.
- [3] S. Ameer-Beg, S. M. Ormson, R. G. Brown, P. Matousek, M. Towrie, E. T. J. Nibbering, P. Foggi and F. V. R. Neuwahl, *J. Phys. Chem. A*, 2001, **105**, 3709–3718.
- [4] S. Lochbrunner, T. Schultz, M. Schmitt, J. P. Shaffer, M. Z. Zgierski and A. Stolow, *J. Chem. Phys.*, 2001, **114**, 2519–2522.
- [5] K. Stock, T. Bizjak and S. Lochbrunner, *Chem. Phys. Lett.*, 2002, **354**, 409–416.
- [6] S. Lochbrunner, A. J. Wurzer and E. Riedle, *J. Phys. Chem. A*, 2003, **107**, 10580–10590.
- [7] C. Schrieffer, M. Barbatti, K. Stock, A. J. A. Aquino, D. Tunega, S. Lochbrunner, E. Riedle, R. de Vivie-Riedle and H. Lischka, *Chem. Phys.*, 2008, **347**, 446–461.
- [8] C. H. Kim and T. Joo, *Phys. Chem. Chem. Phys.*, 2009, **11**, 10266–10269.
- [9] M. Higashi and S. Saito, *J. Phys. Chem. Lett.*, 2011, **2**, 2366–2371.
- [10] J. Lee, C. H. Kim and T. Joo, *J. Phys. Chem. A*, 2013, **117**, 1400–1405.
- [11] L. A. Baker, S. E. Greenough and V. G. Stavros, *J. Phys. Chem. Lett.*, 2016, **7**, 4655–4665.
- [12] J. Pospíšil and S. Nešpurek, *Prog. Polym. Sci.*, 2000, **25**, 1261–1335.
- [13] M. Zayat, P. Garcia-Parejo and D. Levy, *Chem. Soc. Rev.*, 2007, **36**, 1270–1281.
- [14] R. Kumasaka, A. Kikuchi and M. Yagi, *Photochem. Photobiol.*, 2014, **90**, 727–733.
- [15] M. F. Rode and A. L. Sobolewski, *Chem. Phys.*, 2012, **409**, 41–48.
- [16] M. F. Rode and A. L. Sobolewski, *J. Chem. Phys.*, 2014, **140**, 084301.
- [17] G. M. Roberts, H. J. B. Marroux, M. P. Grubb, M. N. R. Ashfold and A. J. Orr-Ewing, *J. Phys. Chem. A*, 2014, **118**, 11211–11225.

- [18] N. K. Schwab and F. Temps, *J. Phys. Chem. A*, 2009, **113**, 13113–13123.
- [19] Y. Zhao and D. G. Truhlar, *Theor. Chem. Acc.*, 2008, **120**, 215–241.
- [20] T. H. Dunning, *J. Chem. Phys.*, 1989, **90**, 1007–1024.
- [21] M. J. Frisch, G. W. Trucks, H. B. Schlegel, G. E. Scuseria, M. A. Robb, J. R. Cheeseman, G. Scalmani, V. Barone, B. Mennucci, G. A. Petersson, H. Nakatsuji, M. Caricato, X. Li, H. P. Hratchian, A. F. Izmaylov, J. Bloino, G. Zheng, J. L. Sonnenberg, M. Hada, M. Ehara, K. Toyota, R. Fukuda, J. Hasegawa, M. Ishida, T. Nakajima, Y. Honda, O. Kitao, H. Nakai, T. Vreven, J. A. Montgomery Jr., J. E. Peralta, F. Ogliaro, M. Bearpark, J. J. Heyd, E. Brothers, K. N. Kudin, V. N. Staroverov, T. Keith, R. Kobayashi, J. Normand, K. Raghavachari, A. Rendell, J. C. Burant, S. S. Iyengar, J. Tomasi, M. Cossi, N. Rega, J. M. Millam, M. Klene, J. E. Knox, J. B. Cross, V. Bakken, C. Adamo, J. Jaramillo, R. Gomperts, R. E. Stratmann, O. Yazyev, A. J. Austin, R. Cammi, C. Pomelli, J. W. Ochterski, R. L. Martin, K. Morokuma, V. G. Zakrzewski, G. A. Voth, P. Salvador, J. J. Dannenberg, S. Dapprich, A. D. Daniels, O. Farkas, J. B. Foresman, J. V. Ortiz, J. Cioslowski and D. J. Fox, *Gaussian 09, Revision D.01*, Gaussian Inc., Wallingford CT, 2013.
- [22] M. L. Laury, S. E. Boesch, I. Haken, P. Sinha, R. A. Wheeler and A. K. Wilson, *J. Comput. Chem.*, 2011, **32**, 2339–2347.
- [23] M. L. Laury, M. J. Carlson and A. K. Wilson, *J. Comput. Chem.*, 2012, **33**, 2380–2387.
- [24] M. Häser and R. Ahlrichs, *J. Comput. Chem.*, 1989, **10**, 104–111.
- [25] F. Weigend and M. Häser, *Theor. Chim. Acta*, 1997, **97**, 331–340.
- [26] F. Weigend, M. Häser, H. Patzelt and R. Ahlrichs, *Chem. Phys. Lett.*, 1998, **294**, 143–152.
- [27] C. Hättig, A. Hellweg and A. Köhn, *Phys. Chem. Chem. Phys.*, 2006, **8**, 1159–1169.
- [28] Turbomole v7.0 2015, a development of University of Karlsruhe and Forschungszentrum Karlsruhe GmbH, 1989–2007, Turbomole GmbH, since 2007; available from <http://www.turbomole.com>.
- [29] A. Hellweg, S. Grün and C. Hättig, *Phys. Chem. Chem. Phys.*, 2008, **10**, 4119–4127.
- [30] R. Ahlrichs, *Phys. Chem. Chem. Phys.*, 2004, **6**, 5119–5121.

- [31] C. Hättig and A. Köhn, *J. Chem. Phys.*, 2002, **117**, 6939–6951.
- [32] A. Köhn and C. Hättig, *J. Chem. Phys.*, 2003, **119**, 5021–5036.
- [33] C. Hättig and F. Weigend, *J. Chem. Phys.*, 2000, **113**, 5154–5161.
- [34] O. Christiansen, H. Koch and P. Jørgensen, *Chem. Phys. Lett.*, 1995, **243**, 409–418.
- [35] J. Schirmer, *Phys. Rev. A: At., Mol., Opt. Phys.*, 1982, **26**, 2395–2416.
- [36] V. V. Troshin, L. A. Sheludyakova and I. V. Mironov, *J. Anal. Chem.*, 2008, **63**, 544–547.

The central goal of this Thesis was the investigation of ultrafast electronic deactivation pathways in both *intra*- and *inter*molecularly H-bonded systems in a time-resolved and structure-sensitive manner. The obtained results provide valuable insight into the crucial role of H-bonding patterns towards efficient electronic deactivation.

- Excited-state *intramolecular* proton transfer (ESIPT) in NPPCA directs the excited-state population towards efficient electronic deactivation within ~ 600 fs at a twisted geometry (*cf.* Chapter 5). Back in the ground state, after structural rearrangement, *intramolecular* H-bonding leads to the formation of a stable photo product within ~ 20 ps.
- As a showcase for *intermolecularly* H-bonded structures, hetero-dimeric frameworks of 2AP·T, which can exist in both the Watson–Crick and Hoogsteen conformations have been investigated (*cf.* Chapter 4). Although electronic deactivation pathways of the 2AP chromophore in the Watson–Crick motif within $\tau = 1.6$ ns remain nearly unchanged when compared to the dynamics of the free monomer (*cf.* Chapter 3), H-bonding in the Hoogsteen form opens up new deactivation pathways associated with a decreased excited-state lifetime (~ 70 ps) and the lack of triplet formation.

Generally, the investigation of photo-initiated de-excitation mechanisms is a challenging task as depopulation of electronically excited states unwinds on the femtosecond-to-microsecond timescale. Spectroscopic pump–probe techniques like transient electronic absorption (TEAS) and time-resolved fluorescence (TRFL) can provide valuable insight into the early molecular dynamics on the ultrafast timescale. However, probing electronic states in the UV/vis region yields rather broad and diffuse transient spectral shapes. Such techniques lack precise information about molecular identity and structural transformations as the dynamics ensue on the potential hypersurface. In order to overcome those limitations, a transient vibrational absorption spectrometer (TVAS) was built within this Thesis. Employing a combination of UV pump and mid-IR probe pulses, this technique allows for identification of individual spectroscopic species on the grounds of structural sensitivity obtained by transient vibrational marker bands that are characteristic for specific molecular structures in different electronic states. Aided by quantum chemical calculations, characteristic vibrational marker bands can be assigned to specific molecular structures in distinct electronic states. Thus, the combination of theoretical calculations and experimental measurements allows for understanding the dynamic electronic deactivation and reaction pathways on the potential energy hypersurfaces encrypted in the spectro-temporal evolution of the time-resolved TVA spectra.

TVAS has been used to elucidate the electronic deactivation and reaction dynamics of 2-aminopurine (2AP) incorporated in *intermolecular* H-bonding motifs with thymine

(T) in Watson–Crick (WC) and Hoogsteen (HS) conformations as a model system for intermolecularly H-bonded systems.

Towards these ends, TVAS was used to investigate the photo-induced dynamics of free 2AP in a first step (*cf.* Chapter 3). Photoexcitation to the $^1\pi\pi^*$ state is followed by initial vibrational and solvational relaxation dynamics within

$$\tau_{\text{VC}} = 3.0 \pm 1.0 \text{ ps.}$$

Upon decay of the initially prepared $^1\pi\pi^*$ state within

$$\tau_{2\text{AP}} = 740 \pm 15 \text{ ps,}$$

the TVA data feature partial ground-state recovery and the concurrent rise of vibrational marker bands associated with $^3\pi\pi^*$ formation. On the grounds of high triplet yields ($\phi_T \sim 0.42$) and kinetic model simulations, a transient short-lived ($\tau \leq 100$ ps) intermediate electronic state of $^1n\pi^*$ character has been proposed to guide the excited-state population towards ground-state recovery and efficient intersystem crossing.

With these premises, a mixture of 2-aminopurine and thymine consisting of free 2AP, free T, homo-dimeric T·T and hetero-dimeric 2AP·T in Watson–Crick and Hoogsteen conformations has been investigated (*cf.* Chapter 4). Upon determination of thermodynamic association equilibria *via* evaluation of concentration-dependent binding constants, spectro-temporal features of 2AP·T in the WC and HS conformations could be isolated from the TVA spectra of the 2AP + T mixture. Aided by *ab initio* quantum chemical structure calculations, the minimum structure of the photo-excited 2AP chromophore within the WC motif resembles the $^1\pi\pi^*$ minimum structure of free 2AP to a high extent. While H-bonding with T exerts little effect on the structural integrity of the 2AP moiety in the WC form, the relative energetic order of the electronically excited states and their respective crossings are strongly affected by H-bonding. Accordingly, electronic deactivation of the photo-excited $^1\pi\pi^*$ state proceeds within

$$\tau_{2\text{AP}\cdot\text{T}, \text{WC}} = 1.6 \pm 0.4 \text{ ns}$$

in the WC conformation, significantly prolonged with respect to de-excitation of free 2AP. Still, in line with the structural similarity of free 2AP and the 2AP chromophore in the WC H-bonding motif, incomplete ground-state recovery and concurrent triplet formation upon $^1\pi\pi^*$ decay within $\tau_{2\text{AP}\cdot\text{T}, \text{WC}}$ hint at mostly unchanged overall deactivation pathways.

Surprisingly, however, the kinetics associated with 2AP·T in the HS conformation revealed a novel route for direct internal conversion towards ground-state recovery within

$$\tau_{2\text{AP}\cdot\text{T}, \text{HS}} = 68 \pm 15 \text{ ps.}$$

As our computed excited-state minimum structure suggests, H-bonding of 2AP with T in the HS motif results in a bent 2AP moiety in the initially prepared $^1\pi\pi^*$ state. This distorted structure opens up new deactivation pathways towards ground-state recovery.

In order to explore the possible coordinates for electronic deactivation, the feasibility of double proton transfer (DPT) in the WC and HS conformations has been investigated on computational grounds. Accordingly, single proton transfer from 2AP to T is predicted to be followed by a second proton transfer from T to 2AP in the photo-excited $^1\pi\pi^*$ state of both H-bonding motifs. Still, only for 2AP·T in the HS conformation, the excited-state DPT is associated with a conical intersection with the ground state as an efficient route for electronic deactivation. While excited-state DPT in the HS form within $\tau_{2AP\cdot T, HS}$ is in perfect agreement with our experimental TVA data, other deactivation pathways for internal conversion may be possible as well. More elaborate quantum chemical calculations would be required to explore other degrees of freedom, like out-of-plane ring puckering modes as possible pathways for direct electronic deactivation towards recovery of the ground state.

Currently, 2AP is widely used as an intrinsic fluorescence probe to gain information about structural motifs within single- and double-stranded DNA. Generally, fluorescence studies on duplex DNA report lifetimes of $\tau_1 < 100$ ps, $\tau_2 \sim 0.5$ ns, $\tau_3 \sim 2$ ns and $\tau_4 \sim 10$ ns. The broad distribution of excited-state lifetimes is widely ascribed to *intrastrand* charge-transfer and stacking interactions. One should note, however, the similarity of τ_1 and τ_3 with $\tau_{2AP\cdot T, HS}$ and $\tau_{2AP\cdot T, WC}$, respectively, found by investigation of purely H-bonded 2AP in the WC and HS conformations in this Thesis. Furthermore, recent research found transient HS conformations as abundant H-bonding motifs in duplex DNA. These findings suggest that the established picture for quenching of excited-state lifetimes of 2AP within duplex DNA may need to be revised. Systematic and more elaborate studies on stacked and H-bonded model systems have to be performed to further elucidate the dynamic interplay of *intrastrand* and *interstrand* interactions within duplex DNA. Towards these ends, future studies may focus on 2AP-labelled dinucleotide model systems and DNA hairpins.

The relaxation and reaction dynamics of 2-acetylpyrrole (2AcPy) were investigated as a model system for excited-state *intramolecular* proton transfer (ESIPT) and compared to respective measurements of its N-methyl analogue 2-acetyl-1-methylpyrrole (Me2AcPy), where *intramolecular* H-bonding is blocked by insertion of a methyl group (*cf.* Chapter 6). For both chromophores, ultrafast initial wave packet dynamics away from the Franck–Condon region was observed within the first 250 fs after photoexcitation to the $S_2(\pi\pi^*)$ state. As inferred from

$$\tau_{VC} \sim 8 \text{ ps},$$

within the ground-state recovery, a significant fraction of the excited-state population deactivates directly towards the electronic ground state. For the remaining excited-state fraction, internal conversion to the lower-lying $^1n\pi^*$ state proceeds within

$$\tau \sim 4 \text{ ps.}$$

The $^1n\pi^*$ state was found to survive on the scope of our time-resolved measurements and is believed to ultimately drive the excited-state population towards intersystem crossing with the triplet manifold. Overall, the combined time-resolved data on 2AcPy resemble the transient features of Me2AcPy, which is incapable of ESIPT. Still, minor indications for formation of an H-transferred species of 2AcPy in the electronic ground-state on the ns-timescale could be obtained from TVA data in acetonitrile solution. In cyclohexane solution, 2AcPy exists in a temperature-dependent equilibrium between free 2AcPy and homo-dimeric 2AcPy. Additional time constants in the TVA spectra could be ascribed to dimer kinetics. Most notably, however, no indications for ESIPT could be found in the 2AcPy monomer signatures in cyclohexane as opposed to the measurements in acetonitrile. Additional vibrational mode calculations and experiments are required to assess all vibrational marker bands in the TVA spectra.

Moreover, the electronic deactivation and reaction pathways of 3-hydroxypicolinic acid (3HPA) were investigated as this compound was proposed as a molecular switch on the grounds of quantum chemical calculations. No evidence for the proposed switching properties upon excited-state *intramolecular* double proton transfer (ESIDPT) could be found in the combined time-resolved experimental data. In fact, transient features in the TVA data did not match the calculated vibrational marker bands of any computed structure. However, in combination with time-resolved fluorescence measurements, the clear consecutive kinetics found in TVA data hint at an excited-state decay of the initially prepared $^1\pi\pi^*$ state within

$$\tau_1 = 48 \pm 3 \text{ ps}$$

towards transient population of a $^1n\pi^*$ state. This dark state is believed to mediate the excited-state population towards intersystem crossing with the triplet manifold within

$$\tau_2 = 410 \pm 120 \text{ ps.}$$

No ground-state recovery was observed on the 1.4 ns scope of our TVA experiment. The occurrence of an additional low-amplitude nanosecond component in fluorescence measurements ($\tau \approx 1.5 - 3.9 \text{ ns}$) is tentatively ascribed to the lifetime of the triplet state.

More elaborate quantum chemical calculations are required to assign the observed transient TVA spectra to distinct excited-state molecular species. Note, however, that 3HPA was contaminated with water residues trapped in the crystalline framework of the sample, further aggravating a distinction between *intramolecular* H-bonding dynamics and

intermolecular dynamics involving water molecules.

Generally, however, *intramolecular* excited-state proton transfer processes belong to the fastest chemical reactions known with timescales down to just a few tens of femtoseconds. Recently, so-called twist-assisted ESIPT has been proposed for the application of efficient bistable photochromic molecular switches. In this approach, the ultrafast timescale of ESIPT is corroborated by efficient electronic deactivation *via* a conical intersection with the electronic ground state at twisted molecular conformation as commonly found for prototypical molecular structural switches like azobenzene and spiropyran.

Within the scope of this Thesis, the twist-assisted ESIPT switch NPPCA was investigated in a comprehensive study in acetonitrile and aqueous solutions by a combination of quantum chemical calculations and time-resolved fluorescence spectroscopy, transient electronic absorption spectroscopy, and transient vibrational absorption spectroscopy (*cf.* Chapter 5). Electronic deactivation after photoexcitation has been found to be completed on the ultrafast timescale within

$$\tau_1 = 90 \pm 10 \text{ fs}$$

and

$$\tau_2 = 610 \pm 10 \text{ fs}$$

via H-transferred transient excited-state species. Upon efficient de-excitation towards the ground state at a twisted structure, incomplete ground-state recovery and, more importantly, formation of a photoproduct with different structural H-bonding motifs and altered electronic absorption properties was witnessed after vibrational cooling within

$$\tau_3 = 5.10 \pm 0.80 \text{ ps}$$

and

$$\tau_4 = 20.0 \pm 1.0 \text{ ps.}$$

The photoproduct is computed to be stable in the ground state and survives on the nanosecond timescale of our time-resolved experiments. Attempts to isolate the product form on the microsecond timescale and beyond, however, were rendered unsuccessful.

In order to further improve bi-stability, chemical modification of NPPCA could be applied. Towards these ends, the reaction pathway established for NPPCA could be extended by an additional stabilizing H-bonded species in the ground state.

For transient vibrational absorption spectroscopy measurements in Kiel, a modified version of the LabVIEW program for transient electronic absorption spectroscopy by Dr. Katharina Röttger was used. All values with respect to distances and positions of the delay stage are given in femtoseconds. The complete graphical user interface for TVAS measurements is shown in Fig. 9.1 and features the following items:

- **Message** gives the current status and type of a measurement or indicates an error message. A measurement in progress is also indicated by the green (busy) light.
- **Current position (fs)** states the current position of the delay stage.
- Additional information about the measurement conditions may be noted in the controls labeled **Sample**, **Solvent**, *etc.*
- **number scans/delay step** refers to the number of transient spectra per delay step and may be set to a maximum value of 10,000.
- The **File path** can be set to save the measured data on a user-defined location on the hard drive. Automatic saving of the data may be disabled by the Boolean **SaveAfterScan**.
- The three **graphs** map the progress of a running measurement at each delay step.
 - The panel **IR spectrum** displays the spectra of the mid-IR probe and reference pulses on the two MCT detector arrays. The assignment of probe and reference on the arrays may be changed by the **switch_probe_ref** Boolean. For probe-only measurements, the **referencing** Boolean is disabled and the intensity of the reference pulses is set to 1. This is the preferred measurement mode at present.
 - The transient change in optical density at each delay step, *i.e.* the current transient spectrum, is depicted in the **IR absorption** panel.
 - **2D plot** maps the spectro-temporal evolution on the fly as the measurement proceeds.

For conducting an actual time-resolved measurement, the following runtime menus may be employed:

- *Spectrometer Control*
 - **Change Spectrometer Settings** in terms of mid-IR probe wavelength, grating with desired spectral resolution, and entrance slit (*cf.* Fig. 2.6).
 - **Set Integration Time** for appropriate read-out of the integrator, which can readily be visualized by the appendant oscilloscope.
 - **Change Gain and Trim** to alter the amplification voltage specific for each of the MCT pixels. Do not change these settings unless you know what you are doing.

- *Translation Stage*
 - **Move absolute** moves the delay stage to an absolute, user-defined position.
 - **Move relative** moves the delay stage by a relative, user-defined value.
 - **Go home** moves the delay stage to a predefined home position.
 - **Get position** updates the current position display on the graphical user interface.

- *Delays*
 - **Set Delays** to manage the temporal profile of the transient measurements. It allows to set the number and size of delay steps and the maximum delay time for a temporal scan. In this sub-VI, two sets of linear step sizes may be entered. The remaining delay distance between the sum of all linear steps and the entered maximum delay time will automatically be supplemented by exponentially increasing delay steps.

- *Measure*
 - **Take Background Measurement (Probe Pulses Blocked)** to set the baseline bias current of the MCT detector pixels prior to measurements.
 - Finally, the option **Take Temporal Scan** performs a time-resolved measurement using all the parameters entered above.

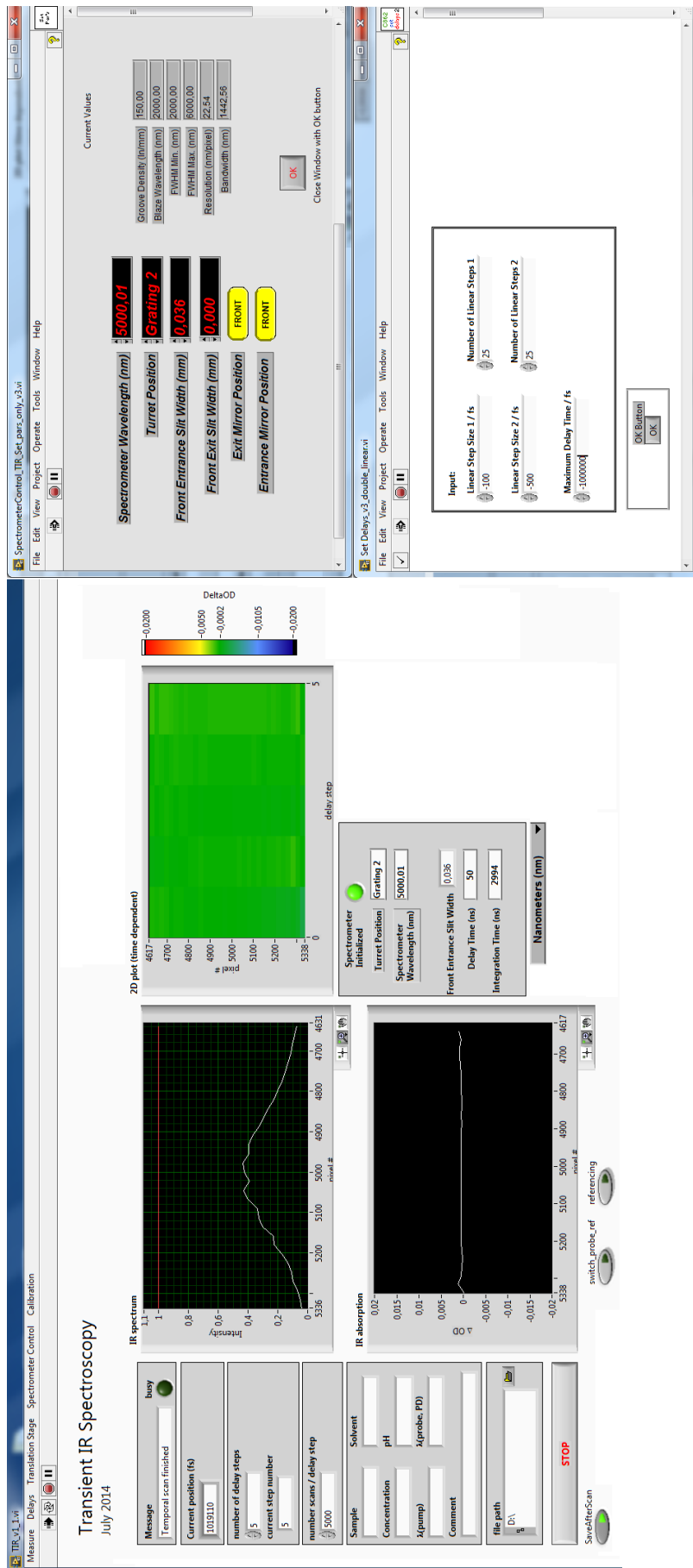


Figure 9.1: Graphical user interface of the LabVIEW program for TVAS measurements in Kiel.

List of Figures

1.1	Schematic H-transfer mechanisms.	2
1.2	Illustration of Watson–Crick H-bonded canonical nucleobases and double-stranded B-DNA.	3
1.3	Structure of 2AP.	4
1.4	Structure of 2AP·Thy.	5
1.5	Structure of 2AcPy and its ESIPT species.	5
1.6	Photochromic bistable molecular switches.	6
1.7	Reaction pathways of NPPCA.	7
1.8	Reaction pathways of 3HPA.	7
2.1	Schematic illustration of TVAS as an example of time-resolved pump–probe spectroscopic techniques.	17
2.2	Schematic flow chart of the experimental TVA setup.	18
2.3	Detailed scheme of the experimental TVA setup.	20
2.4	Phase-matching conditions for near-IR (signal and idler) and mid-IR (DFG) pulses.	22
2.5	Broadband spectral range of mid-IR probe pulses.	23
2.6	Illustration of the mid-IR beampath within the grating spectrograph.	24
2.7	Spectro-temporal two-dimensional TVA data matrix of photo-excited ZnSe.	25
3.1	Steady-state UV absorption spectrum and time-resolved fluorescence time-profile of 2AP in CHCl ₃	39
3.2	Energy diagram of 9Me-2AP in different electronic states.	40
3.3	Comparison of experimental FTIR spectrum of 2APr in CHCl ₃ solution with calculated vibrational marker modes in the GS.	41
3.4	Experimentally observed and calculated vibrational marker modes of 2APr and 9Me-2AP.	42
3.5	Results of the TVA measurements on 2AP in CHCl ₃	44
3.6	Kinetic model predictions for electronic deactivation of 2AP.	49
3.7	Sketch of the proposed electronic deactivation pathways in 2AP after ¹ ππ* excitation.	50
3.8	Atom numbering of the TBDMS protected 2AP riboside.	59
4.1	Calculated and experimental FTIR spectra of 2AP, T, T·T and 2AP·T.	70
4.2	Molecular species present in the 2AP + T mixture.	71

4.3	UV/vis, computed VEEs and TRFL data of 2AP and the 2AP + T mixture.	72
4.4	TVA data of 2AP, 2AP + T and 2AP·T in CHCl ₃	74
4.5	Computed vibrational ground-state modes of 2AP and 2AP·T dimers in WC and HS conformations.	75
4.6	Two-dimensional spectro-temporal plot of TVA data for the 2AP + T mixture.	76
4.7	Proposed electronic deactivation pathways for 2AP and 2AP·T in WC and HS conformations.	80
4.8	Potential energy curves along the H-atom transfer coordinate for 2AP·T in the WC and HS conformations.	82
5.1	Reaction scheme of the bistable ESIPT switch (NPPCA, I) upon UV photoexcitation.	93
5.2	UV/vis absorption spectra of NPPCA in acetonitrile and aqueous solutions.	97
5.3	TEAS data for NPPCA in acetonitrile and aqueous solutions.	99
5.4	Transient absorption–time profiles of NPPCA in acetonitrile.	102
5.5	TVA data following excitation of NPPCA in ACN at $\lambda_{\text{pump}} = 266 \text{ nm}$	104
5.6	Proposed photo-induced proton transfer scheme for ESIPT switch NPPCA.	105
5.7	ORTEP plot of NPPCA with labeling and displacement ellipsoids.	115
5.8	Calculated ground-state structures of NPPCA in form I and form IV	118
5.9	Calculated UV/VIS spectra of NPPCA in forms I and IV at the CC2/aug-cc-pVDZ level of theory.	122
5.10	Computational results pertaining to the ground-state and excited-state potential energy surfaces for NPPCA.	122
5.11	Comparison of the transient absorption-time profiles of NPPCA in acetonitrile and aqueous solutions.	123
5.12	Transient absorption–time profiles of NPPCA in H ₂ O.	124
5.13	Decay-associated spectra and SVD time profiles for NPPCA in H ₂ O.	125
5.14	Decay-associated spectra and SVD time profiles for NPPCA in acetonitrile.	126
5.15	FTIR spectrum of NPPCA in CHCl ₃ compared with calculated vibrational spectra for I and IV	127
5.16	Vibrational marker modes of the electronic ground state species I and IV	128
5.17	Comparison of the measured TVA spectrum at $\Delta t = 850 \text{ ps}$ with calculations for I and IV	129
5.18	Schematic reaction pathways of the next generation ESIPT switch.	130
5.19	Calculated vibrational spectra for the next generation ESIPT switch.	131
6.1	Chemical structures of 2-acetylpyrrole, 2-acetyl-1-methylpyrrole and the H-transferred product of 2AcPy.	135
6.2	Steady-state UV/vis absorption spectra of 2AcPy and Me2AcPy in acetonitrile solution.	139
6.3	Potential energy surface scan along the CO bond length for 2AcPy and Me2AcPy.	140

6.4	Vibrational marker bands of 2AcPy and Me2AcPy in various electronic states.	141
6.5	TEA spectra of 2AcPy and Me2AcPy at different delay times upon 266 nm excitation into the $S_2(\pi\pi^*)$ state.	142
6.6	Transient vibrational absorption spectra of 2AcPy and Me2AcPy in the region of ring vibrations.	144
6.7	Transient vibrational absorption spectra of 2AcPy and Me2AcPy in the region of the CO and CC stretch vibrations.	145
6.8	TVA data for 2AcPy in cyclohexane solution.	149
7.1	Schematic reaction route for 3HPA by intramolecular double proton transfer <i>via</i> possible transient species.	157
7.2	Experimental electronic and vibrational data of 3HPA.	161
7.3	Consecutive reaction scheme of photo-excited 3HPA.	163
9.1	GUI of the TVAS LabVIEW program.	177

List of Tables

2.1	Calculated wavelength range for near-IR and mid-IR generation.	30
3.1	Cartesian coordinates for the optimized structure of 9Me-2AP in the ground electronic state at the M062X / 6-311+G** level of theory.	60
3.2	Cartesian coordinates for the optimized structure of 9Me-2AP in the $^1\pi\pi^*$ state at the RI-CC2 / def2-TZVPPD level of theory.	61
3.3	Cartesian coordinates for the optimized structure of 9Me-2AP in the $^1n\pi^*$ state at the RI-CC2 / def2-TZVPPD level of theory.	62
3.4	Cartesian coordinates for the optimized structure of 9Me-2AP in the $^3\pi\pi^*$ state at the RI-CC2 / def2-TZVPPD level of theory.	63
3.5	Calculated vertical excitation energies (VEEs) for 9Me-2AP.	64
4.1	Vertical excitation energies (VEEs) calculated for free 2AP and H-bonded Watson–Crick (WC) and Hoogsteen (HS) 2AP·T dimers.	89
5.1	Calculated vertical excitation energies for NPPCA.	97
5.2	Crystal data and structure refinement parameters for NPPCA.	116
5.3	Bond lengths and angles for NPPCA.	117
5.4	Hydrogen bond lengths and angles between acceptor A and donor D in the NPPCA crystal structure.	117
5.5	Cartesian coordinates for the optimized structure of I at the RI-MP2/aug-cc-pVDZ level of theory.	119
5.6	Cartesian coordinates for the optimized structure of IV at the RI-MP2/aug-cc-pVDZ level of theory.	120
5.7	Vertical excitation energies of I , IV , V , VI and VII at the CC2/ cc-pVDZ level of theory for MP2/cc-pVDZ optimized geometries.	121
6.1	Vertical excitation energies of 2AcPy, 2HEP and Me2AcPy at the RI-SCS-CC2/ def2-TZVPP level of theory for RI-SCS-MP2/def2-TZVPP optimized geometries.	140
6.2	Results of the meta-optimization for important points on the PES of 2AcPy.	154

